THE UNIVERSITY *of* EDINBURGH

This thesis has been submitted in fulfilment of the requirements for a postgraduate degree (e.g. PhD, MPhil, DClinPsychol) at the University of Edinburgh. Please note the following terms and conditions of use:

This work is protected by copyright and other intellectual property rights, which are retained by the thesis author, unless otherwise stated.
A copy can be downloaded for personal non-commercial research or study, without prior permission or charge.
This thesis cannot be reproduced or quoted extensively from without first obtaining permission in writing from the author.
The content must not be changed in any way or sold commercially in any format or medium without the formal permission of the author.
When referring to this work, full bibliographic details including the author, title, awarding institution and date of the thesis must be given.

The Fracture Mechanics of Bacterial Colonies Growing in Soft Gels

Edward Muir

Doctor of Philosophy
The University of Edinburgh
October 2020

Abstract

When submerged in agarose gels, growing *Escherichia coli* (*E. coli*) form lenticular colonies. In this thesis I first present a study on the origin of this morphology. Using single plane illumination microscopy, I record the full 3D morphology of growing *E. coli* colonies for the first time. By adding fiducial markers to the gel, I measured the displacement of the gel surrounding the growing colonies. These measurements revealed that as *E. coli* undergo binary fission, growing from a single bacterium into a colony of $\sim 10^6$ cells, they fracture the gel around them.

However, this fracture process cannot be described by simple linear elastic fracture mechanics. Instead, fractures opened up by expanding colonies undergo a transition in propagation mode, changing from one where the gel is fractured over the entire crack surface, to one where the gel is fractured in a single plane. To my knowledge, this is the first time this transition has been measured, showing the potential of using bacteria to explore small scale fracture mechanics. The observed transition in fracture mode is consistent with cavitation theory, suggesting that at small scales the pressure required for colony growth is independent of the gel's fracture energy. This independence may mean that bacteria can grow in far tougher materials than would previously have been expected.

In a second study I develop an apparatus that can inject oil bubbles into agarose at the same length and time scales as bacterial colonies grow, effectively creating a physical simulation of colony growth. With this apparatus I show that there is little difference between fractures propagated by a Newtonian fluid and those propagated by a colony of *E. coli*. In fact, what morphological differences could be observed can be plausibly explained by the difference in interfacial energy between the agarose-*E. coli* and agarose-oil interface. This means that in the future hydraulic fracture theories may be applied wholesale to predictions of bacterial infiltration into materials.

In a final study, the elastic and fracture properties of agarose were measured using a custom apparatus to perform Rivlin and Thomas's pure shear test. The fracture energy was found to be in reasonable agreement with the theory of Lake and Thomas, being of order $0.4\,\mathrm{J\,m^{-2}}$ for 2 % agarose. The fracture energy was found to be independent of the fracture rate below cross head speeds of $0.01\,\mathrm{mm\,s^{-1}}$, meaning that the viscous dissipation in the gel surrounding the colonies is small and that the measurements made in this study are applicable to predictions of the slowly growing colony morphology.

Lay Summary

Many discoveries in science have come as a result of studying structures found in the natural world. For example studying the structure of beetle scales has helped scientists to create better iridescent materials or, by looking at the shape of kingfisher bills, they have created more aerodynamic bullet trains. In this work I attempt to use bacteria growing submerged in a gel to reveal new physics concerning fracture mechanics.

I first observed bacteria growing submerged in a gel. Starting with a single cell, the bacteria replicate and grow into a colony consisting of many millions of cells. In doing so they break the gel around them. However, the shape of the resulting colony is not what would be expected if the bacteria were to break the gel in accordance with classical theories of fracture. Bacterial colonies therefore present an opportunity to observe how the propagation of fractures changes at small scales.

The change in fracture mechanism has to do with a concept called flaw size independence. The effect of this concept can be observed using a simple experiment. Hold a sheet of paper along opposite edges and attempt to pull it apart. Now take a new sheet of paper and make a cut several cm long with scissors to introduce a "flaw". Attempt to pull this flawed sheet apart, you will find it much easier than with the unflawed sheet. This is because stress concentrates at the tip of the flaw, magnifying the force that you apply to the paper. However, when the flaw is smaller than a certain size, this force magnifying effect breaks down and the same force will be required to break the material independent of the flaw size. The physics behind the break down of the magnifying effect is not well understood, primarily because it is difficult to design experiments with which to observe small scale (and often rapidly growing) flaws. Bacterial colonies may present a solution to these experimental problems.

The bacterial colonies that I observed straddle the material length scale important for flaw size independence. In this work I report how the transition between growth at a length scale where stresses are not concentrated to one where they are can explain colony morphology. The transition in growth modes has implications for the growth of bacteria in solids, allowing them to grow in far tougher materials than would previously have been assumed.

Of course determining how much of the colony shape is due to the biology of the bacteria and how much is due to this transition in fracture mode is a concern. Therefore, in a second study, I create a physical simulation of the growing bacterial colonies, by injecting oil into the gel. This reveals that the fractures filled by bacterial colonies in this work grow in the same way as fracture filled with a simple fluid. By making this comparison, theories to do with the propagation of fluid filled fractures can be safely applied to bacterial colonies.

Declaration

I declare that this thesis was composed by myself, that the work contained herein is my own except where explicitly stated otherwise in the text, and that this work has not been submitted for any other degree or professional qualification except as specified.

(*Edward Muir, October 2020*)

Acknowledgements

First I'd like to thank Wilson Poon for his insight into matters both on and off topic throughout my PhD. I would also like to thank various members of the soft matter physics group. Specifically my second supervisor Bartek Waclaw, for his crucial role in the inception of many of the ideas in this work. I give my thanks to Andrew Schofield, Jochen Arlt, Angela Dawson and Thomas Glen for their help and patience with all things experimental. I'd also like to thank Andrew Garrie for turning many of my half-baked plans into functioning experimental equipment.

I'd like to thank the EPSRC for funding my PhD. I am especially grateful for their swift response during the pandemic, providing additional funding to cover the delays that it incurred to my research.

I am indebted both to Robert Style and Eric Dufresne at ETH Zürich and to Christopher Barney and Alfred Crosby at UMass Amherst. Both of these groups contributed a great deal to the ideas in this work and their enthusiasm for science was truly an inspiration, helping me see the usefulness of my research.

Thanks to all the people of Faff and Ratclifffe Terrace, Joshua Williams especially for dragging me up mountains and proofreading this thesis. Also to Samuel Griffith for putting up with all of my irrelevant questions.

Finally I'd like to thank my parents, grandparents, William, and Oscar for their constant reminder to do what makes you happy.

Contents

List of Figures

List of Tables

Chapter 1

Introduction

The study of morphology in nature is one with a long history. With its foundations in works such as D'Arcy Thompson's 'On Growth and Form' who described the correlations between physical forms and mechanical phenomena, there has been a long quest to describe the shapes seen in nature using physics [1–4]. For example, pollen tubules grow by supplying one region of their cell wall with new material so that it is kept in a fluid state. The cell wall expands in the direction of the fluid region by exploiting the pressure differential across the cell wall. It was found that curvature at the tip of these tubules could be described by a single parameter relating the material transport rate and pressure differential. Moreover, this simple relationship was enough to broadly explain the variation of tubule forms seen across many species of plants, fungi and some bacteria [5–8]. Such examples have shown how seemingly complex systems can be described with surprisingly simple physics.

On the other hand, the morphology of nature has taught us a great deal about physics. Examples include the study of beetle scale structures that has lead to advances in structural colour [9, 10], or how ultra adhesive pads have been made by mimicry of the fibrillar structure found on the foot pads of geckos [11, 12], amongst many others [13, 14].

This work began as an exercise in describing the morphology of nature with physics. Specifically, I study how bacteria grow when they are immobilized in a gel. Undergoing binary fission, and given a sufficiently abundant nutrient source, a single submerged bacterium will grow into a colony of $\sim 10^6$ cells over a 24 hour time period. Such colonies have been observed to form lenticular or ellipsoidal

morphologies under certain conditions. Like the early works of D'Arcy Thompson et al. I attempt to explain the origin of this morphology using physical theories, in this case fracture mechanics.

The work then progresses into an attempt to use colony morphology to reveal new physics. By showing that colonies of bacteria behave similarly to a Newtonian fluid, I use the colonies as a novel probe of small scale fracture mechanics. I attempt to observe deviations from the classical theory of fracture mechanics at small scales and show that once again nature may inform our understanding of physics.

The thesis is structured as follows:

Chapter 2 briefly introduces previous research on bacterial colonies. The transition from growth in a two dimensional plane to the third dimension is discussed, as well as the relevance of 3D colonies to applications such as food safety and cancer metastasis.

Chapter 3 presents an overview of fracture mechanics at small scales and in soft materials. The chapter covers the theory of linear elastic fracture mechanics and then introduces research into how this theory might be modified for the soft materials that bacterial colonies grow in.

Chapter 4 describes the methodology used to image and analyse the growth of submerged bacterial colonies.

In **Chapter 5** the results of my study on the morphology of bacterial colonies are presented. I show that colonies grow by fracturing the gel around them and that the scale of that fracture makes colonies a unique tool for studying small scale fracture mechanics.

In **Chapter 6** I show that bacterial colonies behave in the same way as a hydraulic fracture by comparing their growth to that of oil droplets grown at similar length and time scales.

Chapter 7 gives the results of ancillary experiments performed to measure the properties of the materials used in the previous chapters. Specifically a method of measuring the fracture energy of extremely soft materials is outlined.

Finally, in **Chapter 8** conclusions are drawn and the main findings of the thesis underlined.

Chapter 2

Bacterial Colonies

2.1 Introduction

The ancestors of modern bacteria were amongst the first life forms on Earth and have since expanded into almost every available habitat [15–17]. From mundane soils and water bodies to the depths of the Mariana Trench [18] and even in radioactive waste [19], bacteria have been able to adapt and grow. By adapting to these environments, bacteria have developed numerous biochemical and mechanical mechanisms that have proved both beneficial and detrimental to humanity. For instance, bacteria are able to break down almost any material by evolving new chemical processes. This ability has been put to great use in bioremediation, where bacteria find applications from sewage treatment to cleaning up oil spills [20–23]. Of course this same adaptability has allowed bacteria to flourish on (and in) nearly all food stuffs, contaminating them and causing spoilage which leads to disease.

One of the most important adaptations that bacteria can develop to aid their growth in hostile environments is the ability to form colonies or biofilms. Colony formation is caused by the immobilization of bacteria, either due to encapsulation in a material or adhesion to a surface. Once immobilized, bacteria are forced to grow in tightly packed clusters, forming clonal populations. Being part of a colony can confer multiple selective benefits to a bacterium, for example nutrient sources can be trapped for the sole exploitation of a bacterium's progeny or, due to the structure of the colony, resistance to hostile environs such as increased

temperature or the presence of antibiotics can be improved [24, 25].

Biofilms take the advantages of colonies a stage further. By excreting an extracellular polymeric substance, bacteria form a matrix in which they can both cooperate metabolically with other cells in the biofilm and provide another degree of protection against mechanical or chemical attack [26, 27]. In fact the degree of mechanical protection that a biofilm provides can cause many problems, for example biofilms that adhere to to hulls of ships cause additional drag or damage propellers [28]. Another advantage that biofilm formation holds over clonal colony formation is the ability for multiple species of bacteria to be present in the biofilm, the different species form complex networks of cooperation dividing chemical breakdown pathways amongst themselves to minimize their energy expenditure [27, 29, 30].

In this work I am interested in the simpler of the two systems, clonal colonies formed by immobilization. On surfaces, these colonies display a wide range of morphologies, from circularly symmetric disks to rhizoidal or umbonated forms[1]. These forms are used as species or phenotype identifiers in applied microbiology [31] and have drawn the attention of physicists in the past, as examples, e.g., of fractal growth under nutrient limited conditions [32]. There is currently a renaissance of interest in such simple multi-cellular communities on surfaces. Inter-cellular and cell-substrate mechanical interactions have been shown to be important in determining morphology [33]. Two-dimensional bacterial colonies have also been studied as a new class of "active nematic liquid crystal" in which particle number is not conserved [34, 35]

Sub-surface colonies have received considerably less attention, likely due to the shortage of suitable imaging techniques. To date, research on submerged bacterial colonies has been driven by the need to understand food contamination. These studies [36–40] focus on the biological challenges faced by cells growing in an immobilizing matrix, investigating their growth rates, the pH gradients established around colonies, or their resistance to decontamination treatments. However, in striking contrast to surface colonies, the morphologies of submerged bacterial colonies and their origins have remained largely unknown.

[1] A rhizoidal form is one that resembles the root structure of a plant, whilst an umbonated form is one which has a conical protuberance on its surface.

2.2 Submerged Bacterial Colonies

The first to look at the structure of submerged bacterial colonies were Mitchell and Wimpenny in 1996 [41]. Using a simple light microscope they looked at the effect of agar concentration, cell motility and cell species on the growth and structure of submerged colonies. They were the first to observe that above a critical agar concentration of 0.65 %, motile species of bacteria including *Pseudomonas aeruginosa*, *E. coli*, *Salmonella enterica* and *Listeria monocytogenes* formed lenticular/ellipsoidal shaped colonies, Figure 2.1a. The lenticular shape was hypothesised to result from the splitting of the agar along some fault line in the agar due to the hydrostatic pressure exerted by the growing colonies, though no further evidence for this splitting was given.

Several other morphologies were observed. When the species of bacteria were known to hydrolyse agar, as was the case for *Bacillus cereus*, dendritic or rhizoidal colonies were formed independent of the agar's concentration, Figure 2.1b. When motile species were grown in agar below the critical 0.65 % concentration, large spherically symmetric and diffuse colonies were formed, presumably due to the free movement of the bacteria through the gel network so that the shape was determined by diffusion as much as any mechanical interaction with the gel, Figure 2.1c. For non-motile species grown in agar above 0.65 %, small and dense colonies were formed with pronounced lobes, Figure 2.1d.

Beyond Wimpenny's first observations little further research has been carried out with regards to characterizing and explaining the morphology of submerged bacterial colonies. What research there is generally concerns their effect on the chemical environment around the colony. For example, Malakar et al. measured the pH change around colonies of *Lactobacillus curvatus*. They found a distinct pH gradient between the interior and exterior of the colonies, hypothesizing that this would produce zones of differing growth rate [42]. Another study looked at the effect of inoculum concentration. They found that final colony dimensions decreased with increasing inoculation concentration and, more interestingly, were independent of the initial nutrient (glucose) concentration [37].

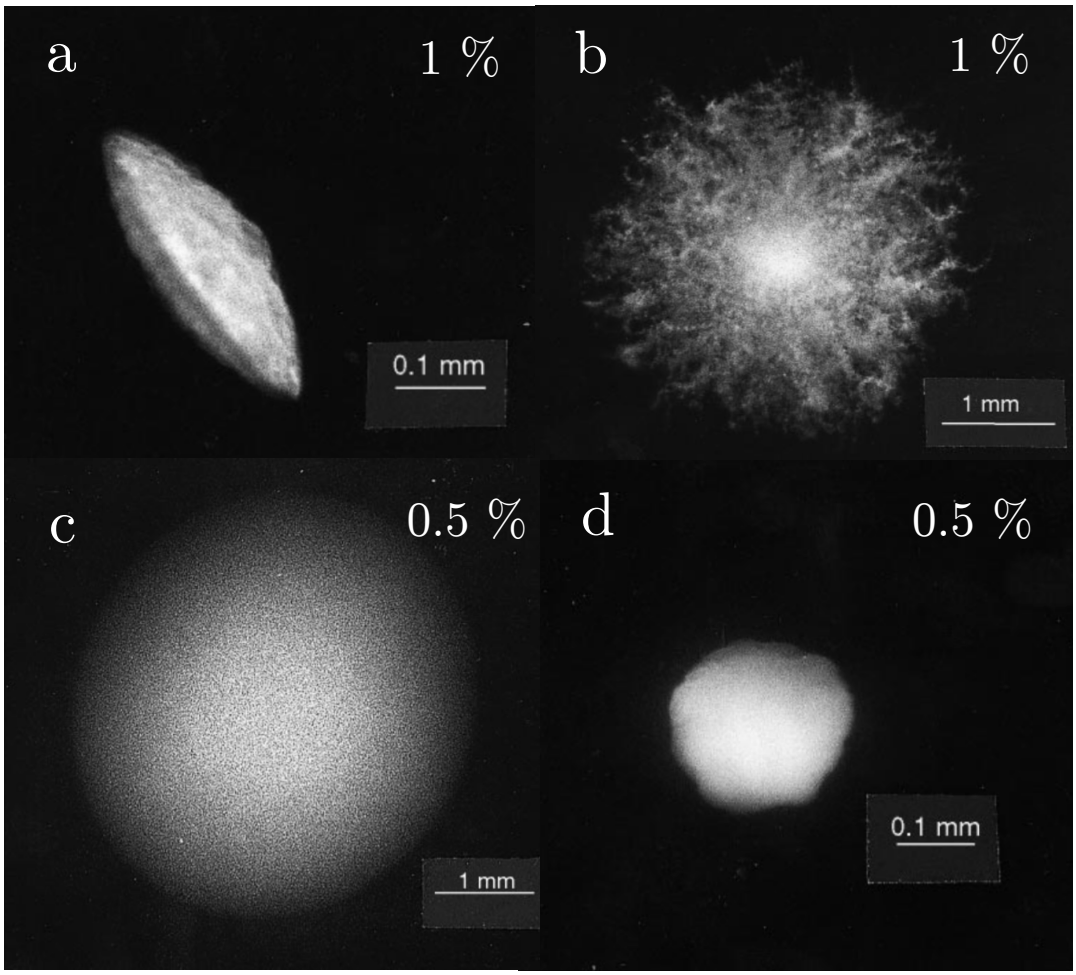

Figure 2.1 *Morphology of submerged colonies of bacteria. (a) Pseudomonas aeruginosa in 1 % w/v agar forms a lenticular shaped colony. (b) A dendritic colony formed by Bacillus cereus in 1 % w/v agar. Bacillus cereus are able to degrade the agarose, allowing partial free movement. (c) In 0.5 % w/v agar Pseudomonas aeruginosa forms large "wispy" colonies that are thought to result from free movement of the motile bacteria through the agar. (d) A small, almost spherical, colony formed by the non-motile species Enterococcus faecalis in 0.5 % w/v agar. Reproduced from [41]*

2.3 Parallels with ellipsoidal Tumours

Finally I wish to highlight a system with many similarities to submerged colonies, tumour growth in an extracellular matrix. Tumours grown in hydrogels have been observed to form oblate ellipsoids, figures 2.2a-c, that become more spherical when grown in more compliant hydrogels [43–45]. As shown by Winpenny in the last section and will be repeated in Chapter 5, bacterial colonies grow into very similar morphologies and so it is possible that their formation shares some common physics with tumour growth.

A couple of studies have put forth theories for the origin of ellipsoidal tumours. Figures 2.2a-c, shows a tumour consisting of human colon adenocarcinoma cells that was embedded in a 0.5 % agarose gel [43]. In the associated study the morphology was hypothesised to stem from a minimization of the elastic free energy in the gel, with no contribution of fracture to the shape. In fact they use figures 2.2a-c as evidence for the absence of fracture, I suspect because there are no obvious signs of deformation in the gel near the apex of the tumour, however the tumour itself may mask any signs of deformation. They calculate (using a non-linear finite element model) that as the stiffness of the gel is increased compared to the stiffness of the tumour, ellipsoid with higher aspect ratios should be more favoured.

In a second study, fluorescent marker beads were co-embedded with a tumour consisting of murine mammary carcinoma cells in 0.5 % agarose gels, figures 2.2d-f [44]. Using the marker beads they were able to visualise gel deformations around the growing tumours. In this study they observed both ellipsoidal and spherical tumour morphologies, though they do not speculate on why such a difference was observed in tumours grown under the same conditions. They recognise that the gel must fail at the apex of the ellipsoidal tumours, however they then hypothesise that the ellipsoidal morphology stems from an anisotropic stress distribution within the tumour that is supposedly caused by this failure. They conclude that the stress distribution within the tumour leads to a higher fraction of cell death along its minor axis, driving the tumour to grow into an ellipsoidal morphology.

Interestingly the second study ([44]) observed no deformation near to the spherical tumours, whereas ellipsoidal tumours compressed the gel along one axis. As will be seen in Chapter 5, this is reminiscent of the different fracture growth modes

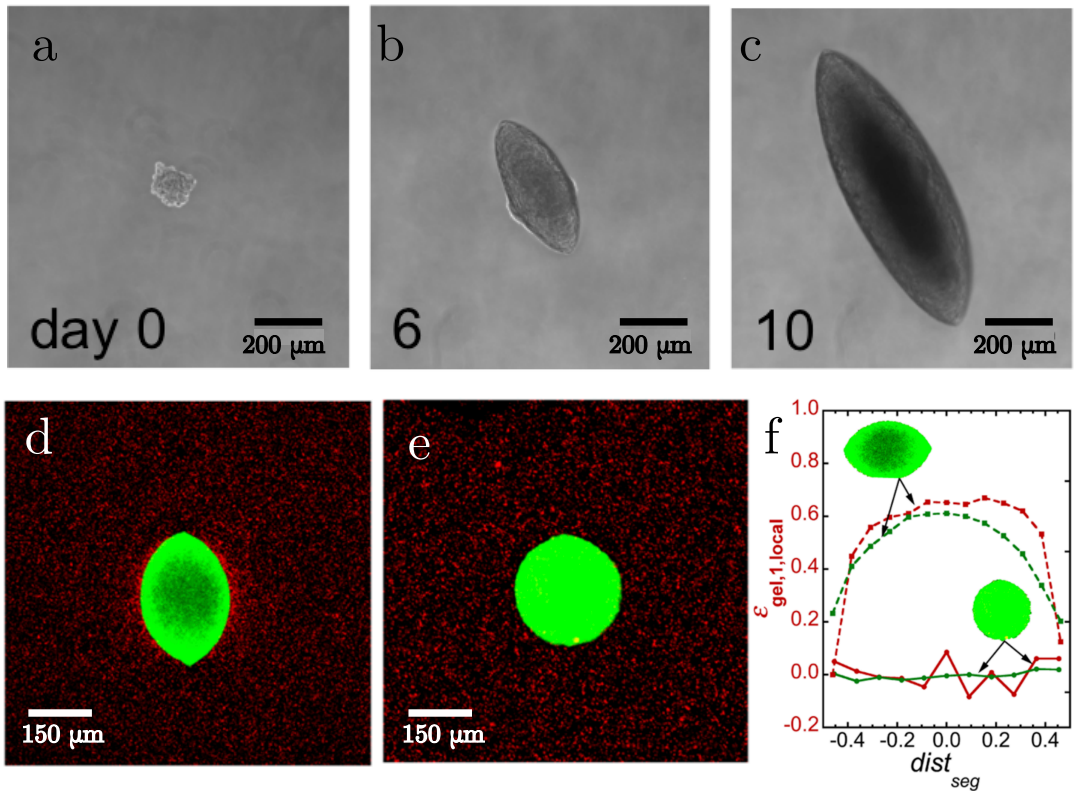

Figure 2.2 *Tumours have been observed to grow into spheroidal morphologies when immersed in agarose gel. (a-c) A tumour consisting of human colon adenocarcinoma cells was embedded in 0.5 % agarose gel containing a culture medium. The tumour grew into an ellipsoidal morphology, reproduced from [43]. (d,e) In another study tumours consisting of murine mammary carcinoma cells were co-embedded with fiducial (reference) markers in 0.5 % agarose gel. For some of the tumours an ellipsoidal morphology war observed (d) and in others a spherical morphology (e). The "strain", ϵ, in the gel was estimated according to the density, ρ, of fiducial markers ($\epsilon = 1 - 1/\rho$) within* $10\,\mu\mathrm{m}$ *bands around the tumour surface, figure (f) plots this "strain" as a function of distance from the tumour surface. Around the ellipsoidal tumours, the "strain" was observed to increase near the tumour surface. Around spherical tumours, no increase was observed.Figures d-f are reproduced from [44]*

seen around bacterial colonies.

As far as I am aware [44] and [43] represent the only studies where a biologically inert gel has been used in an attempt to explain the morphology of ellipsoidal tumours. In these idealized systems mechanical interactions should play a more clear role in morphogenesis when compared to *in vivo* systems where numerous other factors at play [46]. Tumours with ellipsoidal morphologies are still observed *in vivo* [45, 47], though in general these tumours form more spherical shapes .

Chapter 3

Fracture Mechanics and the limits of LEFM

A large portion of this thesis is dedicated to describing how submerged colonies of bacteria grow by fracturing the material around them. Moreover, the size of these colonies with respect to various material length scales results in fractures that do no obey simple, linear-elastic, theories of fracture. Instead it will be shown that bacteria can create fractures than transition across multiple length scales and modes of fracture. Indeed bacterial colonies will be shown to represent a novel tool with which current theories of fracture at small scales can be tested. With this in mind, a brief review of fracture mechanics is in order.

The aim of this review is to first outline linear elastic fracture mechanics (LEFM) and how it applies to cracks that are loaded at their faces (hydraulic fractures). The limits of LEFM will then be discussed, with an emphasis on the length scales at which transitions in fracture behaviour might be expected. Finally current theory and experiments regarding fracture at small scales are reviewed.

3.1 The theoretical strength of a solid

Failure, in essence, is the separation of a body into two or more parts. The fracture strength of an ideal body can be found using the concept of surface energy. Here a body refers to a collection of elements (e.g. atoms or cross-link regions of a polymer) that are held together by bonds (e.g. covalent bonds or

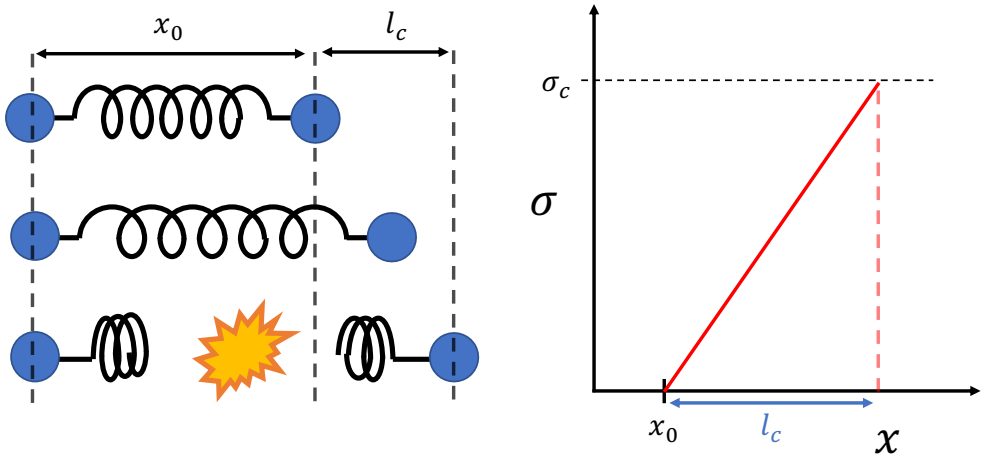

Figure 3.1 *The failure of a model bond. (a) A Hookean spring of equilibrium length x_0 is stretched to length $x_0 + l_c$ whereupon it breaks. (b) The stress-displacement (σ-x) relationship for the spring.*

polymer chains between cross-links).

Consider a model bond, a Hookean spring with equilibrium length x_0 between two elements of a body. The stress required to separate the elements to some distance $x' = x - x_0$, is given by

$$\sigma = \frac{x'}{l_c}\sigma_c, \tag{3.1}$$

where σ_c and l_c are the stress and length at which the spring breaks respectively, Figure 3.1.

The Young's modulus of the spring is defined as

$$E \equiv \frac{\sigma}{\epsilon}, \tag{3.2}$$

where the strain, ϵ, is given by

$$\epsilon = \frac{x'}{x_0}. \tag{3.3}$$

Substituting Equation 3.1 and 3.3 into 3.2, we find

$$l_c = \frac{x_0}{E}\sigma_c. \tag{3.4}$$

Here, the surface energy, γ, is defined as the work done in creating a new surface by breaking the bond. It is given by the area under the stress-displacement curve of the spring (Figure 3.1b), halved as the broken bond contributes to two new

surfaces. Thus, we find

$$\gamma = \frac{1}{2}\int_0^{l_c} \frac{x'}{l_c}\sigma_c dx' = \frac{1}{4}\sigma_c l_c. \tag{3.5}$$

The stress at which a body held together by this spring will fail (fracture) is therefore found by substituting Equation 3.4 into 3.5. Hence, the cohesive stress of the material is given by

$$\sigma_c = \sqrt{\frac{4\gamma E}{x_0}}. \tag{3.6}$$

For silica glass $\gamma = 4.6\,\mathrm{J\,m^{-2}}$, $E = 72\,\mathrm{GPa}$ and $x_0 \approx 0.2\,\mathrm{nm}$ [48], so σ_c can be estimated to be of the order 60 GPa. However when silica glass undergoes tensile testing[1], it typically fails at an applied stress of order 7 MPa, some four orders of magnitude less than the predicted σ_c [49].

The difference between the cohesive stress and observed failure stress of materials can usually be explained by one or more of the following factors:

1. Flaws exist that magnify the stress applied to the material, so that the local stress might equal σ_c.

2. The surface energy within the material is anisotropic (e.g. γ may be smaller along domain boundaries in polycrystalline materials), so σ_c may be lower locally.

3. The stress applied to break the material is applied in an anisotropic way (e.g. a shear stress), which may induce flaw nucleation at stresses lower than σ_c [50].

In this work I consider homogeneous, amorphous, materials and stresses applied with no shear component[2], therefore I will focus on quantifying explanation 1. The next section will look at Griffith's theory of fracture, which aims to explain the discrepancy between the theoretical and measured strength of materials by supposing that materials are interspersed with flaws.

[1] A tensile test is a mechanical test in which a sample is subjected to a controlled tensile stress until failure.

[2] A crack made to propagate without any shear component of stress is called a mode I or opening mode fracture.

3.2 Griffith's Theory of Fracture

Modern fracture mechanics began with A. A. Griffith's energy-based analysis of cracks in 1920 [51]. To explain the discrepancy between the theoretical and measured strength of solids, he supposed that materials such as glass contained many small flaws (e.g. notches or cracks), which act to concentrate stress locally. This idea was not new. Inglis had shown that flaws in a material concentrate stress, which lowers the strength of the flawed material [52]. However, as will be discussed in later sections, his approach is difficult to make predictions from. Inglis held that a crack should propagate if the local stress, σ_l, at any point in a material exceeds σ_c,

$$\sigma_l \geq \sigma_c. \tag{3.7}$$

This seemingly sensible idea encounters a problem when one considers the stress around an elliptical hole in a sheet of material, which we consider to be a model flaw. The tensile stress applied to the material will be magnified by a factor K, given by

$$K = 2\sqrt{\frac{a}{\rho}} \tag{3.8}$$

at the apex of the ellipse [52], where a is the ellipse's semi-major axis and ρ is the radius of curvature at its apex. By flattening the ellipse ($\rho \to 0$) into a line crack, the predicted K tends to infinity, meaning that any material with a line crack in it would fail at the slightest applied stress. This extreme fragility is (thankfully) not observed. Griffith avoided this infinite stress magnification problem using an energy-based failure principle.

Griffith reframed the cracked material as a thermodynamic system. The total energy of the cracked system, U, is the sum of the strain energy stored in the material, U_E, the energy required to create the crack surfaces, U_s, minus work done on the system, U_W,

$$U = U_E + U_s - U_W. \tag{3.9}$$

A crack will propagate (fracture) if there is a decrease in the total energy of the system, as per any thermodynamic process. If no work is done on the cracked system ($U_W = 0$), then the crack will spontaneously propagate if $\frac{dU}{da} < 0$, thus

Griffith's condition for fracture is

$$-\frac{dU_E}{da} > \frac{dU_s}{da}. \tag{3.10}$$

To illustrate how Equation 3.10 can be used to determine the stress, σ_f, that needs to be applied to a material for it to fracture, I consider the system Griffith originally solved for in the next section. I will then show how plasticity can be accounted for in Section 3.2.2, and then how σ_f can be found for a hydraulic fracture in Section 3.2.3.

3.2.1 Griffith's example

Griffith initially considered the stress required to propagate a crack in an infinite sheet of material, with thickness B, subject to uniaxial tension, Figure 3.2. The crack considered was a flattened ellipse[3] with major axis a and radius of curvature $\rho \to 0$. The strain energy stored in an infinite sheet of material is given by the strain energy density, W, in the sheet multiplied by the sheet's volume, V, i.e.

$$U_E = WV. \tag{3.11}$$

For an un-cracked, linear elastic. material under uniaxial tension the strain energy density is uniform, and can be expressed as

$$W = \frac{\sigma_\infty^2}{2E} \tag{3.12}$$

where σ_∞ is the tensile stress applied (at infinity) to the sheet and E is the Young's modulus of the material. The strain energy is reduced by the presence of the crack. If the tensile stress is applied perpendicular to the crack's major axis, then the crack unloads a volume πBa^2 of the sheet[4] [51], Figure 3.2a. Thus U_E is given by

$$U_E = \frac{\sigma_\infty^2}{2E}\left(V - \pi Ba^2\right). \tag{3.13}$$

The energy required to create new crack surfaces is given by the surface energy,

[3]This was exactly the case that Inglis's stress intensity approach made nonphysical predictions for.

[4]The prefactor π is reached in the limit that the dimensions around the crack are much greater than a.

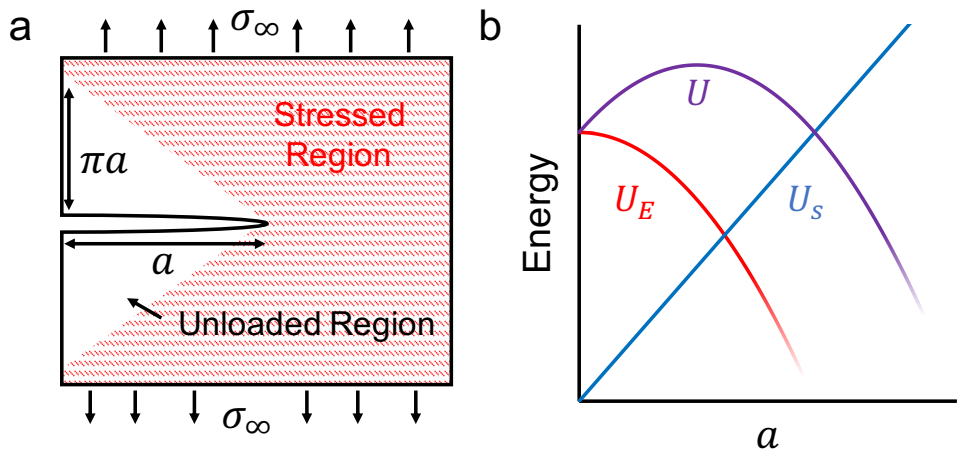

Figure 3.2 *The system originally considered by Griffith, an elliptical crack in a sheet of linear elastic material. (a) Schematic of a sheet of material with an elliptical crack of length, a, a uniform tensile stress, σ_∞, is applied to the sheet at infinity. The presence of the crack effectively unloads an triangular region with volume $\pi B a^2$, where B is the thickness of the sheet. (b) The material will fracture when an increase in a decreases the total energy of the system, U, (Equation 3.9).*

γ, multiplied by the area of broken bonds, therefore

$$U_s = 2\gamma B a. \tag{3.14}$$

The factor of 2 in Equation 3.14 comes from the fact that two surfaces are created during fracture. Substituting Equations 3.13 and 3.14 into 3.10, the condition for fracture becomes

$$\frac{\sigma^2}{E}\pi B a > 2\gamma B. \tag{3.15}$$

Note that any dependence on the volume of the sample is removed. Thus, the critical stress for fracture is:

$$\sigma_f = \sqrt{\frac{2\gamma E}{\pi a}}. \tag{3.16}$$

Notably σ_f scales with the reciprocal square root of the crack length. This means that in a uniformly stressed material there exists some critical crack length above which a crack will spontaneously propagate.

3.2.2 Plasticity at the crack tip

Equation 3.16 works well for brittle materials, however it greatly underestimates the critical stress when significant plastic deformation occurs at the crack tip. In 1948 Irwin introduced an additional dissipative term to the energy balance of the system (Equation 3.10) that accounted for the energy lost to plastic deformations in the material [53, 54]. Using Griffith's infinite sheet geometry (Figure 3.2), the dissipative energy, U_p scales with the crack area and is given by

$$U_p = \Gamma_p B a. \tag{3.17}$$

Γ_p is the energy dissipated due to plastic deformations per unit crack area, measured in Jm^{-2}. Substituting Equations 3.13, 3.14 and 3.17 into the following energy balance,

$$-\frac{dU_E}{da} > \frac{dU_s}{da} + \frac{dU_p}{da}, \tag{3.18}$$

the fracture stress accounting for plastic deformations is found:

$$\sigma_f = \sqrt{\frac{\Gamma E}{\pi a}}, \tag{3.19}$$

where

$$\Gamma = 2\gamma + \Gamma_p. \tag{3.20}$$

For polymeric materials Γ_p can be much larger than 2γ. For example, Rivlin and Thomas found that the fracture energy of rubber ($\sim 10^5$ Jm^{-2}) is some 7 orders of magnitude larger than it's surface energy ($\sim 10^{-2}$ Jm^{-2}) [55]. The reason for this disparity is that the surface energy only accounts for the energy required to bring a monomer unit from the bulk of the material to the surface, it is the same as the surface energy of an uncrosslinked polymer liquid, e.g. for new surfaces of a hydrogel being exposed to air γ would be approximately $72\,\mathrm{mJ\,m}^{-2}$ (the surface energy of a water-air boundary). On the other hand, the fracture energy, Γ, measures the energy required for the scission of polymer chains and viscous dissipation [56].

The inclusion of the dissipative term in Equation 3.18 requires that the energy dissipation due to plastic deformation is localized to a region that is small compared to the region that is regulated by elastic deformations, this is called the small scale yielding (SSY) criterion [57]. Why this condition is necessary and the scale at which the SSY criterion is violated will be discussed in Section 3.3.

A comparison can now be made between Griffith's energetic approach to fracture and Inglis' cohesive stress approach. Using Griffith's approach, σ_f is couched in terms of Γ and E instead of the cohesive stress, σ_c, the former two quantities can be measured in bulk tests (see Chapter 7) whilst σ_c requires more careful measurement. It often difficult to measure σ_c as macroscopic samples may contain flaws which will cause the sample to fracture before the applied stress reaches the cohesive stress, as was discussed in Section 3.2. Therefore the only way to truly measure the cohesive stress of a material is to test a flawless sample[5]. In other words, the relative measurability of E and Γ compared to σ_c is the key to the success of Griffith's approach.

3.2.3 Griffith's critical stress for a hydraulic fracture

As will be discussed in Chapter 5, colonies of bacteria can be observed to fracture the gel surrounding them in a disk shape. For this reason I will now look at how Griffith's theory can be applied to disk shaped fractures where stress is applied at the faces of a crack: this configuration is called a hydraulic fracture. Later this treatment will form the basis of a simple model of colony formation.

In Griffith's example $U_E(a)$ was found by considering the volume unloaded as the crack length, a, increased. The unloaded volume had uniform strain energy density, W (equal to the far field W, Equation 3.13), and as such it was clear that U_E should decrease as a increases (as more volume is unloaded). However when one considers a hydraulic fracture, the far field W is zero and there is no region of uniform W. Therefore, it is not immediately clear that U_E should decrease as the crack propagates, or that U_E should scale with the volume of the region surrounding the crack. In this section Sneddon's solution for the work done in deforming a disk shaped crack is used to show that, for a hydraulic fracture, σ_f does in fact scale in the same way as Equation 3.19 .

Consider a crack in a plane that is bounded by a circle of radius a in a body of material. A crack of this kind is termed a "penny-shaped" crack. When a uniform pressure, P, is applied to the faces of this penny-shaped crack it will deform into an ellipsoid with two equal semi-diameters in the crack plane [59–

[5]A solution to this problem is to measure the fracture stress, σ_f, for ever smaller samples of material, when σ_f becomes independent of the sample size then $\sigma_f = \sigma_c$, [58]. Another solution may be presented in Chapter 5, by using a bacterial colony grown inside the material, the flaw size can be controlled whilst the boundary stresses are zero so the cohesive stress of the material should then be the maximum observable stress at the fracture tip prior to fracture.

61]. The volume of that ellipsoid with semi-major axis, a, and aspect ratio, x, is given by

$$V = \frac{4\pi}{3}\frac{a^3}{x}. \tag{3.21}$$

Sneddon calculated the aspect ratio of the ellipsoid as a function of the pressure in [60] to be

$$x = \frac{\pi}{4}\frac{E}{(1-\nu^2)P} \tag{3.22}$$

Therefore the work done in deforming the penny-shaped crack into an ellipsoid and thus the strain energy stored in the material (given no energy loss to plastic deformation) can be found:

$$U_E = \int PdV = \int P\frac{dV}{dP}dP = -\frac{8(1-\nu^2)}{3E}P^2a^3. \tag{3.23}$$

The energy cost of creating the crack surfaces is

$$U_s = 2\pi\gamma a^2, \tag{3.24}$$

and the energy lost to plastic deformations is given by

$$U_p = \pi\Gamma_p a^2. \tag{3.25}$$

Substituting Equations 3.23, 3.24 and 3.25 into Griffith's fracture criterion (Equation 3.18) and using Equation 3.20, the pressure at which a penny-shaped fracture should propagate, P_f, is found to be

$$P \geq P_f = \sqrt{\frac{\pi\Gamma E}{4a(1-\nu^2)}}. \tag{3.26}$$

There is seemingly a contradiction here, Equation 3.23 assumes no plastic deformations are present whilst Equation 3.25 accounts for plastic deformations. This contradiction is resolved by the assumption that the region in which the plastic deformations occur is very small, so that U_E is largely unchanged by those plastic deformations, this is called the small scale yielding (SSY) criterion.

Section 3.3 will explore the length scale over which plastic deformations dominate and where the SSY criterion should fail. But first I will more closely examine the shape that a hydraulic fracture assumes when it is deformed by a hydrostatic pressure equal to P_f.

3.2.4 The morphology of a hydraulic fracture

Given that a hydraulic fracture will propagate at a pressure given by Equation 3.26, Sneddon's solution for the stress distribution around a penny-shaped crack [60] can be used to determine the morphology of the fracture. As stated previously, when a penny-shaped crack is pressurized to some pressure, P, linear elasticity predicts that the crack will be deformed into an oblate ellipsoid with aspect ratio given by Equation 3.22. The minor axis, b, of that ellipsoid is a function of the pressure applied to the surface of the crack. Given a uniform pressure distribution,

$$b = \frac{4(1-\nu^2)aP}{\pi E}, \tag{3.27}$$

where ν is the Poisson's ratio of the material. When the pressure inside the crack reaches P_f (Equation 3.26) the fracture will propagate, increasing the crack volume and lowering the pressure. If the pressure is constantly increased, say by the injection of a fluid into the crack, then of increasing pressure followed by fracture and depressurization will repeat[6]. When the pressure on crack faces reaches P_f, the morphology of the crack can be found by substituting Equation 3.26 into 3.27, the minor axis of the propagating hydraulic fracture should therefore be given by

$$b = \sqrt{\frac{4(1-\nu^2)\Gamma a}{\pi E}}. \tag{3.28}$$

Using Equation 3.28, the radius of curvature, ρ, at the edge of the circular crack can be found:

$$\rho = \frac{b^2}{a} = \frac{4(1-\nu^2)\Gamma}{\pi E}. \tag{3.29}$$

If the material is nearly-incompressible ($\nu \approx 0.5$) then

$$\rho = \frac{3}{\pi}\frac{\Gamma}{E} \approx \frac{\Gamma}{E}. \tag{3.30}$$

3.3 The limit of small scale yielding

The critical stresses and fracture propagation pressures predicted in Section 3.2 are based on the assumption that the strain energy stored in the material around

[6]This process of repeated pressurisation has been observed in experiments where gas is injected into gelatin [62].

the fracture can be calculated using linear elasticity. Any plastic deformations (that will change the energy stored in the material) are confined to a small region compared to the region described by linear elasticity and so that their effect on the stored energy is vanishingly small, this is called the small scale yielding (SSY) criterion. As will be seen in Chapter 5, colonies of bacteria grow at a size where the region of elastic deformations is not always large compared to the region of plastic deformations and the assumption of small scale yielding cannot be taken for granted. Therefore this section will look at the length scale at which SSY will become invalid.

To determine the length scale over which SSY does not apply one needs to look at the stress field near the crack tip and determine where this exceeds the cohesive stress, σ_c, of the material. Regardless of geometry and stress application, linear elasticity holds that the stress field near a crack tip will be singular, and take the form of an inverse square root dependence on the distance, r, from the crack tip:

$$\sigma(r) \sim \frac{K}{\sqrt{r}}, \tag{3.31}$$

where K is the stress intensity factor and is approximately given by

$$K \sim \sqrt{GE}, \tag{3.32}$$

where G is the strain energy release rate ($\frac{dU_E}{da}$). When the material fractures G will be equal to the critical strain energy release rate G_c. When there is no viscous dissipation, as I will show to be the case for fractures propagated by the slowly growing colonies[7], all of the energy is released at the crack tip and $G_c = \Gamma$. Therefore, when the fracture is propagating, Equation 3.31 becomes

$$\sigma(r) \sim \sqrt{\frac{\Gamma E}{r}}. \tag{3.33}$$

A length scale[8], ℓ_D, can therefore be defined where the singular stress field (Equation 3.33) is equal to σ_c:

$$\ell_D \sim \frac{\Gamma E}{\sigma_c^2}. \tag{3.34}$$

[7]See Section 7.4.4 for more details on the quasi static nature of the fractures propagated by bacterial colonies.

[8]The subscript D is for Dugdale, who first suggested the idea of a "cohesive zone" [63].

At a distance $r < \ell_D$ from the crack tip the material will be plastically deformed, Figure 3.3a, this region is termed the cohesive zone. All energy that is dissipated due to bond breakage does so within the cohesive zone. The next section will look at a model of the physical process that occurs in the cohesive zone and how these processes might affect the shape of the tip.

3.3.1 Barenblatt's Cohesive zone

The singular stress field at the propagating crack tip can be regularized by the Barenblatt cohesive zone model [64]. In this model stresses that would open up the crack tip are balanced by closing or cohesive stresses, so that the singularity in the stress field (Equation 3.31 as $r \to 0$) will be cancelled out by the cohesive stresses resulting in a stress field without nonphysical singularities. The closing stresses are described by stress-separation relationships that stem from intrinsic attractive surface forces (like those discussed in Section 3.1) between the material faces. An example of a simple stress-separation relationship was shown in Figure 3.1b (Equation 3.1). In reality the stress-separation relationships are more complicated, exhibiting non-linearities and tailing attractive terms after a peak cohesive stress [65, 66]. Experimentally, they must be inferred from crack tip opening displacements or stress field measurements [67].

For simple stress-separation relationships the crack tip profile can be determined. Perhaps the simplest model is the Dugdale-Barenblatt model [68] which holds that for a crack of length/radius a there is a constant cohesive stress σ_c over the cohesive zone between a and $a + \ell_D$.

The crack tip profile of a propagating hydraulic fracture with a Dugdale-Barenblatt cohesive zone is considered by Mokryakov in [69]. The shape of the inflated penny-shaped crack is determined in a similar fashion to the calculation by Sneddon [60], however instead of a uniform pressure over the surface of the crack, there is a region of negative pressure between a and $a + \ell_D$, Figure 3.3c. According to Mokryakov, the crack tip should be cusp-like, with the width , w, near the tip of the crack being described by, $w \sim X^{3/2}$, where X is the distance from the crack tip, Figure 3.3d. Far from the tip the ellipsoidal morphology discussed in Section 3.2.4 will be recovered. The displacement perpendicular to

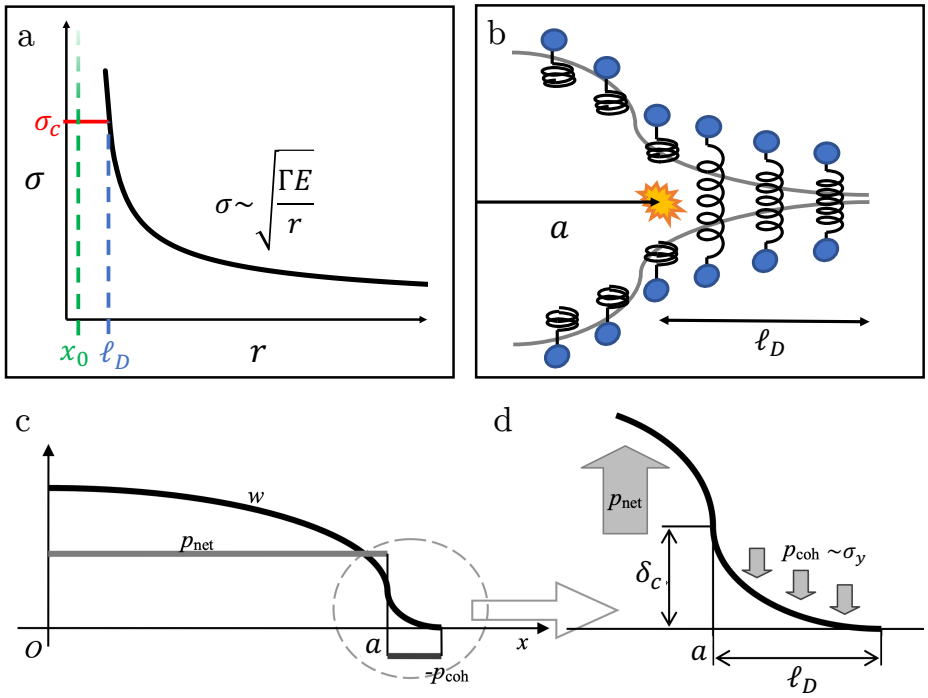

Figure 3.3 *The cohesive zone. (a) According to linear elasticity, the stress, σ, near the crack tip is singular. A length scale, ℓ_D, can be defined where σ is equal to the cohesive stress, σ_c. The Barenblatt model holds that for $r < a$, $\sigma = \sigma_c$. (b) Schematic of Barenblatt's Cohesive zone. Surface forces balance out opening stress resulting in an extended dissipation zone. (c,d) The Dugdale-Barenblatt model applied to a hydraulic fracture. The pressure, p_{net}, inside the crack is uniform from $x = 0$ to a, from a to $a + \ell_D$ the pressure is equal to some cohesive pressure $p_{coh} \sim \sigma_c$. The cohesive zone results in a cusp-like crack tip. Reproduced from [69].*

the crack plane at the edge of the cohesive zone, $\delta_c = w(\ell_D)$, is given by

$$\delta_c = \frac{4\sigma_c \ell_D \ln\left(\frac{a+\ell_D}{a}\right)}{E' \arcsin\left(\frac{a}{a+\ell_D}\right)} \sim \frac{\Gamma}{\sigma_c}. \tag{3.35}$$

E' is the plane-strain Youngs modulus, $E' = E/(1-\nu^2)$, Figure 3.3d. As E grows with respect to σ_c, ℓ_D increases whilst δ_c decreases so that the Barenblatt cohesive zone forms a long flat damage zone ahead of the fracture. In the opposite case when σ_c approaches E the zone will become blunted and the crack tip profile will tend to the smooth ellipsoid predicted by Sneddon (section 3.2.4). Thus, one might only expect to observe an extended Barenblatt's Cohesive zone in a truly brittle material ($\sigma_c \ll E$).

Indeed, in materials for which the cohesive stress approaches or exceeds their

elastic modulus, it has been shown that the cohesive zone becomes smaller than the region that could possibly account for the measured Γ [70].[9] For the hydrogel used in this work the cohesive stress is an appreciable fraction of the elastic modulus, therefore it is necessary to expand upon the theory of yielding. In doing so a new fracture regime is identified, in which dissipation can occur in a region larger than the cohesive zone. The theory of, and evidence for, an extended region of energy dissipation is discussed in the next section.

3.4 Crack tip blunting

One possible explanation for dissipation beyond the cohesive zone is blunting. It has been shown that for materials whose cohesive stress exceeds their elastic modulus, blunting occurs at the crack tip prior to fracture [71]. This section will look at the condition for blunting and how blunting might dissipate energy (and thus contribute to Γ).

Blunting occurs in the following way: Consider an infinite sheet of material with a elliptical crack, as considered in Section 3.2.1, Figure 3.2a. Given the magnification of the applied stress by the crack tip (Equation 3.8), the maximum stress in the material, $\sigma_{\max}$, is located at the crack tip and is given by

$$\sigma_{\max} = 2\sigma\sqrt{\frac{a}{\rho}}, \tag{3.36}$$

where σ is the stress applied at infinity. Now consider what will happen to $\sigma_{\max}$ as a function of σ. If SSY applies, then the radius of curvature at the crack tip will be constant (cf. Equation 3.30) and the relationship between the applied stress and the local maximum stress will scale with $\sim 1/\sqrt{a}$ as predicted by Griffith. However, *if finite strains are allowed*, ρ can increase. Blunting will occur when an increase in loading, $d\sigma$, yields zero change in the maximum stress at the crack tip, i.e. when[10]

$$d\sigma_{\max} = 2\sqrt{\frac{a}{\rho}}d\sigma - \sigma\sqrt{\frac{a}{\rho^3}}\frac{d\rho}{d\sigma}d\sigma = 0. \tag{3.37}$$

This is the blunting condition. The change in ρ with $d\sigma$ can be found from the result of Timoshenko and Goodier [72], near the crack tip the shape of the

[9] Given that $\Gamma \sim \ell_D W$, it has been shown that the theoretical strain energy density, W, lost in the volume ℓ_D^3 cannot account for the measured Γ in materials where $\sigma_c > E$.

[10] Assuming that the material is linear elastic and incompressible.

elliptical crack, $y(X)$, (X being the distance form the crack tip and y being the displacement perpendicular to the crack plane.) is given by

$$y = y_0(1 + \alpha d\sigma), \tag{3.38}$$

where[11]

$$\alpha = \frac{2}{E}\sqrt{\frac{a}{\rho}}. \tag{3.39}$$

From [71], Equations 3.38 and 3.39 imply that

$$\frac{d\rho}{d\sigma} = \alpha\rho. \tag{3.40}$$

Substituting Equation 3.40 into 3.37 the blunting condition can be stated as

$$\sigma = E\sqrt{\frac{\rho}{a}} \tag{3.41}$$

Using Inglis's condition for fracture (that $\sigma > \sigma_c$, Equation 3.7) the maximum stress in the material is given by the cohesive stress, $\sigma_{\max} = \sigma_c$, thus, using Equation 3.36 the blunting condition is given by

$$\sigma_c = 2E. \tag{3.42}$$

In other words, if the cohesive stress of a material exceeds twice its elastic modulus then any increase in load on the crack will cause the radius of curvature at the crack tip to increase at a rate such that the cohesive stress at the crack tip is not exceeded. Thus the condition for fracture is never met.

The blunting condition can be important even in brittle materials (where $\sigma_c \ll 2E$) at small length scales. To see why, examine the evolution of the maximum stress in the material with respect to the applied stress as a function of the crack size, i.e. determine $\sigma_{\max}(\sigma, a)$. Substituting Equations 3.40 and 3.39 into 3.37 and using Equation 3.29 results in

$$\frac{d\sigma_{\max}}{d\sigma} = 2\sqrt{\frac{a}{\rho}}\left(1 - \frac{a\sigma}{Eb}\right). \tag{3.43}$$

Equation 3.43 can be restated using Equation 3.36 and 3.29 as

$$\frac{d\sigma_{\max}}{d\sigma} = \frac{\sigma_{\max}}{\sigma}\left(1 - \frac{\sigma_{\max}}{2E}\right) \tag{3.44}$$

[11] Assuming sheet is large and thin so that the plane stress condition holds ($E' = E$).

Integrating Equation 3.44, the stress at the crack tip can be given as a function of the applied stress as

$$\frac{\sigma_{\max}}{E} = \frac{2\sigma/E}{\sigma/E + C}, \tag{3.45}$$

where C is the constant of integration. For large σ/E, $\sigma_{\max}/E \to 2$ as stated in Equation 3.42. When σ/E is small, the linear relationship between σ and $\sigma_{\max}$ (Equation 3.36) should be recovered, thus

$$C = \left(\sqrt{\frac{\rho}{a}}\right)_i = \left(\frac{b}{a}\right)_i, \tag{3.46}$$

where the subscript 'i' refers to the initial aspect ratio of the elliptical crack. The scaling of the initial aspect ratio can be estimated by taking the a to be the crack length and b to be the displacement at the edge of the Dugdale-Barenblatt cohesive zone (Equation 3.35). Thus, ignoring prefactors,

$$C \sim \frac{\Gamma}{\sigma_c a} \tag{3.47}$$

The maximum stress at the crack tip (Equation 3.45) is plotted as a function of the applied stress in Figure 3.4 for various crack sizes in a material with $E = 60\,\mathrm{kPa}$, $\Gamma = 0.4\,\mathrm{J\,m^{-1}}$ and $\sigma_c = 0.4E$, so that $\Gamma/E \approx 7\,\mu\mathrm{m}$[12]. When $\sigma_c/E > 2$ then no magnitude of σ will result in the fracture criterion ($\sigma_{\max} = \sigma_c$) being met. When $\sigma_c \ll E$ then the blunting condition will only be relevant at small length scales. For large cracks (bluer lines), small magnitudes of applied σ result in large $\sigma_{\max}$. When the crack is small, large σ's can be applied without the fracture criterion being met, due to blunting. In other words, even in materials where $\sigma_c < E$, at small length scales one must apply σ greater than σ_c to meet the fracture criterion due to blunting.

Broadly, the blunted zone can be viewed as a cohesive zone with a modified cohesive strength $\sigma_c \approx E$ (as the crack is not propagating, thus deformations are elastic) [71, 73]. The size of this effective cohesive zone is given by substituting the modified cohesive stress into Equation 3.34, the equation for the Dugdale cohesive zone size, giving

$$\ell_{\mathrm{EF}} \approx \frac{\Gamma}{E}. \tag{3.48}$$

Which is approximately the elasto-fracture length scale. Below this length scale cracks will blunt and the condition for fracture will not be met, thus the crack

[12]These are approximately the properties of 2% agarose, see Chapter 7.

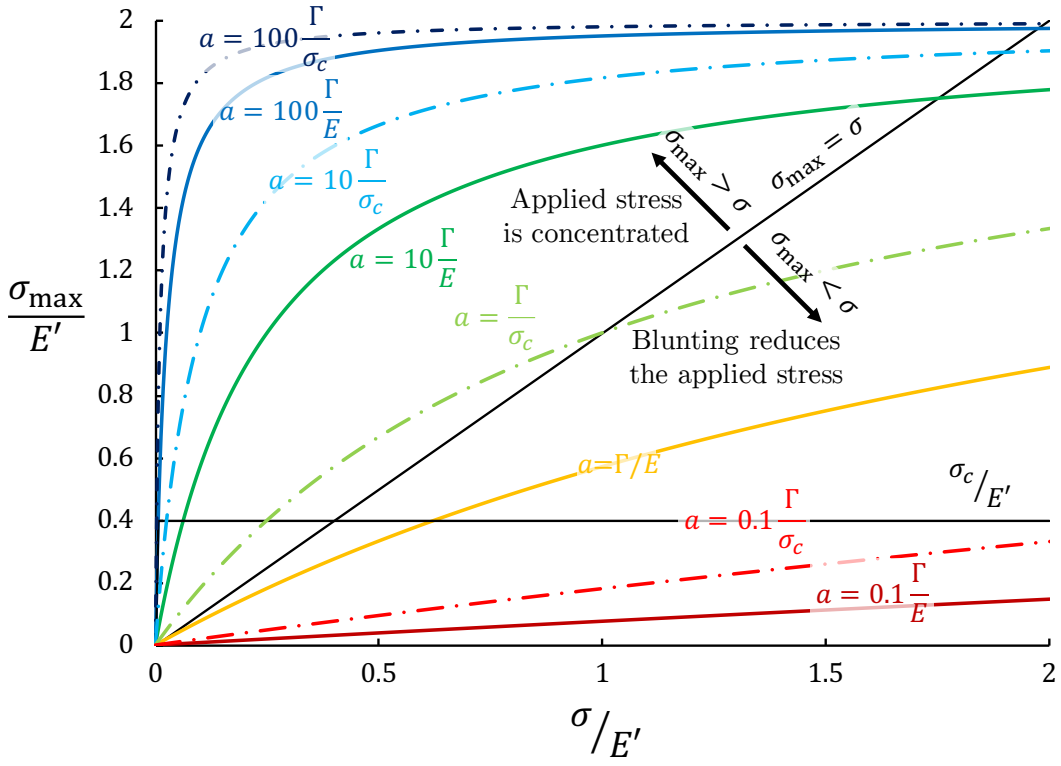

Figure 3.4 *The maximum stress at the crack tip σ_{max} is plotted as a function of the applied stress σ (stresses are given w.r.t. E) for different crack length, a. When the coloured lines cross the $\sigma_c/E = 0.4s$ line, the fracture criterion is met and the crack will fracture instead of blunting. When $\sigma_c/E > 2$, no magnitude of σ will result in the fracture criterion being met. When $\sigma_c \ll E$ then the blunting condition will only be significant at small length scales. When the crack is large (blue lines), small σ's result in large σ_{max}. As the size of the crack decrease (redder lines) then large σ's can be applied to the material whilst $\sigma_{max} < \sigma_c$, due to blunting at the crack tip. In other words, even in materials where $\sigma_c < E$, at small length scales cracks will blunt.*

will become more spherical.

If the condition for fracture is never met in the blunted zone, then how does a blunted crack tip propagate? Hui outlined three possible mechanisms by which a blunted crack might propagate [71]:

1. When the hydrostatic tension is of the order of the elastic modulus, as it is in the blunted zone, Gent and Lindley showed that the cavities can form in the material by an elastic instability [74]. The crack may propagate by the nucleation and coalescence of these cavities.

2. The maximum extensibility of the material might be reached. This may cause strain stiffening so that locally either E increases, or Γ decreases. Thus, micro-cracks can form in regions where ℓ_{EF} is effectively reduced, allowing for propagation with little to no blunting.

3. Sample geometry might come into play. For example if a certain radius of curvature is imposed upon the crack face (e.g. by the curvature of a blade) then the stress at the crack tip must increase with the loading stress.

This thesis considers fluid filled fractures[13], therefore no geometry is imposed on the crack tip. The next section will therefore discuss mechanisms 1 and 2, examining evidence for the respective processes and the relationship between them.

3.5 Cavitation and micro-fracture

The two possible mechanisms for blunted crack propagation relevant to hydraulic fractures are cavitation and micro-fracture by strain stiffening. However it is not clear that the two processes are entirely separate. The following section looks first at purely elastic cavitation, determining the pressure at which a spherical defect will expand, and then shows how this theory might be modified by fracture at the cavity surface.

[13] A comparison between colonies of bacteria and hydraulic fractures is made in Chapter 6.

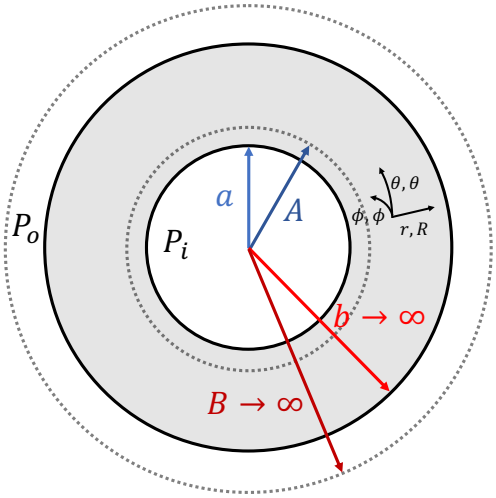

Figure 3.5 *Cross section of a thick walled shell. The cavity in the shell is pressurised to a pressure $P = P_i - P_o$. After pressurization the cavity wall is deformed from a radius of a to A. The outer radius b is deformed to B.*

3.5.1 Cavitation

When the hydrostatic tension inside a material is of the order of the elastic modulus, it has been observed that cavities begin to appear in the material [74, 75]. This process is called cavitation. The blunted zone is under exactly this state of hydrostatic tension, with ρ increasing with applied σ instead of the stress concentrating in a specific region of the defect [71]. The initiation and coalescence of these cavities represents a possible mechanism by which blunted cracks might propagate.

To explain why cavities should appear when the hydrostatic tension is of the order E, one can consider the deformation that is induced in any small[14] defects that might be present in the material. To do so, consider that when the hydrostatic tension is first applied, small defects will be made spherical by the blunting effect described in the previous section. The deformation-tension relationship can then be determined by considering the congruent problem of the deformation of a spherical shell of infinite thickness having an initial internal radius a, Figure 3.5.

The deformation in the cavity can be characterised by the stretch at the inner wall, λ_a, which is given by

$$\lambda_a = \frac{A}{a} \tag{3.49}$$

[14]Here "small" refers to a defect size where $\sigma_{\max} < \sigma$ below σ_c/E (Figure 3.4), or else when the defect size is smaller than $\sim \Gamma/E$.

where A is the deformed radius of the cavity with initial radius a. The problem will now be to determine the relationship between λ_a and the pressure inside the cavity, P, for a material with an arbitrary strain energy density function[15], W. The solution to this problem is given in appendix A and results in $P(\lambda_a, W)$ being given by

$$P(\lambda_a, W) = \int_1^{\lambda_a} \frac{1}{\lambda^3 - 1} \frac{dW}{d\lambda} d\lambda \tag{3.50}$$

Now that I have an expression for $P(\lambda_a)$, I can examine the relationship for a specific W. Analysis of this kind was first applied to the problem of cavitation by Gent and Lindley [74]. They considered a cavity in a neo-Hookean material [76], that is a material characterized by a strain energy density function of the form

$$W = C_1(I_1 - 3), \tag{3.51}$$

where $C_1 = E/6$. The first invariant of the strain tensor, I_1, for the spherical cavity shown in Figure 3.5 is given by

$$I_1 = \frac{1}{\lambda^4} + 2\lambda^2, \tag{3.52}$$

where the principle stretch, λ, is defined as

$$\lambda = \frac{R}{r}. \tag{3.53}$$

Thus, using Equations 3.51, 3.52 and 3.53, W can be written in terms of the principle stretch,

$$W = \frac{E}{6}\left(2\lambda^2 + \frac{1}{\lambda^4} - 3\right). \tag{3.54}$$

Substituting 3.54 into 3.50 and carrying out the integral

$$P(\lambda_a) = \frac{E}{6}\left(5 - \frac{4}{\lambda_a} - \frac{1}{\lambda_a^4}\right). \tag{3.55}$$

It can immediately be seen that when $P = 5E/6$, $\lambda_a \to \infty$. In other words when some critical pressure,

$$P_c = \frac{5}{6}E, \tag{3.56}$$

is reached the cavity will expand unboundedly, this is called the cavitation

[15] W is the strain energy density as a function of the deformation gradient (stretch or strain). For isotropic materials W can be written purely in terms of the invariants of the strain tensor, $W = W(I_1, I_2, I_3)$.

condition[16].

The cavitation condition has been shown to predict the onset of cavitation in many experimental setups, from cavities induced by the separation of two well bonded cylinders in a rubber, Figure 3.6a-b, to cavitation rheology, where hydrostatic tension is applied at the tip of a needle via a fluid, Figure 3.6c,d. After the initial cavitation process each of these experiments showed a transition into a rapid fracture mode, see Figure 3.6c at high volume fractions (ϕ) and needle radii r_s. These observations suggest that the initial cavitation process is the result of elastic deformation rather than a fracture process, as the cavitation pressure does not depend on Γ [78]. In addition, the cavities in these experiments appeared to be smooth-walled prior to fracture, suggesting elastic deformations. Though, as discussed in Section 3.4, this may be due to the blunting of any fractures present.

At some critical stretch ratio the material reaches its maximum extensibility and the material at the cavity wall will fracture. This transition from cavition to fracture has been suggested to obey the Griffith fracture condition for a penny-shaped crack (Equation 3.26, with $\nu = 0.5$) [78, 79], whereby the cavity will fracture when the hydrostatic pressure reaches

$$P_f = \sqrt{\frac{\pi \Gamma E}{3a}}. \tag{3.57}$$

That the cavity should fracture at P_f suggests that only a single fracture plane is present. The radius at which the void will switch from growing due to cavitation to fracture, a_t, can thus be found by comparing P_c to P_f. Ignoring prefactors, the cavitation to fracture transition will occur when $P_f < P_c$,

$$\frac{P_c}{P_f} \approx \frac{E}{\sqrt{\frac{\Gamma E}{a_t}}} = \sqrt{\frac{a_t E}{\Gamma}}. \tag{3.58}$$

Thus the defect length at which the transition will occur is

$$a_t \approx \frac{\Gamma}{E} = \ell_{\mathrm{EF}}, \tag{3.59}$$

which is approximately the elasto-fracture length scale.

[16]The numerical prefactor in Equation 3.56 will depend on the strain energy density function of the material, though in general it has been shown to lie between 0.5 and 2.0 [77].

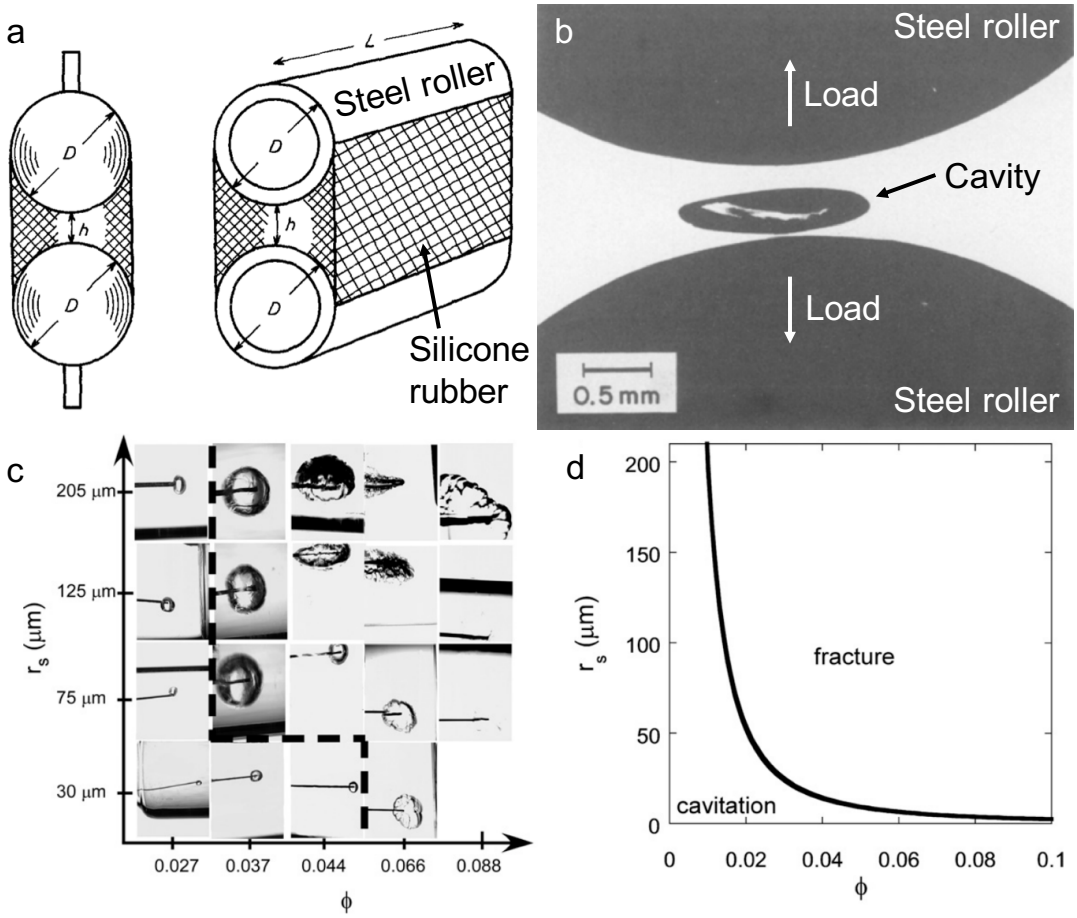

Figure 3.6 *Two examples of cavitation experiments. (a) Schematic of a cavitation experiment where silicone rubber is bonded to two steel cylinders, reproduced from [75]. The cylinders apply a tensile load to the silicone. (b) At some critical pressure (Equation 3.56), that is independent of the fracture energy of the material, a cavity is formed. (c) In cavitation rheology the fluid in an embedded needle with tip opening size r_s is pressurized. At P_c the material at the tip of the needle expands, seemingly elastically. When $P_f < P_c$ (Equation 3.59) the cavity begins to expand via fracture. The transition length scale is a function of the material properties Γ and E which are a function of the polymer volume fraction, ϕ. (d) plots the two phases of cavity expansion as a function of crack size (r_s) and ϕ, reproduced from [79].*

3.5.2 Cavitation with surface fracture

However, even below the elasto-fracture length scale, the cavitation process might be thought of as a fracture process. Evidence that cavitation might involve fracture first came from the fact that cavities grown from small initial defects require more pressure to expand than larger ones [78]. That the cavitation pressure should depend on the initial defect's size is reminiscent of Griffith's fracture criterion Equation 3.18 and so suggests that fracture might be occurring.

The work of Williams and Schapery [80] was the first to consider what happens when the initial cavity is allowed to expand not only elastically but also by fracture at the cavity wall. This approach seems more realistic as the strain[17] at the surface of these small cavities far exceeds the yield strain of most materials.

To determine the pressure at which a cavity expanding via surface fracture might propagate, Williams and Schapery (and later others including Gent and Wang [78–81]) applied Griffith's criterion. Williams and Schapery considered a system consisting of the same infinitely thick-walled neo-Hookean spherical shell as discussed in the previous section (Figure 3.5) when an external hydrostatic tension is applied to the shell[18]. To apply Griffith's criterion, Equation 3.10, the variation of the total energy of the system, U, with the crack size must be found, i.e.

$$\frac{\partial}{\partial a}(U) = \frac{\partial}{\partial a}(U_E + U_s - U_W) = 0, \tag{3.60}$$

where the size of the crack has been taken to be equal to the cavity radius a. The potential energy of the external tensile stress, is given by

$$U_W = -PV = -\frac{4}{3}\pi P B^3, \tag{3.61}$$

which can be expressed in terms of a and the stretch, λ, using the incompressibility condition,

$$b^3 - a^3 = B^3 - A^3, \tag{3.62}$$

[17] The radius of the cavity might grow by an order of magnitude, so that $\epsilon \gg 100\%$

[18] If the material is incompressible then any uniform pressure field can be added to the stress field without violating equilibrium. This field will have no affect on the strain energy or the deformation in the material. Therefore, the problem of a shell subject to an external hydrostatic tension applied at infinity is equivalent to the problem of the same shell inflated by an internal pressure [77]

and Equation 3.49 as

$$U_W = -\frac{4}{3}\pi P\left[b^3 + a^3\left(\lambda_a^3 - 1\right)\right]. \tag{3.63}$$

The strain energy stored in the shell, U_E, is equal to the work done by the external tension during deformation,

$$U_E = \int_V P dV = 4\pi \int_b^B P B^2 dB, \tag{3.64}$$

where P is given by Equation 3.55. Performing the integral,

$$U_E = \frac{2}{3}\pi E a^3 \left(\frac{5}{3}\lambda_a^3 - 2\lambda_a^2 + \frac{1}{\lambda_a} - \frac{2}{3}\right). \tag{3.65}$$

Finally, surface energy and plastic dissipation energy are rolled into U_s, which is simply Γ multiplied by the surface area of the cavity,

$$U_s = 4\pi a^2 \Gamma. \tag{3.66}$$

Upon carrying out the variation in Equation 3.60 Williams and Schapery make the somewhat controversial decision to assume that λ_a is independent of a. They justify this by assuming that as the crack grows the material around the cavity is removed (fractured) rather than stretched, therefore a increases proportionality with A such that λ_a is constant. This assumption is often stated to be incorrect in later papers [78], however the results of these papers (at least qualitatively) agree with Williams and Schapery's result and it remains unclear whether this assumption is valid. Substituting Equations 3.63, 3.65 and 3.66 into 3.60 yields

$$\lambda_a^6 - \left(\frac{3}{2} + \frac{6\Gamma}{Ea}\right)\lambda_a^4 + \frac{1}{2} = 0, \tag{3.67}$$

the roots of Equation 3.67 define the critical cavity extension ratio, λ_{ac}, at which new surface area will be created at the cavity wall. The Williams and Schapery critical pressure, P_{WS}, can be found by eliminating λ_a from Equations 3.67 and 3.55, the result of which is plotted in Figure 3.7 for a material with $E = 60$ kPa, $\Gamma = 0.4$ Jm^{-2}. The analytical expression for P_{WS} is cumbersome, but as can be seen in Figure 3.7 constant fracture pressure ($P = \frac{5}{6}E$) is regained in the limit where $a \ll \frac{\Gamma}{E}$ and the pressure for spherical fracture exceeds that for

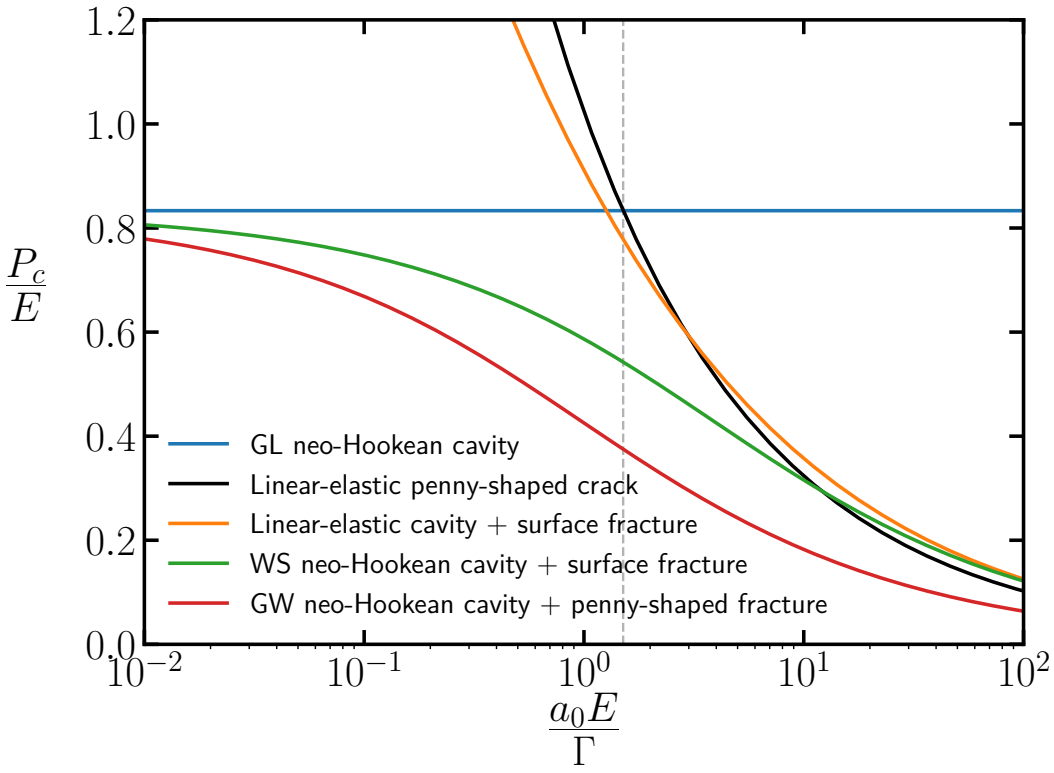

Figure 3.7 *The cavitation pressure is lower than that required for the propagation of a penny-shaped crack, when the defect is small. Plots of cavitation pressures as a function of defect size, compared to the propagation pressure of a penny-shaped fracture, eqn 3.57 (the black line). Blue, Gent and Lindley's purely elastic, neo-Hookean, cavitation pressure, eqn 3.56; Green, Williams and Schapery's neo-Hookean cavitation pressure with surface fracture criterion, eqns 3.55 and 3.67; Red, Gent and Wang's neo-Hookean cavitation pressure with penny shaped fracture criterion, eqns 3.55 and 3.74; Orange, Linear elastic cavity with surface fracture criterion.*

penny-shaped fracture at a transition defect size, a_t, given by

$$a_t \approx 10\ell_{\mathrm{EF}}. \tag{3.68}$$

Williams and Schapery's model was modified by Gent and Wang in 1991 to avoid the assumption of λ_a being independent of a. They took a different approach to finding the equation for λ_{ac}. Instead of fracture across the entire surface of the cavity, the cavity is assumed to fracture in a single penny-shaped plane. The penny-shaped crack is then taken to deform into a sphere with no additional work done ($U_W = 0$). Whilst we know from Section 3.2.4 that the deformed shape of a penny shaped fracture will depend on the fracture size and internal pressure,

we saw in Section 3.4 that at scales smaller than $\sim \ell_{\mathrm{EF}}$ cracks will blunt and so perhaps when $a \ll \ell_{\mathrm{EF}}$ treating the penny shaped crack as spherical is not so far fetched.

The volume of Gent and Wang's spherical crack is given by

$$V = \lambda_a^3 V_0 = \lambda_a^3 \frac{4\pi a^3}{3}, \tag{3.69}$$

whilst the crack area α is given by

$$\alpha = \pi a^2. \tag{3.70}$$

Griffith's condition can therefore be expressed in terms of the area as

$$-\frac{\partial U_E}{\partial \alpha} \geq \frac{\partial U_s}{\partial \alpha} + \frac{\partial U_W}{\partial \alpha} = \Gamma + 0. \tag{3.71}$$

Similarly to Equation 3.64

$$U_E = \int_{V_0}^{V} P dV, \tag{3.72}$$

and as such Equation 3.71 can be rewritten in terms of λ using Equation 3.69 as

$$\lambda_a^4 \frac{\partial}{\partial \lambda_a} \left[\frac{1}{\lambda_a^3} \int_1^{\lambda_a} \frac{P(\lambda_a)}{E} \lambda_a^2 d\lambda_a \right] \geq \frac{\Gamma}{2aE}. \tag{3.73}$$

Substituting the neo-Hookean $P(\lambda_a)$ from Equation 3.55 and carrying out the integration/differentiation, the equation for the critical cavity stretch is

$$\lambda_a^2 - \frac{2}{\lambda_a} + 1 = \frac{3\Gamma}{2aE}. \tag{3.74}$$

The Gent-Wang critical pressure for fracture, P_{GW}, is again found by substituting the roots of Equation 3.74 into the neo-Hookean $P(\lambda_a)$ relation (Equation 3.55). P_{GW} is plotted in Figure 3.7 for a material with $E = 60$ kPa, $\Gamma = 0.4$ Jm^{-2}. In this case P_{GW} is always less than the pressure required to propagate a penny shaped fracture, P_f, due to strain energy stored around a sphere of radius a being strictly greater than that around an oblate spheroid with major axis a. However the importance of this model is that it shows that a constant fracture propagation pressure can again be recovered for $a \ll \ell_{\mathrm{EF}}$. Given a constant fracture propagation pressure, if we consider the deformation of a penny shaped fracture (Equation 3.27) then for $a \ll \ell_{\mathrm{EF}}$ a penny shaped fracture will grow in

a self-similar fashion, i.e. $a \propto b$.

P_c, P_{WS} and P_{GW} represent the three most prolific cavitation pressures cited in the literature. The fact that models considering purely elastic deformations (P_c) predict similar critical cavitation pressures as models considering fracture (P_{WS} and P_{GW}) at small scales has been the subject of much research in recent years, with experimentalists and theorists vying to determine the extent to which the fracture properties of materials are relevant to the onset of cavitation. The challenge facing experimentalists is that the length scale at which the cavitation to fracture transition take place (Equation 3.59) is often of the order $\sim$10 µm and, once the critical pressure for cavitation or fracture is reached, the cavitation process can occur with stretch rates of the order 100 s^{-1} [82] making observations difficult.

The clearest experimental evidence for a transition between elastic cavity growth and fracture is given by Poulain et al. [82]. They used a similar apparatus as shown in Figure 3.6a and b, bonding two glass spheres to polydimethylsiloxane (PDMS). The glass spheres are used to produce a triaxial stress state. They claim to have observed three distinct growth regimes, Figure 3.8. First, latent flaws expand elastically, this process appears to occur rapidly with a lower bound on the stretch rate of at least 100 s^{-1}. Then the expansion of the cracks slows. They hypothesise that the slow down is due to strain stiffening and fracture at the cavity walls. However the cavities remain spherical during this phase, indicating that fracture occurs over the entire surface of the cavity. Finally, the cavities/cracks transition into a phase where fracture in a single plane dominates and a teardrop like shaped void forms. When the glass spheres are returned to their initial position (removing any stress) a penny shaped crack remains in the PDMS. This experiment shows clear evidence for a transition in fracture behaviour, however observations of the exact deformation of the cavities (that might provide insight into the cavitation process) are limited by the speed of the process.

The next section will look at an experiment that appears to solve the problem of rapid expansion by growing bubbles within a gel.

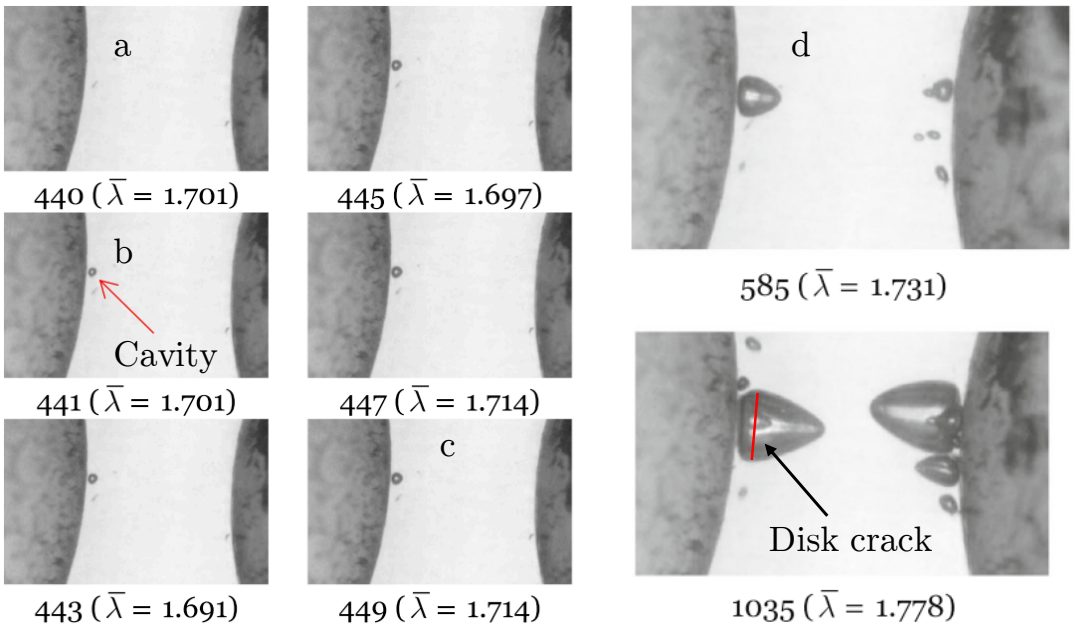

Figure 3.8 *Three phases of cavitation, reproduced from Polain et al. [82]. Two glass spheres were bonded to PDMS and separated to produce a stretch $\bar{\lambda}$ in the material. This stretch produces a triaxial stress state, a high speed camera was used to observe cavitation. Between (a) and (b) the cavity nucleates. An initial stretch rate $>100\,\mathrm{s}^{-1}$ was found by dividing the change in flaw size by the temporal resolution (66.7 ms), the upper bound on the size of the initial flaw is given by the distance from the cavity to the glass sphere. The cavity then expands at a slower rate supposedly due to fracture at the surface of the cavity. Finally, between (c) and (d) a single fracture dominates. When the spheres are returned to their initial position (removing any stress) a penny shaped crack remains in the PDMS.*

3.5.3 Observing small-scale fracture

A method of creating a cavity at a controllable rate below the elasto-fracture (ℓ_{EF}) or Dugdale (ℓ_D) length scales has been developed by Robert Style et. al [83, 84]. By exploiting the cooling driven phase separation of silicone and fluorinated oil within a silicone gel, they were able to controllably nucleate cracks in the gel with sizes smaller than ℓ_{EF}, Figure 3.9A-D. Using this method the problems encountered by prior cavitation experiments (namely process speed, viscoelastic effects and boundary effects) were avoided.

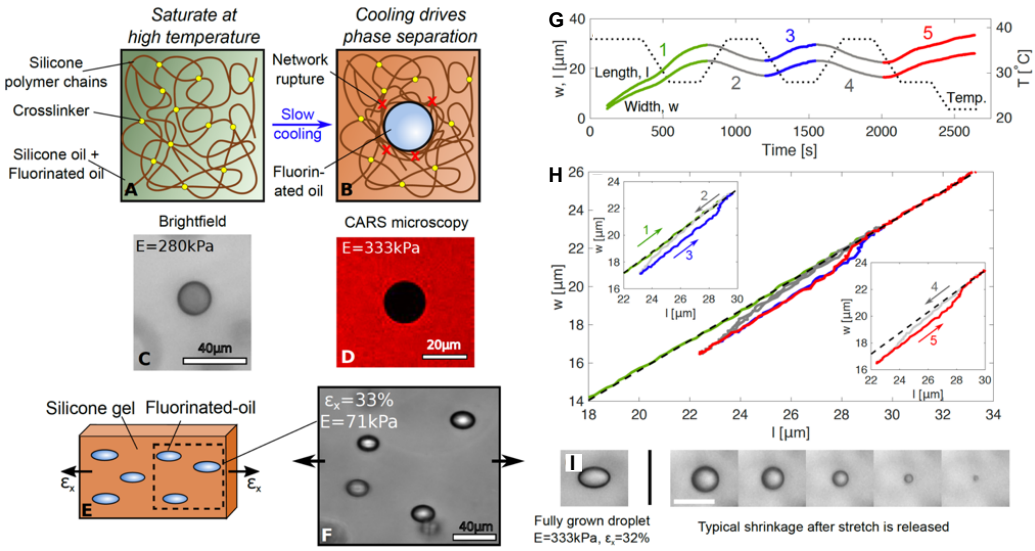

Figure 3.9 *Observing small scale fracture with a phase separation technique, reproduced from [83]. (A-D) By cooling a gel consisting of silicon polymer chains, swelled with a mix of silicone and fluorinated oil, cavities could be formed via phase separation of the oils. (E-F) By stretching the gel before inducing phase separation, fracture mechanisms could be inferred from the aspect ratio of the cavities in the following way (G) The gel was periodically heated and cooled, causing the cavities to expand and contract. (H)The hysteresis in the aspect ratio shows the irreversibility of the process, suggesting bond breakage. (I) When the gel is unstretched, the cavity remains spherical as it shrinks, implying distributed damage.*

By stretching the gel prior to phase separating the oils, the aspect ratio of the resulting cavities could be used to infer the damage mechanism around the crack. Periodically growing and shrinking the cavity showed evidence of irreversibly, the droplets were more elongated when they grew below a size that they had previously been expanded to, Figure 3.9G-H. This suggested that the gel network had been broken, or at least had stress-softened. They also note that the damage mechanism must involve breaking of the network over the entire surface of the

crack, as when the imposed strain is removed and the droplets are allowed to shrink they remain spherical. If a single (highly blunted) fracture were present instead, then the cavity would be expected to collapse into a penny shaped crack as was observed by Poulain, Figure 3.8.

No transition between this growth by apparently omni-directional fracture and growth by a single penny-shaped fracture has been observed in Style's system, however this is likely due to the cavities being unable to grow larger than ℓ_{EF}. This a problem that can be solved by the bacterial colonies described in this thesis, the problem of observing the presence of distributed damage can be solved by tracking the displacement of the gel around the colony.

Constant fracture pressure $P_c \sim E$ when a cavity is smaller than ℓ_{EF} is also supported by Style's observations. No transport of flurinated oil is observed between cavities of different sizes [85], if the cavities were at different pressures then ripening would be expected. Again this constant fracture pressure supports the idea of growth via distributed damage or cavitation as discussed earlier in the section.

3.6 Summary

Finally, I wish to summarize the discussed mechanisms of fracture and the length scales at which they are expected to be relevant. Three length scales have been recognized during this discussion, they are

1. The length of a stretched bond, $\ell_c = \frac{2\gamma E}{\sigma_c^2}$.
2. The cohesive zone size, $\ell_D = \frac{\Gamma E}{\sigma_c^2}$.
3. The elasto-fracture length scale, $\ell_{\mathrm{EF}} = \frac{\Gamma}{E}$.

The expected crack propagation pressure, P_c, as it depends on these length scales is plotted in Figure 3.10. A crack will expand elastically ($P_c \approx E$) when it is smaller than ℓ_c as deformations can be accommodated by the stretching of bonds. ℓ_c can be estimated by multiplying the bond length and yield strain of the material. Agarose has a bond length of order[19] 10's-100's nm [86–88] and

[19]The "bond" length I am referring to is the length of polymer chain between polymerised points in a network. I have used measurements of the pore size as an estimate of the bond length.

yield strain at least of the order[20] 0.2-0.4 [86, 89], so ℓ_c is also of orders 10 nm to 100 nm. ℓ_c is therefore unlikely to be relevant on the scale of bacterial colonies, as the size of a single bacterium ($\approx 1\mu$m) $\gg \ell_c$.

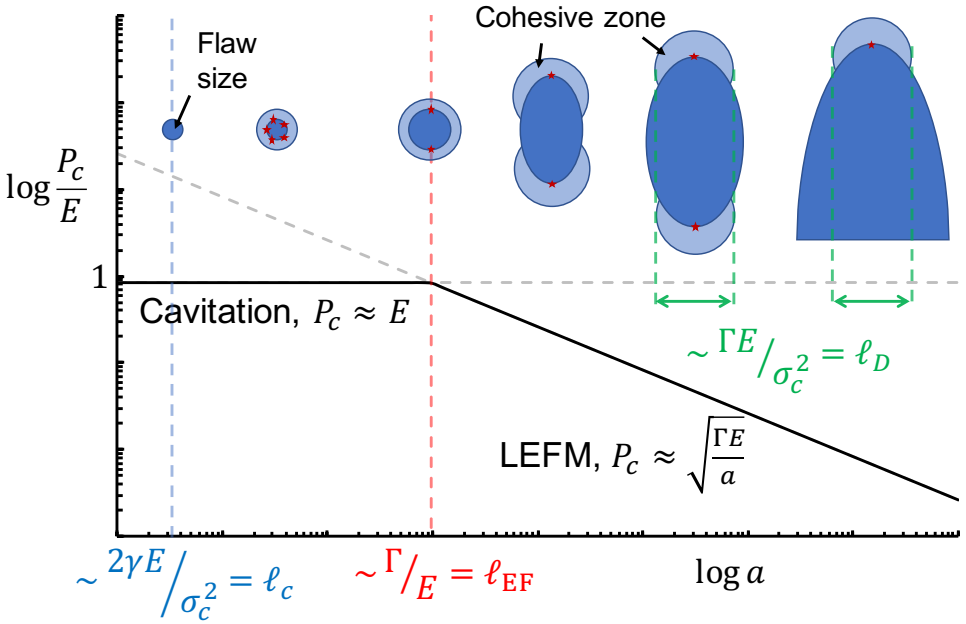

Figure 3.10 *Hypothetical scaling of the crack propagation pressure with crack size a in a material where $\sigma_c \gtrsim E$. Below $a \sim \ell_c$ the cavity expands elastically with $P_c \sim E$. For $\ell_c \lesssim a \lesssim \ell_{EF}$ the elastic limit of the material is reached and the cavity expands by bond breakage over the entire surface of the cavity. When $a > \ell_{EF}$ a single fracture plane dominates and the SYY criterion becomes valid. Throughout these length scales the material is damaged in a region of size ℓ_D which initially grows with the crack size and then becomes localized to the crack tip. Reproduced from [83].*

When the crack grows larger than ℓ_c, bonds will break when the maximum stress in the material, $\sigma_{\max}$, reaches the cohesive stress, σ_c. However, dependent on the relative magnitude of the cohesive stress of the material compared to its elastic modulus, crack tip blunting may be important. When $\sigma_c \ll E$, there is little blunting as the cohesive zone size ℓ_D, is larger than the size over which blunting occurs ℓ_{EF}. Therefore a cohesive zone will form in which plastic deformation and

[20]The cited measurements of the failure strain are debatable. In the first study cited, the same failure strain was measured for all agarose concentrations tested despite the average bond length of the agarose decreasing with concentration. The consistency of failure strain measurements suggests that cracks of a uniform size were present in all samples, meaning that the 'failure strain' was governed by the sample geometry rather than representing an intrinsic material property. The second study agrees with the first at low agarose concentrations, however concentrations above 1% w/v were not tested. These studies represent a lower bound on the yield strain.

fracture occurs. Such a process has been observed in ductile metals where the fracture stress of the metal does not decrease when cracks smaller than ℓ_D are present. This flaw insensitivity is thought to be due to cracks smaller than ℓ_D propagating when $P_c \sim \sigma_c$, independent of the crack size [90, 91].

When $\sigma_c \gtrsim E$, the process zone becomes smaller than the blunted zone ($\ell_D \lesssim \ell_{\mathrm{EF}}$) and substantial blunting can occur whereby the crack deforms without increasing $\sigma_{\max}$. In this case the fracture is thought to be propagated via cavitation and/or surface fracture as discussed in Section 3.5. Due to cavitation, the pressure required to propagate the fracture is modified to be $\approx E$.

When the fracture is larger than ℓ_{EF} and ℓ_D, the pressure required for fracture in a single plane becomes lower than that required for fracture over the entire surface. In this case a single fracture plane is thought to dominate and a penny-shaped crack should be formed, with the crack propagating when $P_c \propto 1/\sqrt{a}$. At larger scales still ($a \gg \ell_{\mathrm{EF}}$ and ℓ_D) SSY becomes valid and the predictions of linear elastic fracture mechanics are restored.

For agarose $\sigma_c \sim E$, as such the extent to which blunting is important to fracture propagation is not clear. The same situation is true for many hydrogels and is likely the reason for their notoriously contradictory behaviour, being both soft and brittle [79]. By tracking the morphology and deformations caused by the growth of bacterial colonies this work aims to shed light on the fracture process at this intermediate length scale.

For comparison I have plotted ℓ_{EF} for several materials in Figure 3.11. Note that for many typically brittle materials ℓ_{EF} is on the order of the atomic lattice size, in these materials $\Gamma \approx 2\gamma$.

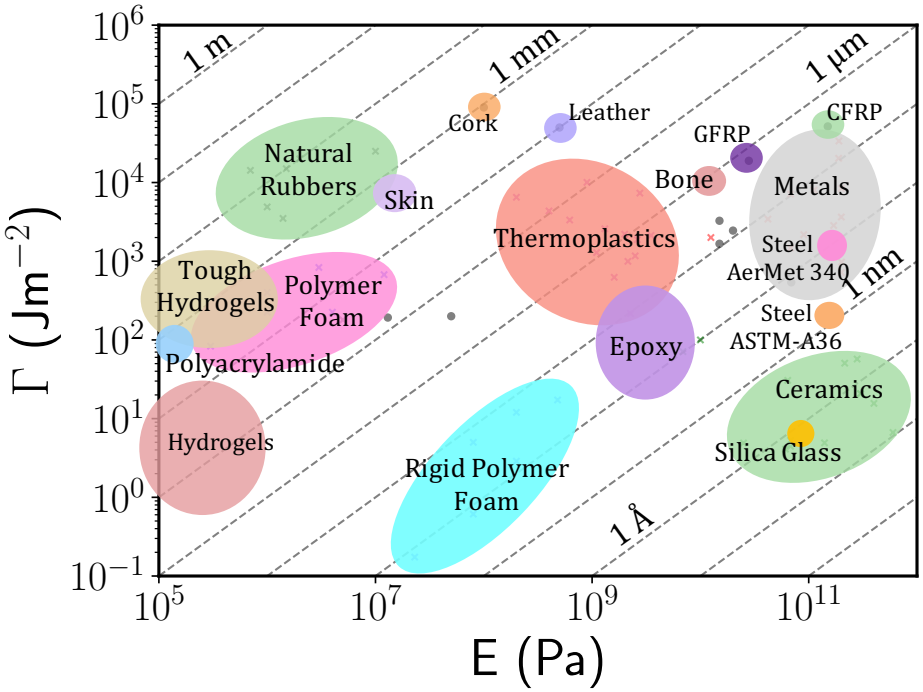

Figure 3.11 *Ashby plot of fracture energy vs Young's modulus for various groups of materials. The elasto-fracture length scale, ℓ_{EF}, is given by the diagonal dashed lines. For many brittle materials ℓ_{EF} is on the order of the atomic lattice size, in these materials $\Gamma \approx 2\gamma$. [56, 92–98].*

Chapter 4

Materials and Methods

4.1 Introduction to methods

In this chapter experimental and computational methods used to measure the morphology and displacement field surrounding growing colonies of bacteria are described. Adjustments to these protocols, needed for individual experiments, will be addressed in the relevant results chapters.

The chapter begins with a description of the microbiological methods necessary to sparsely inoculate agarose gels with single cells of *E. coli*. I then describe the operation of single plane illumination microscopy (SPIM)[1], discussing how colonies can be grown inside the SPIM sample chamber and how various experimental difficulties were overcome. In the second half of the chapter, methods for fusion and deconvolution of the image data sets are discussed. Methods used to extract the relevant colony dimensions from the images are outlined and a process for tracking and interpolating the displacements of fiducial markers embedded in the gel is explained.

4.2 Microbiological Methods

The following section describes the bacteria, culture media and culturing methods used in my experiments.

[1] Also known as selective plane illumination microscopy

4.2.1 Bacteria

The K-12 derived strain of *Escherichia coli* MG1655 was used for all experiments in this thesis. The MG1655 strain was transformed by Dr. A. Dawson to introduce the green fluorescent protein (GFP) expressing and teracycline resistance encoding pHC60 plasmid [99]. The pHC60 plasmid was chosen as it gives rise to a range of GFP expression levels in *E. coli*, so that cells in a colony have a range of brightnesses when exposed to excitation light. This range in fluorescence intensity is useful as it can help distinguish between cell progeny and reveal more of the internal structure of the colonies.

4.2.2 Culture Media

M9-glucose minimal media was used as the growth media for all experiments in this work. A minimal growth medium is one that contains just enough ingredients to support the growth of a bacterial population. Minimal media are often preferred for quantitative experiments because the ingredients are well controlled leading to more consistent growth behaviour. Bacteria in minimal media often exhibit slower growth[2] compared to "rich" media, which is advantageous for my experiments as it allows for finer temporal resolution when tracking changes in colony morphology. Another important benefit of using M9 minimal growth media is that it exhibits lower levels of auto-fluorescence than typical growth medias such as Lysogeny broth.

M9 media was prepared by adding 100 ml of M9 salts, consisting of 197.2 mM Na_2HPO_4, 88.2 mM KH_2PO_4, 34.2 mM NaCl and 74.8 mM NH_4Cl to 300 ml dH_2O. 8 ml of 20% glucose, 800 µl of 1M $MgSO_4$ and 40 µl of 1M $CaCl_2$ were then added to the solution. The solution was swirled until the $CaCl_2$ precipitate had dissolved. The media could then be sterilized using an autoclave or, more commonly, sterile ingredients were used and aseptic practice observed.

Agar plates and glycerol stocks were used to store cultures between experiments, for these applications Lysogeny broth (LB) (a non-minimal media) was used. LB was prepared by adding 10 g tryptone, 5g yeast extract and 10 g NaCl to $\approx$ 750 ml dH_2O. The mixture is stirred until free of precipitate before adding the final 250 ml of distilled H_2O, bringing the total volume to 1L. The media could then

[2]The time between bacterial fission events (known as the doubling time) is increased.

be sterilized using an autoclave.

4.2.3 Culturing and storing bacteria

When inoculating gels for experiments using *E. coli*, cells are harvested from a culture in the exponential phase of growth. By using an exponential culture most of the cells used to inoculate the gel were viable[3]. To obtain exponentially growing *E. coli*, cells needed to be transferred from long term storage to an exponentially growing culture. This section will describe the various stages of this process, taking cells from long term storage in a $-80\,^{\circ}\mathrm{C}$ freezer, through medium term storage on an agar plate and then finally to an exponentially growing starter culture.

Long-term storage

To ensure that the *E. coli* used for each experiment are of the same strain (isogenic), freezer stocks were kept. These freezer stocks contained small volumes of concentrated bacteria, kept at $-80\,^{\circ}\mathrm{C}$ to prevent degradation of the cell over years of storage. The freezer stocks were created from overnight cultures (described in Section 4.2.3). Falcon tubes containing the overnight cultures were spun down in a centrifuge at $1500g$ for 5 minutes, after which the supernatant was discarded and the remaining pellet was resuspended in 1ml of a LB-glycerol mix. Glycerol at a concentration of 30% was used to prevent damage to cell membranes by ice crystal formation. The resuspended cells and glycerol solution were then aliquoted into 1.5 ml freezer tubes, frozen in liquid nitrogen, and stored at $-80\,^{\circ}\mathrm{C}$. Repeated freezing and thawing will eventually reduce cell viability, therefore 'working' freezer stocks were made up from master freezer stocks annually.

LB-agar plates

LB-agar plates were used to store bacteria over a few week time span, so that isogenic populations of bacteria were readily available for experiments. An LB-

[3]Here, viable means able to reproduce. If a stationary phase culture were to be used, then a significant fraction of bacteria in the culture would be non-viable. This is because the growth rate and death rate of the cells in the culture are equal.

agar plate was made by adding agar powder (Oxide number 3) to LB at a concentration of 15g per litre of LB. The mixture was then autoclaved to melt the swollen gel before being poured, whilst still molten, into petri dishes in ≈ 25ml aliquots. Alternately, the autoclaved LB-agar gels could be allowed to set. The set gels could then be used to pour plates at a later date by melting them in a microwave. Once the LB-agar plates had set they were placed upside down in an oven for ≈ 20 minutes, this removed any excess moisture which would condense on the plate lid during storage. The plates were then sealed in a plastic bag and kept at 4 °C for up to a month.

Once LB-agar plates had been created they could be used for storing colonies of bacteria. Using an inoculation loop *E. coli* could be scraped from a freezer stock and streaked onto a LB-agar plate. Streaking involved scratching zigzag patterns with an inoculation loop into the agar. Successive zigzag patterns start by crossing the previously scratched pattern with a sterilized loop, in this way the concentration of cells per streak is reduced. The end result of the streaking was that a few cells were isolated from the rest and, after being incubated at 37 °C for 24 hours, formed clonal colonies on the agar surface. Plates with clonal colonies on them could then be stored for up to two weeks at 4 °C.

Starter Cultures

To generate cells in the exponential phase of their growth the clonal colonies from the agar plate were used. Cells from a single colony were picked with a pipette tip from the agar plates and used to inoculate 5ml of M9 minimal media in a falcon tube. The pipette tip was left in the falcon tube to aid mixing. The culture was then incubated overnight (16 hours) at 37 °C in a shaking incubator at 200 rpm. After a night's incubation, a population of *E. coli* in the stationary phase of growth was created. 10 µl of the stationary phase population in the overnight culture was added to 10 ml of fresh M9 media in a 100 ml conical flask. The freshly inoculated media was again incubated at 37 °C in a shaking incubator at 200 rpm until the culture had reached an optical density at 600nm incident wavelength (OD_{600}) between 0.1 and 0.3. At this OD_{600} Diarmuid Lloyd has shown that MG1655-pHC60 is in the exponential phase of growth. The optical density of the culture was measured by pipetting a 1 to 9-fold dilution of culture to pure media into a cuvette and using a spectrophotometer to measure the transmission of light through the sample. The OD_{600} of a sample is given by the log of the

ratio of the incident flux, I to the transmitted flux, T, at wavelength, $\lambda = 600$ nm, i.e.

$$\mathrm{OD} \equiv \log_{10}\left(\frac{I}{T}\right). \tag{4.1}$$

Before each spectrophotometry measurement I was calibrated using pure media, taking this OD to be 0. A Hach Lange DR5000 was used for all spectrophotometry measurements. Once the culture had reached an OD between 0.1 and 0.3 (after ≈ 3 hours) the *E. coli* could be used for experiments requiring exponential phase cells.

The length of time taken for the starter culture to reach an OD of 0.1 was indicative of problems with the media or the cells. If the culture had not reached an OD of 0.1 after $\approx 3\frac{1}{2}$ hours from initial inoculation then the experiment would be aborted and the cause investigated. The two problems that caused slow growth during my experiments were picking colonies from old LB-agar plates (> 2 weeks since inoculation) and improperly prepared M9 media.

4.3 Preparation of a sparsely inoculated gel

In this section I describe the creation of a gel that was sparsely inoculated with *E. coli*. Agarose was chosen as the inoculation gel because it is more optically clear than alternatives such as agar-agar, it also exhibits reduced autofluorescence [100]. Once agarose had been selected, two problems presented themselves:

1. Agarose melts at >90 °C and becomes highly viscous around 50 °C, both of these temperatures are higher than the inactivation temperature of *E. coli* (≈ 45 °C [101, 102]).

2. *E. coli* must be introduced to the gel in way that presents no preferred direction for their growth.

The only previous imaging study of bacterial colonies in a 3D was by Wimpenny [103], he solved the first of these problems by inoculating an agar surface and then pouring molten agar over the top of that surface, limiting the time that the bacteria were exposed to high temperatures. However it is possible that this method introduced a flaw in the agar along the surface of the first layer of agarose, leading to a preferred direction of growth. In this study both problems

are solved by using low melting point agarose (BP165 from Fisher). Low melting point agarose has a melting point of ≈65 °C (which is still high compared to the inactivation temperature of *E. coli*) but its gelling temperature is 25 ± 5 °C[4] and it retains a low enough viscosity to allow for inoculation at temperatures as low as 50 °C. Although 50 °C is higher than the inactivation temperature reported in [101] and [102], brief submersion in molten gel at 50 °C was not found to inactivate a significant number of *E. coli* (see Section 4.3.3).

4.3.1 Preparation of agarose gel

An amount of low melting point agarose was transferred into a transport tube (according to the desired concentration) before M9 minimal media was added to the powder until the mixture weighed 10 g. The mixture was vortexed and then heated at 85 °C in a water bath. The mixture was left to melt[5] for 1 hour. The agarose was melted at 20 °C above its ≈65 °C melting point as this resulted in a smoother, more uniform, gel. After melting, a stir bar was added to the mixture and it was transferred to a water bath held at 50 °C. The melted mixture was stirred at 300 rpm for 1 hour. The gel was then ready for mixing with cells.

To promote fluorescence intensity variation amongst the cells, no antibiotic was added to the gel. Fluorescence intensity variation was desired so that the movement of individual cells in a colony might be observed. The reason that the presence of antibiotic in the gel might reduce fluorescence intensity variation was that the same plasmids that code for the cells antibiotic resistance also code for GFP production. The range in fluorescence intensity between *E. coli* cells was likely due to stochastic variation in the number of GFP coding plasmids in each cell[6]. Therefore by adding antibiotic to the gel, cells with more GFP producing plasmids might be favoured leading to less fluorescence intensity variation. Antibiotic was not needed to select for *E. coli* as only a few cells were added to the gel, this meant that is was easy to tell whether a group of cells were *E. coli* or some contaminant species.

[4]This figure is taken from the Fisher webpage, in reality the gelling temperature was found to be closer to 30 °C.

[5]In other experiments the physical properties of agarose were not seen to change significantly when held at 85 °C for between 20 minutes and ≈ 4 hours.

[6]Stochastic variation might be due to low absolute numbers of pHC60 plasmids present in the cells.

4.3.2 Addition of fiducial markers to the gel

Before adding bacteria to the gel, fluorescent silica beads were mixed into it. Adding the beads before the bacteria minimised the time that bacteria were exposed to the 50 °C molten agarose. The silica beads were used as fiducial markers for both the registration[7] of different views of the samples and to track the displacement of gel around the growing colonies. There were two constraints on the size of the beads:

1. The beads had to be large enough that they were not free to move through the agarose network. Independent motion of the beads would prevent accurate tracking of displacements in the gel.

2. The beads were used to measure the point spread function of the system in order to carry out deconvolution, see Section 4.6.2. To get a good estimate of the point spread function the beads had to be smaller than the resolution of the system.

Silica beads[8] of radius 399 nm were used for all experiments as this is significantly larger than the reported pore size of agarose[9], so the beads should remain stationary unless the gel is displaced. The beads are also slightly smaller than the resolution of the SPIM system (≈1.4 µm, Section 4.6.2).

The concentration of fiducial markers needed to be controlled. A higher concentration of markers would allow for higher resolution displacement measurements, however there were several limiting factors. The first of these was the displacement of the beads between time steps. If this displacement was larger than the inter-bead distance then simple tracking algorithms based on minimization of the total distance moved by the beads cannot be used. The second factor was the registration algorithm (see Section 4.6.2). The algorithm works by matching constellations of markers. When too many markers are present, constellations cannot be distinguished and registration becomes difficult.

[7] Registration refers to the transformation of multiple images onto one coordinate system.

[8] Beads were synthesised by Dr. Andrew Schofield via a condensation reaction. By converting tetraethyl orthosilicate to silicon dioxide with the addition of water in the presence of Fluorescein isothiocyanate and (3-aminopropyl)triethoxysilane, silica spheres (beads) with bound fluorescein were made. By varying the temperature at which the condensation reaction occurs the size of the beads could be controlled.

[9] As discussed in Section 5.2.1, Agarose's pore size is smaller than 500 nm in the range of concentrations used in my experiments [104, 105].

By trial and error the second of these factors was found to be the limiting one, with the maximum number of beads per field of view found to be ≈ 10,000.

To achieve a concentration of ≈ 10,000 beads per field of view (294.12 × 221.71 × 300 µm^3) beads kept in storage at a volume fraction of ≈ 40% were diluted to a volume fraction of ≈ 0.04%. This dilution was achieved by simply piptetting 10 µl of the thick bead suspension into the molten agarose. This transfer was completed prior to adding the bacteria. Stirring at 300 rpm, for 2 minutes was found to be adequate for homogeneous mixing. Care was taken that the beads were not left in the molten gel for longer that around ten minutes, after which beads aggregated noticeably.

4.3.3 Addition of E. coli to the gel

After beads had been mixed into the gel, the gel was inoculated with *E. coli*. The inoculation concentration of the bacteria had to be such that the mechanical and chemical interactions between colonies were limited whilst the practical need to find cells within the gel was met. The spatial extent of mechanical interactions can be estimated by considering the range of the expected elastic deformations. If the colony elastically displaces the gel, then the displacement in the gel should decrease with the square root of the distance from the colony surface (c.f. Equation 3.31). For example if the colonies elastically displace the gel by ≈ 100 µm at their surface[10] then the displacement in the gel will fall to ≈ 5 µm at a distance of ≈ 400 µm from the colony. In reality the extent of the deformations around the colony only extended to about half this distance. Therefore, to ensure that displacements from surrounding colonies did not interfere with observations of displacements around the subject colony, cells should start at least 400 µm apart (equivalent to ∼ 2-3 cells per µl).

The chemical interaction between the colonies has been the subject of many studies in food science [36–40]. In general, the maximum size of a colony in a population of submerged colonies is controlled by the inoculation concentration. At the concentration of ∼ 2-3 cells per µl, informed by the previous reasoning from mechanical interactions, colonies grew to fill the field of view of the SPIM apparatus. Therefore a lower inoculation concentration to avoid chemical interactions was unnecessary for this study.

[10]This approximately the maximum major axis length of colonies studied in this work.

In order to dilute starter cultures of *E. coli* so that the gel could be inoculated at a concentration of $\sim$ 2-3 cells per µl, the concentration of cells in the starter culture had to be estimated. The gold standard for such estimations comes from spreading the starter culture onto a LB-agar plate and counting the number of colonies that form (known as colony forming units, CFU), each colony is assumed to result from a single cell in the starter culture. However this process requires days of preparation, therefore the optical density (OD) of the starter culture is used to quickly estimate the cell density. To do so OD must be calibrated against CFU. Calibration of the CFU density vs OD for MG1655-pCH60 had been performed previously by Dr. Diarmuid Lloyd [106], Figure 4.1. By performing a linear regression (weighted by standard deviation), the relationship between CFU and OD was found to be:

$$\text{CFU/ml} = ((6.62 \pm 0.41) \times \text{OD} + 0.05 \pm 0.03) \times 10^8. \tag{4.2}$$

A 200,000× dilution of a 0.1 OD starter culture was used for all experiments in this study. This resulted in an average of 7.3±1.2 cells per µl, slightly higher than the 3.3 per µl equation 4.2 would predict[11]. This concentration was slightly higher than the $\sim$ 2-3 cells per µl target discussed previously and was used because the variance in distances between colonies was large enough that isolated colonies ($\approx$ 1mm from any others) were easily found.

4.3.4 Mounting the sample in the microscopy setup

After mixing bacteria and silica beads into the molten gel the next challenge was to mount a sample of the set gel in the SPIM setup. The gel had to be separated from the water in the sample chamber to prevent leaching of the M9 salts and glucose from the gel. This separation was achieved using fluorinated ethylene propylene (FEP) tubing. FEP is a biocompatible fluoropolymer with good optical clarity and a refractive index (1.344) very close to that of water (1.335), so that there was little refraction of the light sheet as it passed through the material. Tubes of FEP, 3 cm long, were cut and a pipette was used to suck the molten agarose, cells and silica bead mix into the tube, Figure 4.2.

An air gap a couple of millimeters in length, made by removing the pipette tip,

[11] Observed cell concentrations were measured by counting the number of colonies formed in the FEP tubes (see Section 4.3.4 after experiments were complete.)

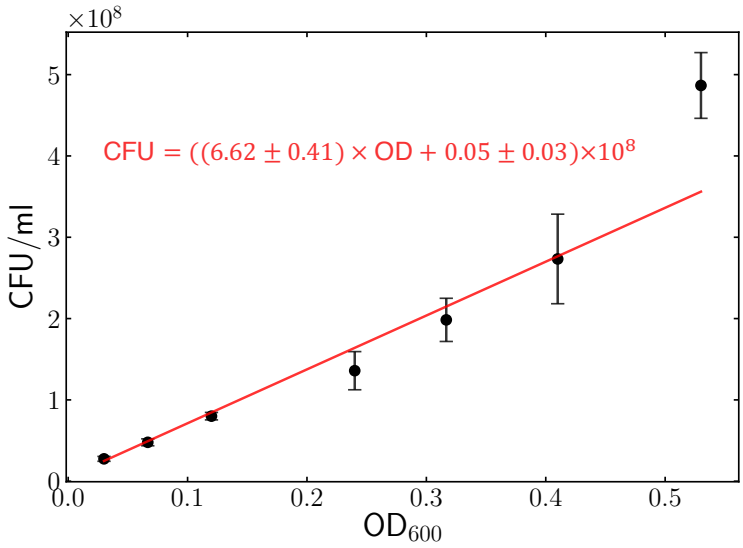

Figure 4.1 *Colony forming units (CFU) per ml of culture as a function of the optical density at 600 nm (OD_{600}). A fit, weighted by the standard deviation of the CFUs, is plotted in red with the Equation of the fit also given in red. The highest OD measurement lies far from the weighted fit line, however it is far from the OD that I typically work with ($\sim$ 0.1 OD) and, due to its large uncertainty, contributes very little to the weighted fit. Data collected by Diarmuid Lloyd [106].*

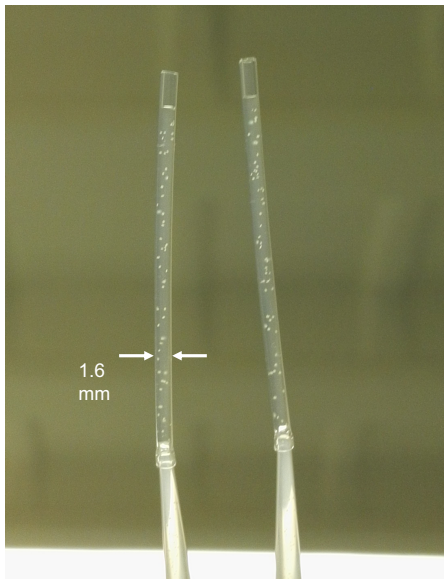

Figure 4.2 *Two 1.6 mm diameter FEP tubes containing agarose and dispersed bacterial colonies. Colonies are spaced 500 µm apart on average, however there is a large variance in spacing The pipette tip used to suck the molten agarose and E. coli mix into the tubes can be seen at the bottom of each tube. An air gap no greater than 2mm in length is created when the pipette is removed.*

was left at one end of the tube. This air gap prevented contact between the water of the sample chamber and the gel. This separation was important as otherwise the nutrients (M9 salts, glucose) in the M9 media would leach out of the gel and prevent colonies from growing.

The FEP tubing with set gel then had to be mounted in the microscopy system. The mounting point was on the arm of the 4D stage, Figure 4.4a. The main obstacle that any mounting solution had to overcome was to remain stationary relative to the arm of the 4D stage over the duration of a day long experiment. The first design used, 4.3a, failed as the rubber stopper used to hold the FEP tubing would warp as its temperature changed. The second design, Figure 4.3b, was made out of a perspex cylinder. A 1.6mm hole was drilled in one end of the perspex to hold the FEP tubing. A second hole was drilled radially into the cylinder, perpendicular to the axial hole, to allow air to escape when the FEP tubing was inserted into the axial hole. The axial hole was filled with M9 media prior to sliding the FEP tubing to prevent desiccation of the gel. This sample holder was used for the majority of experiments. A final sample holder, Figure 4.3c, was used after the microscopy system had been modified for the use of oil droplets (see Chapter6). A pin vice was used to hold the sample in place, the top of the FEP tube was sealed with Vaseline in this case. This sample holder was only used for two experiments using bacteria as it required more careful monitoring of the temperature in the sample chamber due to the increased thermal conductance of the metal holder. Each sample holder was held in place in a cuff attached to the rotating bearing embedded in the arm of the 4D stage using three grub screws.

4.4 Single plane illumination microscopy

Having encapsulated *E. coli* in agarose, single plane illumination microscopy (SPIM) was used to image the cells as they underwent binary fission and grew into colonies. SPIM is a type of fluorescence microscopy where a sheet of light is used to optically section the sample. The sample can be moved through the sheet of light to create volumetric images, Figure 4.4b. The sample can be rotated and the imaging process repeated from multiple angles. By combining multiple volumetric images taken from different angles, regions occluded by highly scattering samples can be uncovered. This is a major advantage when imaging bacterial colonies, which severely scatter light, and allows for three dimensional acquisition of their morphology.

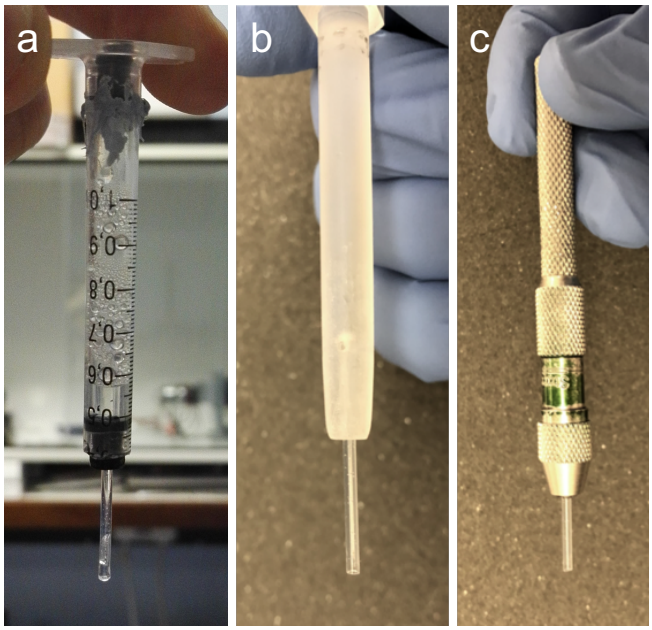

Figure 4.3 *SPIM sample holders. (a-c) Examples of sample holders. a shows an early sample holder with a syringe plunger used to hold the FEP tube. The plunger would warp when heated and cause the field of view to drift. b was the holder used for most growth experiments. c was used for two growth experiments after the 4D stage had been modified for oil droplet experiments that will be discussed in Chapter6.*

In principle the 3D morphology of the colonies could be imaged using confocal microscopy by rotating the sample. This could provide higher resolution images of the colonies. However, there are two more advantages of SPIM that cannot be reproduced by confocal microscopy. The first is that each plane in the sample is illuminated only once for each volume scan. This results in lower levels of photobleaching[12] compared to confocal microscopy, where for each scan of a plane the entire sample will be exposed to laser light. Reduced photobleaching allows for extended measurement times in the sample. The second advantage is the speed of measurements. By illuminating an entire field of view at once, images are collected in a widefield manner, which is much faster than a typical point-scanning microscope.

Figure 4.4 show schematics and a photograph of the SPIM apparatus. First a light sheet had to be created and focused in the sample chamber. A 488nm sapphire single frequency laser was used to create an $\approx$ 1mm diameter, coherent and collimated beam. The beam was then expanded by a telescope to a diameter of 2mm before it passed through a neutral density filter, the purpose of that filter

[12]Photobleaching is the reduction in fluorescence intensity caused by destruction of fluorescent molecules.

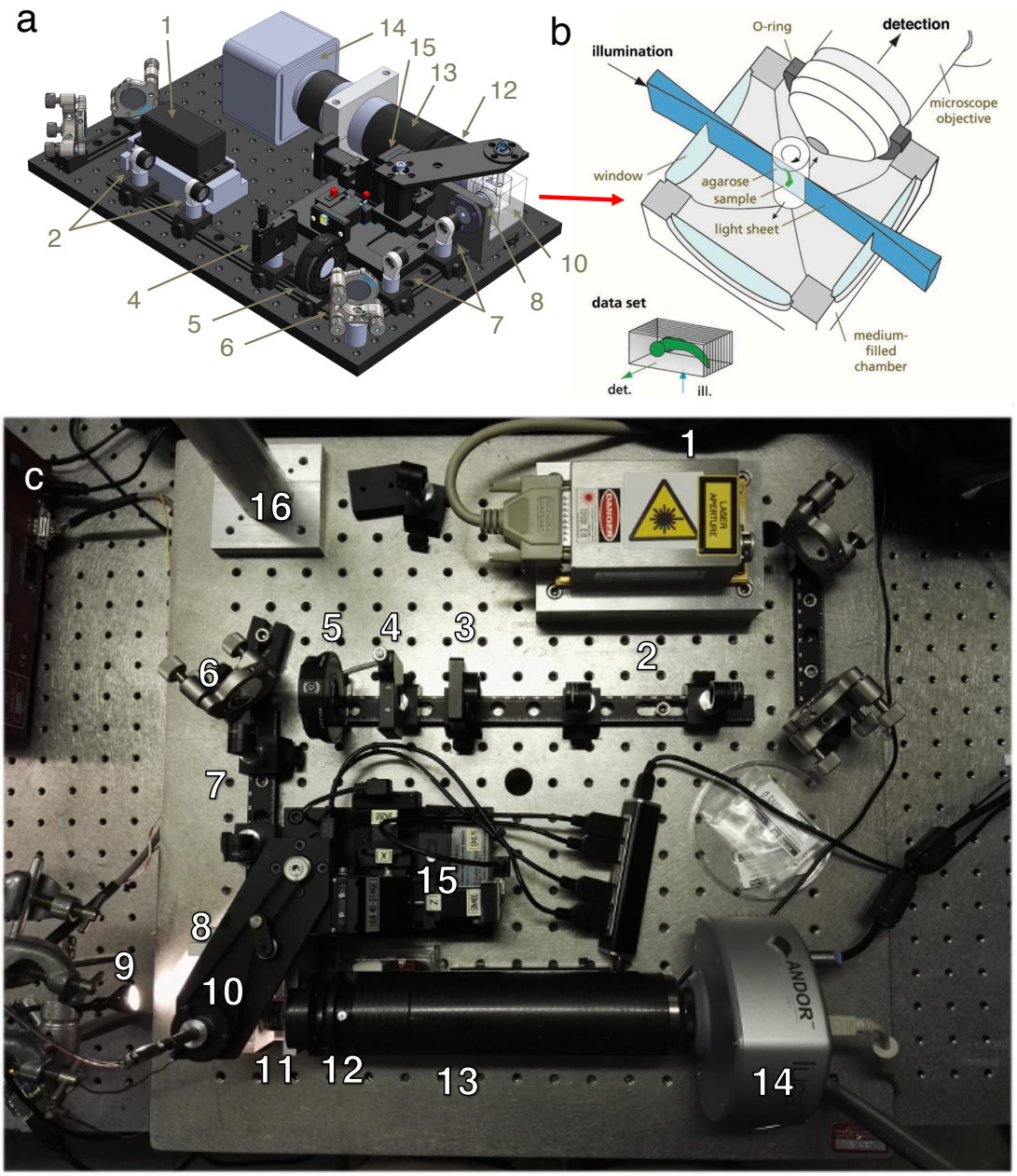

Figure 4.4 *SPIM apparatus. (a) Schematic of the SPIM apparatus. (b) Schematic of sample chamber. (a) and (b) have been reproduced from [107]. (c) Photograph of SPIM apparatus. (1) 488nm Sapphire laser. (2) Beam expanding telescope. (3) Neutral density filter. (4) Vertical optical slit. (5) Cylindrical lens. (6) 1" tilting mirror. (7) Back focal plane telescope. (8) Illumination objective. (9) Backlight, diffuser not shown. (10) Sample chamber, covered by arm of 4D stage. (11) detection objective. (12) Emission filter. (13) Infinity space tube. (14) Camera. (15) 4D Stage; (16) Pillar used to prop up blackout cloth. See main text for full description.*

will be explained in Section 4.4.4. The beam then passed through a vertical optical slit, which controlled the width of the beam[13]. The beam was then focused into a sheet using a cylindrical lens. The focal point of the cylindrical lens coincided with a 1" tilting mirror which was made conjugate to the back of the illumination objective using another telescope. The illumination objective, a water dipping Olympus UMPLFLN 10×/0.3, was then used to focus the light sheet onto the sample. The light sheet excited fluorescent molecules in a thin slice of the sample and the light emitted by those molecules was captured by an Olympus UMPLFLN 20×/0.5 water dipping objective. Captured light was passed through a dichroic filter to exclude any reflected illumination light and only capture light in the wavelengths emitted by the fluorescent molecules. The captured light was collimated and traveled down the infinity spacer tube before being focused onto the CCD of a Luca S 658M camera.

Accurately rotating the sample was an issue in early experiments. A Picard 4D stage, consisting of XYZ kinematic piezo positioning actuators plus a rotational piezo motor, was used to control the position of the sample. The O-ring belt connected the motor and sample holder bearing would occasionally slip due to the bearing sticking. This caused the field of view to shift and made long term experiments impossible. The slipping problem was overcome by two changes to the apparatus, first the O-ring drive was replaced by a more precise toothed drive belt[14] with a larger pulley ratio, the larger pulley ratio increased the torque on the bearing preventing sticking. Secondly, the bearing was lubricated prior to each experiment with Dlube.

4.4.1 Pixel size measurement

Measurement of the pixel size[15] was crucial for all measurements such as the light sheet thickness, particle tracking and morphology measurements. The pixel size was measured by mounting a grating with a 25.5 µm period to a pin vice mounted on the 4D stage. The position of the grating was adjusted until its surface was in focus under the back light illumination, Figure 4.5a. The grating was at an oblique angle to the camera, to find this angle the fast Fourier transform (FFT) of the image was taken, Figure 4.5b. The angle between the camera vertical and

[13]The beam expansion was carried out to improve the precision with which the optical slit could be adjusted.

[14]The toothed drive belt had a minimum rotation of 0.5°.

[15]That is the size which a single pixel samples in the captured image.

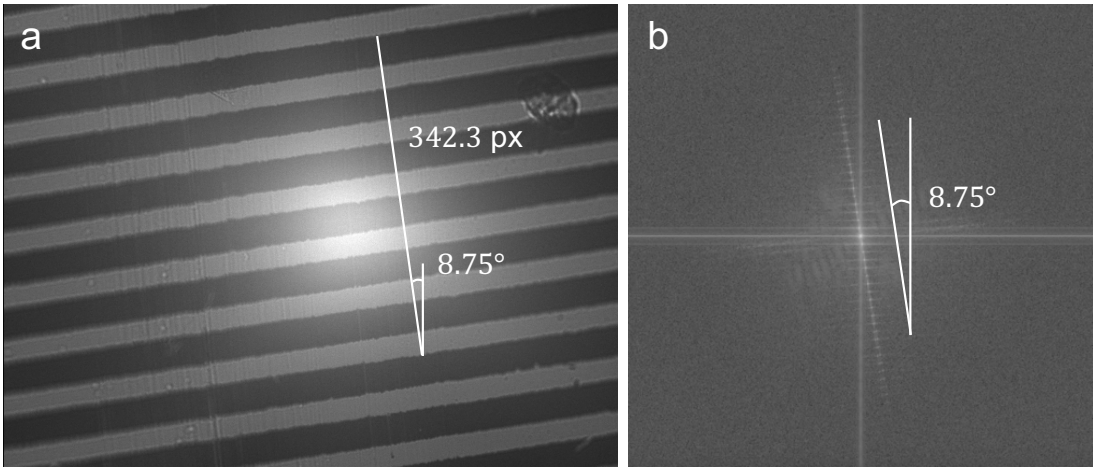

Figure 4.5 *Pixel-Size calculation. (a) A grating with* 25.5 µm *period was imaged using the SPIM apparatus. (b) The Fourier transform of (a) was used to determine its angle w.r.t. the camera. Using that angle (a) could be rotated allowing for more accurate measurement of the pixel size.*

the direction perpendicular to the grating lines can be determined from the bright dotted line feature in the FFT corresponding to the grating spaces. Having found the angle perpendicular to the grating lines, the image in Figure 4.5a could be rotated and the distance (in pixels) over several grating periods measured. This distance was measured in several positions and, by comparison to the known grating period, the average distance per pixel was found to be 0.447 ± 0.002 µm.

4.4.2 Light sheet alignment and calibration

Figure 4.6a defines the coordinate system used for the discussion of the SPIM apparatus in this section. The z-axis is parallel to the axis of the detection objective, while the x-axis is parallel to the axis of the illumination objective. A y-axis is defined to perpendicular to the x and z-axis, so that the xy-plane is parallel to the focal plane of the detection objective and the yz-plane is parallel to the focal plane of the illumination objective.

The light sheet must be exactly perpendicular to the objective (z-axis) and its central plane must lie in the xy-plane, Figure 4.6a,b. The light sheet is not of uniform thickness along the x-axis, instead having a Gaussian beam cross-section in the xz-plane. The thinnest section of the light sheet should be aligned with the centre of the field of view to give maximum z-axis resolution. This section will explain how alignment was achieved and discuss obstacles to achieving this.

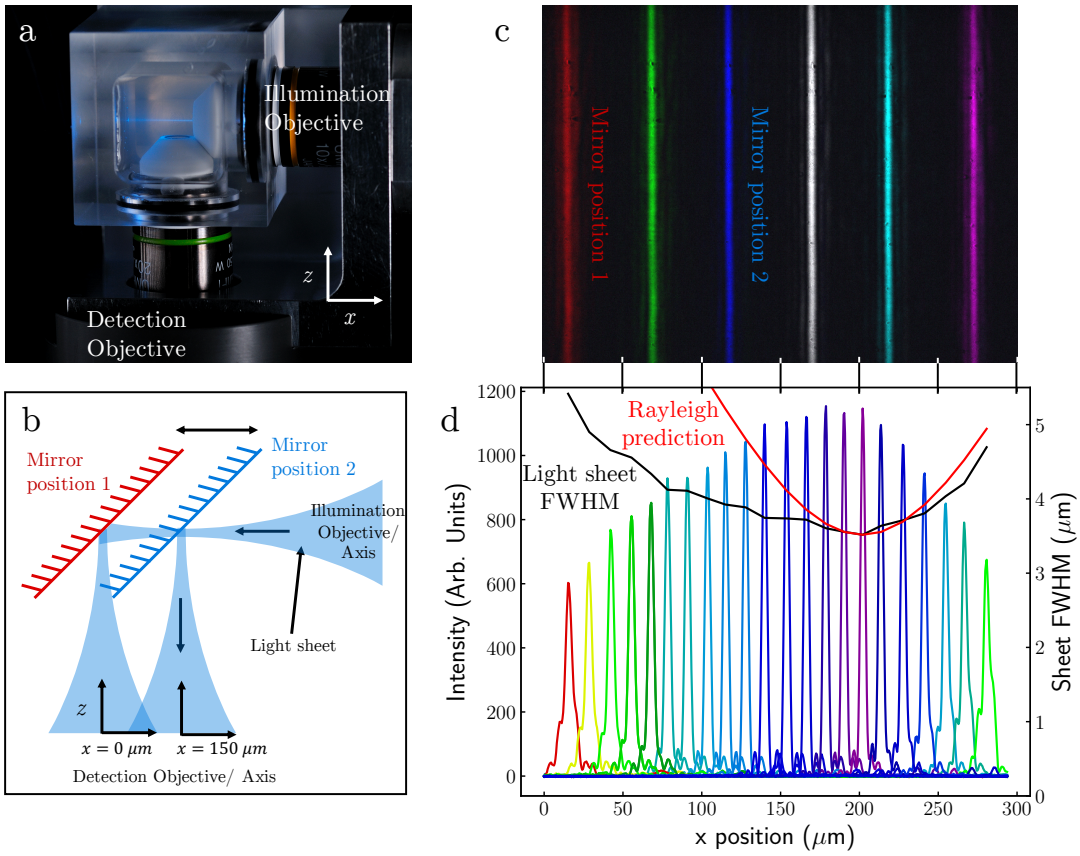

Figure 4.6 *Calibration of the light sheet. (a) Photograph of SPIM chamber, light sheet is focused with 10x objective, taken from OpenSPIM website. (b) To calibrate the light sheet a mirror is place at 45° to the incoming sheet. The light sheet width can be examined by re-positioning the mirror along the x-axis. (c) A composite image of the light sheet at 6 different mirror positions. (d) Pixel intensity as a function of position in the field of a view for 22 different mirror positions, the FWHM of the light sheet is plotted in black along with the predicted FWHM. The FWHM of the light sheet varies from* 3.5 µm *to* 5.4 µm*, with an average of* 4.1 µm *and a standard deviation of* 0.5 µm*.*

The initial step in aligning the light sheet was to move the sample chamber, and objectives attached to it, along the z-axis until the light sheet exited the illumination objective parallel to the x-axis, Figure 4.6a. A mirror was positioned at the focal point of the detection objective using the backlight to illuminate the mirror surface. The mirror was then rotated to a 45° angle to both the x and z-axis, Figure 4.6b. A neutral density filter was placed in the light path to protect the camera. The back focal plane telescope (Figure 4.4a7,c7) was adjusted until the thinnest section of the light sheet coincided with the mirror. By adjusting the back focal plane telescope the position of the thinnest section of the sheet moves along the z-axis, this was corrected for by adjusting the tilting mirror (Figure 4.4a6,c6). After iteratively adjusting the the tilting mirror and back focal plane telescope, the inserted mirror was made conjugate with the tilting mirror and the light sheet was in focus in the detection objective. The orientation of the light sheet could be adjusted by rotating the cylindrical lens.

Once the light sheet was in focus on the mirror and with the detection objective, the width of the light sheet could be adjusted. As the z-axis resolution was controlled by the the light sheet thickness, the aim was to make the width of the light sheet as thin as possible. However, the sheet thickness should also remain roughly constant across the field of view. This introduced a compromise for the following reason. The width of the sheet in the z direction, w, as a function of the distance, x, from the position of the focal point, x_0, can be expressed as

$$w^2(x) = w_0^2 \left[1 + \left(\frac{\lambda(x - x_0)}{\pi w_0^2} \right)^2 \right], \tag{4.3}$$

where λ is the wavelength of incident light and w_0 is the width of the sheet at the focal point [108, 109]. From Equation 4.3 a length scale x_R can be defined[16] as,

$$x_R = \frac{\pi w_0^2}{\lambda}. \tag{4.4}$$

This length scale defines the point at which the sheet width increases by a factor of $\sqrt{2}$, and characterises the size of the light sheet's field of focus. Importantly the Rayleigh range goes as the square of the sheet width, therefore high z-axis resolution limits the size of the field of focus. Quantifying the acceptable range of light sheet width across the field of view was difficult because, as I will discuss in Section 4.6.2, fusion of images from multiple points of view improves z-axis resolution and improved z-resolution will make the deconvolution process more

[16] x_R is known as the Rayleigh range.

accurate in the periphery of the image. Therefore, in practice, the main goal of this step of the light sheet alignment was to ensure that x_0 was as close to the centre of the field of view as possible. The width of the light sheet was then adjusted in a later step to ensure that the intensity of fiducial markers was uniform across the field of view (Section 4.4.3).

To find x_0 the light sheet width across the field of view was sampled by translating the inserted mirror along the x-axis, Figure 4.6b,c. The back focal plane telescope was adjusted until the sheet appeared thinnest at the centre of the field of view.

To accurately determine the final position of x_0 the intensity profile of the image[17] was measured at several x positions, Figure 4.6d. The light sheet width could then be characterised by its full width at half maximum (FWHM). The FWHM was found by measuring the width of the intensity peak at half the maximum intensity, $I_{\frac{1}{2}\max}$. In this case the peak was only ≈ 10 pixels across, therefore the sub pixel position of the half maxima point, $P_{\frac{1}{2}\max}$ could be found using linear interpolation, i.e.

$$P_{\frac{1}{2}\max} = P_i + \frac{P_{i+1} - P_i}{I_{i+1} - I_i}\left(I_{\frac{1}{2}\max} - I_i\right), \tag{4.5}$$

where I_i and P_i are the intensity and position measurement at the pixel position just before $I = I_{\frac{1}{2}\max}$ and I_{i+1} and P_{i+1} are the next intensity and position measurements (just after $I = I_{\frac{1}{2}\max}$). The FWHM is then given by the difference between the two $P_{\frac{1}{2}\max}$ that are found before and after the intensity peak. Figure 4.6d plots the intensity profile of the light sheet as a function of its x position along with the FWHM. The FWHM varied between 3.5 and 5.4 μm and it is clear that x_0 is not in the centre of the field of view, instead being $\approx 200\,\mu$m from the left of the frame. Whilst this was clear upon looking at the processed data, during the experiment images like those shown in Figure 4.6c were all that could be used, so determining the exact x position of x_0 was quite difficult in practice.

The light sheet FWHM as a function of distance from x_0 does not agree with the Rayleigh prediction (Equation 4.3, red line in Figure 4.6d). This is because Equation 4.3 is only rigorously valid when the numerical aperture of the lenses is $\ll 1$. The numerical aperture of the illumination lens is 0.3, therefore diffraction will change the coefficients in Equation 4.3 [110], however x_R should remain proportional to w_0^2 (as seen in Figure 4.6d).

[17] That is the average of pixel intensities at position x as a function of x.

4.4.3 Adjusting the width of the light sheet

After the light sheet had been aligned so that its focal point was as close to the centre of the field of view as possible, the width of the light sheet could be adjusted. The width was adjusted so that the Rayleigh range was approximately equal to half the size of the field of view, or in other words so that the light sheet thickness was relatively uniform across the field of view. This adjustment was most easily carried out when imaging fiducial markers embedded in agarose gel, so that the light sheet width could be gauged by the sharpness of the beads. Adjustment of the width was carried out before each experiment to ensure good image quality and that the PSF was reasonably uniform throughout the imaging volume.

The sparsely inoculated agarose in FEP tubing was mounted in the 4D stage. A region containing no bacteria was illuminated with the light sheet. The vertical optical slit (Figure 4.4d) was adjusted until the beads appeared reasonably uniform in brightness across the field of view, Figure 4.7a. Of course due to Equation 4.3 the beads at the periphery of the image would always appear dimmer than those near the centre of the field of view, a balance between central bead sharpness and minimizing out of plane illumination was sought.

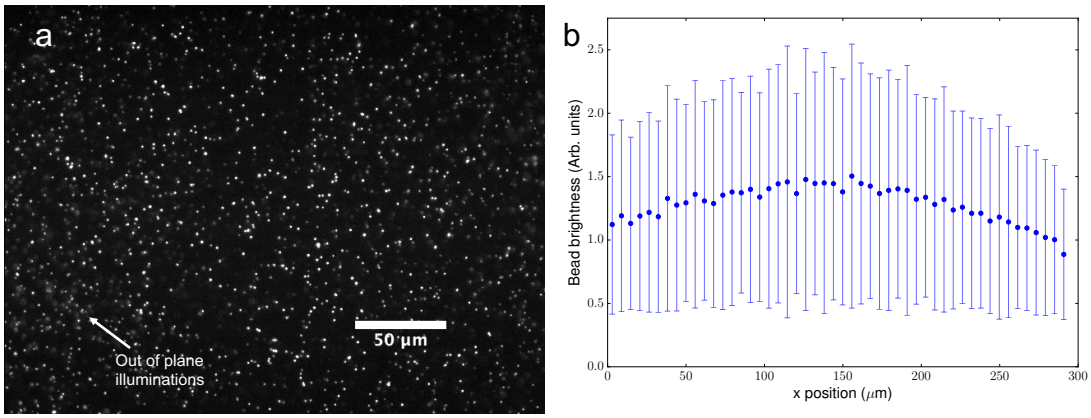

Figure 4.7 *Bead brightness across the field of view. (a) Image of the beads used as fiducial markers, by eye the beads closer to the centre of the field of view are sharper than those at the periphery. Near to the periphery of image, where the light sheet is wider, the out of plane beads become slightly illuminated. (b) Plot of bead brightness as a function of x-position in the field of view. The bead brightness peaks near the centre.*

To quantify the uniformity of the light sheet, bead brightness was measured. The bead brightness (BB) is the zeroth moment of the bead's intensity distribution

(above background intensity, I_B,) within 3 pixels of the bead centre, defined as

$$\mathrm{BB} = \sum_i \begin{cases} I(i) - I_B, & \text{if } |P(b) - P(i)| < 3 \text{ pixel widths} \\ 0, & \text{otherwise} \end{cases}, \tag{4.6}$$

where i corresponds to a voxel in the image, $I(i)$ and $P(i)$ are the intensity and position of that voxel respectively. $P(b)$ is the position of the centre of the bead. The method to determine the central voxel of the beads will be discussed in Section 4.6.4. I_B is found by taking the mean of the intensities of voxels that were not within 3 pixels of a bead centre. The BB is measured for all beads in a 658 px × 496 px × 201 frame volume (294.12 × 221.71 × 300 µm^3 volume). Figure 4.7b plots the mean bead brightness for beads grouped by their x position into bins, along with the standard deviation of the BB in that bin. Figure 4.7b shows that whilst the mean BB peaks near the centre of the field of view, the range of mean BB does not exceed one standard deviation from the mean BB at any other x position. Visually this means that the bead brightness appears uniform.

Figure 4.7 demonstrates another interesting feature of the beads, they have a large standard deviation (compared to their mean) in brightness. This is likely because some beads uptake more Fluorescein during condensation. As will be discussed further in Section 4.6.4, the bead brightness can be used to distinguish between beads in successive time points, which increases the maximum trackable bead density.

4.4.4 Photobleaching and laser-camera synchronization

Photobleaching is caused by the photochemical destruction of fluorescent molecules by excitation light, resulting in fluorescent objects becoming dimmer over time [111]. It is a significant issue when performing fluorescence microscopy over long periods of time. In initial runs of the experiment photobleaching of the Fluorescein infused silica beads prevented registration and tracking of later timepoints, it was therefore crucial to find a way of minimising photobleaching during experiments.

An auto shutter can be used to minimize photobleaching by switching the laser off between exposures. This meant that during sample translation and rotation the sample was not exposed to photobleaching light. The movement time was

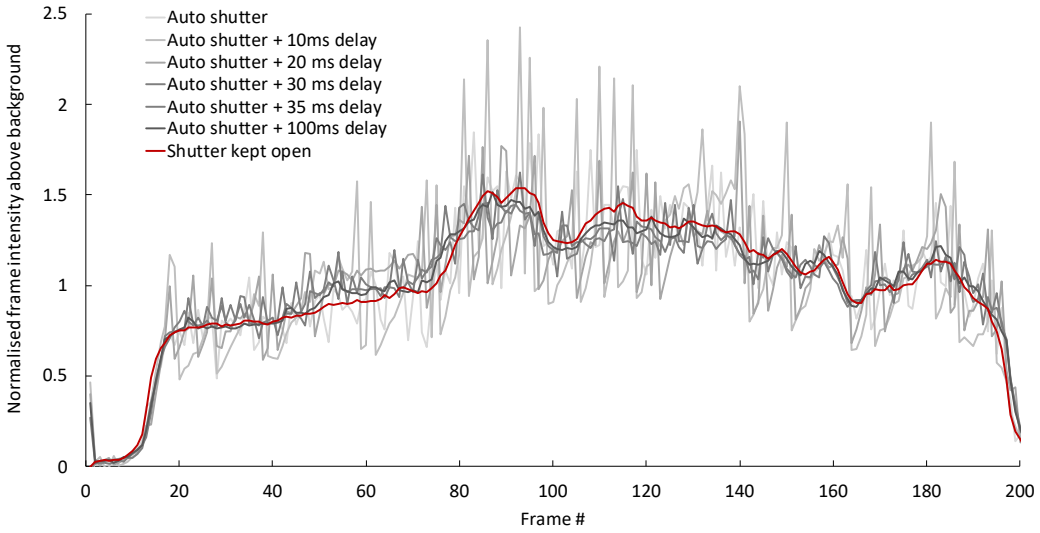

Figure 4.8 *Plot of the mean intensity above background of frames taken with different delays before exposures using the auto-shutter. Mean intensities are normalised by the mean intensity across all frames to account for photobleaching. The red line is the mean intensity of each frame when the shutter was kept open, keeping the shutter open removed any desyncing problems.*

significant, taking around 1 minute per view compared to 2 seconds of exposure time (10 ms exposures per view). However, it was found that the auto shutter did not synchronize with the exposure period. This desynchronization resulted in the sample being illuminated for different lengths of time each exposure, causing some frames to appear much brighter than others, Figure 4.8. To solve this desynchronization problem a delay was added before each exposure to ensure the laser was switched on for the exposure's duration. There were two problems with this solution. First, even with a short delay, the frame intensity remained inconsistent (Figure 4.8) and second, the ≈100 ms delay needed to solve the issue was longer than the exposure itself (≈10 ms), negating any reduction in photobleaching. Therefore another solution to photobleaching was sought.

The solution to the photobleaching problem was to reduce the laser power by introducing a neutral density filter[18] to the illumination path. Images could then be captured with longer exposure times so that the proportion of time spent translating the sample was small compared to the exposure time, effectively maximising the useful exposure time. To examine the effect of laser power on bleaching, the power of the 488nm sapphire laser was set to 1.5 mW and a fixed

[18] A neutral density filter is a filter that reduces the intensity of all wavelengths of light that pass through it.

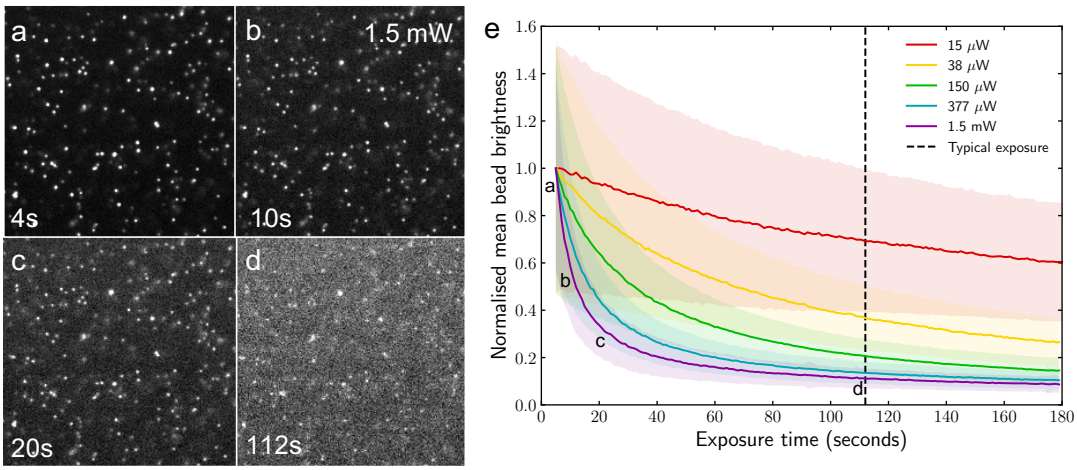

Figure 4.9 *Bead bleaching. (a-d) The effect of exposure to 1.5 mW laser after 4, 10, 20 and 112 seconds, images have undergone auto contrast. By 112 seconds many beads are no longer observable above the background brightness. (e) Plot of mean bead brightness normalised by starting brightness for different laser powers. The shaded regions represent a 1σ deviation from the mean. The typical exposure time during a colony growth experiment is marked by the dashed line.*

slice of the gel with embedded fiducial markers was illuminated, the power of the laser could then be attenuated by adding neutral density filters (Figure 4.4c3) of varying optical density[19]. Figure 4.9a,b shows the effect on the bead brightness of exposure to the laser after its power has been attenuated by a neutral density filter. With no filter the beads are exposed to the 1.5 mW laser and bleach rapidly. When a neutral density filter with optical density 2.0 is added to the illumination path, the laser power is reduced to 15 µW and the bead brightness does not reduce significantly over the typical exposure time of a ∼1 day experiment (≈112 s).

The neutral density filter with optical density 2.0 was used for all experiments in this work. Whilst this filter reduced photobleaching, it extended the exposure time required to achieve a good signal to noise ratio in the images significantly. The end result was that each volume scan took approximately 100 s and the full set of volume scans (that would be fused into the final image) took approximately 12 min. The colonies would grow by a small amount over this time period, resulting in a slight blurring of their internal structure.

[19]Here optical density (OD) refers to the fraction of light transmitted through the neutral density filter ($= 10^{-\mathrm{OD}}$).

4.5 Protocol for growth experiments

I will now describe how the protocols from the previous sections (4.3 and 4.4) are combined to image colonies of bacteria submerged in agarose gel over a period of 20-24 hours. After having mixed exponentially growing bacteria and silica beads into the molten agarose, drawn the mix into a FEP tube and mounted that tube into a sample holder, I mounted the sample holder to the rotating cuff embedded at the end of the 4D stage of the SPIM setup. This meant that the sample was suspended in the sample chamber between the illumination and detection objectives. The sample chamber was filled with distilled water at 37 °C.

The water in the sample chamber was kept at 37 °C for the duration of the experiment using a thermostatic water bath and pump system. A Techne RB-5A refrigerated bath and Techne TE-10A thermoregulator were used to keep a waterbath, filled with tap water, at ≈ 60 °C. A long rubber tube was coiled into a flask filled with distilled water which was submerged in the water bath[20]. The ends of the tube were fixed in the sample chamber using wire and a clamp stand whilst one section of the rubber tubing was fed through a peristaltic pump whose rollers circulated distilled water through the tube. The rubber tubing between the flask and the outlet was insulated using foam and bubble wrap. To keep the temperature of the sample chamber at ≈ 37 °C over a period of 20-24 hours the temperature of the water bath needed to be adjusted according to the temperature in the room, this adjustment was performed before the start of each experiment over a few hours to ensure stability. The temperature was measured using a USB connected thermocouple held near the sample in the sample chamber using a clamp stand. Figure 4.10 shows a plot of the temperature over the duration of an experiment. After an initial warming to 38 °C the temperature fluctuated around 37 °C until the end of the experiment. This temperature profile was typical of all experiments, with the temperature fluctuating within 1 °C of 37 °C.

Under bright field illumination single cells are almost indistinguishable from the silica beads. Therefore the sample was left to incubate at 37 °C for between 4 and 6 hours. After this time the cells had undergone ≈ 4 to 6 divisions forming cluster of ≈ 8 to 32 cells, these clusters could be more easily distinguished from beads under bright field illumination, Figure 4.11. To aid initial colony location

[20]The flask was used to separate water that potentially contained *E. coli* (in the case of a leak in the tubing) from the waterbath. In addition, the tubing and flask were flushed out with 70% ethanol after each experiment to prevent contamination of the waterbath

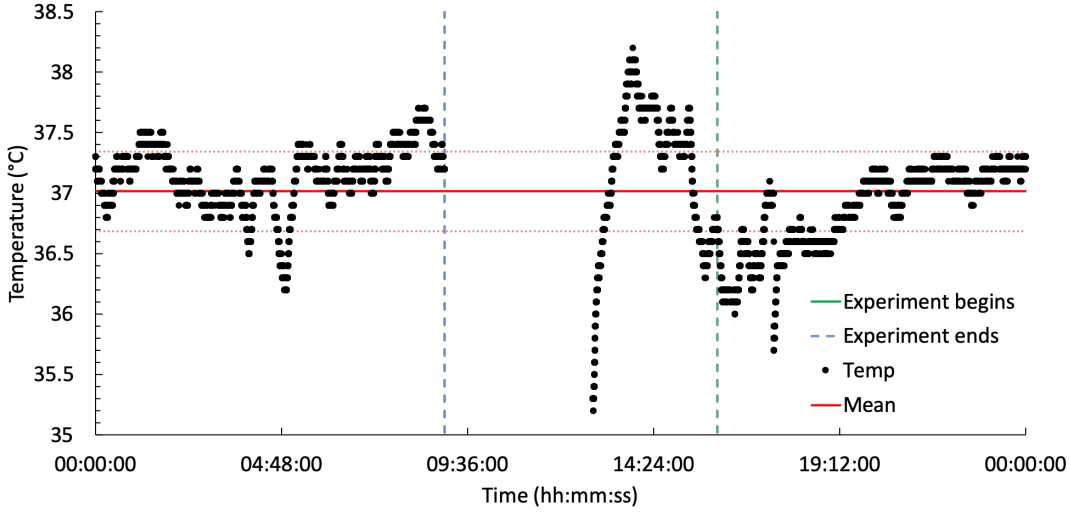

Figure 4.10 *The temperature of the SPIM sample chamber during a growth experiment. The water bath and pump system were switched on at 12:00 and the system was allowed to equilibrate for 4 hours before the experiment was started at 16:00. The red line is the mean temperature over the duration of the experiment, dashed lines are 1σ deviations from the mean. At 09:00 the experiment was stopped.*

the back lighting of the sample was deliberately made non-uniform, this made it easier to differentiate between the colonies and the beads. I attempted to find a colony that was both far from the walls of the FEP tube and isolated from other cell clusters by at least a two fields of view ($\approx 500\,\mu m$). A centrally located colony also reduced the problem of z-stretching, which occurs due to the mismatch in refractive index between the FEP tubing, agarose and water, causing the light sheet to be deflected by slightly different amounts depending on the z position of the tube [112, 113]. z-stretching becomes more apparent towards the walls of the tube due to the increased curvature of the boundary that the light sheet must travel through. This z-stretching aberration can be fixed when the stacks are registered, see Section 4.6.2.

When the FEP tubing was first inserted into the water bath it underwent a small amount of thermal expansion. This thermal expansion resulted in the field of view shifting by $\approx 100\,\mu m$. By leaving the sample to incubate at 37 °C for between 4 and 6 hours before beginning imaging, there was little movement of the FEP tubing after the initial thermal expansion, meaning that the growing colonies stayed in the center of the field of view.

Micro manager was used to control the position of the 4d stage and camera settings. Once a colony had been selected for imaging its position was entered

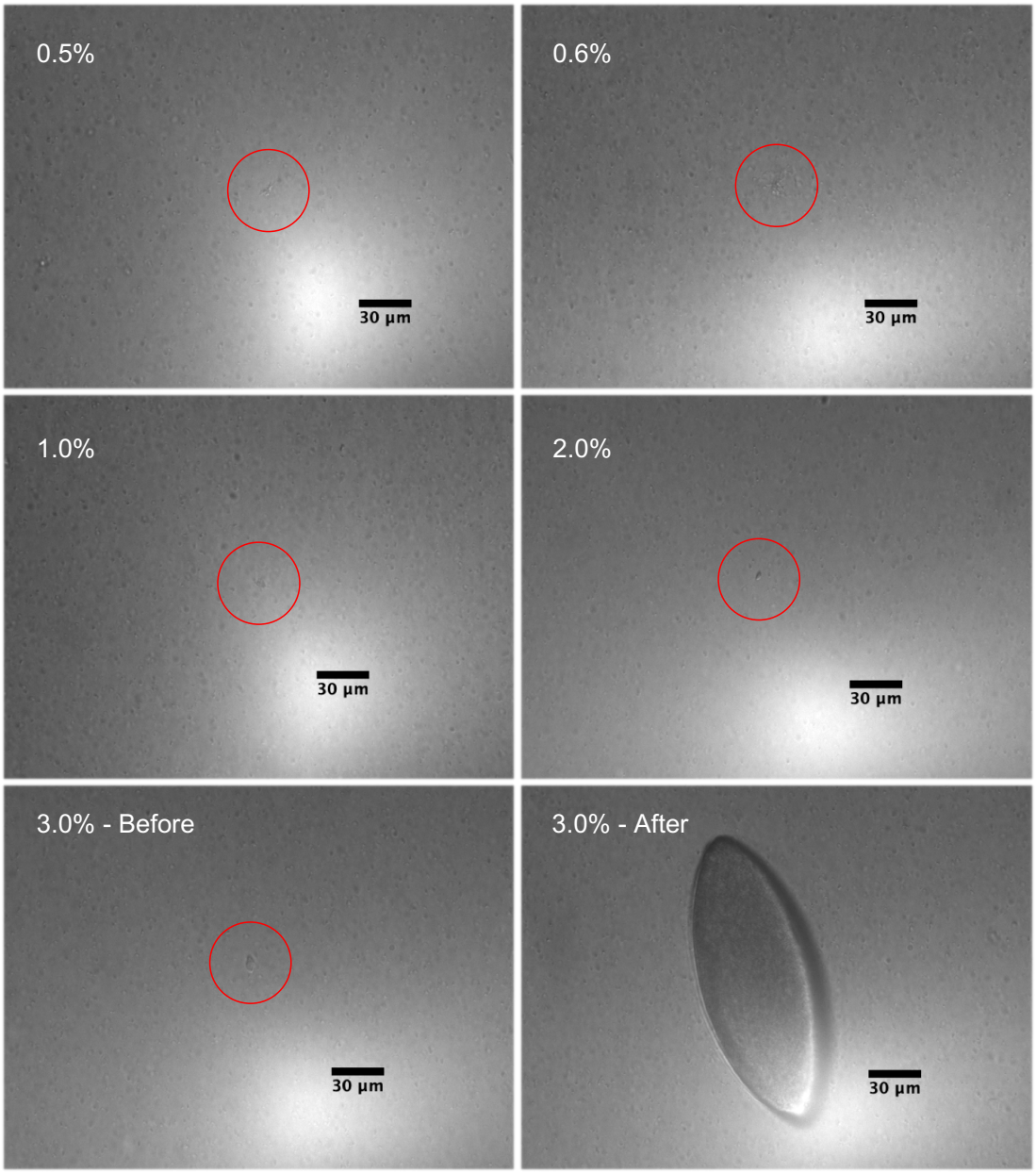

Figure 4.11 *Bright-field images of initial colonies found after 4 hours of growth in various concentrations of diffusely inoculated agarose. The red circle highlights the position of the colony. In the final panel (3.0 % - After) the same colony as in the panel 3.0 % - Before is shown. The back lighting of the images is intentionally irregular to aid locating the colonies.*

into Micro-Managers multidimensional imaging menu. The sample was rotated using the 4D stage and the position of the colony was entered for at least 6 different views. Sometimes, due to the tube not being mounted to the sample holder squarely, the colony could not be moved to the center of the field of view for some rotations. When this was the case views would be taken between the maximum rotations that the sample could be centered. Straightening of the FEP tubes prior to their being filled with agarose usually avoided this problem.

Once the positions of the colony had been set in Micro-Manger they could be automatically returned to for each timepoint. Due to the long exposure times needed to prevent photobleaching (see Section 4.4.4), volume scans took ≈ 100 seconds for each rotation so that a single timepoint (with 7 rotations) would take ≈ 12 minutes. For this reason time points (sets of volume stacks at each rotation) were taken every 15 minutes to allow for any variation in imaging time. Images were then taken for between 20 and 24 hours.

A second, control, FEP tube of the same length as the first tube was filled with the same bacteria, bead and agarose mix for each experiment. The control tube was incubated in a static 37 °C incubator for the same duration as the tube in the SPIM setup. The control tube was used to check whether incubation in the SPIM sample chamber had any effect on the numbers of colonies formed. The number of colonies in the control tube (≈ 40) was usually within 20% of the number in the tube incubated in the SPIM setup. However, colonies growing close to where the FEP tube was mounted to the sample holder were significantly smaller than those where the FEP tube made contact with the water of the sample chamber, probably due to heat dissipation from the sample holder. For this reason colonies further from the sample holder were selected for imaging.

4.6 Computational Methods

I will now describe how the raw image stacks taken with SPIM are cleaned of artifacts and fused into a single aberration free stack for each timepoint. Image fusion and aberration removal were performed using ImageJ, specifically employing the plugin "Multiview reconstruction" written by Stephen Preibisch et al. [114, 115]. Analysis of the processed images was then performed in Python.

To give an idea of the typical data storage requirements for an experiment, a

typical 20 hour long experiment would run for 80 time points and capture 7×201, 663 kB frames per time point. Each experiment therefore took up about 80 GB of storage space for the raw images.

4.6.1 Hot pixel removal

The first artifact to be removed from the images were hot pixels. Hot pixels are pixels that appear much brighter[21] than the surrounding pixels, usually due to current leakage. These pixels will often be completely saturated (have maximum pixel value) and so are easily distinguished from the fiducial markers, they are also not part of the normal intensity distributions that originate from a real photon source. To remove hot pixels the median value of of pixels surrounding a target pixel is calculated, if the difference between the calculated median and the value of the target pixel is greater than some visually determined threshold the the value of the target pixel is replaced by the median value.

Raw images are saved in the OME-TIFF format, whilst removing hot pixels the opportunity is also taken to convert them into the TIFF file format. Raw images are collected into stacks corresponding to the same orientation and timepoint, the hot pixels are removed and the stacks are then saved to a new directory (one for each timepoint) in the TIFF file format.

4.6.2 Image Registration and Multi-view Deconvolution

Image Registration

The cleaned TIFF stacks must then be orientated with respect to one another (registered) before they can be fused and deconvolved. This is done in three steps using the Multiview reconstruction plugin for ImageJ.

First, interest points are located in each stack for each view in a particular time point. These interest points will be used to orientate the stacks. Points are located by taking the difference between two images that are convolutions between the original image and Guassians of slightly different standard deviations[22]. This

[21] 'Brighter' is defined as having higher pixel/voxel intensity.

[22] For the images collected in this work standard deviations of ≈ 1.7 and ≈ 2.0 pixels picked out the majority of beads.

"difference of Gaussian" image has the effect of making regions where the intensity changes rapidly (at the locations of the beads) much more intense than other regions of the image. The beads can then be located by finding local minima in the difference of Gaussian image[23]. Interest points are further filtered by a threshold which excludes local minima that are small in magnitude, the remaining local minima are saved as points of interest. Sub pixel locations of the interest points can then be found by fitting a 3D quadratic function around the neighbourhoods of the local minima. This method results in many interest points that are centered on noise in the image rather than beads, however this was not a problem for registration. As interest points that did not correspond to bead locations were not present in the same positions in other views of the sample, they were be filtered out in the next part of the registration process.

The second part of the registration process uses the locations of the interest points to perform geometric hashing. Geometric hashing involves developing rotationally and translationally invariant local geometric descriptors (i.e. constellations of beads) using the interest points. These local descriptors can then be found in the other views so that a transform between the different views of the sample can be found. A geometric descriptor is made for each interest point by finding its three nearest neighbours and defining a local coordinate system between the interest point and its closest neighbour. The descriptor is stored as a list of positions in the local coordinate system ordered by distance from the original bead located at (0,0,0) (so that the closest bead is located at (1,0,0)). The descriptors are then compared between image stacks, using the sum of square differences to determine the best match[24] Due to the number of beads in the image there are often multiple good matches with similar errors, to solve this problem Random Sample Consensus (RANSAC) [116] is used to reject false matches. RANSAC is performed using a random sample of pairs of matching interest points, the matches that do not agree with the majority on a transformation between the two sets of corresponding interest points are taken to be false matches. In this way interest points that do not correspond to beads are removed.

[23]The local minima in the difference image are found by applying a minimum filter, that is a filter which replaces each pixel value with the minimum of the surrounding pixel values. The positions of the local minima are the points where the difference of Guassian image equals the minimum filtered difference image.

[24]By using a local coordinate system for each bead, kd-trees can be used to quickly find pairs of descriptors between stacks that have similar coordinates, making this seemingly computationally heavy task extremely quick ($\mathcal{O} \sim N \log(N)$ rather than $\mathcal{O} \sim N^2$). A kd-tree is a type of binary space partitioning tree which allows for rapid searches of nearest neighbours.

The matching of the interest points introduced a constraint on the concentration of beads that could be used in the sample. At a concentration of $\approx 1.5 \times 10^6$ beads per µl (a volume fraction of $\approx 0.04\%$) the number of false matches was around 20-30 %, up from $\approx$ 1-4% at a concentration of $\approx 1.0 \times 10^5$ beads per µl. Adding more beads would increase the number of false matches further and increase the likelihood that no transformation between the views could be found. At the concentration used ($\approx 1.5 \times 10^6$ beads per µl), the standard deviations of the difference of Gaussian filter had to be finely tuned to decrease the number of interest points not localised on beads or else the registration process would fail.

Finally, the transformation between the the stacks can be found using the matching interest points between the stacks. The correct transformation is the affine transform that minimizes the sum of the square differences between corresponding interest points. An affine transformation is used rather than a purely transitional and rotational (rigid) transform as it can correct for the slight z-stretching that occurs due to the difference in refractive index between the water, FEP tubing and agarose [112, 113].

Efficient Bayesian Based Multi-view Deconvolution

Once the affine transformations between views for a given time point have been found, the image stacks can be fused and deconvolved. This will result in an image stack where no region is occluded, the point spread function is no longer asymetric and colony surfaces are sharp which aids further image analysis (detailed in Section 4.6.3). This section will discuss the deconvolution algorithm used and the effect of deconvolution parameters.

All images are the result of some convolution between some distribution of point photon sources and the impulse response, or point spread function (PSF), of the imaging system. Deconvolution is the approach used to reverse this convolution, granting improved accuracy when locating sample features. Many deconvolution algorithms have been developed such as Myopic [117], Pixon [118] and alternating maximum a posteriori estimation [119]. Each method applies best under different noise conditions or levels of foreknowledge of the PSF. When the PSF of the imaging system is known and a not insignificant amount of noise is present, the Richardson-Lucy (RL) Bayesian deconvolution algorithm is often most applicable.

Richardson first outlined a Bayesian based approach to deconvolution in 1972

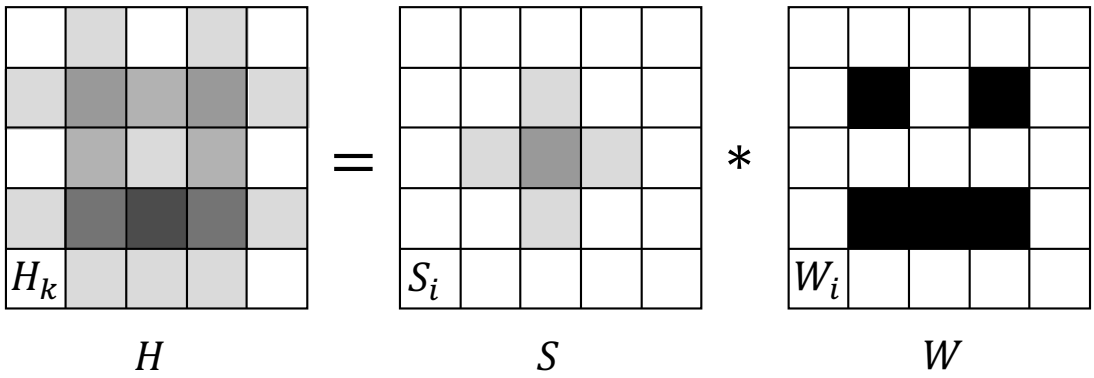

Figure 4.12 *The degraded image H is the convolution of the point spread function S and the original image W. The grey value of the pixels in the grids represent the probabilities of finding a photon in that position. The probabilities in H are given by Equation 4.9 given that $P(H_k|W_i) = P(S_{i,k})$ and $P(W_i) = W_i/W$ etc.*

[120, 121]. Given that a degraded image H is the convolution of the original image W with a PSF S, Figure 4.12,

$$H = S * W, \tag{4.7}$$

then the problem can readily be couched in the language of Bayes's theorem. The conditional probability that a photon should have originated at W_i given that it was detected at H_k (the subscript denotes a position in the image) is given by,

$$P(W_i|H_k) = \frac{P(H_k|W_i)P(W_i)}{P(H_k)}. \tag{4.8}$$

The denominator in Equation 4.8 is equal to the probability of detecting a photon at position k in H,

$$P(H_k) = \sum_j P(H_k|W_j)P(W_j), \tag{4.9}$$

i.e. the probability of detecting a photon at H_k is given by the sum of the probabilities of a detection at H_k given that the photon originated at W_j, multiplied by the probability of a photon originating at W_j . The inverse of Equation 4.9 can also be made, with the probability of a photon originating at W_i given by,

$$P(W_i) = \sum_k P(W_i|H_k)P(H_k). \tag{4.10}$$

Substituting Equation 4.8 into 4.10 and noting that the desired solution $P(W_i)$ appears on either side of the equality, an iterative procedure can be set up

(constraining the summation to unity), where the probability of a photon having originated at W_i in the r^{th} iteration, $P_r(W_i)$, is given by

$$P_r(W_i) = P_{r-1}(W_i) \sum_k \frac{P(H_k|W_i)P(H_k)}{\sum_j P(H_k|W_j)P_{r-1}(W_j)}. \tag{4.11}$$

The initial condition $P_0(W_i)$ can be estimated using the fusion of the image stacks, that is the addition of each transformed image's pixel values weighted by the distance of a pixel from the fused image's pixel coordinates.

The conditional probability term in Equation 4.11 ($P(H_k|W_i)$) is the point spread function $P(S_{i,k})$, i.e.

$$P(H_k|W_i) = P(S_{i,k}). \tag{4.12}$$

Equation 4.11 can then be shifted into a more actionable form by equating the probabilities to relative photon counts at each pixel, e.g.

$$P(W_i) = \frac{W_i}{\sum_i W_i}. \tag{4.13}$$

Then, given that the number of photons is conserved ($\sum W_i = \sum H_i$), the iteration can be rewritten as

$$W_{r,i} = W_{r-1,i} \sum_k \frac{S_{i,k}H_k}{\sum_j S_{j,k}W_{r-1,j}}. \tag{4.14}$$

It has been shown that each step in this iterative process strictly increases the likelihood of the processed image corresponding to the original image [122].

In 2014 Preibisch et al. expanded the RL deconvolution method to better utilise the multiple views of the sample afforded by SPIM [123]. The impetus for this expansion was the large dataset sizes that light sheet microscopy produced. Even though the RL deconvolution method was the preferred choice for large data sets, due to its simplicity and speed, convergence times remain prohibitive for large images.

With multiple views the iterative process in Equation 4.14 becomes:

$$W_{r,i} = W_{r-1,i} \prod_v^N \sum_k \frac{S_{i,k,v}H_{k,v}}{\sum_j S_{j,k,v}W_{r-1,j}}. \tag{4.15}$$

where N is the number of views. This multiplicative combination of the RL updates for each view is equivalent to an ordered subset expectation maximization (OS-EM) algorithm and can improve convergence times by a factor of $N/2$. An OS-EM simply involves evaluating only a subsection of $v \in N$ for each iteration. Using different subsections sequentially has been proven to produce similar results to the full evaluation [124].

Further improvement in convergence time can be made by using the inverse point spread function, $P(W_i|H_{k,v})$, to recreate one view from another. The difference between the two views can be used as a computationally light update to the expected image, improving convergence time by a factor of two.

An important feature of the multi-view deconvolution algorithm is regularization. Regularization adds a smoothness constraint to the deconvolution algorithm to prevent amplification of noise in the image. Tikhonov regularization[25] is used in Preibisch's algorithm. Figure 4.13 displays the effect of adjusting the number of deconvolution iterations and the Tikhonov regularization parameter on image quality. A very small region (177×151×72 px) of a larger, fused, image ($\approx$ 658×824×496 px) was selected for deconvolution to decrease computation time for this analysis. The left most column of Figure 4.13 shows the effect of fusing seven views of the colony. The images become sharper as more deconvolution iterations are applied. With increasing Tihonov parameter, the images sharpen more slowly but with reduced levels of noise. In practice 12 iterations and and Tihonov parameter equal to 6×10^{-4} were used. This combination of parameters were employed due to limitations on computer memory and time. 12 deconvolution iterations would require $\approx$ 100 GB of RAM and take $\approx$ half an hour, the small improvement in image quality beyond this iteration was not deemed worthwhile.

To limit the memory and computation time requirements of the deconvolution process only a select region was deconvolved from the fused image. The boundary of the region to be deconvolved was set to be 10% larger in each Cartesian dimension than the cuboid that contained every matching interest point. An ImageJ macro was written to automate the registration, fusion and deconvolution process using the Multiview Reconstruction plugin.

The result of this deconvolution process were images that had no occluded regions and where the surface of the colony and bead positions could be more accurately thresholded (see Section 4.6.3). Figure 4.14 shows a colony that had been

[25] Also known as ridge regression.

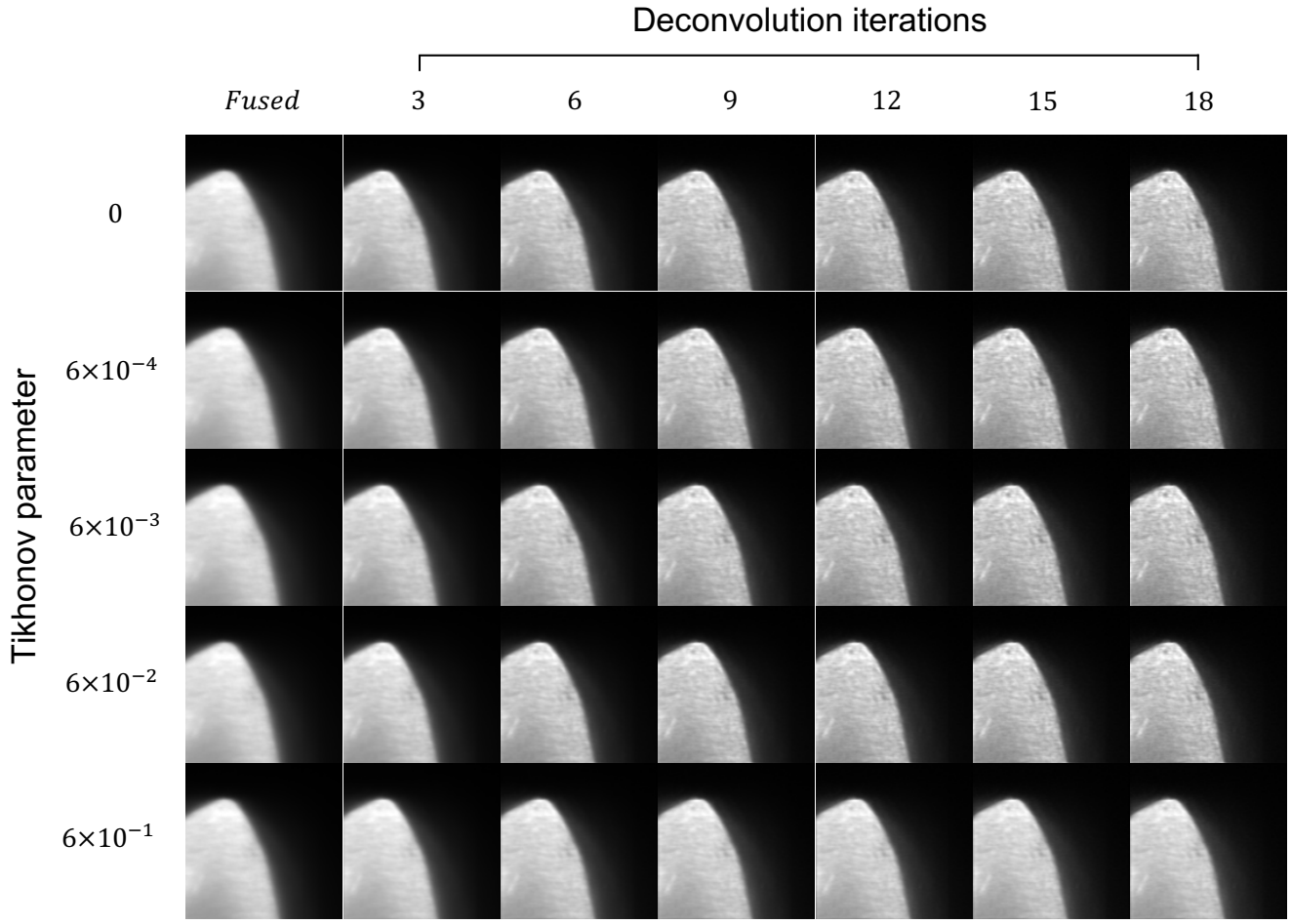

Figure 4.13 *The effect of the number of deconvolution iterations and Tikhonov regularization parameter on image quality. Increasing the number of iterations increase image sharpness. A smaller Tikhonov parameter will result in the images converging quicker at the cost of increased noise. 12 iterations and a Tikhonov parameter equal to* 6×10^{-4} *were used in practice due to computer memory limitations.*

incubated for ≈ 24 hours from three orthogonal perspectives at different stages of image prepossessing. In the first row, the colony as imaged from a single rotation is displayed. There are several artefacts in the single view image. On the side of the colony that was furthest from the detection objective emission light is scattered when travelling from the fluorophore to the detection objective, the result is a blurring of the image, in the fused image this blurring manifests as a corona of bright voxels around the colony. Another artefact is lensing, caused by the shape of the colony. The result of this lensing is a double image of the colony being detected on the side of the colony furthest from the detection objective. This effect is most evident for large (≈100 µm radius) colonies when the apex of the colony is angled towards the detection objective. The last major artefact present in the unfused images is streaking. Streaking is caused by objects (usually aggregates of beads or debris on the FEP tube surface) obstructing the light sheet, causing shadows. As streaks, lensing effect and coronas are present in locations that depend on the rotation of the colony with respect to the illumination direction, fusing images taken at different rotations averages out these artefacts.

Given that simply fusing the images removes the aforementioned artifacts (Figure 4.14 second row) and that the resolution of the deconvolved images (Figure 4.14 third row) is insufficient to resolve individual bacteria amongst the colony, it may seem that deconvolution is unnecessary. However, the largest advantage of deconvolution came when tracking the beads. Figure 4.15 shows the effect of the deconvolution process on the photon distribution originating from the beads. Figure 4.15a shows the photon distribution (averaged over all beads) as a function of the distance from the peak intensity position for each Cartesian direction for a single view of the sample. The widths of the distributions are characterised by Gaussian fits to the intensity distributions. The inset images show the 2D intensity distribution for a given slice in the xy and yz-planes, see Figure 4.6 for coordinate reference. Notably, the intensity distribution along the z-axis (across the light sheet) is wider by about a factor of 2.6 due to the thickness of the light sheet. Deconvolution also sharpens the boundary between the colony and the gel which is important when segmenting the images (see Section 4.6.3).

The standard deviation of the fitted Gaussians in the xy and xz-planes can give an estimate of the resolution of the SPIM setup. The resolution according to the Reyleigh criterion is the distance at which the peak of one intensity distribution coincides with the first minimum of another, this is approximately equal to the

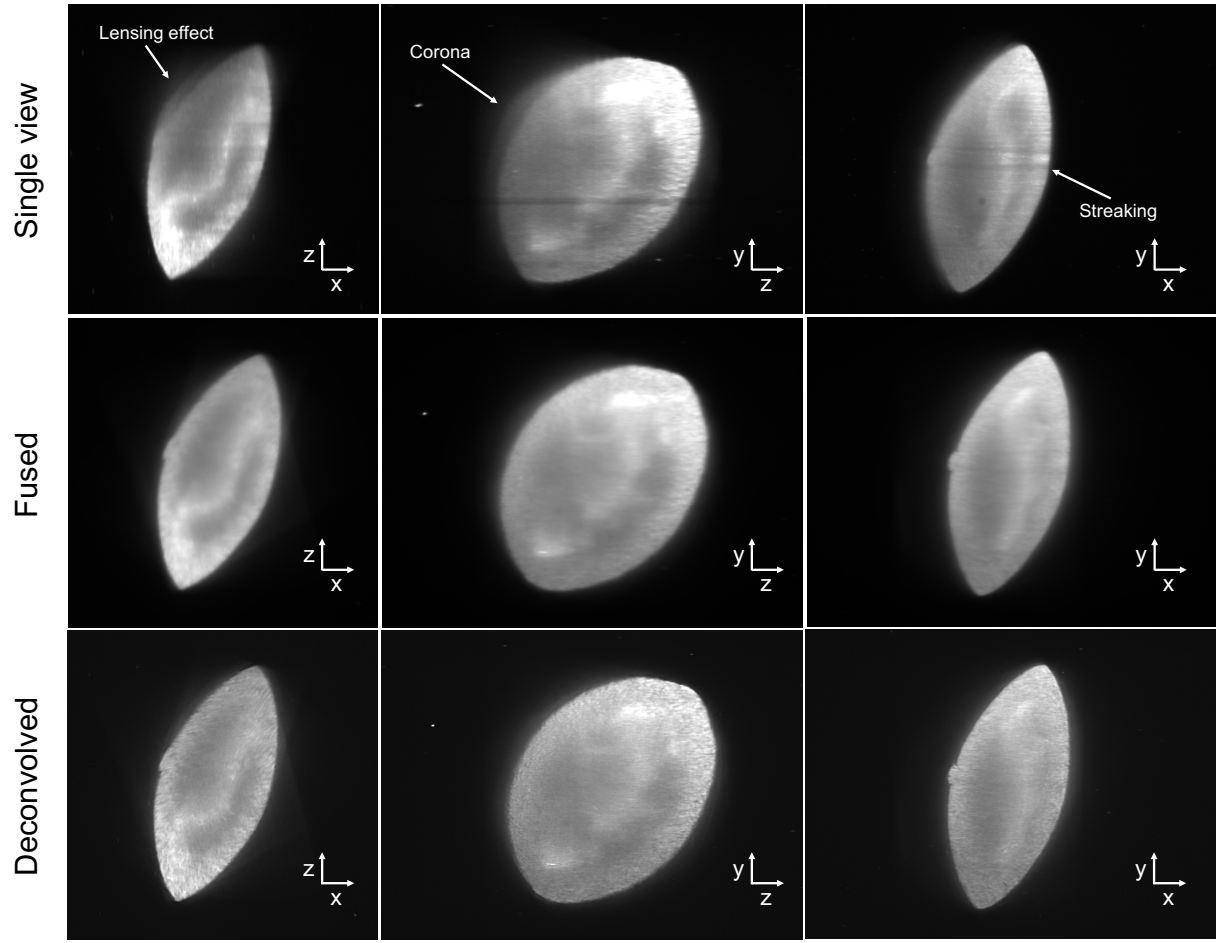

Figure 4.14 *A colony grown in 2% agarose for ≈ 24 hours, from three perspectives, taken from a single view, after the fusion of 7 different views and after deconvolution. The effect of fusion and deconvolution on image artefacts and image detail are apparent. Image artifacts such as distortions to the colony surface caused by lensing, streaking and the corona of scattered light near to the surface are reduced/removed.*

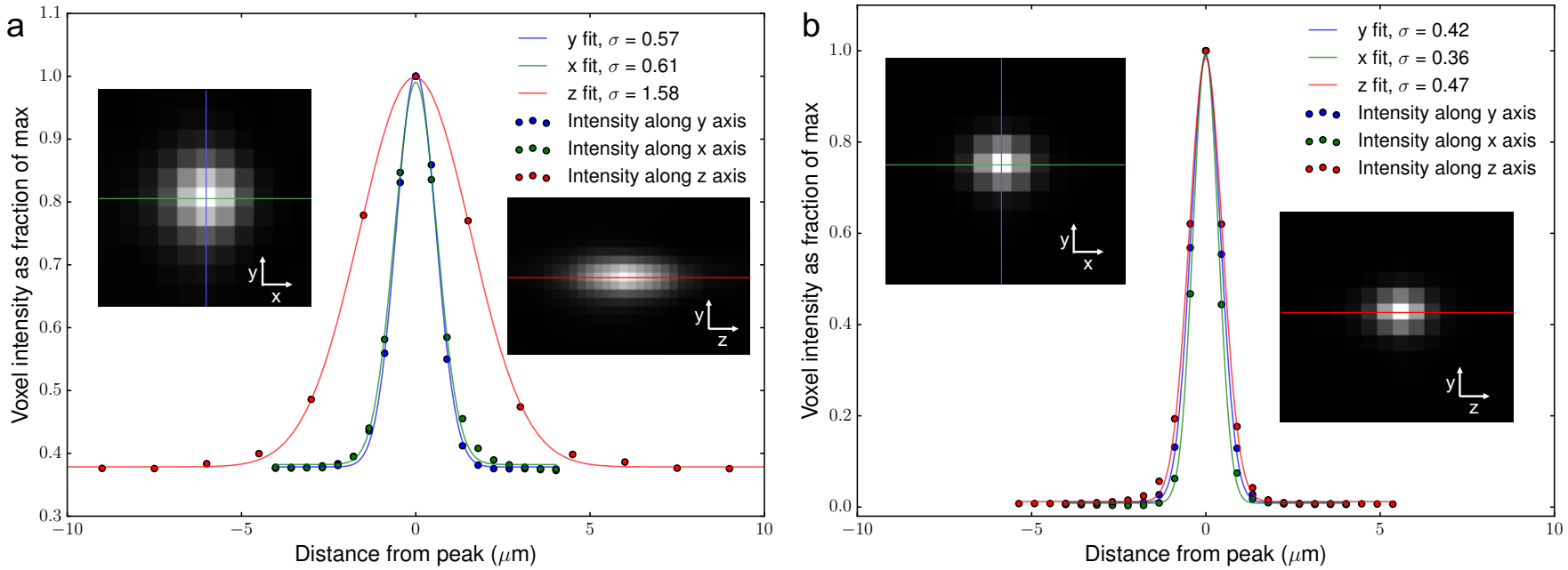

Figure 4.15 *The effect of fusion and deconvolution. (a) The mean voxel intensity distribution of beads in the field of view along x, y and z-axis with origin at the bead centres. Insets: The PSF of raw images prior to deconvolution, the central slice of a 3D image is shown. The PSF is wider along the z-axis due to the thickness of the light sheet. (b) After fusion of the various views and deconvolution, the intensity distribution of the beads is narrower and isotropic.*

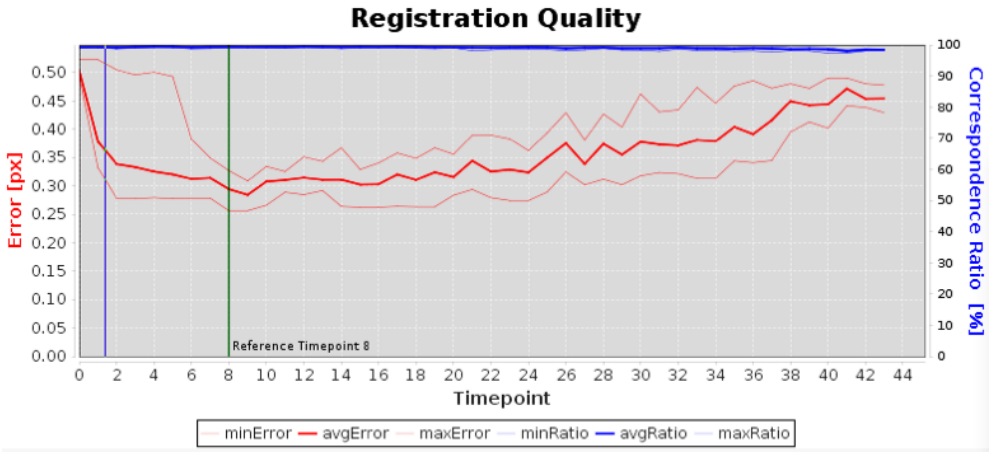

Figure 4.16 *An example of the registration quality for one experiment. For each time point the percentage of interest point correspondences between time points (in a 5 time point range) are plotted in blue. In red, the average distance between an interest point and the transformed position of that interest point at another time point (called the error) is plotted. Correspondence percentages were typically $\gtrsim$ 99%, whilst the position error was typically between 0.3-0.7 pixels.*

FWHM ($2\sqrt{2\ln 2}\sigma$). The resolution of the SPIM setup prior to deconvolution is therefore $\approx 1.4\,\mu m$ parallel to the light sheet and $3.7\,\mu m$ perpendicular to it. The perpendicular resolution is roughly equal to the light sheet FWHM shown in Figure 4.6. After deconvolution (Figure 4.15b) the resolution is approximately equal to 1.0 ± 0.1 µm in all Cartesian directions due to multi-view deconvolution.

Inter time point registration

After the image stacks from each time point had been fused and deconvolved, the same registration method as described in Section 4.6.2 was used to determine the transform between time points. Figure 4.16 plots (in red) the average distance between beads and the transformed position of that bead at another time point (called the error), in addition the percentage of beads that have correspondences at another time point are plotted in blue. Position errors were generally around 0.3-0.7 pixels for all timelapse experiments. The correspondence ratio was usually $\gtrsim$ 99%, which is unsurprising as deconvolution increases the likelihood of a real bead being selected as an interest point over noise. The fact that beads could easily be differentiated from noise confirms that using a larger Tikhonov parameter to prevent noise amplification during deconvolution was unnecessary.

4.6.3 Analysis of SPIM images

Once the SPIM images had been deconvolved and registered across each time series the images were ready to be analysed. As will be discussed in Chapter 5, the following characteristics of the colonies were of interest: their volume; their centre of mass; their orientation; some measure of their diameter and width; their radius of curvature; and finally the displacement of the gel around the colonies. This section will discuss the various image processing methods used to measure these properties.

Segmentation of the colony

Central to all methods in this section is the separation of the images into regions that correspond to the colony and regions that correspond to gel or beads, i.e. segmentation. One of the largest advantages of fluorescence microscopy is that the object of interest is fluorescent whilst the background is not, therefore segmentation can be performed by a simple threshold. The threshold value, t, can be found using Otsu's method [125]. After binning voxel intensities, I, into a histogram (ranging between 0 and $I_{\max}$), Otsu's method splits the histogram into two classes at a t that minimises the intra-class variance, $\sigma^2(t)$, given by

$$\sigma^2(t) = \sigma_0^2(t) \sum_{I=0}^{t-1} f(I) + \sigma_1^2(t) \sum_{I=t}^{I_{\max}} f(I), \tag{4.16}$$

where $\sigma_i^2(t)$ is the variance of the i^{th} class and $f(I)$ is the number of voxels with intensity I. Setting those voxels with $I > t$ to some Boolean true value and the others to false, a binary image is created with voxels corresponding to the colony having value true, Figure 4.17. Otsu's method was chosen over any other threshold method because the value of t that it output was most similar to the value of t chosen by manual thresholding.

Some colonies appear dimmer towards the centre of the colony, either due to the attenuation of the light sheet through the colony or cell stress. These dimmer regions can have voxel values below t. Therefore, after the images have been thresholded, holes in the region that should correspond to a colony can appear. These holes need to be filled. Holes in a binary image[26] can be filled by first flood

[26]When the object of interest does not intersect the edge of the image.

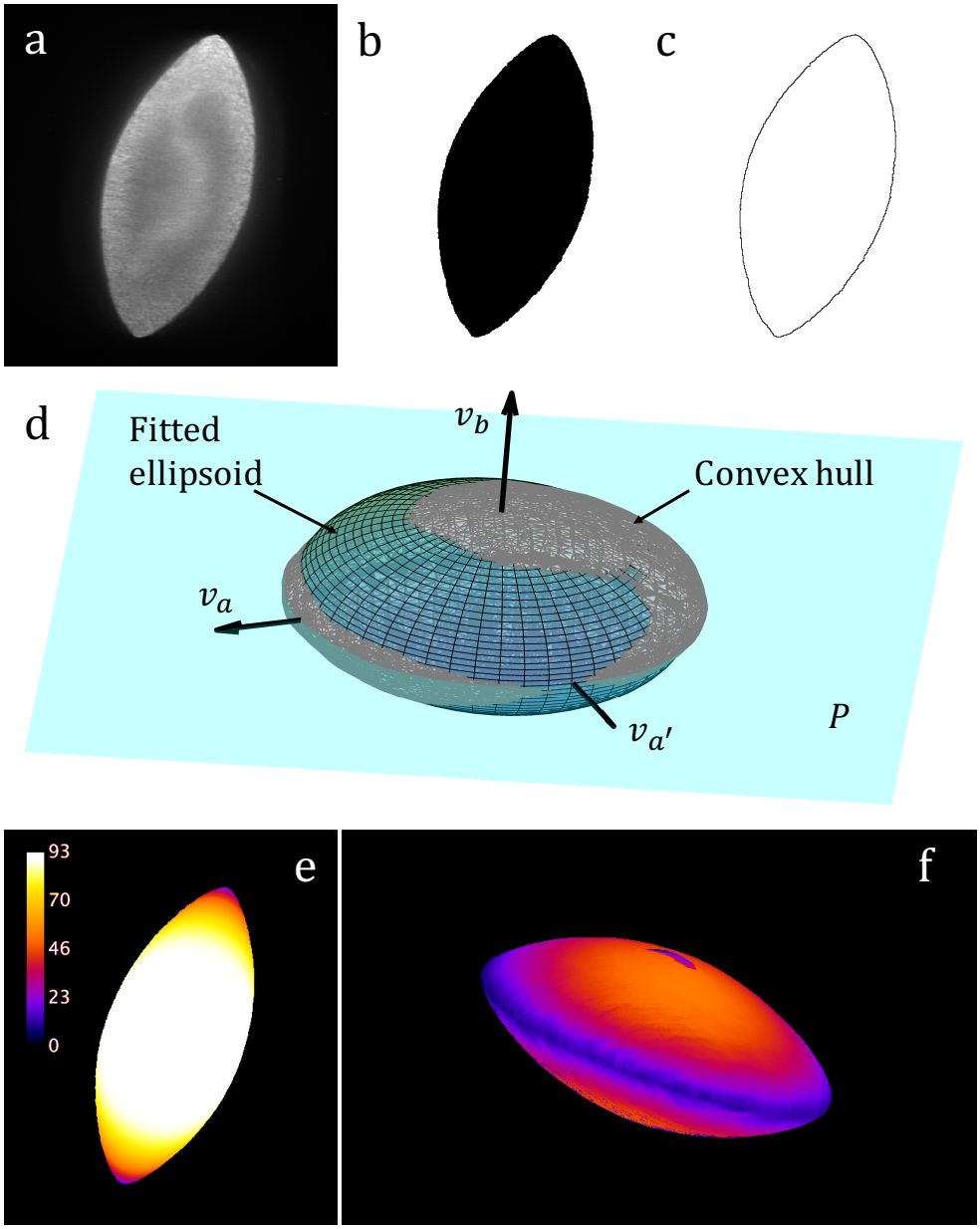

Figure 4.17 *A colony at various stages of image processing. (a) A slice of a deconvolved image stack. (b) Segmentation is carried out using an Otsu threshold. (c) Surface voxels are identified. (d) The inertia tensor of the voxels inside the colony is used to calculate the principle axes* $\mathbf{v}_b, \mathbf{v}_a$ *and* $\mathbf{v}_{a'}$*. Using the corresponding eigenvalues* a *and* b *can be calculated, defining an ellipsoid. The convex hull of voxels inside the colony is shown in grey, with fitted ellipsoid overlain. The plane,* P*, defined by* $\mathbf{v}_b$ *and* C *is shown in cyan. (e) The local thickness of the colony, voxel values corresponds to the local thickness in pixel widths. The local thickness is lowest at the apex of the colonies. (f) A nearest point projection of the local thickness image stack. The local thickness was measured at the intercept between* P *and the colony surface.*

filling the image from an edge with true values, inverting the image and then applying a logical OR to the original and filled/inverted image.

The colony is distinguished from the beads in the binary image by its size. The python module scikit-image was used to label distinct objects in the image and to determine their size [126]. The largest object in the image was taken to be the colony, the value of the voxels corresponding to all other objects was set to false/0. An example of a segmented image is shown in Figure 4.17b. Using this final binary image, the volume of the colony could be calculated by multiplying the number of true voxels in the image by the voxel volume (8.93×10^{-2} µm^3).

Measuring colony morphology

Having segmented the image, the morphology of the colony could be characterised. The first characteristics measured were the colonies orientation and the length of their principle axes. The semi-major and semi-minor axis of the colony (a and b respectively) were measured in various ways. Methods included, setting a to the Feret diameter[27] of the colonies, and b to the length of the longest line perpendicular to the Feret vector, contained within the colony; setting a to the largest distance from the colony centre of mass to the surface. By finding the next several largest distances a perpendicular axis could be found, b was set to the distance along that perpendicular axis between the centre of mass and colony surface; finding the plane with maximum area inside the colony, setting $2a$ equal to the vector with maximum length in that plane within the colony, and setting b equal to the maximum distance from the plane to the colony surface in the direction orthogonal to the plane. However each of these methods was extremely sensitive to noise in the image, for example if the colony had a small sub-colony on its surface values for a and b would change drastically. To solve this problem a and b were determined from the colonies tensor of inertia by approximating the colony as an ellipse, Figure 4.17.

To determine a and b from the tensor of inertia, the centre of mass of the colony, $\mathbf{C}$, had to be determined. $\mathbf{C}$, assuming all colony voxels have equal weight, is found by taking the average of the voxel positions in the Cartesian coordinates.

[27]The Feret diameter, also known as the maximum caliper diameter, is the longest distance between any two points in the segmented region.

The elements of the inertia tensor of the colony, T_{ij}, are then given by:

$$T_{ij} = \sum_{k=1}^{N} \left(||\mathbf{r}_k||^2 \delta_{ij} - x_i x_j \right), \tag{4.17}$$

where the summation is over the N voxels inside the colony and $\mathbf{r}_k (= (x_1, x_2, x_3)_k)$ is the vector between $\mathbf{C}$ and the k^{th} voxel. To determine the orientation of the colony, the eigenvalues (λ_b, λ_a, $\lambda_{a'}$) and eigenvectors ($\mathbf{v}_b$, $\mathbf{v}_a$, $\mathbf{v}_{a'}$) of $\mathbf{T}$ are calculated, where the subscript denotes the orientation of the eigenvector or corresponding eigenvector. For example, the eigenvector $\mathbf{v}_b$, with corresponding eigenvalue λ_b, points in the direction of the minor axis, b, of the colony, the remaining eigenvectors lie in the plane of the major axis. The eigenvector with the maximum corresponding eigenvalue is $\mathbf{v}_b$. The length of a and b can then be determined from these eigenvalues. Assuming that the colonies are ellipsoidal, the semi-major and semi-minor axes are given by

$$a = \sqrt{\frac{5\lambda_b}{2N}} \tag{4.18}$$

and

$$b = \sqrt{\frac{5(\lambda_a + \lambda_{a'} - \lambda_b)}{2N}}. \tag{4.19}$$

Figure 4.17d shows a Delaunay triangulation of a colony surface with the principle axes $\mathbf{v}_b$, $\mathbf{v}_a$, $\mathbf{v}_{a'}$ and fitted ellipsoid superimposed.

To more precisely measure the shape of the colony, the width in the $\mathbf{v}_b$ direction was measured as a function of the distance from the colony edge. To measure these widths, voxels within one pixel width of the plane, P, defined by the vector $\mathbf{v}_b$ and $\mathbf{C}$ were found, i.e. where $\mathbf{v}_b \cdot \mathbf{r} < 1$ px. For these voxels the distances in the $\pm\mathbf{v}_b$ direction to the colony surface and in the direction from $\mathbf{C}$ to the voxel to the colony surface were determined.

Another characteristic length of the colonies was the radius of curvature at their apex. The radius of curvature could be found by first calculating the local thickness map of the segmented image. The local thickness at a given voxel, inside the colony, is equal to the radius of the largest sphere that both contains that voxel and lies wholly within the colony. The radius of curvature at the crack tip is then found at the intersection of P and the colony surface in the local thickness map.

Programmatically the local thickness array is found by first taking the distance

transform of the segmented image. A distance transform labels each voxel in the image with its distance from the boundary between colony voxels and outside voxels creating the image D. The values of voxels outside the colony are set to 0. For each unique distance value, r_i, in D, a binary image, B_{r_i}, where $r_i \geq D$ is created. Each B_{r_i} is then inverted and the distance transform of the inverted image, $D_{B'_{r_i}}$, is found. $D_{B'_{r_i}}$ is equal to the local thickness where $D_{B'_{r_i}} \leq r_i$, where this is true the voxel values of a local thickness image, L, are updated. By applying this algorithm sequentially from smallest to largest r_i, and overwriting previous maps, L is created. Programmatically this is carried out using the following code snippet taken from the PoreSpy library [127], where sp refers to the scipy module [128] and spim refers to the ndimage package of scipy:

```
dt = spim.distance_transform_edt(Colony_Image)
sizes = sp.unique(sp.around(dt, decimals=0))
Colony_Thickness = sp.zeros_like(Colony_Image, dtype=float)
for r in sizes:
        im_temp = dt >= r
        im_temp = spim.distance_transform_edt(~im_temp) <= r
Colony_Thickness[im_temp] = r
```

A binary erosion was implemented to remove any features smaller than a $2 \times 2 \times 2$ voxel cube from the final local thickness array. The final local thickness array is shown in Figure 4.17e and f.

4.6.4 Particle image velocimetry

In addition to the morphology of the colony, the displacement of the gel surrounding the colony was measured. This displacement was visualised using fiducial markers added to the gel (see Section 4.3.2). After performing deconvolution and registration across the time points, as described in sections 4.6.2 and 4.6.2, the fiducial markers could be tracked using the ImageJ plugin Mosaic [129]. Mosaic tracks the markers in two steps: First the locations of the markers are determined in each frame, then the detected marker positions are linked into trajectories.

Markers are localized by first normalizing the intensity, I, of voxels in the images by the range of intensities, $I_{\max} - I_{\min}$, in the time series, i.e. the normalized intensity, I_n, is given by

$$I_n = \frac{I - I_{\min}}{I_{\max} - I_{\min}}. \tag{4.20}$$

The images can then be de-noised by convolving the image with a Gaussian filter

with standard deviation equal to the estimated radius of the markers, R. Markers are then taken to be located at voxels brighter than all other voxels within R of themselves (local maxima) and in the top p^{th} percentile of voxel intensities. Voxels that are brighter than surrounding voxels can be found by taking a maximum filter with radius R, brighter voxels are located where the maximum filtered image is equal to the original image. An R of 3.0 pixels was chosen as that contains the PSF of the deconvolved beads shown in Figure 4.7. The top 2% of local maxima were designated as marker locations. By choosing this p, many of the designated marker locations were contained within the colony, however these will be removed during linking or in post-processing. Sub-voxel locations of the markers are then calculated by determining the intensity weighted centroid of voxels within R of the marker voxel. When calculating the centroid, the zeroth and second moments of the intensity distribution, m_0 and m_2, are calculated for each marker location. These moments will be used for linking particles later. These moments can also be used for non-particle discrimination, however in the deconvolved images the fraction of markers not localised on beads or inside the colony was so low that this feature of Mosaic was not implemented.

Now the marker positions have to be linked together to create trajectories. Consider images at two time points H_t and H_{t+a}, where H_{t+a} is a time points ahead of H_t. The images have N_t and N_{t+a} markers in each of them at positions $\mathbf{p}_i$ and $\mathbf{p}_j$ respectively. A sparse association matrix $\mathbf{g}$ between the markers in H_t and H_{t+a} can be be defined as

$$g_{ij} = \begin{cases} 1 & \text{if } \mathbf{p}_i \text{ in } H_t \text{ corresponds to } \mathbf{p}_j \text{ in } H_{t+a}, \\ 0 & \text{otherwise.} \end{cases} \tag{4.21}$$

The set of corresponding markers between the time points can then be found by minimizing the cost function:

$$\Phi = \sum_{i}^{N_t} \sum_{j}^{N_{t+a}} \phi_{ij} g_{ij}, \tag{4.22}$$

where ϕ_{ij} is the cost associated with matching $\mathbf{p}_i$ to $\mathbf{p}_j$. ϕ_{ij} is given by the sum of the square differences between the markers distance and, importantly, the moments of their intensity distribution:

$$\phi_{ij} = (x_i - x_j)^2 + (y_i - y_j)^2 + (z_i - z_j)^2 + (m_{0,i} - m_{0,j})^2 + (m_{2,i} - m_{2,j})^2 . \tag{4.23}$$

By adding the moments of the marker's intensity distributions to the cost, markers whose appearance is similar between time points are more likely to correspond. To improve the computation time of this minimization, a maximum allowable displacement between $\mathbf{p}_i$ and $\mathbf{p}_j$ is defined as L. When $\phi_{ij} > (La)^2$ the corresponding element in g_{ij} is considered impossible and so can be ignored during the minimization of Φ. For time series of bacterial colonies L was set to 10 pixels and a was set to 2.

Once the trajectories of markers had been determined, spurious trajectories could be removed in post processing. First, only trajectories that both started at the first time point and ended at the time point of interest were considered. Second, any trajectories that ended within the colony were removed. This left a set of trajectories that, at least by visual inspection, tracked the majority of the beads with few spurious trajectories.

4.6.5 Interpolation of displacement fields

To compare measured displacements to theoretical displacements, measurements must be interpolated into continuous displacement fields. By interpolating the measurements, the strain and stress in the agarose could also be calculated. Interpolation was performed using a hierarchical set of radial basis functions.

Radial Basis Function Interpolation

Radial basis function (RBF) interpolation can be an efficient method of interpolating scattered data. The core concept of radial basis function interpolation is that value at any point in space can be found by summing contributions from the measured data points. The contributions of the measured data points are weighted by both the measured value at the data point and the distance from the data point to the interpolation point according to some radial symmetric function.

A Gaussian is one example of a RBF, with the value of the function at a point $f(x, y, z)$ determined from N measured data points using the formula,

$$f(x, y, z) = \sum_{i=1}^{N} w_i \exp\left(-\frac{|\mathbf{r}_i|^2}{R_0^2}\right), \tag{4.24}$$

where

$$|\mathbf{r}_i|^2 = (x_i - x)^2 + (y_i - y)^2 + (z_i - z)^2 \tag{4.25}$$

and R_0 is the width of the Gaussian. The measured value of the function is bundled into the weight coefficient , w_i. To determine the weight coefficients a least square regression is carried out,

$$\min \left[\sum_{j=1}^{N} \left(f(x_j, y_j, z_j) - \sum_{i=1}^{N} w_i \exp \left[-\frac{|\mathbf{r}_i|^2}{R_0^2} \right] \right)^2 + \lambda_v \sum_{i=1}^{N} w_i^2 \right], \tag{4.26}$$

minimising the sum of square differences between measured and interpolated values at each measurement point (given by Equation 4.24). A regularization term (λ_v) is added to the minimization to prevent over-fitting by reducing sensitivity to individual weights. Once the weight coefficients have been determined, Equation 4.24 can be evaluated at any point in space.

To create an interpolation model that is independent of R_0, a hierarchical set of interpolation models can be calculated. First long range features of the data set can be captured by choosing the initial width, R_0, to be several times the average distance between data points. Subsequent interpolation models can then be fitted to the residuals of the previous interpolation models, halving R_0 for each model after the first. This process reveals progressively finer details of the data set. The final model is the sum of all models and, given that the initial width is larger than the largest feature size in the system, independent of R_0 [130].

However this method can easily over-fit the data, i.e. residuals can be minimised by setting $R_0 \to 0$ and w_i to the measured values. Therefore correctly setting λ_v becomes very important for producing correctly fitted models, however the optimum value of λ_v will depend on the other hyperparameters of the model such as R_0 and the number of layers (N). Furthermore, this over fitting problem is exacerbated by experimental uncertainty in the measured displacements. To overcome this over-fitting problem, the model hyperparameters can be optimized using simulated data.

Optimization of interpolation hyperparameters

To optimise interpolation hyperparameters displacement data was simulated. Displacements at 5000 random positions in a $300 \times 300 \times 150$ µm^3 volume[28] were

[28]This was approximatively the same as the density of observations made in experiments.

calculated according to equations 5.9 and 5.10 by considering that the volume had been deformed by pressurizing the surface of a circle of radius 100 µm centred at (0,0,0) into a half ellipsoid with minor axis 15 µm, Figure 4.18a. These 5000 data points were used to create interpolation models with various hyperparameters. To test how well each interpolation model fit the underlying displacement field the Lagrangian displacement, u_z, along a line running from (0,0,0) to (0,0,150), and four parallel lines beginning at (0,50,0), (50,0,0), (0,-50,0) and (-50,0,0) were calculated. The gradient of the displacement along those lines, ∇u_z, was also calculated. After calculating the weights of the interpolation models according to Equation 4.26, the models were used to calculate displacements using Equation 4.24 along the same lines at which the exact displacement was calculated. The sum of squared differences between the displacements calculated from Equations 5.9 and 5.10 and the displacements interpolated from the models (Δu_z) were calculated. The sum of the squared differences of the gradients of these displacements ($\Delta \nabla u_z$) were also calculated, Figure 4.18b.

A score could then be determined for the goodness of fit of each of the interpolation models using Δu_z and $\Delta \nabla u_z$. Dividing Δu_z and $\Delta \nabla u_z$ by the median value of the set of Δu_zs and $\Delta \nabla u_z$s respectively to give $\widetilde{\Delta u_z}$ and $\widetilde{\Delta(\nabla u_z)}$ (which are of a similar order of magnitude). A score can then be defined as,

$$\text{Score} = \log\left(\widetilde{\Delta u_z}\right) + \log\left(\widetilde{\Delta(\nabla u_z)}\right). \tag{4.27}$$

The worst score calculated for each of the five lines tested is taken to be the score for the interpolation model. Scores are plotted as a function of model hyperparameters in Figure 4.18c.

The best interpolation model was found to have the hyper parameters $R_0 = 200$, 4 layers and $\lambda_v = 8.0$ though, in the absence of noise, many sets of hyperparameters fit the data well. So long as the final Gaussian width ($R_f = R_0/2^{N-1}$) was comparable to the inter measurement distance and λ_v was not set too high the models reproduced the underlying displacement field well.

In experiments the displacements have some uncertainty associated with them. To check whether noise has any effect on the optimum hyperparameters, Gaussian distributed noise with widths, w_G, between 0.25 µm and 10 µm was added to the components of the simulated displacement vectors. The same analysis as above was carried out with sum squared differences between interpolated and calculated values of Δu_z and $\Delta \nabla u_z$ being calculated. Figure 4.19a shows these

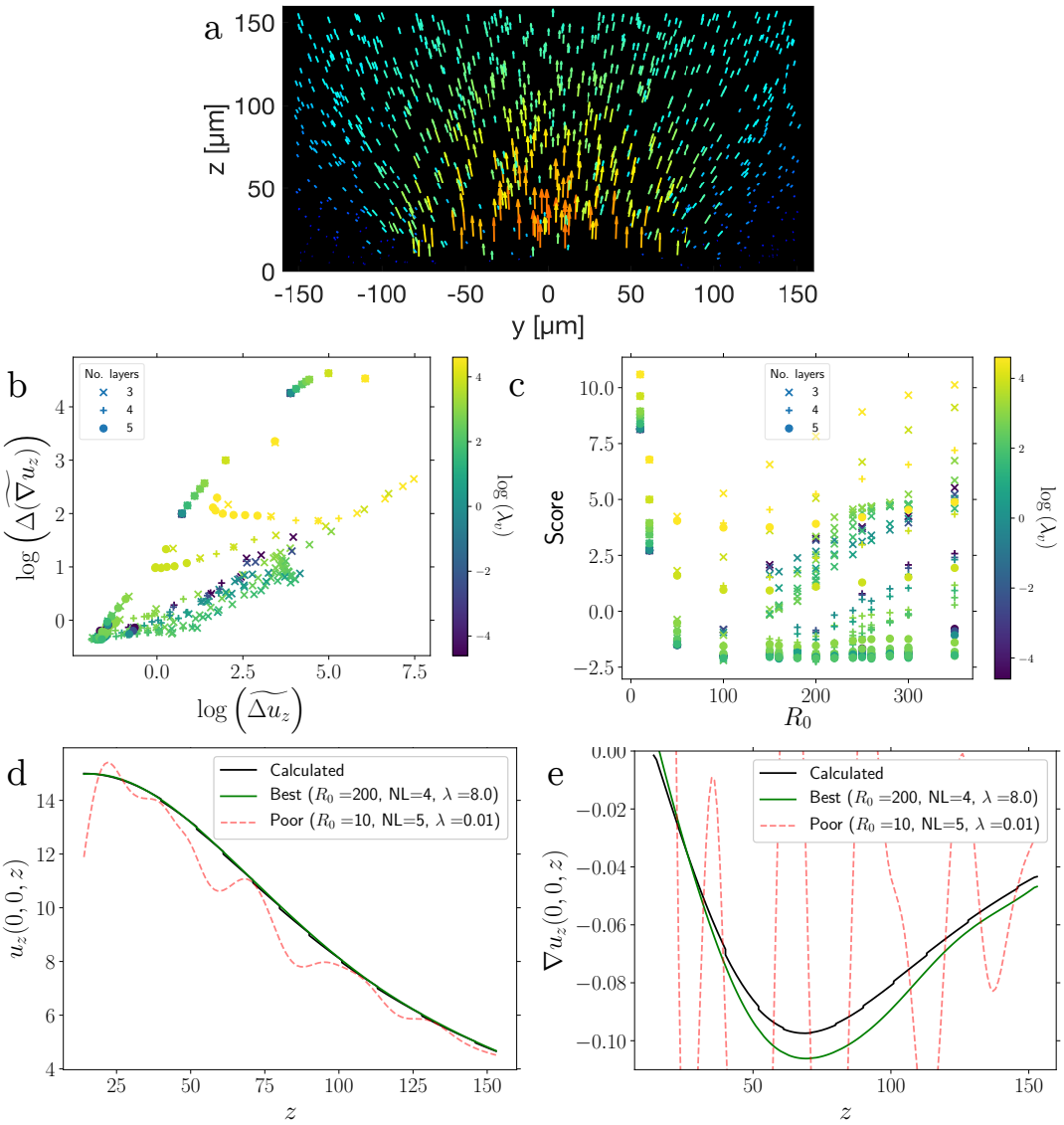

Figure 4.18 *Optimising interpolation parameters without noise. (a) Displacements are calculated at 5000 randomly distributed points in a volume surrounding a pressurised circle centred at $x = 0$, $y = 0$ and $z = 0$ (only 20 % of the data is plotted). (b) The sum squared difference between the interpolated displacement, Δu_z and gradient of that displacement, $\Delta \nabla u_z$, is calculated along five lines for a spread of interpolation hyperparameters. (c) A goodness of fit score, Equation 4.27, is used to compare combinations of hyperparameters. (d,e) The RBF model with the best fitting set of hyperparameters almost exactly reproduces the underlying displacement field from a set of scattered observations. A poor choice of hyperparameters is shown for comparison.*

differences for various sets of interpolation parameters when w_G =0.5 µm whilst Figure 4.19b shows the corresponding scores for the models. It can be seen that models with small R_f fit the data poorly and optimal values of λ_v now lie in a range between ∼1.0-10.0. In general as the level of noise increases, models with larger R_f are needed to smooth the data and return the underlying displacement field. When w_G =0.5 µm, which is roughly the level of uncertainty in the particle image velocimetry results[29], the underlying displacement field is most accurately reproduced by a model with the hyperparameters $R_0 = 260$, 4 layers and $\lambda_v = 8.0$, Figure 4.19. This model has similar hyperparameters to the model that best reproduced the displacement field in the absence of noise, however when noise was present fewer models perform similarly well[30] and the variety of acceptable model parameters decreases.

Surprisingly, even after adding noise with w_G =10.0 µm, so that the displacement field looks random to the naked eye, the underlying displacement field can be reproduced with a maximum error in Δu_z of ≈10%. This shows a weakness in using Gaussian noise to simulated experimental uncertainty, in reality a systematic uncertainty might be present in the data[31], which would have a more significant effect on the resulting interpolated field.

[29]The uncertainty in the particle image velocimetry data is similar to the registration error (c.f. Figure 4.16) as both methods localise the particles in a similar way.

[30]Note that whilst the score for the interpolation models with noise is lower than that without noise this is only the result of a larger spread of Δu_z and $\Delta \nabla u_z$ in the noisy data.

[31]For instance, where beads in subsequent frames are inaccurately linked by the method in Section 4.6.4.

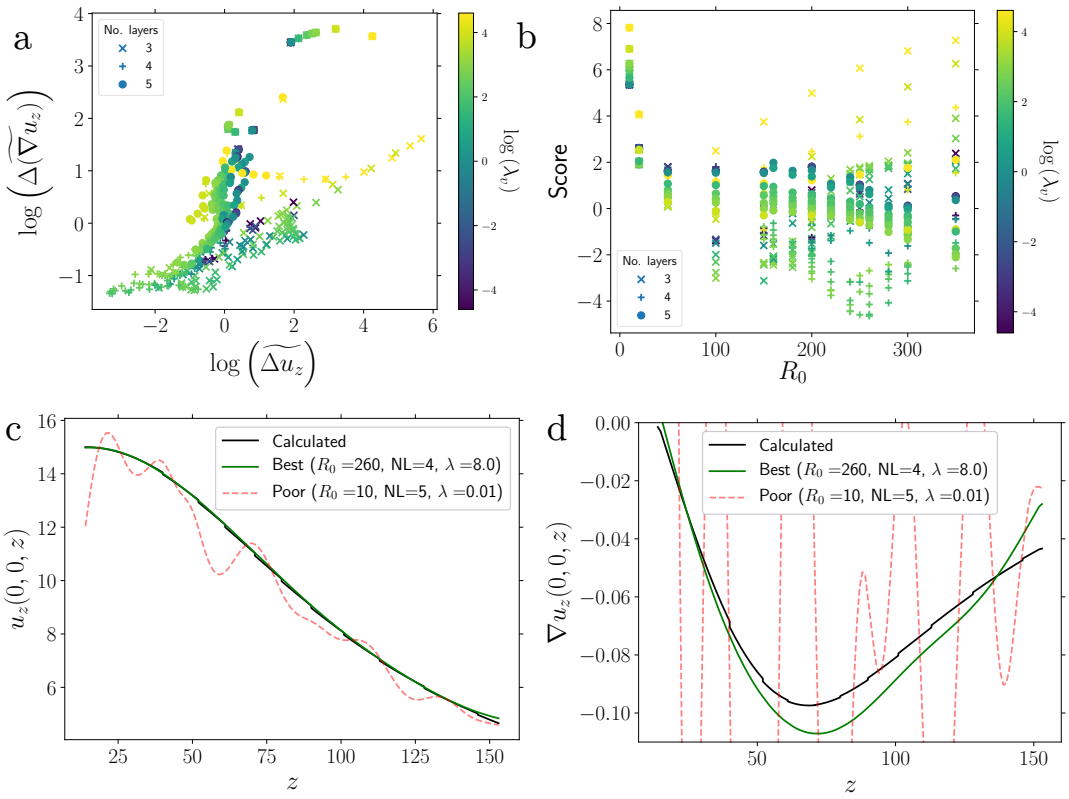

Figure 4.19 *When Gaussian noise with a width of* 0.5 µm *is added to the scattered data, the optimum hyperparameters for the interpolation model change. (a) The sum squared difference between the interpolated displacement,* Δu_z*, and gradient of that displacement,* $\Delta \nabla u_z$*, is calculated along five lines for a spread of interpolation hyperparameters. Compared to Figure 4.18b, models that ignore finer details perform better. (b) A goodness of fit score, Equation 4.27, is used to compare combinations of hyperparameters. (c,d) The RBF model with the best fitting set of hyperparameters almost exactly reproduces the underlying displacement field from a set of scattered observations. A poor choice of hyperparameters is shown for comparison.*

Chapter 5

The Morphology of Submerged Colonies

5.1 Introduction

This chapter presents an experimental study of colonies of bacteria grown submerged in agarose gels. Previously it has been observed that when bacteria are submerged in a gel above some critical concentration they grow into lenticular or ellipsoidal colonies [41], see Section 2.2. The primary aim of this study was to investigate the origin of that lenticular morphology. By growing bacteria in agarose gels of varying stiffness and fracture properties, and by using SPIM to make quantitative measurements of the colony's morphology, I attempt to correlate the colonies morphology with the physical properties of the gel. By correlating colony morphology to gel properties I hope to reveal the underlying physics that guides bacterial colony formation.

Understanding the physics of bacterial colony formation may prove important for various applications. For instance, in food science the conditions under which bacteria can grow in a gel could be used to help model food contamination [38–40]. For this application the gel would represent a model system of food stuffs or comminuted products[1]. Another application could be as a model system of tumour growth and metastasis. As discussed in Section 2.3, some types of tumour have been observed to form lenticular shapes similar to bacterial colonies [43–45].

[1]For example growth of bacteria in the interstices of fermented sausages [131]

Given that human tissue is a hydrogel (albeit more complex than agarose) it is possible that the formation of these tumours and submerged bacterial colonies share some common physics.

As will be discussed later in the chapter, bacteria grow by fracturing the gel around them. Therefore bacterial colonies might also be used as a probe for exploring small scale fracture mechanics in soft materials. The advantage of using bacterial colonies over more conventional experimental setups stems from two factors:

1. Fractures typically propagate at high speeds due to the fact that the stress required to propagate a fracture is inversely proportional to the size of the fracture[2]. This inverse proportionality means that once the fracture reaches a critical size (if the applied stress is held constant) it will continue to propagate at near the sound speed of the material[3] ($\sim 1\,\mathrm{m\,s^{-1}}$ to $10\,\mathrm{m\,s^{-1}}$ in hydrogels).

2. The size of the process zone around a crack where processes of interest to current research (plastic deformation, cavitation, blunting) takes place is small ($\sim 10\,\mu\mathrm{m}$ in hydrogels, estimating from equations 3.34 or 3.48) [79, 82].

The combination of these factors has made it very difficult to design experimental systems to observe the processes that occur near a crack tip. By fracturing a gel with a growing bacterial colony these difficulties might be alleviated. First, as the initial fracture in the gel is approximately the size of a single bacterium ($\sim 1\,\mu\mathrm{m}$), it will be smaller than the process zone in most hydrogels, allowing for detailed observation of that zone. In addition, the propagation rate of the fracture is limited by the growth rate of the bacteria. The bacteria grow extremely slowly compared to the sound speed in the material, allowing for the morphology (and displacement around) a fracture to be measured at small scales. However, as the fracture is filled with bacteria instead of a fluid (as it might be in a more conventional experiment [79]) one might expect different physics to be at play. The differences between fractures propagated by bacterial colonies and a Newtonian fluid are therefore explored in the next chapter.

[2] c.f. Equation 3.16.

[3] More accurately, a fracture will propagate at speeds approaching the Rayleigh wave speed. The Rayleigh wave speed is the sound speed with a small correction for the compressibility of the gel. At speeds ~50% of the Rayleigh wave speed, crack tip branching slows the propagation speed [132–134].

This chapter is structured as follows: First I compare the morphology of colonies grown in my set-up to that seen previously, finding the concentration of agarose at which colonies form lenticular shapes and using measurements of gel deformation to show that the colony fractures the gel around it. I then check that my method of gel preparation does not influence the fracture direction. Given that the colony fractures the gel, the next section of the chapter compares the measured morphology to a simple model where the colony is considered to be a source of pressure opening up a disk shaped crack. Doing so shows that the colony's shape and displacement field deviate from what would be expected from the simple model. The final section of the chapter then attempts to explain these deviations using the more recent theories of cavitation and fracture mode transition that were discussed in Section 3.5.

5.2 Experimental Results

5.2.1 The morphology of a submerged bacterial colony

First the concentration of agarose at which ellipsoidal colonies form is determined. To explore this, colonies of *E. coli* were grown submerged in agarose gels at a range of concentrations using the methodology detailed in Chapter 4. Figures 5.1a-f show bright field images of colonies grown in 0.4 % to 3 % agarose gels for 24 hours. The images shown are representative of all of the colonies grown at that concentration. Each gel had been inoculated with the same concentration of cells (as detailed in Section 4.3.3). In 0.4 % agarose, Figure 5.1a, many clusters[4] of cells formed, few of these clusters were over 50 µm in diameter. Between the larger ($\sim$ 50 µm) cell clusters, smaller clusters of cells formed that were spread throughout the gel. The collection of smaller and larger clusters were $\sim$ 300 µm across and formed with about the same frequency as colonies were observed in higher agarose concentrations, suggesting that they had a common progenitor cell. *E. coli* could be seen moving in the gel. For the most part these moving cells were pinned in place (precessing about one spot), but the dispersed nature of the cell clusters suggests that *E. coli* became unpinned with some frequency and spread throughout the gel.

[4]I call these "clusters" of cells rather than "colonies" as there was no definite boundary between concentrations of cells and the surrounding gel.

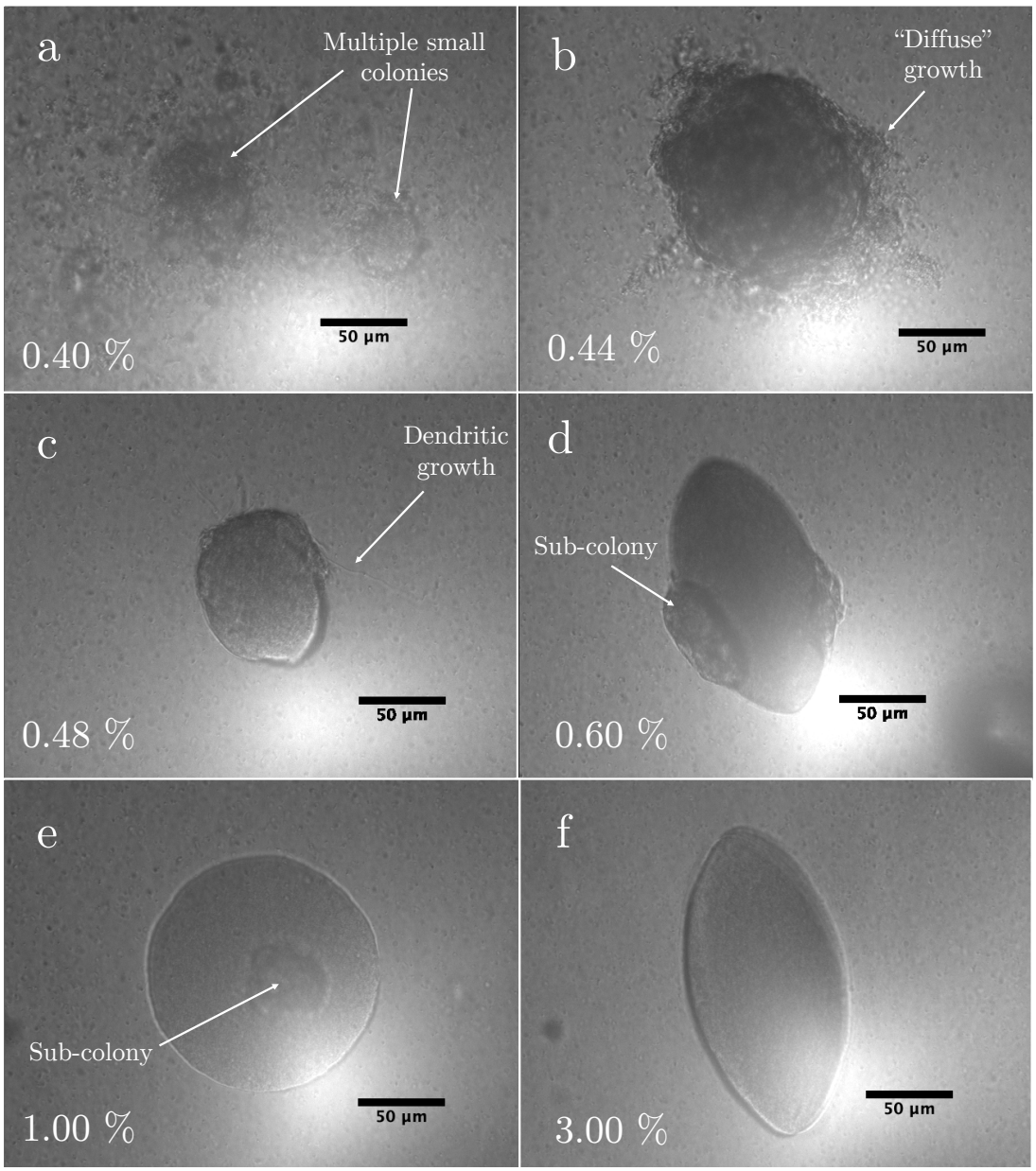

Figure 5.1 *Bright-field images of colonies grown in various concentrations of agarose for 24 hours, each gel was inoculated with the same concentration of cells. The images shown are representative of colonies grown at that concentration. See text for a full description.*

At agarose concentrations of 0.44 %, colonies with a more definite boundary between *E. coli* and the surrounding gel began to form, Figure 5.1b. These colonies were covered in "diffuse" formations at the outskirts of a more dense mass of cells. *E. coli* were not observed to be moving in the gel. The colonies grown in 0.44 % formed uneven spheroidal shapes. At agarose concentrations of 0.48 %, Figure 5.1c, the diffuse growth at the edges of the colonies was reduced in extent. Long tendrils seemingly comprised of multiple *E. coli* cells were observed trailing away from the main colony. The main colonies now took on more even spheroidal/ellipsoidal morphologies. Many colonies had what appeared to be smaller colonies (sub-colonies) growing at/on their surfaces. By agarose concentrations of 0.6 % regions of diffuse growth were gone and the colonies formed shapes similar to those seen by Wimpenny et al., Figure 5.1d. Many colonies still had sub-colonies growing at their surface however. Similar lenticular shapes were observed for colonies grown in all agarose concentrations above 0.6 %, Figure 5.1e,f. The frequency with which sub-colonies formed and the size of those sub-colonies seemed to reduce with increasing agarose concentration. By an agarose concentration of 3 % no sub-colonies were observed, leaving only lenticular/ellipsoidal masses of cells.

Colonies formed in agarose concentrations of 0.6% and above were consistent with those seen by Wimpenny et al. for *E. coli*, *Pseudomonas aeruginosa*, *Salmonella typhimurium*, *Enterococcus faecalis* and *Lactococcus lactis* colonies grown in agar gels [37, 38, 41]. Inability to hydrolyse agar polymer chains is the common feature amongst these species[5].

In previous studies only 2D projection of colonies at single time points were recorded, and the formation of sub-colonies was not reported[6]. Now, using SPIM, the full 3D structure of the colonies can be observed from the point where the colonies consist of only ~ 10's of cells up until they form colonies of $\sim 10^6$ cells.

The first thing that more extensive observations reveal is the origin of the sub-colonies. Figure 5.2a-i show fluorescence images of a colony grown in 0.6 % agarose, from a time point where the colony consisted of only 10's of cells up to time point where the colony consisted of 100,000's of cells. The colony is observed to initially grow in a dendritic fashion, spreading in all directions without the ellipsoidal morphology observed at later time-points, Figure 5.2a-d.

[5]For species that could hydrolyse agar, wispy or dendritic colonies were observed.
[6]Though there is some evidence for sub-colony formation in the figures of [41].

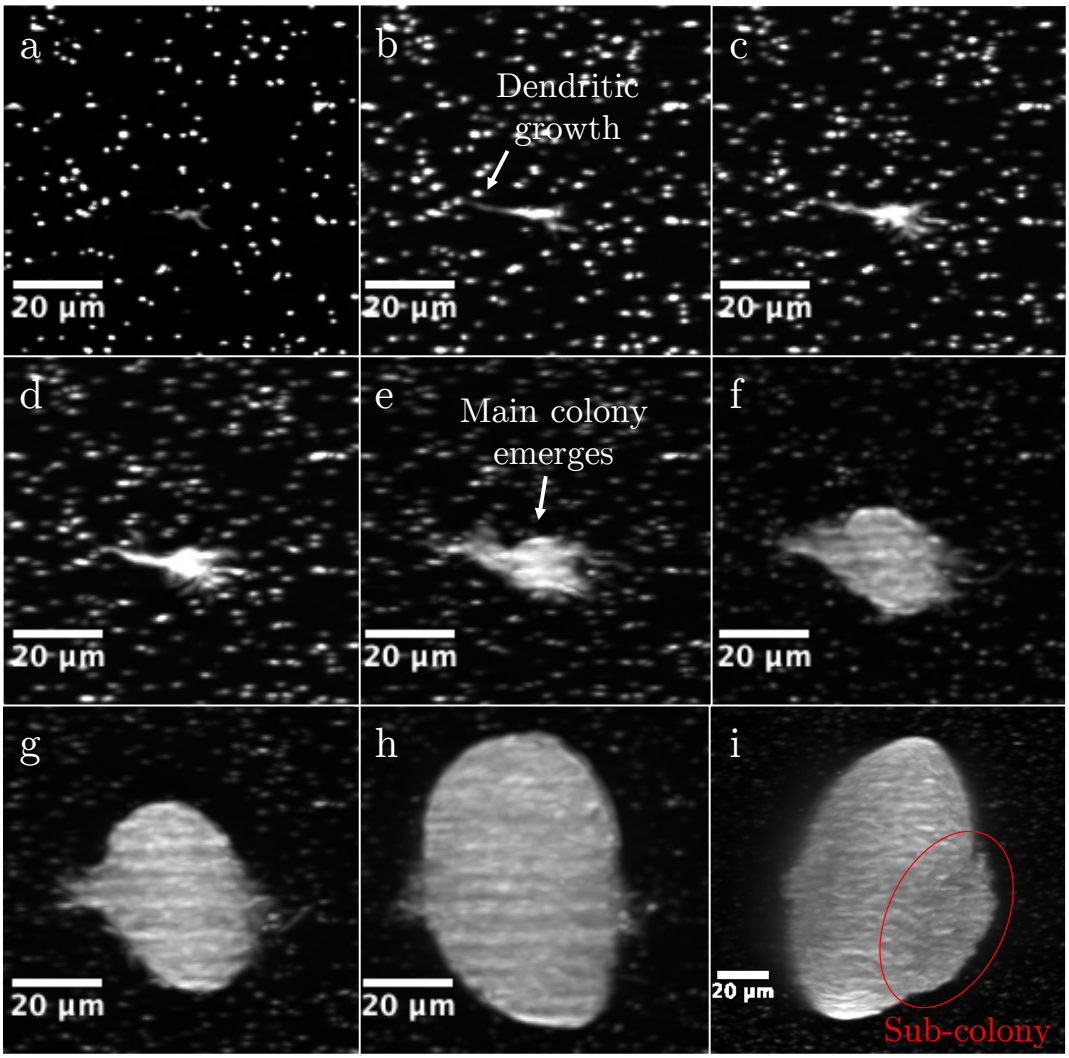

Figure 5.2 *z-projections of image stacks taken with SPIM of a colony growing in 0.6 % agarose. (a-d) When cells first start dividing they extend in random directions making a dendritic structure. (e-h) Then at some point a more cohesive cluster of cells forms near the centre of the dendritic structure, this cluster grows into the main colony. (i) Cells outside the main colony early on continue to divide and form sub-colonies that are eventually deformed onto the surface of the main colony.*

Next, emerging from the center of the dendritic growth, a more cohesive clump of cells forms, Figure 5.2e-h. That cohesive clump of cells goes on to form the main colony seen at later time points, Figure 5.2i. After the main colony begins to emerge no new dendritic infiltration of the agarose was observed. Cells in the initial dendritic offshoots do not stop dividing and form their own sub-colonies. These sub-colonies are seemingly deformed onto the surface of the main colony, forming a separate population of cells[7].

The same process as shown in Figure 5.2 was seen for all other colonies grown between 0.6 % and 1.0 % agarose, with a single cohesive colony emerging from a dendritic structure at a certain size. For colonies grown in agarose concentrations above 1.0 %, the 'main' colony seems to form earlier and sub-colony formation is rarer. At an agarose concentration of 3 % and above no sub-colonies were observed. I believe that the cessation of dendritic growth in favour of a single colony cluster can be explained by a transition in fracture mode that occurs at small scales. This phenomena will be the subject of Section 5.4.

The effect of agarose pore size on diffuse and dendritic growth

Two regimes of growth were described in the previous section. In the first, below 0.48 % agarose, small clusters of cells formed or colonies with diffuse boundaries. Then, at higher concentrations, ellipsoidal/lenticular colonies formed with more defined boundaries. The difference between these growth regimes might be explained by the porous structure of agarose.

Agarose forms a macroreticular structure with pore size inversely proportional to to the concentration of agarose, [86, 105, 136, 137]. The size of the pores are reported to be $\gtrsim 500\,\text{nm}$ in 0.5 % agarose, decreasing to $< 50\,\text{nm}$ in higher concentrations (> 3 %) [86, 105, 136]. The width of an *E. coli* bacterium (0.5 µm to 0.8 µm [138]) is comparable to the pore size at low agarose concentrations, possibly allowing them to move/swim through the gel. This movement is possibly the reason why several clusters of cells formed in 0.40 % agarose, with *E. coli* able to move through the agarose before being trapped where the local pore size is reduced, forming denser clusters of cells at those locations. Observations of bacteria moving in the gel at 0.40 % corroborated this hypothesis.

[7]Whilst separate from the main thrust of this work, the conditions under which sub-colonies form might prove interesting to those studying the effect of spatial structure on genetic diversity or competition within biofilms [135].

In 0.6 % agarose, where the colony was initially observed to grow in a dendritic fashion, it is unclear from the literature whether *E. coli* should be able to move through the gel. I would like to determine whether the dendritic growth seen in figures 5.2a-e is due to *E. coli* being able to move through the gel or if the *E. coli* have to break the gel network in order to move. This distinction will be important in later parts of the chapter. Therefore with the help of Dr. Thomas Glen I captured images of the agarose structure with a cryo-electron microscope to determine the pore size of 0.6 % agarose.

Agarose was prepared in the same way as described in Section 4.3.1. Samples were then frozen in a Leica EM HPM High Pressure Freezer to prevent ice crystal formation from destroying the macroreticular structure. The frozen agarose samples were fractured with a blade to expose the inner surface of the gel, this surface was then sputter coated with gold palladium to prevent charging of the surface[8]. Figure 5.3 shows cyro-electron images of 0.6 % agarose and 2 % agarose at 50,000× magnification. A 500 nm scale bar representative of the width of a single *E. coli* bacterium is overlaid on the image.

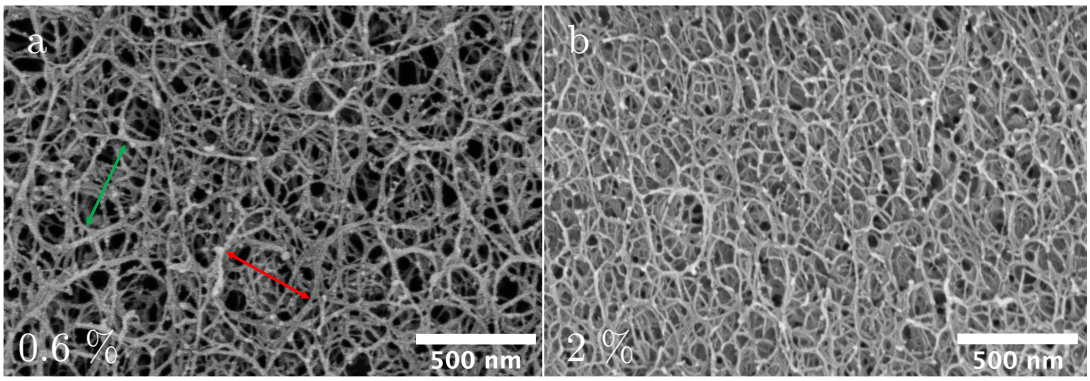

Figure 5.3 *Samples of agarose prepared using a high pressure freezer and imaged with a cyro-electron microscope. The scale bar is approximately the width of an E. coli bacterium. (a) 0.6 % agarose, Green and red arrows highlight the size of the largest pores in the image, both of which are* ≈ 400 nm *in diameter. (a) 2.0 % agarose.*

From Figure 5.3a it can be seen that the very largest pores in 0.6 % agarose are around 400 nm in diameter, making it unlikely that bacteria can freely move through the network. That bacteria cannot move freely through the gel is further corroborated by the fact that the dendritic growth seen in figures 5.2a-d are contiguous, i.e. there are no populations of cells separate from the initial dendritic

[8]When a nonconductive surface is imaged with an electron microscope a static charge builds up that will distort the image.

growth. If *E. coli* could move freely through the 0.6 % gel then one might expect some cells to become separated from the main colony so that multiple clusters of cells would be formed.

The structure of 2 % agarose is shown in Figure 5.3b, it is clearly denser (having a smaller average pore size) than 0.6 % agarose, in agreement with literature observations [86, 105, 136, 137]. This suggests that for all agarose concentrations greater than or equal to 0.6 %, *E. coli* should be unable to move freely through the gel, meaning that the gel has to be deformed or broken in some way for the colony to expand. The next section will look at further evidence for the deformation/breakage of the agarose network during colony growth.

5.2.2 Evidence for equatorial fracture

In Section 5.2.1 I showed that *E. coli* grown in agarose concentrations of 0.6 % and above form lenticular or ellipsoidal colonies[9] (ignoring sub-colonies). Figure 5.4 shows an image of a colony grown in 3 % agarose that is archetypal of the morphology seen in agarose concentrations of 0.6 % and above. The image was captured using SPIM and has been given false colour to highlight the depth of the image. The cross section perpendicular to the colonies minor axis is roughly circular, whilst the cross section parallel to their minor axis has a lenticular or ellipse-like shape.

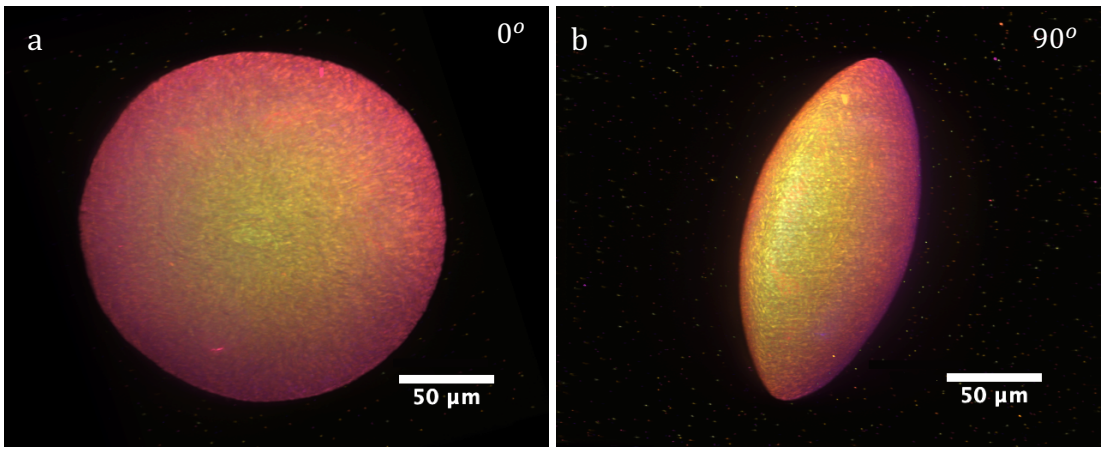

Figure 5.4 *Perpendicular z-projections of a colony grown in 3 % agarose. (a) The colonies are roughly circular in the plane perpendicular to their minor axis and (b) lenticular or ellipse-like in the planes parallel to their minor axis.*

[9]The shape will be examined in more detail in Section 5.3.3

To determine whether the colonies were indeed fracturing the gel, I tracked the displacement of embedded fiducial markers as described in Section 4.6.4. Figure 5.5 shows the trajectories[10] of these markers around a colony grown in 3 % agarose. Trajectories are coloured according to their magnitude. The colony surface is represented by a grey polygonal mesh. The trajectories clearly show that the gel is being displaced in the direction of the colony's minor axis ($\approx z$ axis), whilst in the plane perpendicular to the minor axis ($\approx xy$ plane, the equatorial plane) there is no displacement of the gel. If the colony elastically displaced the gel, then displacements would be expected in all directions normal to the colony surface. Such normal displacements are not observed in the equatorial plane, therefore the gel must be being broken in that plane. Similar trajectories were observed around colonies grown in all agarose concentrations tested, these trajectories will be looked at in more detail in Section 5.3.4.

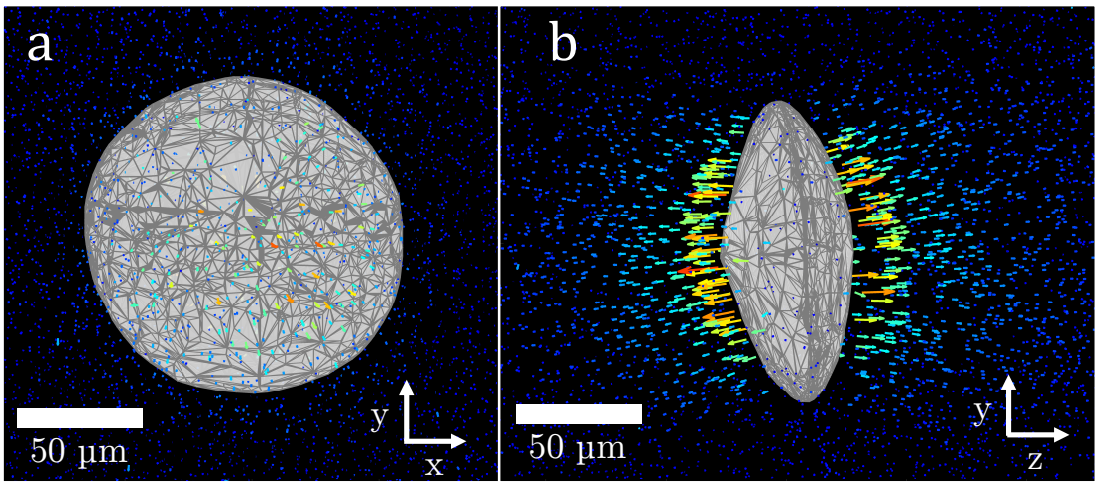

Figure 5.5 *Fiducial markers embedded in the gel were tracked as the colony grew. One third of marker trajectories in the Lagrangian frame of reference are shown by arrows from two orthogonal views, trajectory vectors are coloured according to their magnitude. (a,b) The trajectories reveal that gel is displaced in the direction of the colonies minor axis ($\approx z$-direction) and that there is little displacement in the plane perpendicular to the minor axis ($\approx xy$-plane). There is little displacement around the apex of the colony even in the direction of the minor axis.*

Furthermore, the morphology of the colony is reminiscent of a hydraulic fracture. Experiments involving blowing bubbles into gels to physically model gas bubbles

[10]Trajectories are shown in the Lagrangian frame of reference, which is one of the two common ways that a flow field is specified. For example, consider a point at position a in the undeformed material that moves to position A in the deformed state of the material along the vector $\mathbf{v}$. The Lagrangian frame of reference would plot $\mathbf{v}$ with origin at A (the point A has moved by $\mathbf{v}$) whereas the Eulerian frame of reference would plot $\mathbf{v}$ originating at a (a moves to A).

that form in marine sediments have been shown to form similar shapes [62, 139–141]. Section 5.3 will look more closely at how well the colony shape is described by a hydraulic fracture.

5.2.3 The effect of inoculation method on the direction of fracture

The reason for inoculating the gel in its molten state (see Section 4.3.1) rather than using Wimpenny's method[11] of inoculation was to prevent flaws forming in the gel that might introduce a preferred direction of colony growth. This preferred direction could influence the morphology of the colonies, so ideally this should be ruled out before closer examination of the colony shape is undertaken.

To determine whether there is a preferred direction for colony growth I must determine whether or not the colonies are randomly orientated in gel. This can be achieved by checking whether the observed distribution of colony orientations lies within the range of probable deviations from a uniform distribution. Specifically, a Kolmogorov–Smirnov (KS) like statistic can be used to measure the deviation of the observed distribution from a uniform distribution, the measured statistic can then be compared to the distribution of KS statistics calculated from random samples of a uniform distribution.

A colony's orientation was defined by its principle axis, $\mathbf{v} = (v_x, v_y, v_z)$, with largest corresponding eigenvalue . $\mathbf{v}$ was measured for 61 colonies using the method detailed in Section 4.6.3. The angle, θ, between $\mathbf{v}$ and each Cartesian axis (x,y,z) was calculated. Figure 5.6a, shows the projections of $\mathbf{v}$ onto the xy, yz and zx-planes along with θ.

The probability density as a function of θ for a uniform distribution of vectors pointing to the surface of a unit sphere is given by

$$P(\theta) = \frac{\sin(\theta)}{2}. \tag{5.1}$$

Given the symmetry of the colonies about the fracture plane, $-\mathbf{v}$ can be equally assigned to $\mathbf{v}$, therefore all vectors are flipped so that θ is acute, doubling $P(\theta)$. The uniform cumulative distribution function, CDF_u, can therefore be expressed

[11] Wimpenny inoculated the surface of a gel and then poured molten agar over the surface. This may have formed a boundary along which the gel is more susceptible to fracture.

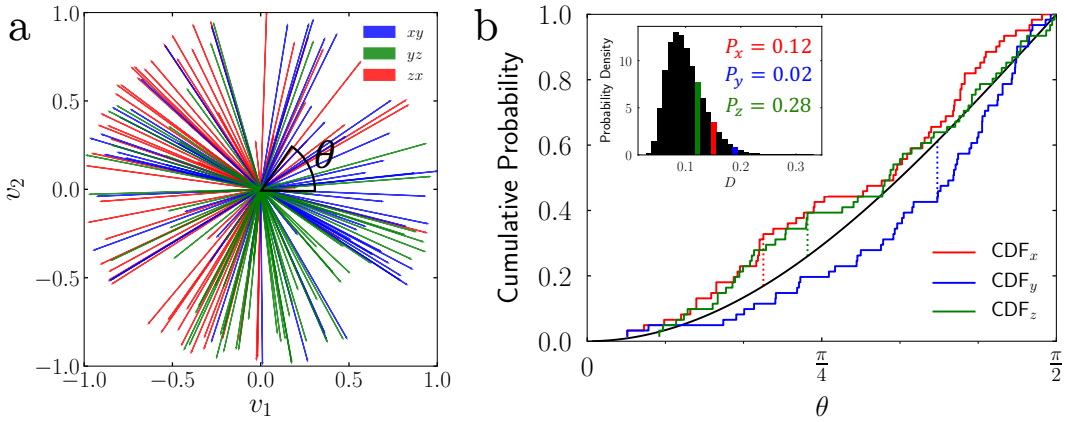

Figure 5.6 *Colonies orientations could not be distinguished from a random distribution. (a) Projections of the colony principle axis onto the xy, yz and zx planes. The angle between the principle axis and each Cartesian axis was measured. (b) A KS-like statistic, D, was calculated from the distributions of θ_m around each axis (coloured step plots) and a uniform distribution (black line). P-values were calculated for each distribution using 100,000 random samples from the uniform CDF (inset). Two of the three distributions had P-values significantly larger than 0.05.*

as

$$\mathrm{CDF}_u(\theta) = \int_0^{\theta} \sin(\theta')d\theta' = 1 - \cos(\theta) \tag{5.2}$$

The measured cumulative distribution function, $\mathrm{CDF}_m(\theta)$, for a set, M, of N measurements of the angle made between the principle axis of the colony and an axis, θ_m, is found by summing over the measurements of θ_m less than θ, i.e.

$$\mathrm{CDF}_m(\theta) = \frac{1}{N} \sum_{\theta_m \in M} \begin{cases} 1 & \text{if } \theta_m \leq \theta \\ 0 & \text{if } \theta_m > \theta \end{cases} \tag{5.3}$$

A KS-like statistic can then be calculated by finding the supremum, D, between $\mathrm{CDF}_u(\theta)$ and $\mathrm{CDF}_m(\theta)$, Figure 5.6b, i.e.

$$D = \sup \left| \mathrm{CDF}_u(\theta) - \mathrm{CDF}_m(\theta) \right|. \tag{5.4}$$

The null hypothesis can be stated as 'The distributions $\mathrm{CDF}_u(\theta)$ and $\mathrm{CDF}_m(\theta)$ cannot be distinguished', it can be tested by comparing the D measured for M to the D that arise from randomly generating 61 angles, θ_g, from $\mathrm{CDF}_u(\theta)$. By generating many such sets of generated θ_gs, the distribution of Ds drawn from

a truly uniform distribution can be found. θ_g can be generated from $\mathrm{CDF}_u(\theta)$ using a random number, R, between 0 and 1 so that

$$\theta_g = \arccos(1 - R). \tag{5.5}$$

P-values[12] for the measured distributions around each Cartesian axis can then be calculated using the generated distribution of Ds. The P-values for the observed D are 0.12, 0.02 and 0.28 around the x, y and z axis respectively, Figure 5.6b,inset.

If one were to set a confidence threshold of $p = 0.05$ then the null hypothesis would be accepted for the distribution around the x and z-axis whilst the null hypothesis would be rejected for the distribution around the y axis. The cause of the deviation of $\mathrm{CDF}_y(\theta)$ from $\mathrm{CDF}_u(\theta)$ is likely due to colonies having a slight preference to align with the xz-plane, shown by the overabundance[13] of colonies orthogonal to the y axis, i.e. with their fracture plane aligned axially along the FEP tubing. The null hypothesis was accepted for $\mathrm{CDF}_x(\theta)$ and $\mathrm{CDF}_z(\theta)$ because the colonies are likely uniformly distributed in the xz plane which masks the non-uniformity along the y-axis. Note that because the three distributions are not independent the rejection of the null hypothesis for $\mathrm{CDF}_y(\theta)$ is not due to p-hacking[14].

The slight preference for colonies to fracture the gel along the axis of the FEP tubing might be explained by agarose polymer chains aligning along the tube axis as the gel was sucked into the tube. If polymer chains were to align with the tube axis then one could imagine that the average pore diameter would be greater along the tube axis than in the radial direction. Recalling that the stress in a material is concentrated where the radius of curvature is minimised (Equation 3.7), it is likely that the polymer chains at the apex of these asymmetric pores would be more likely to break, resulting in fractures that are more likely to be aligned with the tube axis. Overall the deviation of the observed distribution from a uniform distribution is quite slight, even though it it statistically significant, with colonies of all orientations between 0 and 90° observed.

[12]That is the probability of observing a D larger than the D observed from the measured distribution. This is a one-tailed test because I only care about values of D larger than that observed, not the equally extreme but small values of D that are also observed.

[13]I say there is an overabundance because the slope of the CDF is steeper for larger θ.

[14]I.e. if the three distributions about the Cartesian axis were independent then given three measurements of D the likelihood of one having a P-value less than 0.05 is about 14 %. In this case the distributions are not independent of one another.

5.3 Comparison of colony morphology to a simple model of colony formation

Having shown that colonies of *E. coli* grow by fracturing the gel around them and that the method of gel preparation has only a small influence on the fracture direction, I now propose a simple model for colony formation.

Given that the colony appears to fracture the agarose in a disk and that agarose is a reasonably brittle material, it made sense to first model the colony as a linear elastic hydraulic fracture (see Section 3.2.4). In such a model the *E. coli* colony is viewed as filling a disk shaped crack that is opened up by a pressure, P, exerted hydrostatically by the colony due to its growth. As the *E. coli* comprising the colony undergo binary fission and the colony grows, the pressure exerted by the colony grows until P exceeds some critical pressure, P_c, whereupon the disk crack spontaneously propagates, increasing in radius by some small amount. The crack propagation increases the volume available to the colony, lowering P below P_c so that propagation is halted until growth raises the pressure above P_c again[15].

This section compares the observed colony morphology with this simple model. There are two possible outcomes of this comparison. If the colony shape matches the predictions of the simple model, then morphology measurements will inform estimates of the pressure inside a growing colony. Knowing the pressure within the colony would enable measurements of the pressure at which bacteria fission is arrested, measurements that would have a wide range of uses from food safety to the measurement of the force that a single bacterium can apply. If the colony shape does not match the predicted shape, then deviations might give some indication as to how the basic model might be modified to better fit observations.

If the colony were to grow according to the simple model then its morphology would be the same as that described in Section 3.2.4. Therefore there are four characteristics by which I can compare the observed colony morphology to the model:

1. The radius of curvature at the edge of the colony, ρ, should be constant, and can be given in terms of the Poisson ratio ν and elasto-fracture length

[15]Interestingly, the implied periodic pressure jumps in this picture have been seen in experiments observing the growth of injected gas bubbles in gelatin [62, 142].

scale ℓ_{EF} as:

$$\rho = \frac{4}{\pi}\left(1-\nu^2\right)\ell_{\mathrm{EF}}. \tag{5.6}$$

2. The minor axis of the colony, b, should scale with the major axis of the colony, a, in the following way:

$$b = \sqrt{\frac{4\left(1-\nu^2\right)}{\pi}}\sqrt{a\ell_{\mathrm{EF}}}. \tag{5.7}$$

3. The colony should be ellipsoidal, i.e. the displacement of the colony surface in the direction of the colony's minor axis (u_z) as a function of radial distance r along the colony's major axis from the colonies center of mass should be given by

$$u_z(r,0) = b\sqrt{1-\left(\frac{r}{a}\right)^2} \tag{5.8}$$

4. The displacements in the direction of the colony's minor axis and the radial direction orthogonal to the minor axis (u_z and u_r respectively) near to the colony should be given by

$$u_z = b\int_0^\infty \left(1+\frac{\zeta\eta}{2(1-\nu)}\right)\left[\frac{\cos(\eta)}{\eta}-\frac{\sin(\eta)}{\eta^2}\right]e^{-\zeta\eta}J_0(\omega\eta)d\eta. \tag{5.9}$$

and

$$u_r = \frac{b}{2}\frac{1}{1-\nu}\int_0^\infty (1-2\nu-\zeta\eta)\left[\frac{\cos(\eta)}{\eta}-\frac{\sin(\eta)}{\eta^2}\right]e^{-\zeta\eta}J_1(\omega\eta)d\eta \tag{5.10}$$

The terms ω and ζ in Equation 5.9 and 5.10 are the scaled radial and axial coordinates,

$$\omega = \frac{r}{a}, \quad \zeta = \frac{z}{a}, \tag{5.11}$$

and J_α are Bessel functions of the first kind.

The following sections will compare colony morphology and surrounding displacement fields to each of these descriptors. Measurement of ℓ_{EF} is detailed in Chapter 7.

Only data from colonies that had small or no sub-colonies growing on their surfaces[16], that remained wholly within the field of view, and that had no other colonies growing within $\approx 500\,\mu\mathrm{m}$ of themselves were used for comparison. The number of colonies which met these criteria for the duration of their growth at

[16]So that measurements of the colonies inertia tensor and profile were not significantly skewed.

each concentration was as follows: 0.6 %: 3, 1.0 %: 3, 1.5 %: 2, 2.0 %: 5, 3.0 %: 5, 4.0 %: 1. Only one colony was successfully observed at 4 % agarose due to the tendency of the 4 % gel to pull away from the FEP tube wall[17], scattering the light sheet and preventing imaging.

5.3.1 The crack tip radius of curvature

First, I compare the radius of curvature at the colony apex, ρ, to the constant predicted by the model (Equation 5.6). The method used to measure ρ is described in Section 4.6.3. Figure 5.7a plots ρ as a function of a for colonies grown in several agarose concentrations. Individual data points are shown as circles and are coloured according to the concentration of agarose they were measured in. Data from multiple colonies at each concentration is plotted concurrently. Splines are fit to data points at the same agarose concentration to highlight the trend.

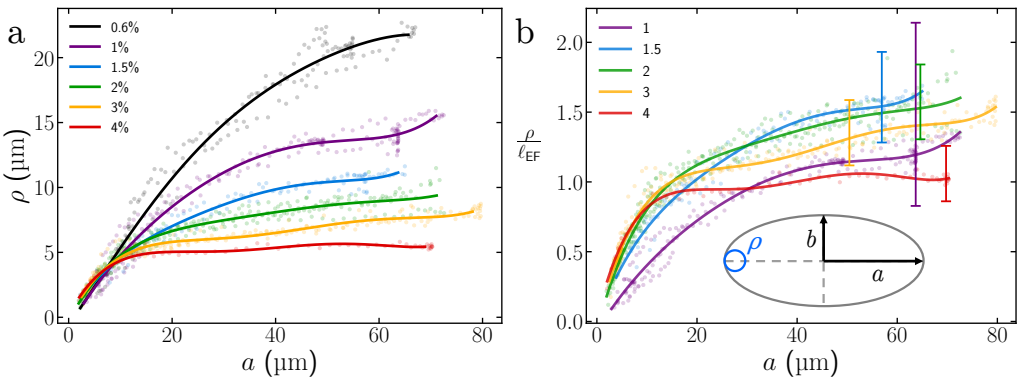

Figure 5.7 *Colony tip radius of curvature vs major axis length. Data points from multiple colonies grown in the same concentration of agarose are shown by dots. Splines fitted to all data at a given concentration have been added to the data to highlight the trend. (a) The radius of curvature appears to plateau at large a and for colonies grown in high concentrations of agarose. (b) By dividing ρ by ℓ_{EF} the data collapses showing that $\rho \approx \ell_{EF}$ for large a.*

For higher agarose concentration and at larger a, ρ appears to be constant, consistent with the model. However, at lower agarose concentrations and for small a, ρ is not constant. It appears as though the value of a at which the plateau value of ρ is reached is inversely proportional to the concentration of agarose.

[17]The tendency of the 4 % gel to pull away from the FEP tube wall may be explained either by the faster desiccation of the gel at higher agarose concentrations or by stress induced in the gel during setting (this effect is described in Section 7.3).

Partial collapse of the data[18] in Figure 5.7a can be achieved by scaling ρ by ℓ_{EF}, Figure 5.7b, this is consistent with Equation 5.6. Splines are fit to the data in order to highlight the trend. A representative uncertainty bar is plotted for each agarose concentration at one value of a. The majority of the uncertainty in the value comes from the uncertainty in ℓ_{EF}, see Chapter 7. The plateau value of ρ falls between 1-1.5 ρ/ℓ_{EF} for all agarose concentrations and there is significant overlap of plateau values between concentrations given the large uncertainty in the value of ℓ_{EF}. For small colonies ($a \lesssim 20\,\mu\mathrm{m}$) there is clearly some transition region for which the model does not account.

5.3.2 The scaling of colony aspect ratio

The second characteristic by which colonies can be compared to a linear elastic hydraulic fracture is the scaling of their aspect ratio, Equation 5.7, $b \approx \sqrt{a\ell_{\mathrm{EF}}}$. Values of a and b were measured using the inertia tensor of the colony as described in Section 4.6.3. To determine the scaling between b and a, Figure 5.8a plots $\log(b)$ as a function of $\log(\sqrt{a})$ for colonies grown in several agarose concentrations. After some initial transition at small $\log(\sqrt{a})$, $\log(b) \propto 0.8\log(a)$ for colonies grown in all concentrations of agarose. This is significantly different from the model's prediction.

However, scaling a by ℓ_{EF} still achieves partial collapse of the data, Figure 5.8b. This collapse shows that the proportionality constant between b and $\sqrt{a}$ is at least correlated with ℓ_{EF}. Data collected in 1.0 % agarose lies quite far from data collected at higher agarose concentrations, likely due to the large uncertainty in ℓ_{EF} ($12 \pm 5\mu\mathrm{m}$) at 1.0 % agarose. This large uncertainty stemmed from 1.0 % agarose being at the limits of what could be measured in my materials testing apparatus, see Chapter 7.

Figure 5.8b more clearly shows a region of roughly spherically symmetric growth for small colonies ($\log\left(\sqrt{a\ell_{\mathrm{EF}}}\right) < 2.5$) grown in 0.6 % and 1.0% agarose. This is evidenced by the scatter plots for 0.6 % and 1.0% agarose following the line where $b \propto a$ (dash-dotted line). This region of spherically symmetric growth corresponds to the Figure 5.2f before the main colony emerges from the initial dendritic growth.

[18] I was unable to measure ℓ_{EF} for 0.6 % agarose, therefore data at 0.6 % is excluded from Figure 5.7b.

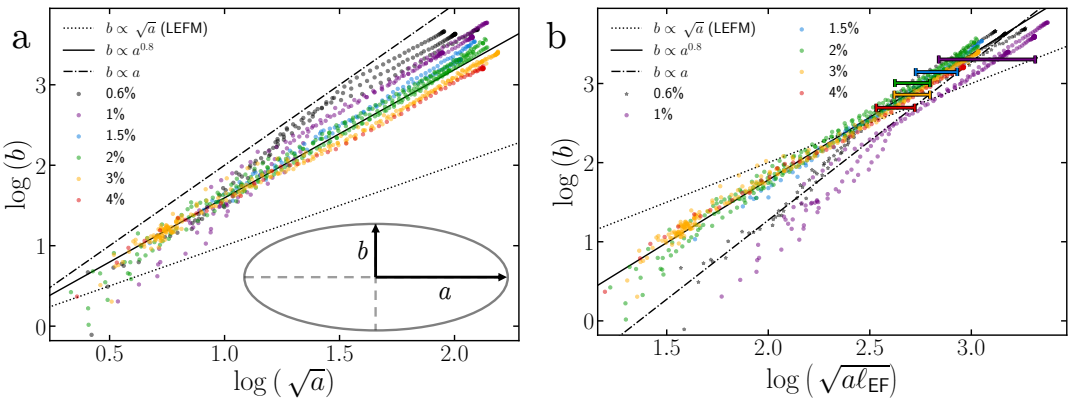

Figure 5.8 *The scaling of colony minor and major axis. (a) The log of the colonies minor axis, b, is plotted against the log of the square root of its major axis. The minor axis does not follow the square root power law predicted by LEFM, instead $b \propto a^{0.8}$. (b) Partial collapse is achieved by scaling $\sqrt{a}$ by $\sqrt{\ell_{EF}}$. Error bars are plotted for a single data point from each concentration given the uncertainty in ℓ_{EF}. Using the correlation between b and $a\ell_{EF}$ the value of ℓ_{EF} for 0.6 % is estimated to be* 10.5 ± 1.5 µm*, the scaled data is represented by black stars. For smaller colonies at lower agarose concentrations growth is roughly spherically symmetric.*

I can use the correlation between b and $a\ell_{\mathrm{EF}}$ at higher concentrations of agarose to estimate the value of ℓ_{EF} for 0.6 % and 1.0 % agarose. By using a least squares fit to colonies at 1.5 % agarose and above, the value of ℓ_{EF} that results in the least square difference between the measured values of b and the line $b = 0.25\,(a\ell_{\mathrm{EF}})^{0.8}$ can be calculated for 0.6 % and 1.0 % agarose. Only values where $\sqrt{a} > 1.5$ are used to avoid fitting to the region of spherical growth. Doing so results in $\ell_{\mathrm{EF}} = 8.6$ µm for 1 % agarose and $\ell_{\mathrm{EF}} = 12.9$ µm for 0.6 % agarose.

5.3.3 Comparing colony profiles.

Next the prediction that colonies should be ellipsoidal is tested. Colony profiles were measured as described in Section 4.6.3. According to linear elasticity, the displacement normal to the surface of a disk-shaped void of radius a, deformed by a uniform pressure so that it's maximum width is b, is given by:

$$u_z(r,0) = w(r) = b\sqrt{1 - \left(\frac{r}{a}\right)^2} \tag{5.12}$$

Colony profiles are compared to Equation 5.12 in 5.9. Representative profiles of colonies in four different agarose concentrations at multiple colony sizes are

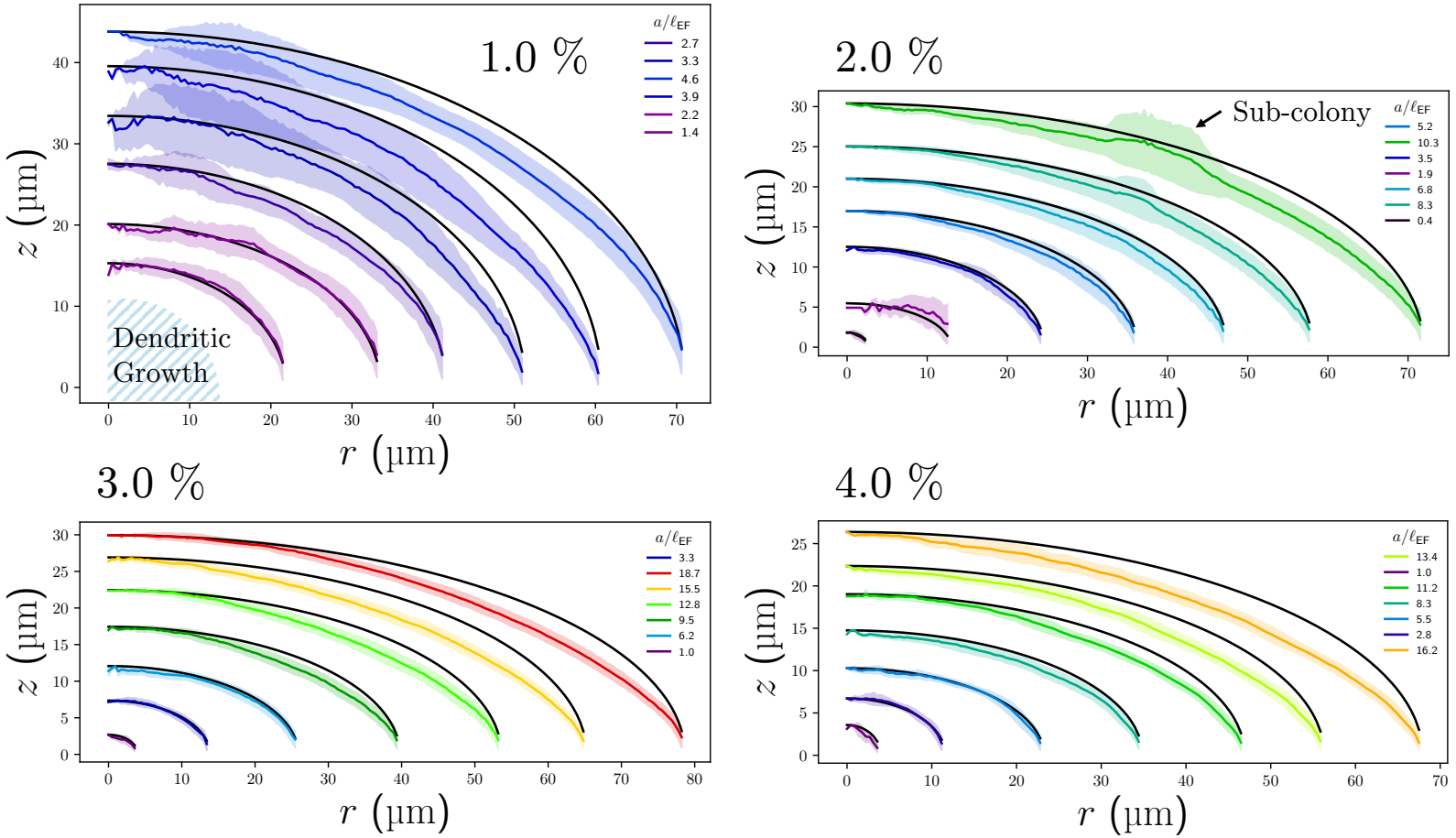

Figure 5.9 *Comparison of colony profiles and Equation 5.12. The profiles of colonies at various time points in four agarose concentrations are shown. The shaded region represent one standard deviation from the measured colony width. Plots are coloured by the size of a compared to $\sqrt{\ell_{EF}}$. Ellipses with major and minor axis equal to a and b respectively are shown in black. For small a, colonies are approximately ellipsoidal. However, as the colonies grow in size they become more lenticular.*

plotted along with the corresponding prediction from Equation 5.12 in black. b and a have been set to the values of the colony minor axis at $r = 0$ and colony major axis at $z = 0$ respectively. Colonies appear to agree with the model prediction at small sizes ($a \lesssim 35\,\mu\text{m}$) but then become more lenticular (having a more cusp like tip) at larger a.

The profiles display another feature of the colonies. At lower agarose concentrations the colonies appeared more irregular in shape, evidenced by larger standard deviations in their profiles. In both the 1 % and 2 % profile plots evidence of a sub-colony can be seen by the increased standard deviation of measurements within a range of r values.

To measure the deviation from the model prediction, curves of the form

$$\left|\frac{r}{a}\right|^{\frac{1}{p}} + \left|\frac{z}{b}\right|^{\frac{1}{p}} = 1 \tag{5.13}$$

were fit to the colony profiles. When $p = 0.5$ this curve forms an ellipse, whilst for $p \neq 0.5$ the curve forms a superellipse. When $p > 0.5$ the curve becomes more "cuspy", forming a more lenticular shape. The width of this curve for a given p is given by

$$w(r) = b\left[1 - \left(\frac{r}{a}\right)^2\right]^p. \tag{5.14}$$

Figure 5.10a plots these fitted superellipse for a colony grown in 4 % agarose. With powers between roughly 0.5 and 0.75 the superellipse fit the measured colony profile within uncertainty. The relationship posited above, that the profile deviates further from an ellipse with increasing a, is confirmed by the increasing value of p needed to fit the profile, Figure 5.10b. This deviation from an ellipse is present in all concentrations of agarose and, interestingly, does not collapse when scaled by ℓ_{EF}.

I am currently unaware of any theory that states that hydraulic fractures should form superellipsoids (the solid of revolution of a superellipse). However, work by Lefranc and Bouchard has shown that in Agar gels the Mode I crack opening displacement in a notch crack deviates significantly from the LEFM prediction when the crack propagates at high velocities [143, 144]. At these high velocities they also observe a more "cusp" like crack tip profile. They attribute the deviation to an increase in Γ with crack tip velocity. With increasing Γ, ℓ_{EF} or ℓ_D increase so that small scale yielding no longer holds, in which case they theorise that the shape of the crack tip will depend on the strain energy density function

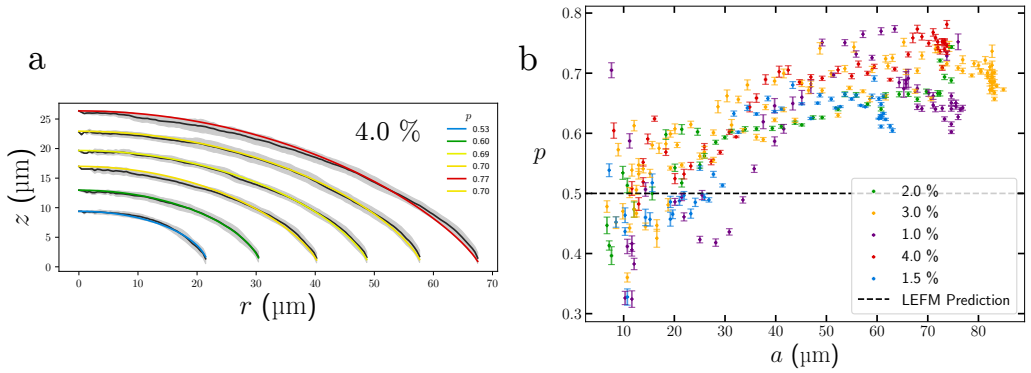

Figure 5.10 *The super-ellipse power of growing colonies. (a) Colony profiles are fit with super ellipses of minor and major axis b and a respectively, p is the only free parameter. Super-ellipses with powers between roughly* 0.5 *and* 0.75 *describe the observed colony profiles well. (b) The dependence of p on the size of the colonies is plotted for the colonies shown in Figure 5.9. p trends from* ≈ 0.5 *at smaller a to* ≈ 0.75 *at larger a, though the scatter in the fitted p is larger than the error bars would suggest. Unlike* ρ *and the aspect ratio, the p vs a plot does not collapse when scaled by* ℓ_{EF}*.*

of the material. Further to this point, Long et al. have computed that for materials with an exponentially stiffening strain energy density function, a cusp like shape should be observed at the tip of a notch crack [145]. Agarose has been shown to exponentially strain stiffen [86, 146], therefore similar analysis to [145] might well reveal that more cusp like hydraulic fractures should be expected in strain hardening materials. Of course this somewhat contradicts what is observed in Figure 5.9 and 5.10a,b where the smallest colonies are best describe by LEFM. This contradiction may be resolved when I look at the small scale fracture transition in Section 5.4.

The lenticular shape of the colonies explains why the crack tip radius of curvature appears to agree with the simple model whilst the scaling of the aspect ratio (b with a) does not. Equation 5.6 (constant ρ) is derived from Equation 5.7 (the scaling of the aspect ratio) given that $\rho = b^2/a$, if the colony morphology agrees with Equation 5.6 but not 5.7 there is an inconsistency. This inconsistency is resolved when one considers that even though the colony aspect ratio does not scale like $b \propto \sqrt{a}$, the lenticular shape of the colony might keep the crack tip radius of curvature constant. However, this raises the question of what physics is giving rise to the constant crack tip radius of curvature if the colony is not ellipsoidal. A clue for the origin of constant ρ can be found by observing the displacements around the colonies in more detail.

5.3.4 Displacement fields near to a colony.

Finally the displacement of the gel around the colony can be compared to the model's predictions. Given the approximate rotational symmetry of the colony, the displacement field can be defined in cylindrical coordinates. Measured displacements, Figure 5.11a, are first split into two sets of measurements, one above the fracture plane and the other below[19]. These fields are interpolated separately according to the method described in Section 4.6.5 and then, by taking an azimuthal average of the data about the colony's center of mass and minor axis, displacements can be compared to equations 5.9 and 5.10.

Looking at displacements along the smallest principle axis (z-axis, Figure 5.11b) of the colony, figures 5.11c-f plot the measured and predicted[20] displacements, u_z, parallel to the z axis (minor axis of the colony) at $r = 0$ for an incompressible gel ($\nu = 0.5$) over a range of agarose concentrations and colony sizes. Plots are coloured by the corresponding minor axis length, b. It is immediately clear that the measured displacements are much smaller in magnitude than the model's prediction. For higher agarose concentrations the discrepancy between measurements and predictions decreases but is still large. For small b, figures 5.11d-f show that no displacement was measured near to the colony, despite the colony having finite width.

Looking at the decay of the displacement fields away from the colonies, Figure 5.12 plots displacements as a function of distance on a log scale. Predicted displacements (dashed lines) are plotted concurrently with measured displacements (solid lines). Displacements predicted for several earlier, smaller, colonies are also plotted (grey lines). Far from the colonies and at larger colony sizes, the scaling of the decay is similar to that predicted by the linear elasticity (the model). The observed displacements appear to be similar to those that would be predicted around far smaller colonies.

Displacements across the azimuthally averaged field surrounding the colonies are plotted in Figure 5.13 and 5.14, along with the corresponding displacement fields predicted by the model. The measured and predicted colony surfaces are superimposed on the fields. Again measured displacements are clearly far smaller in both $\hat{\mathbf{r}}$ and $\hat{\mathbf{z}}$ directions and extend less far into the material.

[19]The displacement field is split in two to avoid the discontinuous change in displacement direction that occurs across the crack plane.

[20]The integral 5.9 was numerically evaluated using the Scipy module for Python.

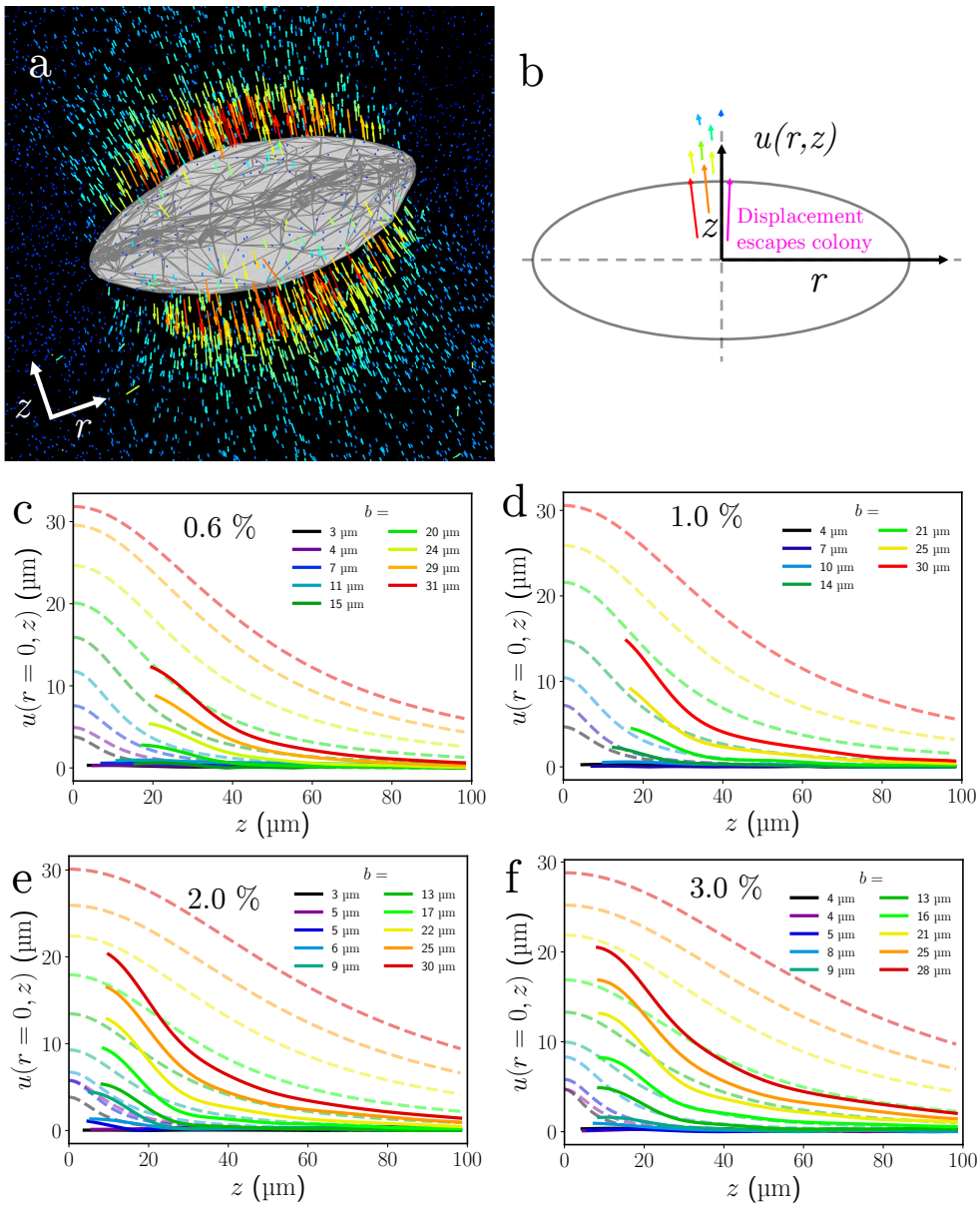

Figure 5.11 *Comparison of measured and predicted Eulerian displacement in the $\hat{z}$-direction along the $\hat{z}$-axis. (a) Raw displacement field around a colony grown in 2 % agarose, Lagrangian displacements are shown. (b) Schematic of the cross section of a colony, the z and r-axis are parallel with the colony's minor and major axis respectively. Displacements are interpolated along the $r = 0$ line from scattered measurements (see Section 4.6.5). (c-f) Displacements parallel to the minor axis of the colony are plotted as a function of distance from the colony center of mass along the minor axis for colonies of various sizes in four different agarose concentrations. The solid lines are the interpolated displacements whilst the dashed lines show the displacements predicted by the model. Interpolated displacements are much smaller in magnitude and are shorter range than the predicted displacements. For higher agarose concentrations the discrepancy between measurements and predictions is smaller but still large.*

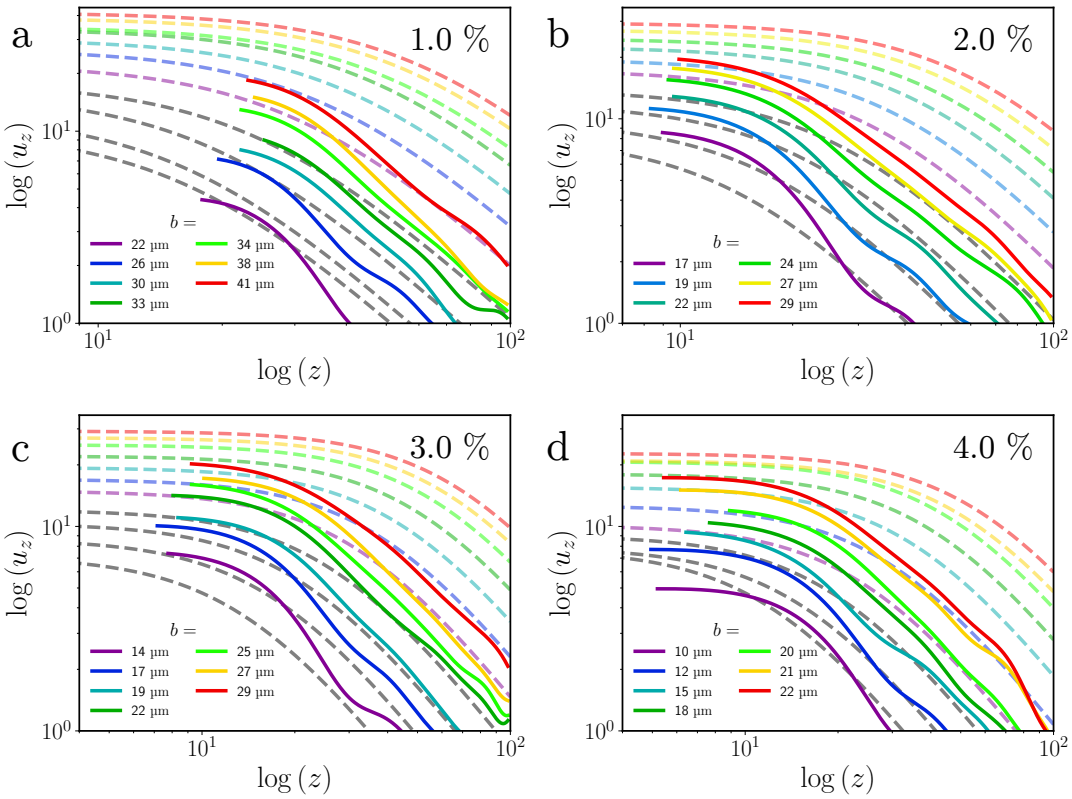

Figure 5.12 *Decay of displacements in the gel surrounding the colony. (a-d) Displacements parallel to the minor axis of the colony are plotted on a log scale as a function of distance from the colony center of mass along each colonies minor axis (solid lines). The predicted displacements (dashed lines) are also plotted with predictions made using the same values of b and a in matching colours. Predicted displacements for colonies at several earlier time points are plotted in grey without the corresponding observed values. Far from the colonies and for larger colony sizes, the power of the displacement decay is similar to that predicted by linear elasticity. The observed displacements are similar to those that would be predicted around far smaller colonies.*

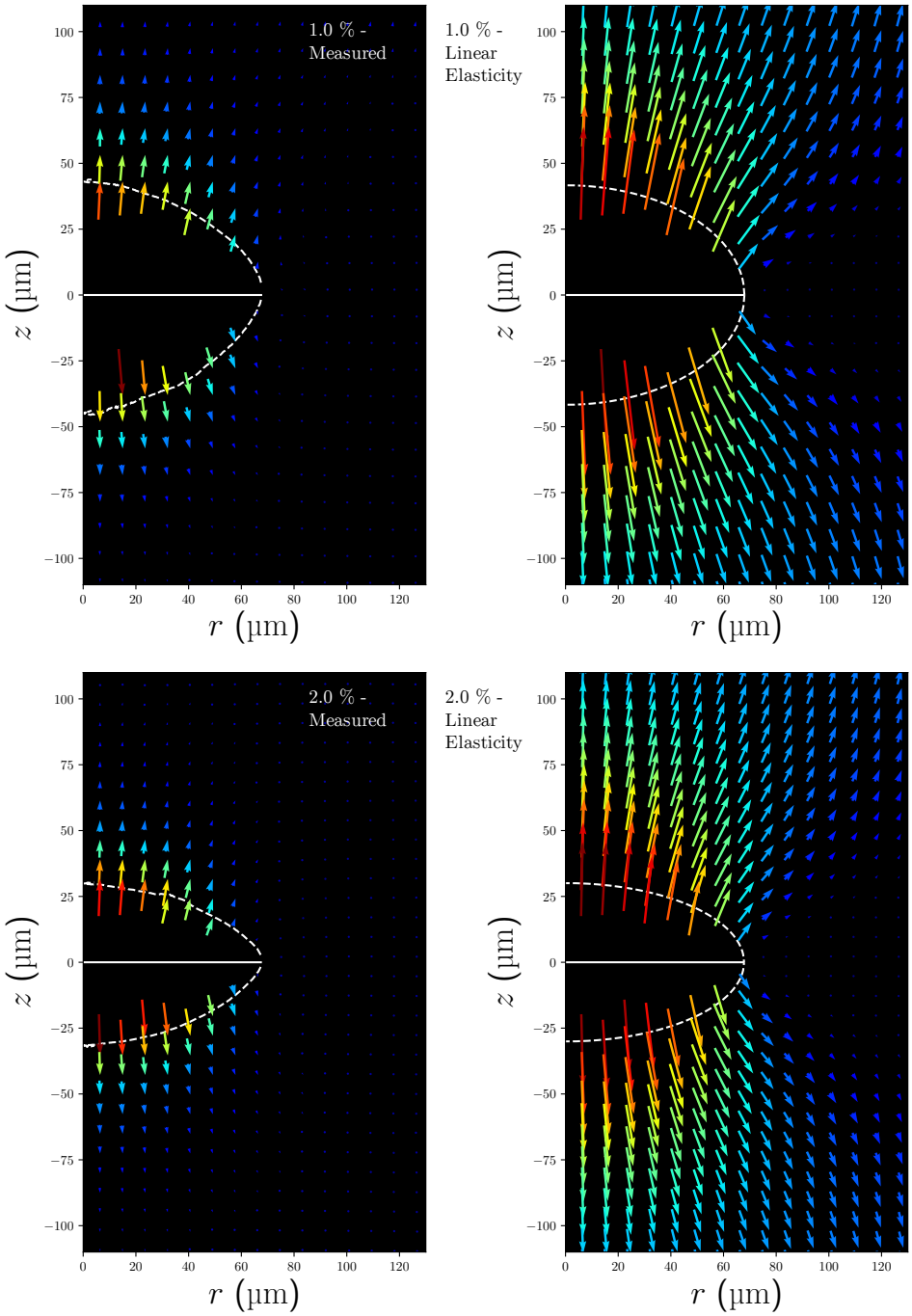

Figure 5.13 *Measured (left) and predicted (right) Eulerian displacement fields around disk shaped cracks, in 1 % and 2% agarose, of length* $\approx 70\,\mu\text{m}$ *and with displacement* $U_z(0,0) = b$*, where* b *is the measured minor axis of the colony. The Poisson ratio* $\nu = 0.5$*. Vector colour denotes their magnitude. Measured displacements are significantly less than would be predicted from a disk shaped crack in a linear elastic material.*

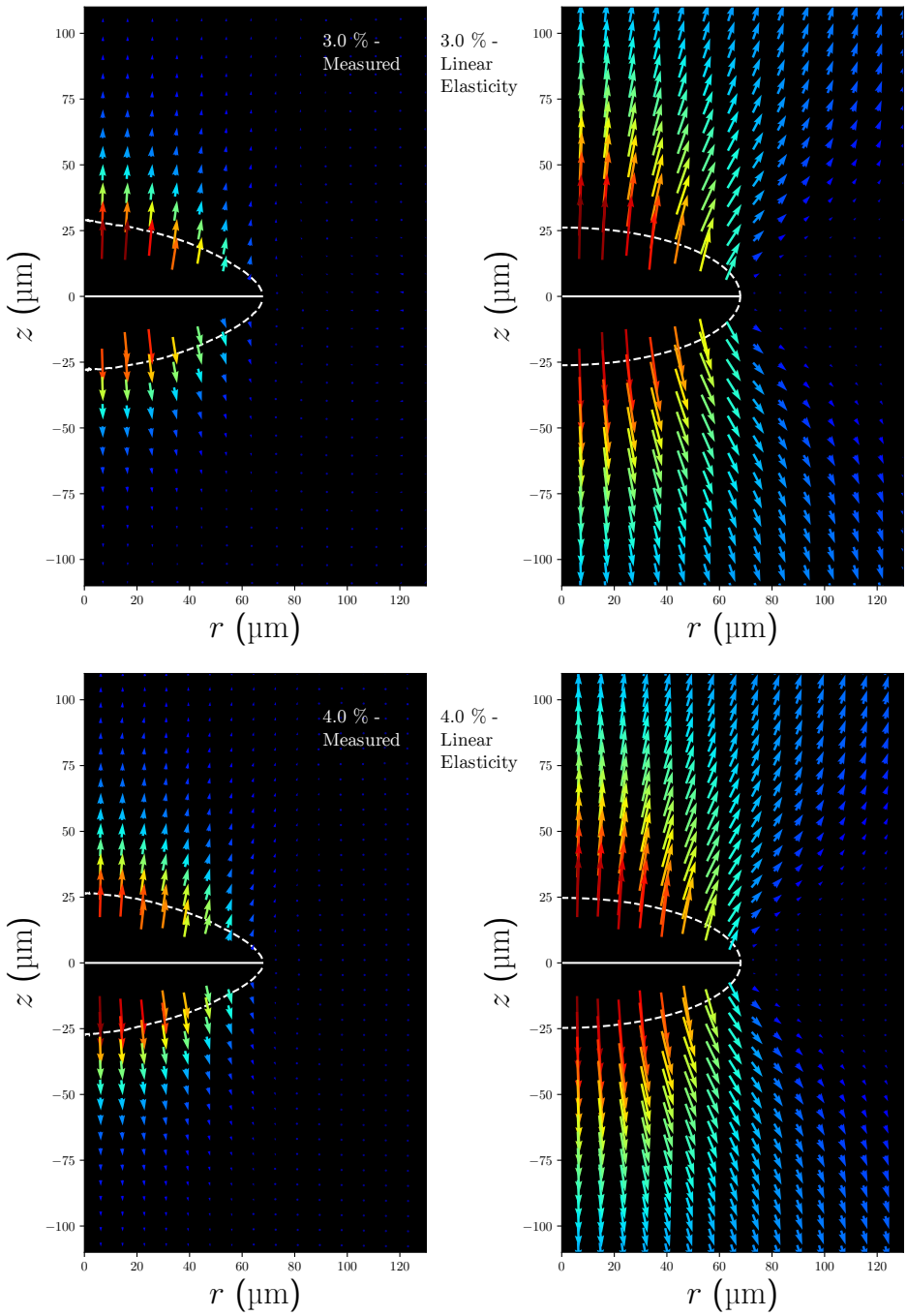

Figure 5.14 *Measured (left) and predicted (right) Eulerian displacement fields around disk shaped cracks, in 3 % and 4% agarose, of length* $\approx 70\,\mu\text{m}$ *and with displacement* $U_z(0,0) = b$*, where* b *is the measured minor axis of the colony. The Poisson ratio* $\nu = 0.5$*. Vector colour denotes their magnitude. Measured displacements are significantly less than would be predicted from a disk shaped crack in a linear elastic material.*

An interesting feature of the data is revealed in figures 5.11c-f: the material at some z positions is insufficiently displaced to move beyond the surface of the colony. In other words, some material near to the original position of the colony ends up inside or compressed onto the surface of the colony. This feature is evidenced by the fact that the first interpolated displacement (the start of the solid lines in figures 5.11c-f), corresponding to the first position, z', that was displaced sufficiently to move beyond the colony surface, does not lie at $z = 0$. The gap in measurements prior to the first point corresponds to positions that did not have sufficient displacement to escape the colony.

Two possible explanations of this observation present themselves, either the material at $z < z'$ has been engulfed by the colony, or that material has been compressed onto the surface of the colony. Given that the agarose gel consisted of 96-99 % M9 media (which is mostly water) it is plausible for the network to have been dramatically compressed by expelling water from the network.

The effect of increased compressibility can be explored by altering the Poisson ratio, ν, in equations 5.9 and 5.10. Increasing the compressibility of the gel (decreasing ν) results in predicted displacements that decay faster close to the colony surface, Figure 5.15a. However predicted z displacements are still greater than double the observed values even when $\nu = 0$. Therefore the compressibility of the gel is not enough to explain the discrepancy between the model's prediction and the observed displacements.

The compressibility of the gel also cannot account for the colony's deviation from the predicted ellipsoidal shape of the colonies described in the previous section. Figure 5.15b shows the predicted profile of a crack in a linear elastic material of varying ν, the profile is ellipsoidal for all values of ν. The reduction of a with respect to b with increasing compressibility has no effect on the scaling of b with a (it only changes the coefficient) and so cannot explain the discrepancy described in Section 5.3.2.

Increased compressibility (decreasing ν) results in displacement fields that are more aligned with the z-axis (having smaller $\hat{\mathbf{r}}$ components), Figure 5.15c-e. By visual comparison to fields calculated with varying ν the measured fields look most like those where $\nu \approx 0.3$. Increased compressibility should result in displacement in the negative $\hat{\mathbf{r}}$ direction along the $z = 0$ line. This -ve $\hat{\mathbf{r}}$ displacement was observed in most of the measured displacement fields, however its magnitude is very small, so that displacements appear as dots in Figure 5.13 and 5.14.

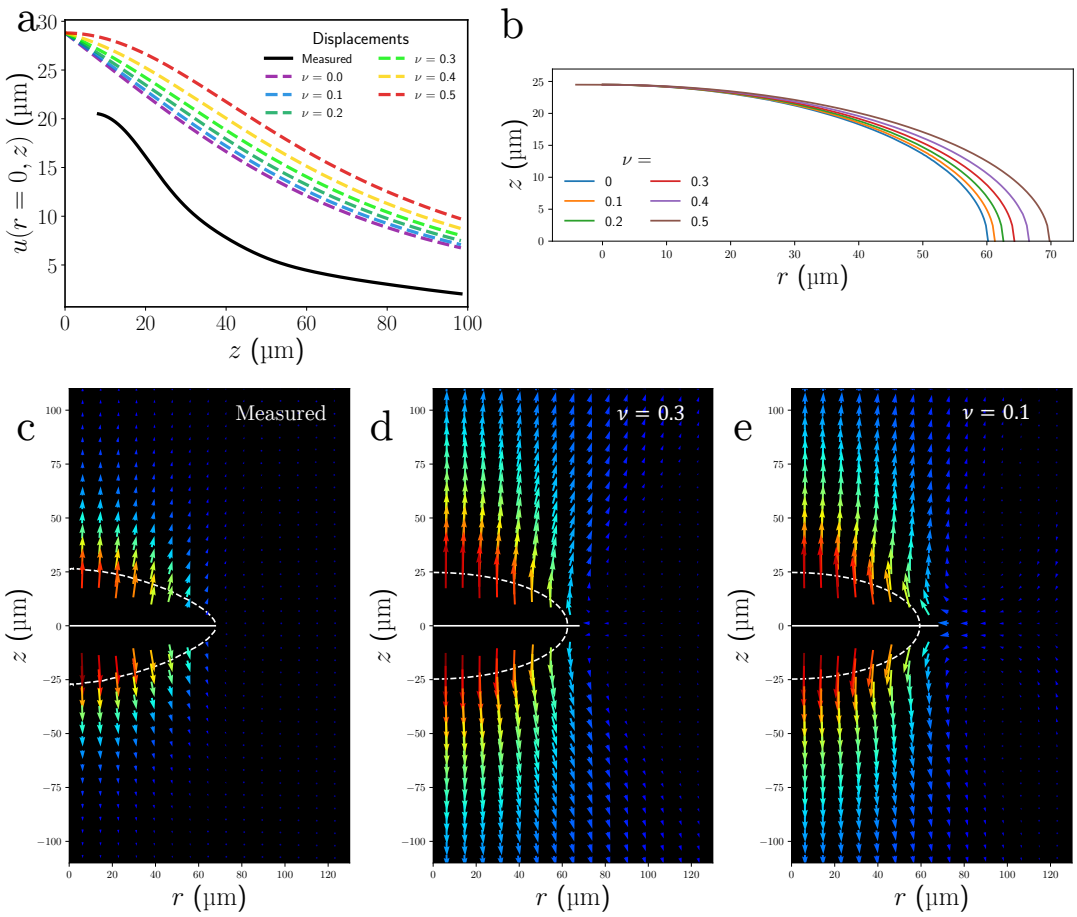

Figure 5.15 *The effects of gel compressibility on the displacement field. (a) The radial components of the displacement field are smaller relative to the axial components which is similar to the measured field. The magnitude of the displacements decreases more rapidly in the compressible gels, d. However the decrease in $u_z(z)$ is not enough to explain the measured displacements. (b) Increased compressibility cannot explain the superellipsoidal shape of the colonies. (c) The displacement field measured around a colony grown in 4 % agarose. (d,e) The predicted displacement field for compressible gels with $\nu = 0.3$ and $\nu = 0.1$. As the gel becomes more compressible the inwards displacement at the apex of the colony becomes larger.*

5.3.5 Summary of discrepancies from the simple model

Overall I have found significant differences between the observed morphology and that predicted by my simple model. For each of the characteristics measured observations are similar to the model's predictions, however in detail they differ significantly. For example, whilst the crack tip radius of curvature appears to agree with the model's predictions, the colony profile is not ellipsoidal, so this congruency between observation and model cannot be a result of the physics present in the model. Likewise, whilst displacement fields far from the colony decay with the same power law relationship predicted by the model, the magnitude of these displacements is far lower than expected. Indeed close to the colony gel displacements are not even sufficient for that material to escape the colony surface.

That the model's predictions deviate significantly from observations is unsurprising. The model assumes that all deformations around the growing crack are linear elastic, which cannot be the case. For the agarose to reach stresses at which it will fracture it must, by definition, reach stresses where it behaves inelastically and become damaged. For the observed morphology to have resembled the model's predictions, the region in which the material reaches stresses sufficient to inelastically deform the gel would have had to be small compared to the size of the colony. From Section 3.3 we can estimate the length scale over which stresses should be sufficient to cause damage to the agarose, this is the cohesive zone size or Dugdale length scale,

$$\ell_D = \frac{\Gamma E}{\sigma_c^2}, \tag{5.15}$$

where σ_c is the cohesive stress of the agarose. From macroscopic experiments a lower bound on σ_c has been measured in [89] to be $\approx 0.4E$ so that the upper bound on ℓ_D is $6\Gamma/E$. For a 2 % agarose gel ℓ_D is at most 30 µm, which is similar to the size of the colony itself.

How then should the colony grow when it is smaller than ℓ_D? What effect should growing at small scales have on the morphology of the colony? To answer these question I will consider deviations from my simple model in the light of more recent theories of fracture at small scales.

5.4 Growth and fracture at small scales

In Sections 3.4 and 3.5 I discussed crack tip blunting, specifically the idea that when a crack is smaller than $\approx \ell_{\mathrm{EF}}$ $(= \Gamma/E)$ or $\approx \Gamma/\sigma_c$ the radius of curvature at the crack tip increases with applied stress in lieu of the stress concentrating at some crack tip. This "blunting" effect results in the crack being in a state of hydrostatic tension. Hydrostatic tension leads to cavitation, i.e. where the crack expands with no preferred direction either by elastic deformation or by breakage of bonds distributed over the entire surface of the crack (called distributed damage). When the crack undergoes cavitation it expands at a pressure directly proportional to the stiffness of the gel. The exact pressure is some function of the strain energy density function of the material but in general is of the order:

$$P_c \sim E. \tag{5.16}$$

This cavitation pressure has no dependence on the size of the cavity. On the other hand, the pressure required to propagate a disk shaped crack is inversely proportional to the size of the crack, i.e.

$$P_f \sim \sqrt{\frac{\Gamma E}{a}}. \tag{5.17}$$

Therefore below some crack length a_t, given by

$$a_t \approx \frac{\Gamma}{E} = \ell_{\mathrm{EF}}, \tag{5.18}$$

the pressure required to propagate the crack via cavitation will be less than that required for a disk shaped fracture. If a crack starts smaller than a_t, then it should begin to grow via cavitation before transitioning to growth in a disk shape along a single plane when it reaches a size equal to a_t. If we assume that the initial crack size in the agarose is the size of a single *E. coli* bacterium (which is smaller than ℓ_{EF} for the agarose concentrations used in this work) then colonies should also induce this transition in fracture propagation mode in the surrounding gel.

This section looks at evidence for growing colonies inducing a cavitation to disk-shaped crack transition in the surrounding gel. I also attempt to show that this transition accounts for most of discrepancies between the observed morphology and the predictions of the simple model.

5.4.1 The absence of early deformations can be explained by distributed damage

Immediately the two proposed methods of cavitation (elastic cavitation and cavitation by distributed damage) can be distinguished by the deformations that they should create in the gel surrounding the growing colony. If the cavity were to expand via elastic deformation then these deformations should be observed around the colony from the start of growth. No deformations were observed early on in colony growth[21], Figure 5.16, therefore elastic cavitation can be ruled out (at least at scales $\gtrsim$1 µm[22]).

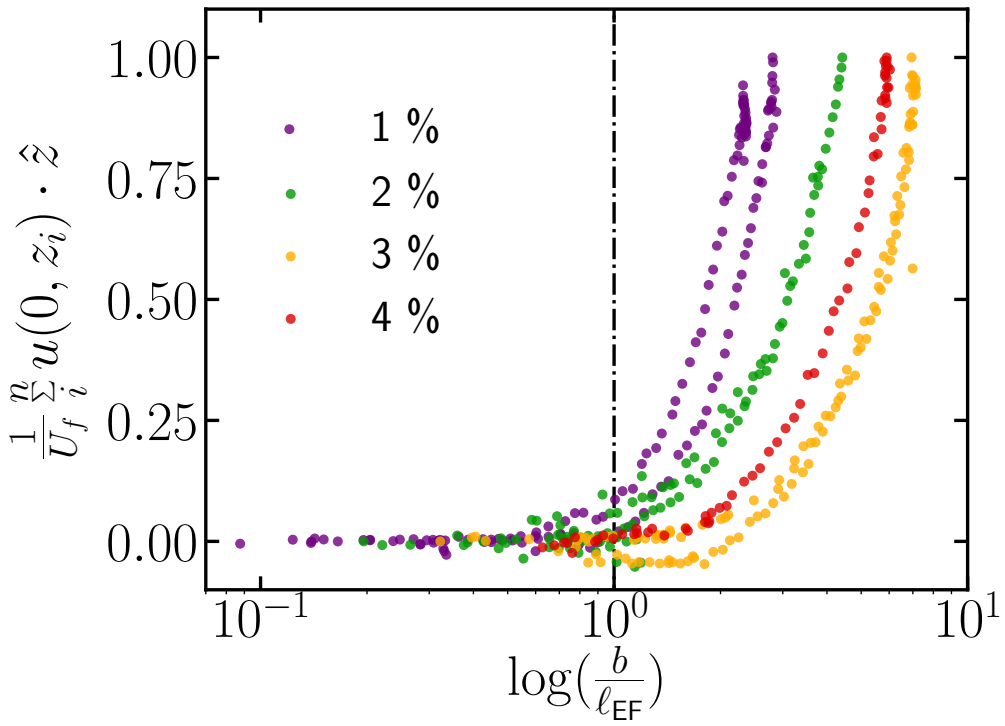

Figure 5.16 *Displacements parallel to the minor axis of the colony at n positions, z_i, are summed and plotted against the colony minor axis length b. Summed displacements are normalised by the sum of displacements at the final time point U_f. The minor axis length is scaled by the elasto-fracture length scale ℓ_{EF}. Prior to $\approx b/\ell_{EF}$, no displacement was observed in the gel.*

[21]Figures 5.11d-f also show no displacement near to the colony despite the colony having finite width.

[22]Any elastic deformation should occur at a size around the order of the agarose chain length multiplied by the critical stretch of that chain. If the critical stretch is of order 1 and the chain length is of the same order as the pore size then elastic deformations might be expected on the $\sim$ 100 nm scale.

Distributed damage can explain the lack of deformations observed early on in colony growth. Under the distributed damage model the crack is stretched as the colony grows. Due to blunting, the radius of curvature at the crack tip increases instead of stress concentrating around the crack tip. Eventually the elastic limit of the bonds at the surface of the crack is reached and a bond breaking event will occur. Bacteria move into the volume opened up by the bond breakage but, importantly, the stress will not concentrate around the region of bond breakage. Therefore the location of the next bond break is equally likely to occur anywhere over the crack surface. A colony growing in this fashion will not deform the gel beyond the length scale of the agarose chains that are breaking ($\sim$ 100's nm).

Distributed damage might also explain the period of dendritic growth that was observed early on in colony formation, Figure 5.2. That there is no preferred direction for crack propagation, along with the fact that the interfacial energy at the *E. coli*-agarose boundary has to be $\leq 0\,\mathrm{J\,m^{-2}}$ (*E. coli* swim when in planktonic cultures, see Section 6.4.4), means that the colony is free to expand in any direction with equal probability whilst not being forced into a spherical shape by surface tension[23], these factors will mean that the dominant force in the system is that driving the binary fission of the *E. coli*. Colonies grown on the surface of agarose, where binary fission is also the main driving force behind colony morphology, have been observed to form extremely rough colonies early in their growth [33, 147], dendritic growth might simply be the 3D extension of this binary fission driven phenomena.

5.4.2 Cavitation via distributed damage can explain the transition size of the colony

If the colony does initially grow via cavitation then we should expect to observe a transition in growth mode, from spherically symmetric at small scales to disk like at larger scales. The transition size should scale with the material parameter ℓ_{EF}. This transition is readily visualised by plotting the radius of curvature at the apex of the colony, ρ, against the scaled size of the colony given by it's major or minor axis, a or b respectively, figures 5.17a,b. Prior to $b/\ell_{\mathrm{EF}} \approx 1$ the colonies grow in a self-similar fashion, i.e. ρ is directly proportional to a or b. When a or $b \approx \ell_{\mathrm{EF}}$ the radius of curvature begins to plateau or at least change in it's

[23] i.e. if *E. coli* were hydrophobic then the surface energy would be minimized by a spherical shape.

scaling with the size of the colony. This transition corresponds to the onset of a single fracture plane forming and the start of elastic deformations being observed around the colony, Figure 5.16. The transition from self similar or spherically symmetric growth can also be seen in Figure 5.8b for smaller colonies in lower concentration.

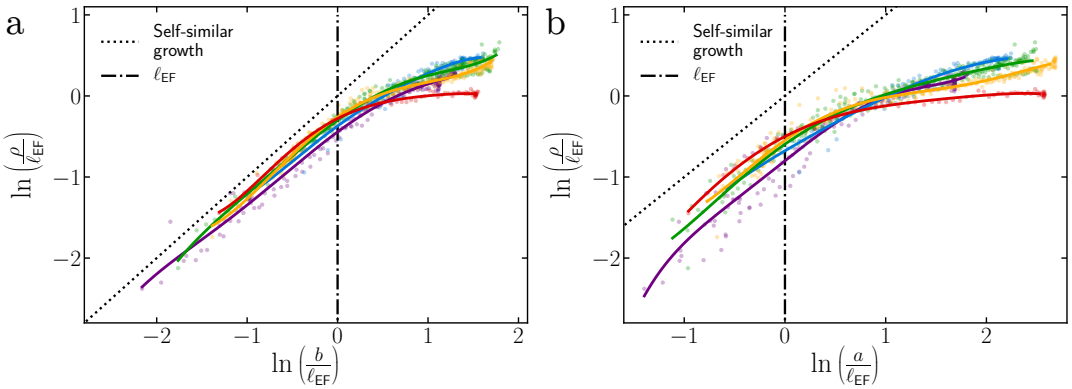

Figure 5.17 *The transition in growth mode can be visualised by the change in scaling of colony dimensions. Measurements are shown by transparent circles whilst splines are fit to highlight the trend. (a) ρ is plotted against b where both have been scaled by ℓ_{EF}. Where $b \lesssim \ell_{EF}$, self-similar growth occurs. This is indicative of distributed damage [148] (b) The same transition can be seen when plotting a against ρ.*

The transition in growth mode appears to occur at colony sizes between 1.5 and $2\ell_{\mathrm{EF}}$. This is interesting because it is closer to the transition size, a_t, that would be predicted from purely elastic cavitation growth ($\approx 1.5\ell_{\mathrm{EF}}$) rather than that which would be predicted for a cavity growing via distributed damage ($\approx 10\ell_{\mathrm{EF}}$), see Section 3.5.

5.4.3 Distributed damage may explain crack tip curvature.

The simple model discussed in the previous section predicted that the crack tip radius of curvature, ρ, should be constant and this prediction was observed in experiments when $a > \ell_{\mathrm{EF}}$. In the model constant ρ was a result of the colony having an ellipsoidal shape, yet in Section 5.3.3 I showed that the colonies were not ellipsoidal, so the physics behind the model's prediction and the observed colony shape could not be the same. Looking at the evolution of the region where distributed damage occurs provides an alternate explanation for constant ρ when a or $b \gtrsim \ell_{\mathrm{EF}}$.

Figures 5.18a-h visualises the damaged region of gel by overlaying the Eulerian displacements (black arrows) that end just outside the colony surface on top of the outline of the colony (orange). Regions where the gel has been insufficiently displaced to escape the colony surface are therefore contained within the convex hull made by the origins of the plotted displacements (grey zone), these regions must have been damaged to end up inside (or crushed onto the surface of) the colony. Looking at the evolution of this damaged region, we see that when $b \lesssim \ell_{\mathrm{EF}}$ there is a period where the damaged region spans the entire colony and I suspect the colony is growing via distributed damage (figure 5.18a). The damaged region then grows with the colony, forming a disk with fixed width approximately equal to the width of the colony prior to the build up of elastic deformations (figures 5.18b-h) as shown by the purple bars which denote $3\ell_{\mathrm{EF}}$. This observation does not fit with the idea that there is a distinct transition between distributed damage and the propagation of a disk shaped crack along a plane, Figure 5.18i. It appears that it is the propagation of this fixed width($\approx \ell_{\mathrm{EF}}$) damaged zone that determines the radius of curvature at the crack tip (rather than the physics outlined in the simple model).

The thick disk shape of the damaged region explains the observation first made in Figure 5.12, that the displacements around the colony appear to be similar to those that would be predicted around a much smaller colony. Because the gel is damaged rather than elastically deformed close to the fracture plane, the observed displacements are similar to those that would result from a colony of lesser width. The thick damage disk will also complicate the morphology resulting from the elastic pressurisation of that disk. This may explain why the colonies have a lenticular shape rather than the ellipsoids predicted by the simple model.

The same period of distributed damage followed by the extension of the damaged region into a thick disk shape was observed in all concentrations of agarose tested, Figure 5.19. At lower concentrations of agarose (0.6 % and 1 %) the formation of the damage disk was not as clear, however this was likely because the colonies did not grow much larger than ℓ_{EF}. Again the disk appears to propagate with a fixed width of $\approx 3\ell_{\mathrm{EF}}$, which is approximately the width of the colony when the transition between distributed damage and disk shaped fracture occurs.

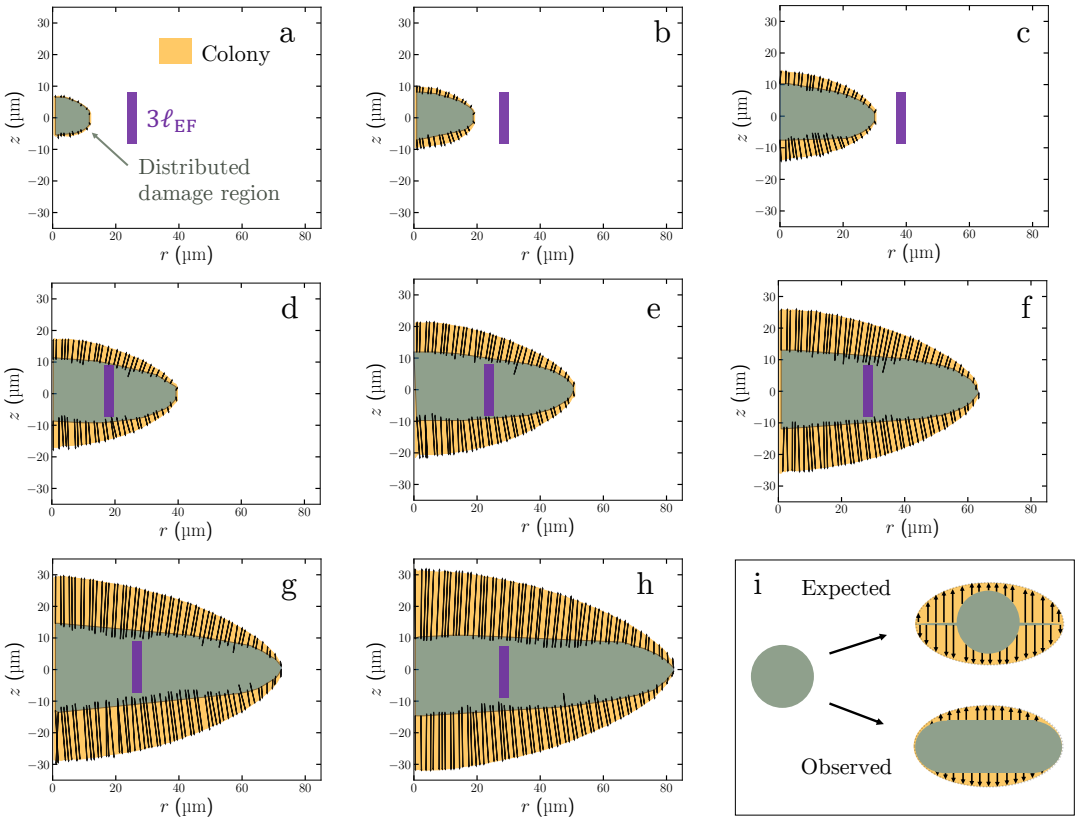

Figure 5.18 *The damaged zone within the agarose gel can be visualized by plotting interpolated displacements that end just outside the colony surface. (a-h) Plotting these displacements (black arrows) against the cross section of a colony grown in 3 % agarose (orange shaded zone), a region which was not displaced beyond the colony surface is revealed (grey zone). Inside this region the gel is suspected to have been damaged, with bond breaking events occurring over the entire surface of the crack rather than at being localised to the apex. (i) The naive expectation from the outline at the start of this section was that the transition in fracture mode should result in the creation of a thin disk shaped crack emanating from a region of distributed damage. Instead, a thick disk of damage is observed.*

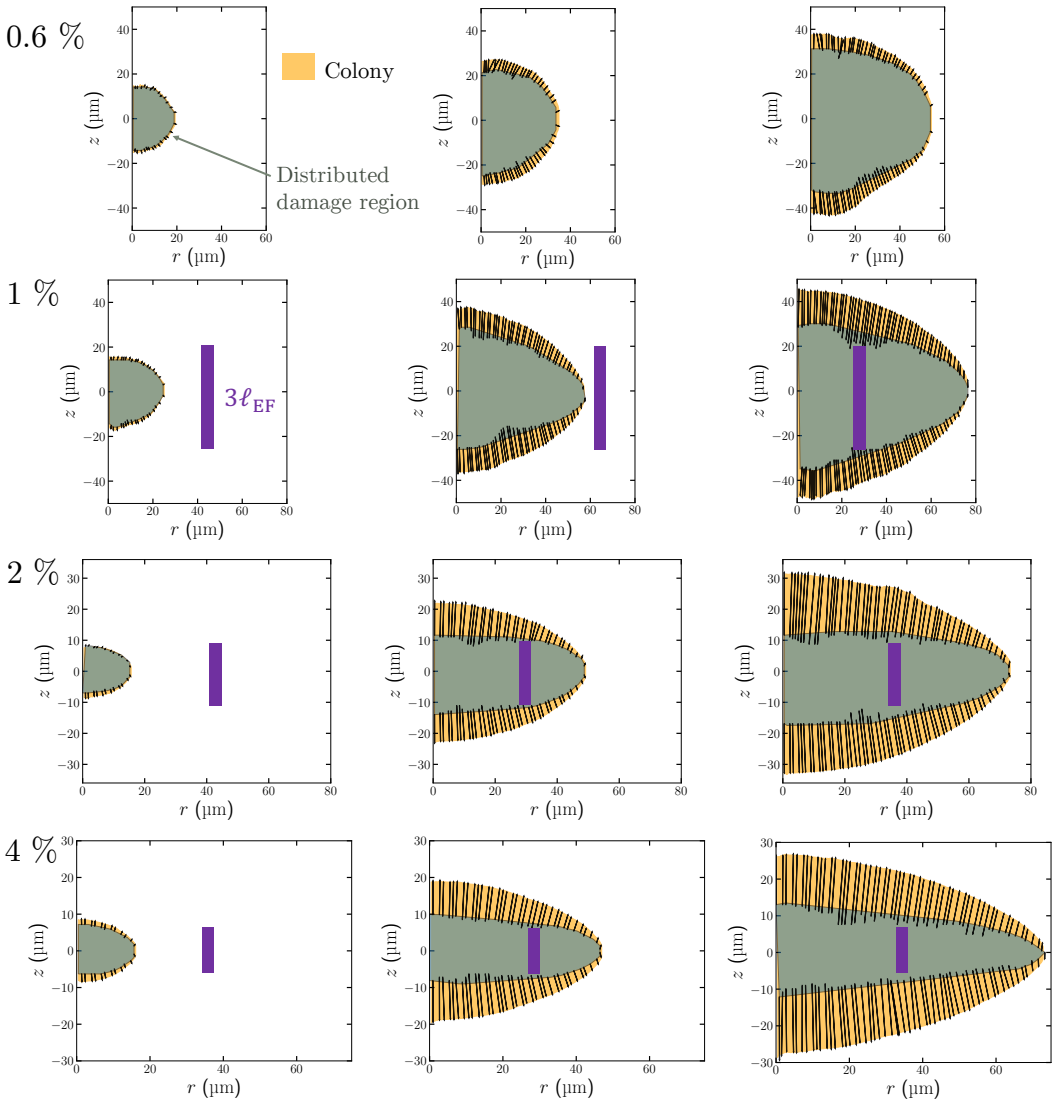

Figure 5.19 *In the same way as Figure 5.18, the damaged zone within the agarose gel can be visualized by plotting interpolated displacements that end just outside the colony surface. These displacements (black arrows) are plotted on top of cross sections of colonies (orange shaded zone) grown in agarose concentration between 0.6% and 4%. In each concentration there is a period in which the colony grows without elastic deformation of the surrounding gel, the volume of gel that the colony expands into is presumably damaged. Then when the colony size is $\gtrsim \ell_{EF}$ the colony begins to elastically deform the gel and the damaged zone extends into a thick disk (grey zone). The size at which this transition begin scales with ℓ_{EF}, Figure 5.17.*

5.5 Conclusions

The origin of the lenticular morphology of submerged colonies was shown to be the result of bacteria fracturing the surrounding gel. This fracture process was imaged in 3D for the first time using single plane illumination microscopy. The inoculation method was shown to have only a minor influence on the propagation direction of the fracture.

I have shown that simple linear elastic fracture mechanics cannot explain colony morphology. Instead, early colony morphology is a result of *E. coli* breaking the surrounding gel by distributed damage over the entire surface of the crack which they inhabit. This distributed damage growth mode was predicted by cavitation theory and can also explain the dendritic structures that were observed early in colony formation. Cavitation predicts that the pressure required to propagate a crack by distributed damage should be independent of crack size when the crack is small. Therefore a transition in fracture mode was predicted when the colony grew larger than $\sim \ell_{\mathrm{EF}}$. This transition was observed to occur when the colony's minor axis exceeded $\approx 1.5\ell_{\mathrm{EF}}$. To my knowledge this is the first direct measurement of transition between cavitation and planar fracture growth modes.

That submerged bacteria might first fracture the material around them at a pressure that is both independent of the initial crack size and fracture energy of the gel has important implications for colony growth in tough materials. Where previously one might naively expect contaminant bacteria to have to overcome extremely high pressures due to the propagation pressure scaling with $1/\sqrt{a}$ (Equation 3.57) now I have reason to believe that the bacteria need only overcome a pressure that is smaller by a factor of $\sqrt{\Gamma/aE}$. Whilst for the agarose used in these experiments[24] this factor is only of the order 3, for tougher gels distributed damage might decrease the pressure required for fracture by one or two orders of magnitude. For example a colony grown in gelatin (which has a higher Γ than the agarose used in my experiments) would grow at appropriately 1 % of the naive pressure prediction [149, 150].

At larger sizes the colonies began to more closely resemble the morphology predicted by the simple model. This would suggest that the conglomerate nature of the colonies (being made up of many individual cells) is unimportant for the colony morphology. In many ways this is an unexpected result, as each cell in the

[24] using the length of a single *E. coli* bacterium for a

colony acts as a "pusher", creating a force dipole by the action of binary fission so that a uniform pressure distribution might be unexpected. Indeed collective motion similar to that observed in 2D could be expected [35]. Though the early dendritic growth may well be the result of there being a modest number of cells in the colony, so that the exerted forces do not average out.

Comparison of colony morphology to hydraulic fracture morphology is a task beyond current theory due to the unknown effect of both the plastic deformations early on and possible non-linear stress-strain response of the agarose. Therefore in the next chapter I will attempt to create hydraulic fractures on the same length and time scales as the bacterial colonies so that any differences in their morphology can be discovered. Such a comparison may reveal more about how bacteria interact with the surrounding gel.

5.6 Future work

The experimental study presented in this chapter showed how bacteria could be used as a novel probe of fracture mechanics. Moving forward I see two main avenues for further development of this idea.

First, colonies should be grown in gels with a wider range of fracture properties. One of my aims was to be able to distinguish between ductile and blunted fracture, however the length scales at which each of these processes occur ($\ell_D \approx \Gamma E/\sigma_c^2$ and $\ell_{\mathrm{EF}} \approx \Gamma/E$ respectively) are very similar in agarose as $\sigma_c \sim E$ (see Section 3.6), which meant that I could not determine whether the transition in fracture mode was due to blunting or not. By using a tougher gel, such as gelatin [151] or other types of agarose [150], ℓ_{EF} could be made significantly larger than ℓ_D, so that the transition to planar fracture could be more clearly shown to scale with ℓ_{EF} (rather than ℓ_D). If a sufficiently tough gel could be inoculated then it's fracture properties could be used to measure the maximum growth pressure of agarose using a system similar to [152].

Another option that could allow me to distinguish between blunted and ductile fracture would be to try to control the cohesive stress of the material. This could perhaps be done using a dense colloidal suspension with controlled surface properties, in this way σ_c could be tuned.

The second avenue for development would be to better utilize the measured

displacement fields. The J-integral [68, 153, 154] is a method of calculating Γ using the stress and strain field around a crack tip. When small scale yielding (SSY) is valid this integral is independent of the path taken around the crack tip and can be used to measure the fracture energy. However when SSY is invalid, not much is known about how the J-integral should be affected, therefore the measurements made in this work could provide an opportunity for discovery.

Chapter 6

The Morphology of Nanolitre Hydraulic Fractures

6.1 Introduction

In the previous chapter I presented a study on the morphology of bacterial colonies grown submerged in agarose gels. It was seen that their morphology was a result of the bacteria fracturing the gel around them. However, a simple model using linear elastic fracture mechanics (LEFM) failed to accurately describe the morphology of this fracture. Ideas of cavitation and distributed damage were employed in an attempt to explain the deviation of colony morphology from that simple model. Whilst these ideas could explain the transition in fracture mode observed around the colonies, they are not yet developed enough to give a full prediction of the shape of a fracture growing at this intermediate length scale where distributed damage gives way to planar fracture.

Without a quantitative theory for the morphology of intermediate scale fractures, the question of whether the morphology of bacterial colonies is governed by the same physics as a hydraulic fracture propagated by a Newtonian fluid remains. The impact of biology (active motion, chemical interaction with the gel etc.) on colony morphology remains unknown and prevents the wholesale use of fracture mechanics theories in predicting the conditions under which submerged bacteria might grow.

To solve this problem I now attempt to inflate oil bubbles at the same length

and time scales as the bacterial colonies grow on, in an attempt to physically model the colonies. By doing so, I can determine whether the morphology of *E. coli* colonies submerged in agarose is governed by the same physics as a hydraulic fracture or whether deviations from LEFM are due to some unknown interaction between the bacteria and agarose.

Creating hydraulic fractures at small scales is interesting in its own right. In the last decade the cavitation rheology technique (developed in large part by the Crosby research group) [79, 81, 155–157] has sought to extract the mechanical properties of soft materials through pressure-monitored fluid injection. Using the theory detailed in Section 3.5, the cavitation pressure can be used to infer the elastic modulus of a material if its strain energy density function is known. So far cavitation studies have mostly looked only at the instantaneous cavitation pressure, that is the pressure at the point of cavitation. This is because the medium used to increase the pressure is usually air, which expands rapidly and prevents observation of the pressure during cavity growth. Some studies have looked at volume controlled expansion of cavities [158, 159], however in these cases the size of the capillary is comparable or larger than the elasto-fracture length scale, ℓ_{EF}. This means that the cavity can initially expand elastically and, when the maximum stretch of the material is reached, the cavity is much larger than ℓ_{EF}, thus fracture in a single plane occurs. For these reasons fracture pressure during the transition from small scale fracture to large scale fracture has gone unobserved. The secondary aim of this study was therefore to observe the pressure required to expand a hydraulic fracture at length scales below ℓ_{EF}, where a transition in fracture pressure should be observed (as described in Section 3.5.1).

The structure of this chapter as follows. First modifications to the experimental apparatus described in Chapter 4 are described. The single plane illumination microscopy set up is modified to enable observations of an oil bubble blown from the tip of a micron sized capillary. Methods for calculating the morphology of these oil droplets are detailed. Next attempts to measure the pressure both at bubble initiation and during the growth of the oil bubbles are described. The morphology of the oil bubbles are then compared to those of the bacterial colonies. It is shown that morphology of hydraulic fractures expanded with silicon oil are similar to those expanded with *E. coli* but with some key differences. I attempt to explain these differences using the differing interfacial energies between the *E. coli*-agarose and oil-agarose interfaces. Therefore the final section of the chapter

is dedicated to measuring the oil-agarose interfacial energy. These measurements allow me to estimate the *E. coli*-agarose interfacial energy.

6.2 Modification of the SPIM apparatus for imaging nanolitre hydraulic fractures.

In order to image micro-scale hydraulic fractures the SPIM apparatus described in Section 4.4 had to be modified. Instead of a growing colony, the tip of a capillary filled with oil had to be made to lie in the focal plane of the SPIM apparatus. Oil could then be injected from the tip of the capillary to form a hydraulic fracture. The rate at which oil was expressed was controlled by modulating the pressure of an oil reservoir connected to the capillary. To achieve this configuration, a syringe pump and pressure sensor were arranged in a pressure-stat setup which could be used to control the pressure of oil in a pulled glass capillary mounted in the 4D stage of the SPIM apparatus.

6.2.1 The pressurestat apparatus

Figure 6.1a-e, shows a schematic and photos of the pressurestat setup. A 50 µl gastight syringe[1] was attached to a liquid chromatography tee union[2]. One port of the tee union was connected via a short (≈7 cm) stretch of fluorinated ethylene propylene (FEP) tubing to a Honeywell absolute pressure sensor. The pressure sensor could measure up to 700 kPa with an accuracy of 0.25%. The other port of the tee union was attached to 50 cm of 1 mm inner diameter FEP tubing. That tubing was in turn attached to a pulled borosilicate capillary. The production of these capillaries will be detailed in Section 6.2.2. The union connections had to be made proof to a few atmospheres of pressure and not come undone when handled. To ensure this, the FEP tubing was sealed in the union pieces using hollow steel bolts. These squeezed the tubing between a ferrule and a length of borosilicate glass, creating a strong seal, Figure 6.1b. The tubing and syringe were filled with fluorescent silicone oil, see Section 6.2.3. When filling the system with oil, care was taken to push the oil through the system, rather than pulling

[1] model 1705 TLL, PTFE Luer lock.

[2] The syringe is connected to the tee via a 16 gauge Luer lock dispensing tip. The Valco tee union had a 16 gauge 0.75 mm bore size.

with a negative pressure gradient, ensuring that no air bubbles became trapped in the system. The gastight syringe was mounted in an AL-1000 programmable syringe pump which could be used to control the position of the syringe plunger and consequently the pressure of the oil in the FEP tubing.

The pressure sensor was connected to an Arduino Uno microcontroller board. The Arduino was then connected to the relevant pins of the transistor–transistor logic (TTL) I/O port of the syringe pump, see appendix B. The Arduino implemented a simple hysteresis control program, i.e. when the pressure sensor recorded a pressure, P, higher than the desired pressure, P_{stat}, (plus some tolerance, ΔP_0) the program took the following action:

1. Switch the syringe pump to withdraw mode.
2. Turn the syringe pump on.
3. Check whether the pump is moving in the correct direction, if not switch the pump off and repeat 1 and 2.
4. Monitor P, as recorded by the pressure sensor. When $P < P_{\text{stat}} + \Delta P_1$, where ΔP_1 is another tolerance ($\Delta P_1 < \Delta P_0$), turn the syringe pump off.

If $P < P_{\text{stat}} - \Delta P_0$ then similar steps would be taken with the syringe pump instead set to infuse mode and step 4 checking whether $P > P_{\text{stat}} - \Delta P_1$. Step 3 was important because the TTL inputs only check for a falling or rising edge in the input signal. In practice the pump missed this signal change about once every ten hours of operation, so it was necessary to check the direction and try switching again if necessary. A check to see whether P had exceeded a set maximum pressure was also implemented as a safety precaution.

To get a more precise P reading the reference voltage of the Arduino was altered. The pressure sensor outputs a voltage between 0.5 V and 4.5 V corresponding to 0 kPa and 689 kPa respectively. When the reference voltage of the Arduino was kept at the default of 5 V, analogue voltage readings between 0 V to 5 V are converted to digital values between 0 and 1023 (10 bit), the resulting precision was 4.9 mV per interval or 0.842 kPa per interval. By connecting a power pin on the Arduino board (the 3.3 V pin in this case) to the analog reference (AREF) pin via a resistor, the internal resistance of the AREF pin acts as a voltage divider allowing for a specific reference voltage to be chosen. Voltages between 0 V and the specified voltage are then converted to digital values between 0 and 1023. This

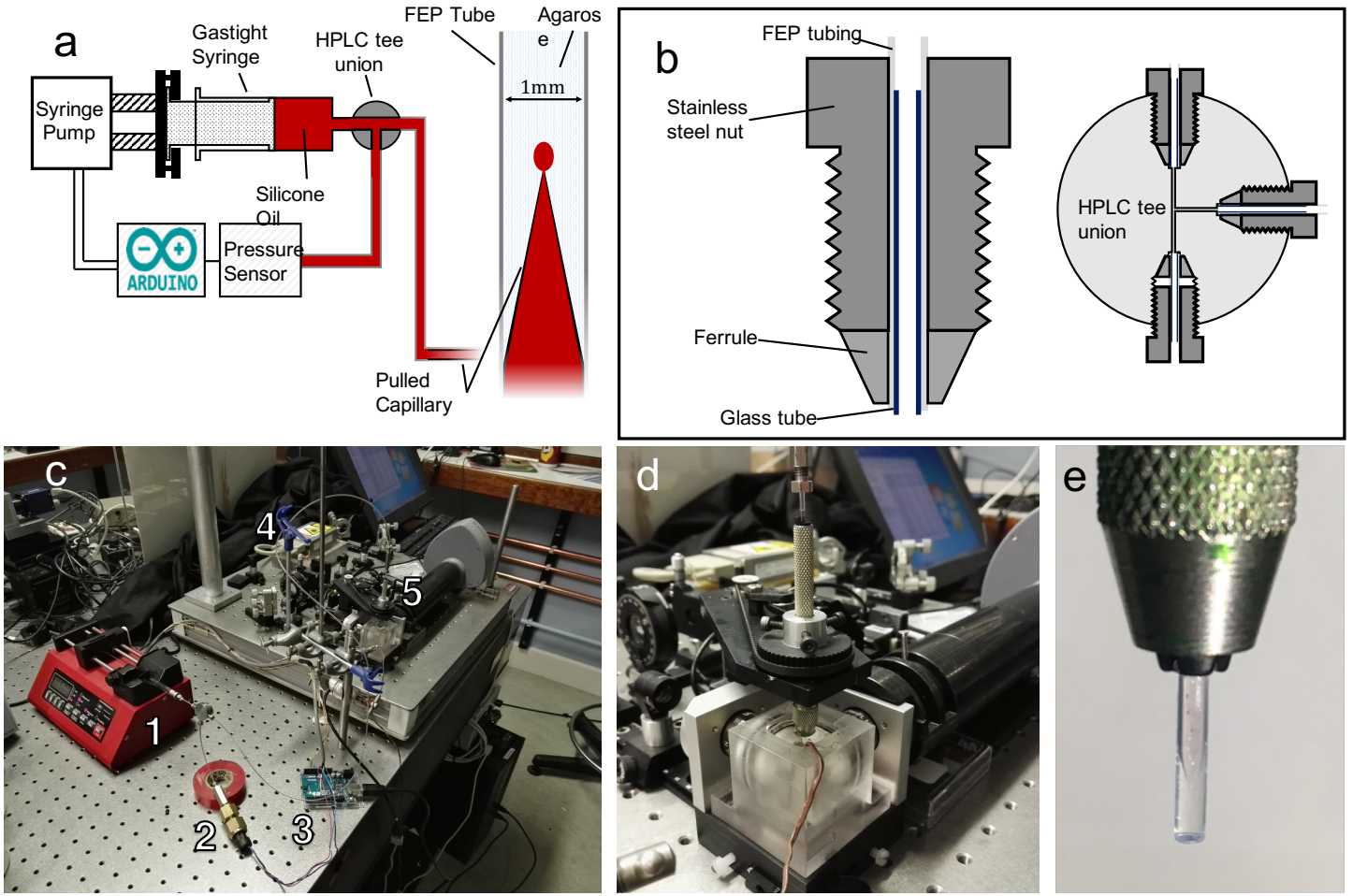

Figure 6.1 *The pressurestat setup. (a) A schematic of the pressurestat setup. A syringe pump is used to apply pressure to a reservoir of oil. A pressure sensor and Arduino then control the syringe pump to modulate the pressure in the oil reservoir. Attached to the oil reservoir is a pulled borosilicate capillary. The capillary is embedded in agarose gel inside FEP tubing and the entire ensemble is held together using a pin vice, (e). (b) Schematic of unions between FEP tubing and components. A borosilicate cylinder is used to seal the FEP tubing to the ferrule. (c) a photo of the pressurestat setup. (1) Syringe pump; (2) Pressure sensor; (3) Arduino; (4) FEP tubing held with clamps; (5) The pin vice holding FEP tube, agarose and capillary. (d) The pin vice is secured to the arm of the 4D stage using a custom jacket and grub screws.*

was useful to increase the precision in the limited range of pressures/voltages used. For the experiments in this section the reference voltage was set to 2.52 V using a 9.94 kΩ resistor. By implementing this voltage divider, precision was improved to 2.5 mV per interval or 0.424 kPa per interval[3]. Using this reference voltage the maximum readable pressure was 348 kPa, slightly greater than the pressure required to initially express oil from the capillaries.

6.2.2 Creating micron diameter capillaries

In order for the oil droplets to be inflated on the same length scale as the colony it was necessary for them to start at the same size as a bacterium. Therefore capillaries with opening diameters on a micron scale needed to be produced. Capillaries on this scale are often used for the patch clamp technique in electrophysiology [160, 161]. With this in mind, capillaries were produced with the help of Dr. Nathanael O'Neill from the Centre for Clinical Brain Sciences, University of Edinburgh.

To pull capillaries with opening diameters between 0.5 µm and 2.0 µm a P-97 pipette puller was used. 6 inch long, filamented, borosilicate capillaries from World Precision Instruments[4] with an outer diameters of 1.0 mm and inner diameters of 0.58 mm were used for all experiments. The puller applied an axial force along the length of the capillary whilst heating a short section. When the heated section of capillary began to melt, the axial force would cause the capillary to taper where it was heated. When the capillary reached a certain velocity due to the pulling force, compressed air was used to rapidly cool the middle of the heated/tapered region, a stronger pull was then applied in order to break the capillary at its mid point. Two tapered capillaries were therefore created, one 4.5 inch to 5.0 inch long and the other composed of the remaining length of capillary. The shorter capillary was used to measure the opening diameter of both capillaries.

The diameter of the capillary openings was measured using a JEOL JSM-6010 scanning electron microscope (SEM), Figure 6.2. Capillary tips roughly 2 cm long were cut from the capillaries. To prevent charging during EM imaging,

[3]Although this results in precision less than the stated accuracy of the pressure sensor, in practice the readout was stable. Overall this step was perhaps unnecessary for the current application, but may help future investigators who might leverage more control over the pressure.

[4]Part number 1B100F-6

the capillary tips were sputter coated with gold in argon gas for 2 minutes at 2.5 kV and 20 mA. This resulted in an approximately 30 nm layer of gold being deposited on the surface of the capillary. The diameter of the openings could then be viewed by mounting the capillary tips upright in metal tubes and inserting them into the SEM Figure 6.2a,b. Images of the capillary tips were captured and opening diameters were measured by fitting ellipses to the opening in ImageJ.

The opening diameter could be adjusted by changing various parameters of the pulling method. For example the pulling force, the temperature of the heating element, the air pressure with which the tip was cooled and the velocity at which the cooling was triggered could be changed. For all tips a "Pull" parameter[5] of 0 was used. This meant that only the counter weight attached to each end of the capillary was used to provide axial force. This value was empirically found to result in capillaries with opening diameters of the order $\sim$1 µm to 10 µm [162]. A "Velocity" between 10 and 35 and an "Air Pressure" between 400 and 900 along with a "Heat" parameter of 636 resulted in capillaries with opening diameters between 0.5 µm and 4.0 µm, Figure 6.2c,d. A range of "Velocity" and "Air Pressure" parameters were used to give a range of capillary sizes. The opening diameters of these capillaries could then be measured in the aforementioned way and capillaries of suitable size selected for the oil droplet experiments.

To ensure that the the opening diameter of the shorter half of the pulled capillary matched the longer half that was used in the experiment, the diameter of both tips from one batch of pulled capillaries was measured, Figure 6.2e. The opening diameters of both sides matched within measurement uncertainty (bar one instance where the tip had broken during handling).

6.2.3 Preparation of fluorescent silicone oil

Even using extremely narrow capillaries, the flow rate of the oil[6] from the capillary tips was too rapid to capture dynamics of the bubbles morphology as it fractured the gel around them. To solve this problem 100 Stoke silicone oil was used. This corresponds to a dynamic viscosity of 9.71 Pa s or a viscosity $\times 11,000$ that of water. Such high viscosity oil slowed the oil's flow rate from the capillary and

[5] I've put quotation marks around the parameters as the units of each parameter are not given. The parameter value instead refers to some arbitrary scale specific to the P-97 pipette puller.

[6] Initially I used 0.1 Stoke silicone oil.

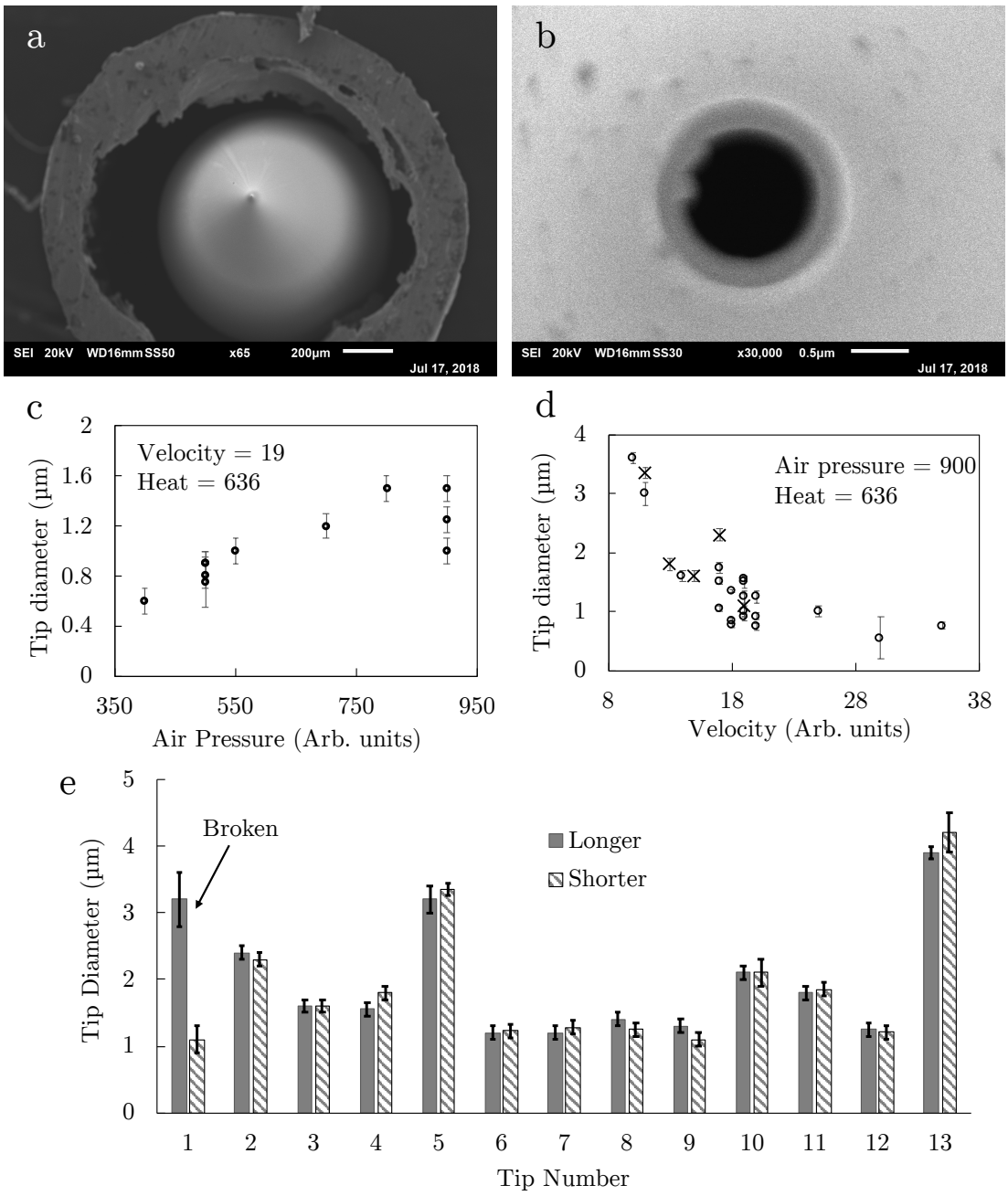

Figure 6.2 *SEM images of capillary openings and correlation with pulling parameters. (a) Top-down, low magnification view of a sputtered capillary tip held upright in a metal tube. (b) High magnification image of the capillary tip. The filament inside the capillary can be seen as a bump on the left of the opening. (c) The tip diameter observed as a function of air pressure used to cool the tip during pulling. (d) The tip diameter observed as a function of velocity threshold at which the tip was rapidly cooled during pulling. (e) Comparison of the two tips that are created after each pull. The tip diameter of both halves of the pulled capillary are the same except where one side had broken as in the case of tip 1.*

allowed for the change in morphology of the droplet to be recorded as it fractured the gel.

The silicone oil needed to be made fluorescent in order for it to be visualized by the SPIM setup[7]. Nile red, a lipophilic dye, was selected for its solvatochromic property [163]. That is to say that its excitation and emission spectrum are highly dependant on the polarity of the solvent. In non-polar solvents such as oil it is highly fluorescent having an excitation peak of $\approx 515\,\mathrm{nm}$, near the wavelength of the 488 nm laser used in the experiment. In polar solvents, like the water in the agarose hydrogel, it is very weakly fluorescent and the excitation peak shifts to $\approx 554\,\mathrm{nm}$ [164].

A practical problem presented itself when adding the Nile red to the silicone oil. The raw Nile red powder consists of many small shards $\sim$1 µm to 50 µm in length. If the mixture of Nile red and silicone oil is not filtered then these shards jam the capillary opening, however when the mixture was filtered the fluorescence intensity of the oil was greatly reduced. Therefore two approaches were taken when adding Nile red to the silicone oil. In the first approach Nile red was added at a concentration of $13.6\,\mathrm{g\,l^{-1}}$ to a few ml of silicone oil. The pressurestat was filled with this dense mixture of Nile red. Using this dense suspension meant that the same capillary could only be used for one or two experiments before a Nile red shard would block the capillary opening. The second approach was to filter the Nile red-silicone oil mixture. The mixture was filtered with a 1 µm filter pad. This took a few days, during which time the mixture was kept covered in a dark room to prevent photobleaching of the Nile red. When the filtered oil was used, images had to be manually thresholded as the contrast between the background and oil droplet was small compared to the contrast between background and reflected by the capillary tip.

6.3 Experimental technique

In this section experiments using the pressurestat system are described. Prior to each experiment a micro-manipulator attached to a low magnification, long working distance, microscope was used to inspect the tip of the pulled capillary. The tip was checked for any damage and it was checked that oil could be expressed

[7]Another approach would be to make the gel fluorescent. However this would preclude the use of fiducial markers in the gel and make visualization of gel deformation difficult.

from the tip of the capillary by increasing the pressure inside the the oil reservoir. It was essential that oil be expelled from the tip prior to an experiment as the tips accumulated water during storage due to the high capillary pressure at the opening.

Agarose was prepared in the same way as described in Section 4.3.1 with silicone beads added to the gel at a volume fraction of $\approx 0.04\%$. A 3 cm long piece of FEP tubing was used to sheath the capillary. This sheath could then be used like a pipette to suck up some of the molten agarose around the capillary tip. A pin vice was used to clamp the FEP tubing to the capillary, locking it in place. Whilst the gel set the pressure inside the oil reservoir was set to 120 kPa, this is slightly above atmospheric pressure but was below the pressure required to overcome capillary pressure, meaning that the oil did not prematurely escape the capillary tip. By holding the oil in the capillary at slightly higher than atmospheric pressure, the molten gel was prevented from entering the tip of the capillary.

A major problem when conducting this experiment was the tip of the capillary separating from the agarose. This separation was caused either by the stresses induced during the setting of the agarose or by the FEP tubing moving independently of the capillary. The FEP tubing could be prevented from moving by only have a short (≈ 2 mm) section of FEP encased agarose protruding past the tip of the capillary, Figure 6.1e. Movement was further reduced by the pin vice. Setting stresses remained a problem and prevented experiments above $\gtrsim 2\%$ agarose where the setting stresses became too great.

Once the capillary was in place, being held by the pin vice in the 4D stage, the tip of capillary could be brought into focus by adjusting the position of the 4D stage. An initial fluorescence image was captured to record the initial positions of the fiducial markers in the gel. The tip was then recorded under bright-field illumination whilst the pressure in the oil reservoir was increased. When oil was first expelled from the tip of the capillary, the pressure was recorded and then decreased back to atmospheric. Decreasing the pressure from ≈ 300 kPa to atmospheric[8] (101 kPa) took around 2 min, in which time the oil formed a lenticular/ellipsoidal bubble. The pressure at which the bubble stopped growing was measured using this bright-field recording and then used to set the pressure at which the bubble would grow overnight.

[8] Atmospheric pressure was calibrated by detaching the capillary from the oil reservoir and allowing the system to reach equilibrium with the atmosphere.

Ideally the pressure would have been reduced at a much faster rate so that the early morphology of the oil bubble could be captured, however using a faster pump speed to reduce the pressure in the oil reservoir resulted in degassing of the silicone oil near the syringe plunger head. The gas bubbles that formed due to this degassing introduced a latency between pump movement and the pressure of the oil reservoir, which then resulted in steadily increasing oscillations in the pressure. A pump speed of $0.2\,\mu l\,min^{-1}$ was used for experiments as it was the highest speed for which the degassing issue was not observed.

After initial bubble formation, the pressure in the oil reservoir was set to approximately 5 kPa above the pressure at which the bubble was observed to stop growing after the initial formation of the bubble. The bubble was recorded under fluorescence microscopy for $\approx$ 20 hours, with seven views of the bubble recorded over each 12 min time step.

The experiment was conducted at room temperature ($\approx 25\,^{\circ}C$). This was a concession to the increased complexity of this experiment compared to the colony growth experiment. The experiment had a high failure rate even without the additional complexity of temperature control and given that the Young's modulus of agarose has been shown to have little temperature dependence in the 20 °C to 40 °C range [165], I decided not to control the temperature.

6.3.1 Modifications to image analysis

Registration and deconvolution of the images could be carried out in the same way as described in Section 4.6. Fusion and deconvolution of the various views was especially important for the oil droplets as they acted like lenses, focusing the light sheet and creating warped views behind them. By the combination of several views this artifact was averaged out.

When carrying out segmentation of the bubble an additional step was introduced to remove the capillary tip from the image. Noting that the connecting point between the tapered capillary tip and the bubble was the thinnest region of the image[9], the bubble could be separated from the capillary tip using a watershed method. The watershed method was carried out as follows:

1. The deconvolved image, Figure 6.3a, was thresholded using Otsu's method

[9]Here "thinnest" means the region with smallest possible cross sectional area.

described in Section 4.6.3, Figure 6.3b. Due to reflections, the capillary tip appears very intense in the image. The high intensity sometimes caused the deconvolution algorithm to assign very low intensities at the boundary between the tip and the bubble. This results in these boundary voxels having intensities lower than the threshold value. These mislabelled boundary voxels were corrected using a median filter whereby the voxel intensity was replaced by the median of surrounding voxel in a radius of 8 pixels. In a couple of cases the tip was so intense compared to the bubble that thresholding had to be completed manually.

2. The distance transform of the thresholded image was calculated using the Euclidean distance transform function "distance_transform_edt" from scipy's ndimage module, Figure 6.3c. This results in an image where the value of each voxel is its Euclidean distance from the boundary of the thresholded region.

3. Coordinates of the local maxima in the image were found using scikit-image's "peak_local_max" function. Two local maxima positions were used for the watershed algorithm, the local maxima with highest value (corresponding to the center of the bubble) and the local maxima nearest the bottom of the image (corresponding to a point in the capillary tip).

4. Using the coordinates of the local maxima a watershedding algorithm was implemented using scikit-image's "watershed" function. The watershedding algorithm essentially treats the image as a topological map, filling regions from large to small values starting at the coordinates of the local maxima. In this way the 'ridges' of the topological map are found where two filled regions meet. These ridges will lie on the thinnest region of the image. The result of the watershedding algorithm is an image with three labelled regions, one corresponding to the background, one to the bubble and one to the tip, Figure 6.3d.

5. The region containing the local maxima nearest the bottom of the image (measured in step 3) was then removed.

After the image analysis I was left with a binary image with value 'True' for voxel locations corresponding to the oil droplet and "False" elsewhere. I could then use the same methodology described in Section 4.6.3 to measure the morphology of the oil droplets.

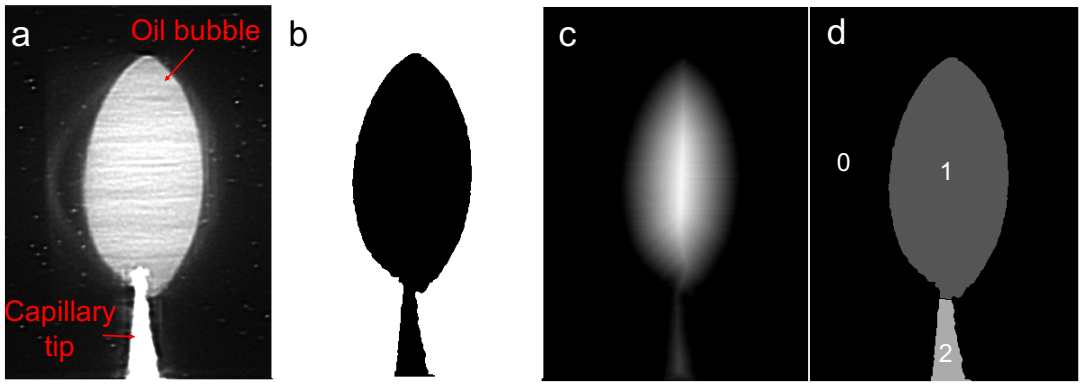

Figure 6.3 *The watershed method was used to separate oil bubbles from the capillary tip. (a) A representative volume slice centered on the capillary tip and oil bubble in 2 % agarose. (b) The image was thresholded and a distance transform was performed, (c). (d) The distance transform could then be used to perform a watershed segmentation of the oil-capillary image.*

6.4 Experimental results and discussion

6.4.1 Fracture initiation pressure

It was hoped that the pressure at which oil was first expelled from the capillary (henceforth called the bubble initiation pressure, P_i,) could be used to distinguish between different modes of fracture. The bubble initiation pressure can provide information about the mode of fracture for the following reason.

For oil to be expressed from the tip of the capillary the pressure in the oil reservoir must be greater than the pressure at the interface between oil and agarose. The pressure at the agarose-oil interface stems from three sources. The first of these is the pressure imposed by the atmosphere, $P_{\text{atm}} \approx 101\,\text{kPa}$; the second is the capillary pressure, P_{cap}. This pressure is a result of the oil tending to move back into the capillary to minimize the interfacial area between the oil and the M9 media in the agarose, minimizing this area minimises the interfacial energy. The resulting pressure is given by

$$P_{\text{cap}} = \frac{2\gamma_{\text{Oil-M9}}}{r} \tag{6.1}$$

where $\gamma_{\text{Oil-M9}}$ is the interfacial energy per unit area and r is capillary radius. The capillaries used in this experiment had opening radii of 1 µm to 4 µm and $\gamma_{\text{Oil-M9}} = 28\,\text{mJ}\,\text{m}^{-2}$ (see Section 6.4.4), therefore $P_{\text{cap}} \approx 30\,\text{kPa}$ to 100 kPa.

The third pressure will depend on the mode of fracture. In order for the oil to move into the gel it must fracture the initial crack in the agarose. As was discussed in the previous chapters this fracture can either occur by the propagation of a single "penny shaped" crack or via distributed damage over the entire crack surface. A penny shaped fracture will propagate at a pressure, P_f, given by

$$P_f \approx \sqrt{\frac{\Gamma E}{2r}}. \tag{6.2}$$

Note that the initial crack length is taken to be the opening diameter of the capillary rather than the entire length of the capillary. This was justified by the observation that the oil droplets did not propagate along the capillary-agarose interface, suggesting that the capillary-agarose bond was at least as strong as the agarose-agarose cohesive bond. Therefore the capillary-agarose interface should not be considered as part of the initial crack. Distributed damage should occur at a pressure, P_c, roughly equal to the Young's modulus of the agarose (bar some coefficient of order 1), i.e.

$$P_c \approx E. \tag{6.3}$$

Therefore different bubble initiation pressures are predicted for each fracture mode. For initiation via penny shaped fracture

$$P_i = P_{\text{atm}} + P_{\text{cap}} + P_f, \tag{6.4}$$

and for initiation via cavitation

$$P_i = P_{\text{atm}} + P_{\text{cap}} + P_c. \tag{6.5}$$

The bubble initiation pressure was measured by increasing the pressure in the oil reservoir in increments of 10 kPa until oil began flow from the capillary tip. The pressure was raised in intervals to allow the pressure throughout the reservoir to equilibrate. Figure 6.4a-e shows a time series of the capillary tip at bubble initiation taken at 2 frames per second. $t = 0$ shows the capillary a single frame prior to bubble initiation. In the next frame, 0.5 s later, oil has been expelled into the agarose and forms what appears to be a spherical bubble, though the exact shape is difficult to distinguish. In the lowest concentration of agarose tested (0.6 %) the initial bubble is more clearly spherical immediately after initiation, Figure 6.4f-i. That the bubbles are initially spherical is indicative of distributed damage for the reasons discusses in the last chapter.

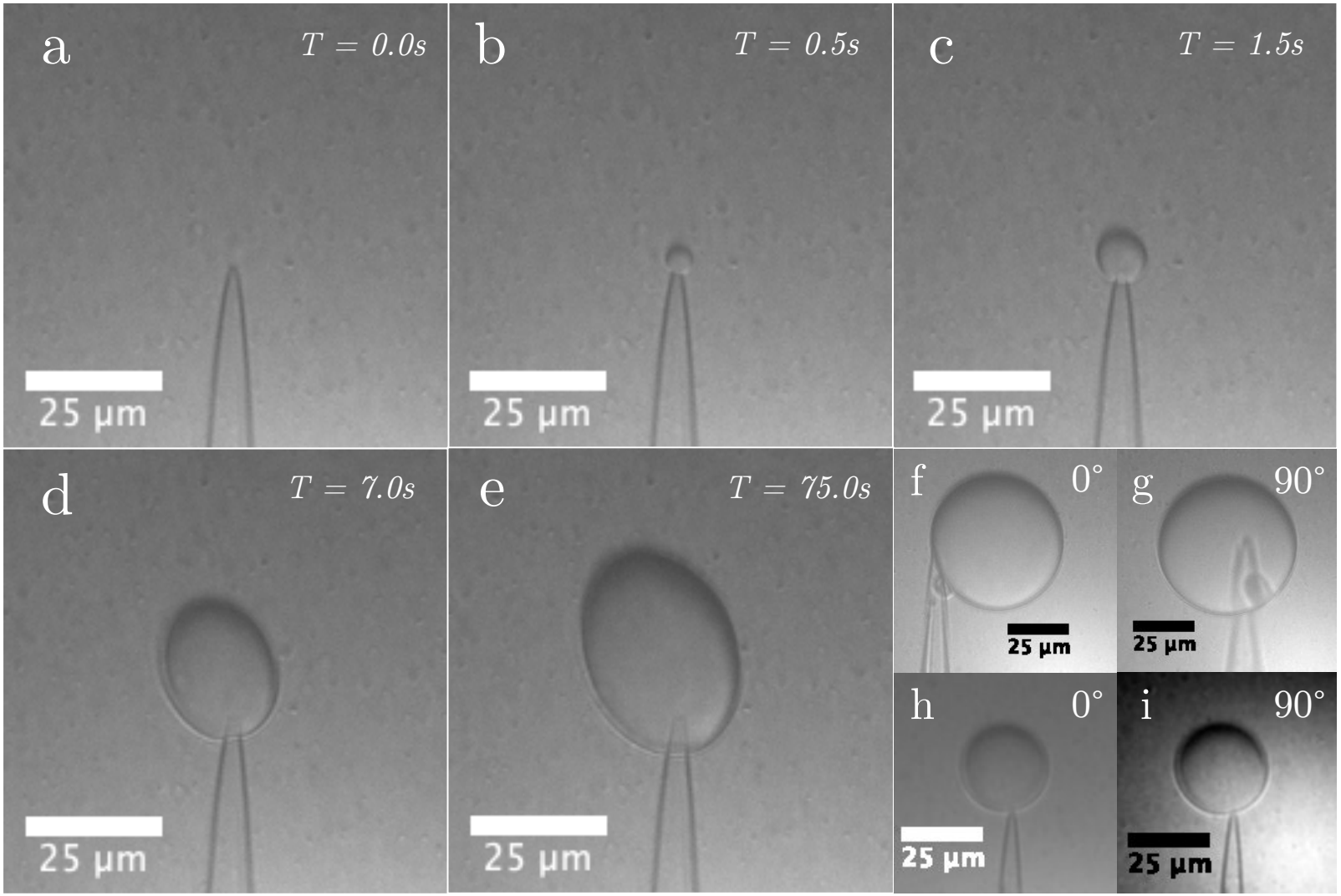

Figure 6.4 *The tip of the capillary at the initiation of a hydraulic fracture. (a-e) The pressure inside the oil reservoir was increased in* 10 kPa *intervals up to* 270 kPa *when oil began to be expelled from the capillary in 2 % agarose. At that point the pressure in the reservoir was returned to atmospheric, this took around* 90 s. 75 s *from fracture initiation the pressure was* 140 kPa *and the bubble had stopped growing. Immediately after initiation the bubble appears spherical, turning to an ellipsoidal/lenticular shape as it grows. (f-i) Two oil bubbles (f,g) and (h,i) grown in 0.6 % agarose are more clearly spherical immediately after initiation.*

Figure 6.5 plots the bubble initiation pressure in 1 %, 1.5 % and 2 % agarose for a range of capillary opening diameters. The initiation pressure predicted by cavitation (solid lines) and penny shaped fracture (dotted line) are plotted alongside the data. Whilst the observed initiation pressures are of the same order of magnitude as the predicted pressures, the observations span both sets of predicted initiation pressures, so cannot be used to distinguish between the cavitation and disk fracture phenomena. In addition, the scaling of the initiation pressure with the capillary opening diameter is obscured by the spread in the data.

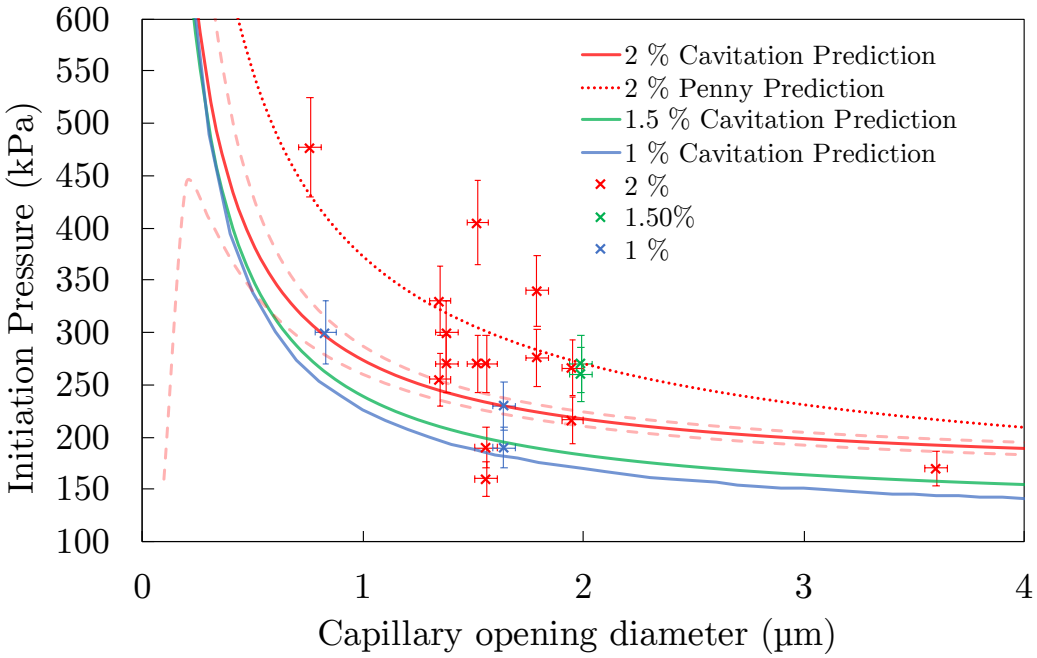

Figure 6.5 *The pressure in the oil reservoir was increased steadily. The pressure at which oil began to be expelled from the capillary was recorded and is plotted against the size of the capillary opening (and coloured by the agarose concentration). The initiation pressure predicted by the combination of the pressure required to cavitate the agarose plus the capillary pressure is plotted alongside the data (solid lines), the uncertainty in this prediction is indicated by the dashed lines. The dotted line is the fracture pressure predicted by a combination of fracture in penny shaped disk and capillary pressure. Recorded bubble initiation pressures span both sets of predictions, so cannot be used to distinguish between the cavitation and disk fracture phenomena.*

There were two probable reasons for the spread in the data. First the capillary tip was very susceptible to blockage by shards of Nile red. Whilst these shards rarely made it to the tip of the capillary, as oil flowed from the tip they collected near the

tip, constricting oil flow through the end of capillary. In later experiments these shards were filtered from the oil but no improvement in bubble initiation pressure variability was observed (both sets of data are plotted in Figure 6.5). The lack of improvement was likely due to another source of uncertainty, the initial state of the gel at the capillary tip. Prior to bubble initiation the gel was sometimes observed entering the tip of the capillary despite the oil in the capillary being held at a pressure greater than P_{atm}. This ingressed gel had to be expelled from the tip prior to the oil which will have some effect on the initiation pressure.

6.4.2 Correlating flow rate, pressure and fracture size

After the bubble had been initiated, the pressure in the oil reservoir was reduced back to P_{atm}. This pressure reduction was not instantaneous due to the speed of the syringe pump, therefore the bubble continued to grow into an ellipsoidal/lenticular shape over the course of ≈ 1 minute. At some pressure above P_{atm} the bubble would cease growing, this pressure was recorded and then the bubble would be left overnight at that pressure plus approximately 5 kPa (called P_s) so that the bubble would grow very slowly.

As the bubble grew its volume was recorded so that the flow rate, Q, from the oil reservoir into the bubble could be calculated, Figure 6.6a-c. The flow rate gives information about the pressure difference between the bubble and the reservoir in the following way. First, the Reynold's number (Re) can be used to estimate the type of flow that can be expected at the tip of the capillary. For a fluid with kinematic viscosity, μ, passing through a pipe of hydraulic diameter, D_H, and cross sectional area, A, the Reynolds number is given by

$$\text{Re} = \frac{QD_H}{\mu A}. \tag{6.6}$$

If D_H is taken to be the inner diameter at the tip of the capillary then for a 1.5 µm opening diameter tip with silicone oil of kinematic viscosity $0.01\,\text{m}^2\,\text{s}^{-1}$ flowing through it at a maximum rate of $\approx 10^{-17}\,\text{m}^3\,\text{s}^{-1}$, Re is of the order 10^{-9}. As the Reynolds number is so small, laminar flow can be expected between the capillary and the oil bubble which will be described by the Stokes flow equations. Given that silicone oil is incompressible and Newtonian [166–168] then, according to the Stokes flow equations, the flow rate will be linearly proportional to the pressure

difference, ΔP between the reservoir and the oil droplet, i.e.

$$Q = \beta \Delta P \tag{6.7}$$

where β is some constant to do with the dimensions of the channel and viscosity of the fluid[10]. In theory β could be measured by expelling oil from the capillary into water at a certain depth (where the pressure difference between the oil reservoir and the bubble would be known) and measuring Q. However in practice β will be specific to each of the capillaries and as each capillary could only be used for a few experiments before breaking, it was not practical to carry out this measurement.

Instead, the coefficient β can be cancelled from Equation 6.7 by considering Q as a fraction of the initial flow rate, Q_i. The scaling (rather than the absolute value) of the pressure difference between the bubble and reservoir, ΔP, with the major axis length, a, of the bubble can therefore be found by measuring the fractional flow rate, $\overline{Q}$, given by

$$\overline{Q} = \frac{Q(a)}{Q_i(a)} = \frac{\Delta P(a)}{(\Delta P)_i\,(a)}. \tag{6.9}$$

This fractional flow rate can be compared to the fractional flow rate expected from the pressure difference between P_s and the estimated pressure required to propagate a hydraulic fracture in a linear elastic material (Equation 3.26) plus capillary pressure (Equation 6.1). The expected fractional flow rate, $\overline{Q_p}$, should be given by

$$\overline{Q_p} = \frac{P_s - \left(\sqrt{\frac{\Gamma E}{a}} + \frac{2\gamma}{a}\right)}{P_s - \left(\sqrt{\frac{\Gamma E}{a_i}} + \frac{2\gamma}{a_i}\right)}, \tag{6.10}$$

where a_i is the size of the oil droplet when measurements began[11].

Figure 6.6d-f plots $\overline{Q}$ or $\overline{\Delta P}$ as a function of the bubble's major axis length (orange) along with the relationship predicted by Equation 6.10 (blue). On one hand, the observed fractional flow rate (and therefore ΔP) does increase with bubble size. This increase suggests that some Griffith theory governed fracture process is taking place, i.e. where fracture propagation pressure decreases with fracture size. The increase rules out cavitation based fracture above 20 µm, which

[10]For example in a long cylindrical pipe of constant cross section, Q is given by the Hagen–Poiseuille equation, [169]:

$$Q = \frac{\pi R^4}{8\mu L}\Delta P. \tag{6.8}$$

[11]Given that $\frac{\pi}{4(1-\nu^2)} \approx 1$ in Equation 3.26.

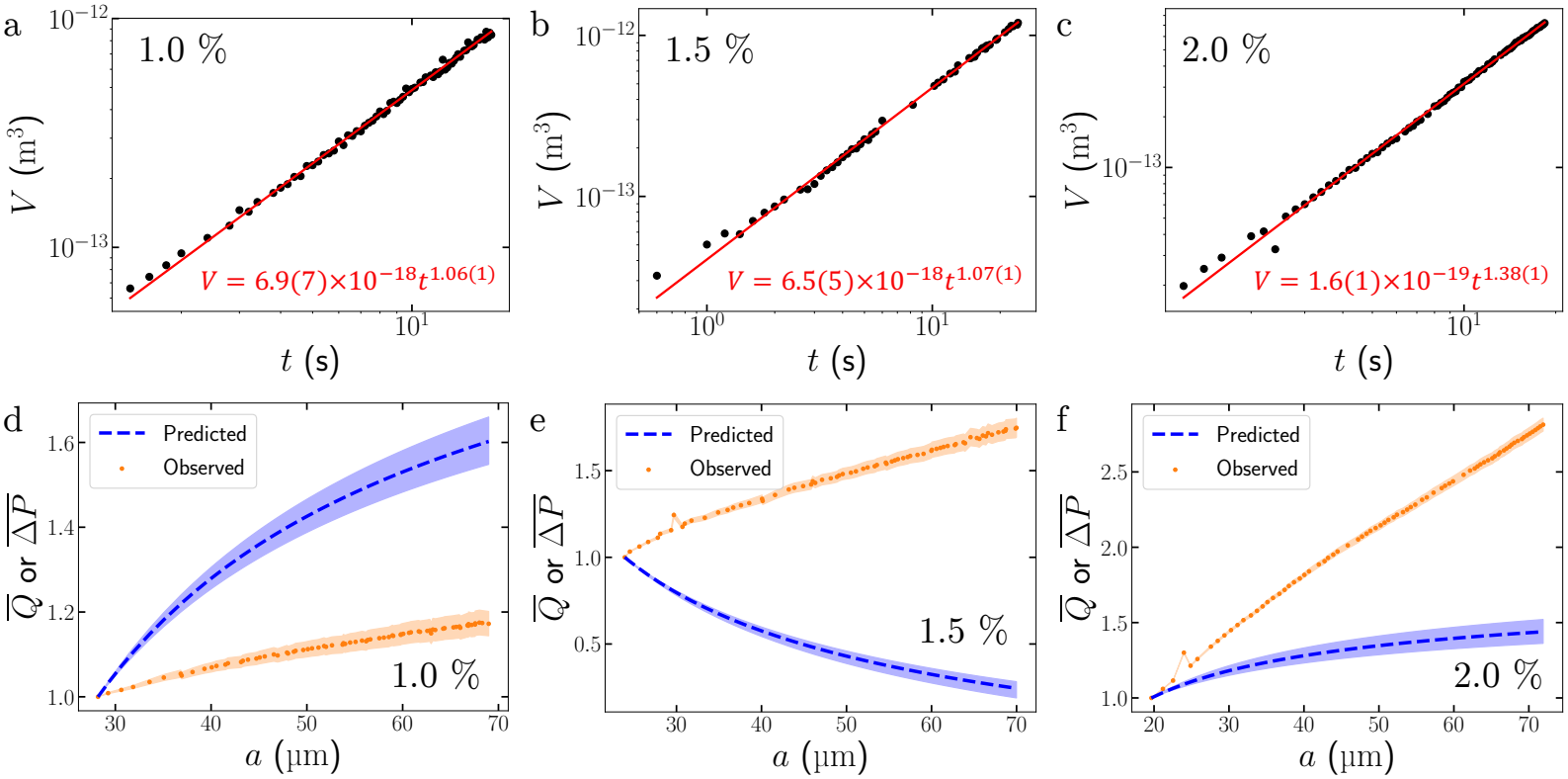

Figure 6.6 *Flow rate can be used to infer the pressure difference between the bubble and the oil reservoir. (a-c) The volume of oil bubbles grown in various concentrations of agarose is plotted against time. A power law is fit to determine the volumetric flow rate. (d-f) The flow rate as a fraction of the initial flow rate is plotted against the size of the oil bubbles a (orange). The flow rate should be linearly proportional to the pressure difference, ΔP, between the oil reservoir and bubble, so the y-axis can also represent ΔP as a fraction of the initial ΔP ($\overline{\Delta P}$). The flow rate predicted by Griffith-Sneddon theory (Equation 6.10) is plotted alongside the observed data (blue dashed line). In (e) the flow rate is predicted to decrease, this is because P_s was lower than the predicted $P_{cap} + P_f$. The uncertainty in $\overline{Q_p}$ is represented by the shaded region and stems predominantly from uncertainty in the measurements of Γ.*

is expected as the size of the bubble is larger than ℓ_{EF} in all cases. However, the increase in $\overline{Q}$ lies far from that predicted by Equation 6.10 and is much more linear than expected. In Figure 6.6b the predicted fractional flow rate decreases, this is because the pressure that the bubble was observed to be growing at (P_s) is less than $P_{\mathrm{cap}} + P_f$. This was despite the bubble being initiated at a pressure higher than predicted (Figure 6.5). The increase in $\overline{Q}$ was extremely inconsistent between experiments, with Q being almost constant in some cases (Figure 6.6a,b) whilst increasing rapidly in others (Figure 6.6c).

Each of the measurements in Figure 6.6 were taken with silicone oil that had been filtered for Nile red shards, so the alteration of flow through the capillary mid experiment cannot explain the discrepancy in flow rates. I'm still uncertain as to why the observed flow rates deviate so much from what was expected.

6.4.3 A morphological comparison of hydraulic fractures and bacterial colonies

The main goal of this chapter was to compare oil bubble morphology to the morphology of the bacterial colonies. This would hopefully reveal the influence of any biological interaction on colony morphology, revealing whether the bacteria do simply create fractures that grow in the same way as a fracture opened up by a Newtonian fluid (a hydraulic fracture).

Figure 6.7 shows z-projections of an oil bubble blown in 2 % agarose that was archetypal of the morphology of oil bubbles blown in concentrations of agarose between 0.6 % and 2 %. The tip of the capillary can be seen at the bottom of the image, it appears larger than its true size due to the strong reflections from the glass. False colour has been added to highlight the depth of the image.

The morphology of the oil bubbles can be quantitatively compared to that of the colonies using the shape characteristics described in Section 5.3, namely their apex radius of curvature, ρ; the scaling of their major and minor axis, a and b respectively; how closely they resemble an ellipsoid (quantified by the super-ellipsoid power that best fits them); and finally by the displacement of the surrounding gel. The following sections compare bubble morphology both to that of the colonies and to the simple model described in the previous chapter using the values for ℓ_{EF} that are reported in Chapter5.

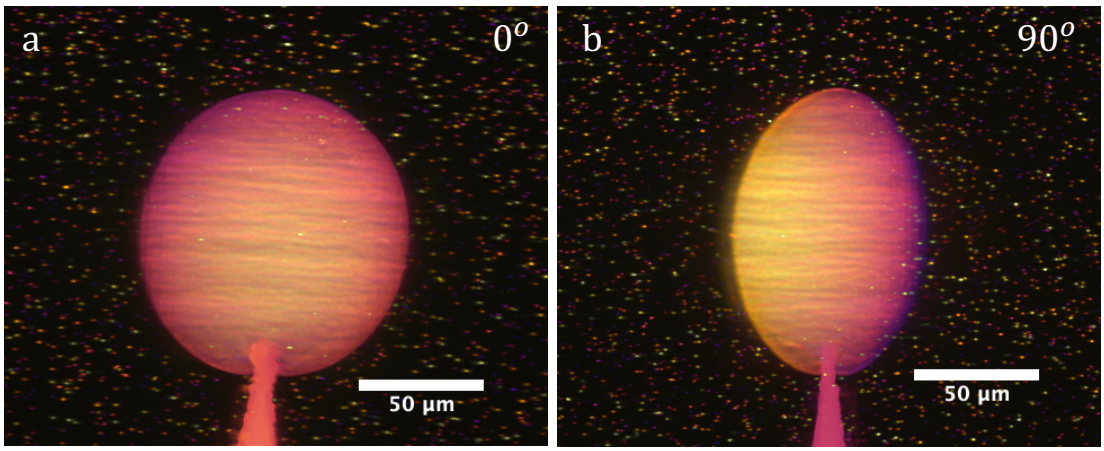

Figure 6.7 *Z projections of an oil bubble blown in 2 % agarose from two angles at 90° from one another. The capillary tip can be seen at the bottom of the image. (a) Like the colonies, the bubbles are approximately circular in the fracture plane and (b) lenticular or ellipsoidal in the planes orthogonal to the fracture plane.*

Many of the bubbles blown into agarose were deformed by the tip of the capillary moving independently of the agarose, fracturing the gel surrounding the capillary tip. This independent movement was caused either by movement of the FEP tubing that held the agarose in place or by setting stresses deforming the agarose around the tip. Only data from oil bubbles that showed no evidence of deformation by extraneous tip fracture and that remained wholly within the field of view are considered in the next section.

The crack tip radius of curvature

First the radius of curvature at the tip or apex of the oil bubbles, ρ, was measured using the method described in Section 4.6.3. Figure 6.8a plots ρ against a for oil bubbles blown into various concentrations of agarose. Individual data points are shown as circles and are coloured according to the concentration of agarose they were measured in. Data from multiple bubbles at each concentration are plotted concurrently. Splines are fit to data points from the same agarose concentration to highlight the trend. The tip radius of curvature for colonies grown in the same concentrations of agarose are shown faintly for comparison.

At larger values of a and for higher agarose concentrations ρ appears to plateau, similar to the bacterial colonies. However the plateau value of ρ is larger for the oil bubbles than the colonies. Early morphologies (a <20 µm) could not be measured for oil droplets due to the rapid expansion of the bubbles during initiation.

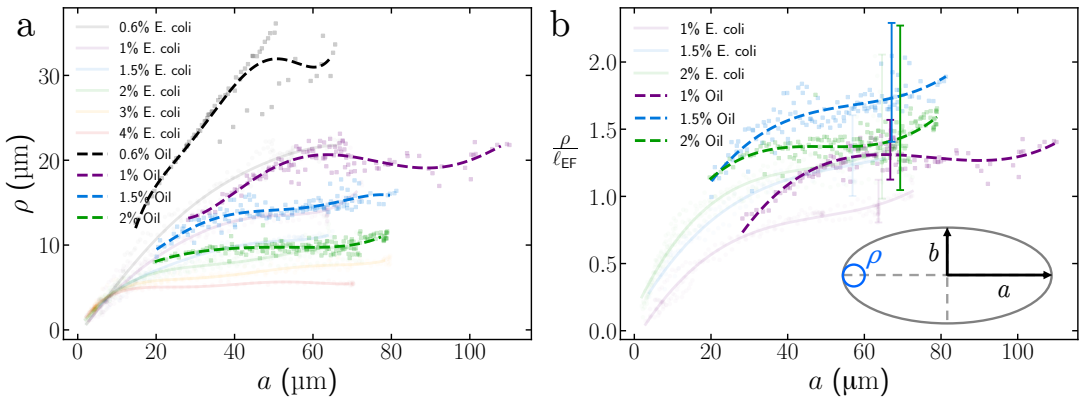

Figure 6.8 *The radius of curvature at the apex of the oil bubbles, ρ, plotted against major axis size, a. Data points from multiple bubbles grown in the same concentration of agarose are shown by dots. Splines fitted to all data at a given concentration have been added to the data to highlight the trend. The results from colonies grown in the same concentrations of agarose are shown faintly for comparison. (a) Similar to the colonies, ρ appears to plateau at larger a. Though the plateau value of ρ is larger for oil bubbles compared to bacterial colonies. (b) Like the colonies, dividing ρ by ℓ_{EF} collapses the data, though again at a value higher than was observed for the colonies.*

Similarly to the bacterial colonies the data in Figure 6.8a can be collapsed to within experimental uncertainties by scaling ρ by ℓ_{EF}, Figure 6.8b. A representative uncertainty bar (stemming from the uncertainty in the measurement of Γ) is plotted for each agarose concentration at one value of a. The plateau value of ρ for oil bubble in all concentrations of agarose falls at around 1.5, slightly higher than that of the colonies.

The scaling of the aspect ratio

Next, oil bubbles can be compared to the bacterial colonies according to the scaling of their aspect ratios. Major and minor axis (a and b respectively) were measured using the inertia tensor of the oil bubbles, as described in Section 4.6.3. Figure 6.9a shows that like the colonies $b \propto a^{0.8}$, rather than the $b \propto \sqrt{a}$ relationship predicted by the simple model. The scaling of oil bubble aspect ratio only differed from that of the colonies in the prefactor, which was larger for the oil bubbles.

Similarly to bacterial colonies, despite the scaling between a and b being different from that predicted by the simple model (Equation 5.7), scaling a by ℓ_{EF} collapses

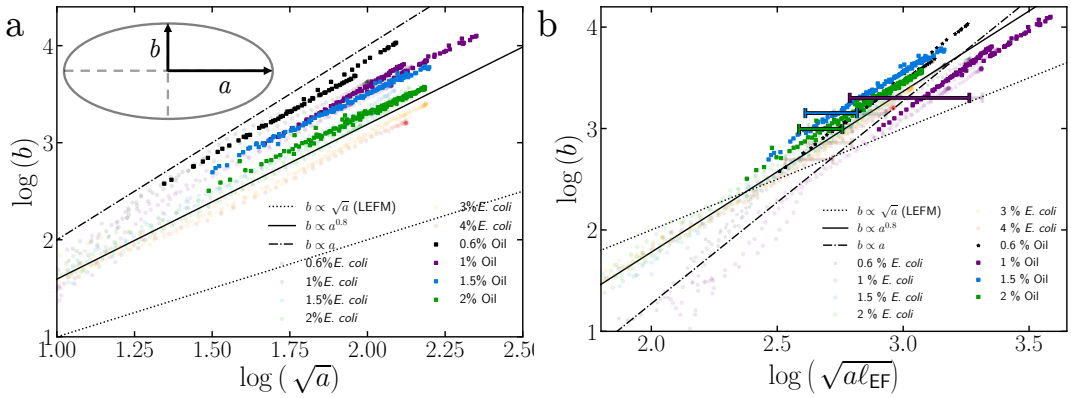

Figure 6.9 *The scaling of oil bubble major and minor axis. (a) The log of the oil bubbles minor axis, b, is plotted against the log of the square root of the major axis, a. Results for colonies grown in the same concentrations of agarose are shown faintly for comparison. The minor axis does not follow the square root power law predicted by LEFM, instead $b \propto a^{0.8}$. (b) Partial collapse is achieved by scaling $\sqrt{a}$ by $\sqrt{\ell_{EF}}$. Error bars are plotted for a single data point from each concentration given the uncertainty in ℓ_{EF}.*

the data, Figure 6.9b. No regions of spherically symmetric growth were observed in the oil bubbles most likely due to measurements starting when $a > \ell_{\mathrm{EF}}$. Looking at the bright-field recordings of bubble growth however(Figure 6.4), a period of spherically symmetric growth is likely when $a < \ell_{\mathrm{EF}}$, though the precise shape could not be determined.

The profile of a hydraulic fracture

Next I can compare the profiles of the oil bubbles to the predictions of the simple model and the bacterial colonies. As discussed in Section 5.3.3, linear elasticity predicts that when a disk shaped void of radius a is expanded by a uniform pressure it will be deformed into an ellipsoid of minor axis length b with width, $w(r)$, given by

$$w(r) = b\sqrt{1 - \left(\frac{r}{a}\right)^2}, \tag{6.11}$$

where r is the distance from the oil bubble's center of mass.

Oil bubble profiles are compared to Equation 6.11 in Figure 6.10. The profiles of oil bubbles grown in four different concentrations of agarose are plotted along with the corresponding prediction from Equation 6.11 in black. For predicted profiles b was set to the average of oil bubble width's between $r = 0$ and $r = a/20$, a was

set to the colony major axis at $z = 0$. Bubble profiles are coloured by the length of a compared to ℓ_{EF}. Oil bubble blown in agarose concentrations between 0.6 % and 1.5 % match the profile predicted by Equation 6.11 very well. In 2 % agarose a more "cuspy" profile, similar to that of the bacterial colonies, was observed.

The large standard deviation in width measurements for the bubble blown in 1.5 % agarose is a result of the lensing effect that the bubble has on the light sheet. When the intensity of the bubble was low (due to a lack of Nile red in the oil) the intensity of the lensing effect was similar to the intensity of the bubble and so was not fully averaged out in the deconvolution process. This resulted in an image of the bubble that had artificial ridges on the surface of bubble which interfered with width measurements. This may be the reason that for larger a/ℓ_{EF} the bubble grown in 1.5 % agarose appears ellipsoidal rather than becoming more "cuspy" like the bubble grown in 2 % agarose.

As with the bacterial colonies the deviation of the oil bubble profiles from Equation 6.11 can be quantified by fitting super-ellipses with the form

$$\left|\frac{r}{a}\right|^{\frac{1}{p}} + \left|\frac{z}{b}\right|^{\frac{1}{p}} = 1 \tag{6.12}$$

to the profiles. Again, when $p = 0.5$ Equation 6.12 forms an ellipse, whilst when $p > 0.5$ a more "cuspy" or lenticular superellipse is described.

Figure 6.11a plots superellipses fitted to an oil bubble grown in 2 % agarose, p was observed between 0.5 and 0.7, generally increasing with the length of the bubbles major axis. The increase in p is smaller and more inconsistent than the increase seen for bacterial colonies grown in the 2 % agarose.

The value of p for bubbles grown in four different concentrations of agarose is plotted against the bubble's major axis, a, in Figure 6.11b. The values of p for colonies are shown faintly for comparison. In general the values of p for oil bubbles are closer to 0.5 than they were for the colonies, the increase in p with a is much less clear or non-existent.

Finally oil bubble profiles can be directly compared to *E. coli* colonies by matching colonies and bubbles with the same a, grown in the same concentration of agarose, Figure 6.12. It is immediately clear that oil bubbles are wider than bacterial colonies of the same major axis length.

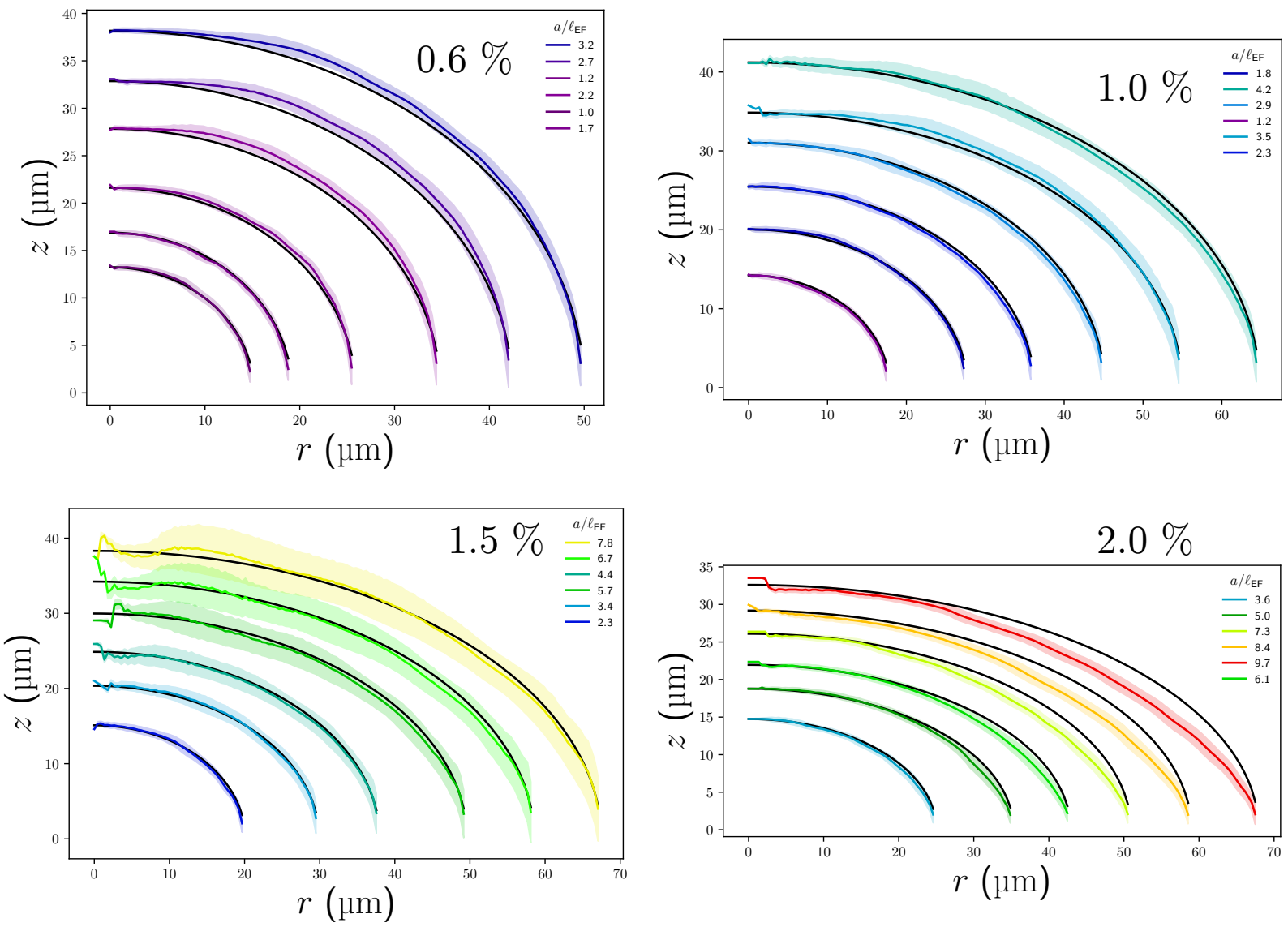

Figure 6.10 *Comparison of the oil bubble profiles to the simple linear elastic model. Profiles are plotted for oil bubbles blown into four agarose concentrations. The plots are coloured by the size of a compared to ℓ_{EF}, shaded regions represent one standard deviation from the radially averaged colony width. Oil droplets are approximately ellipsoidal.*

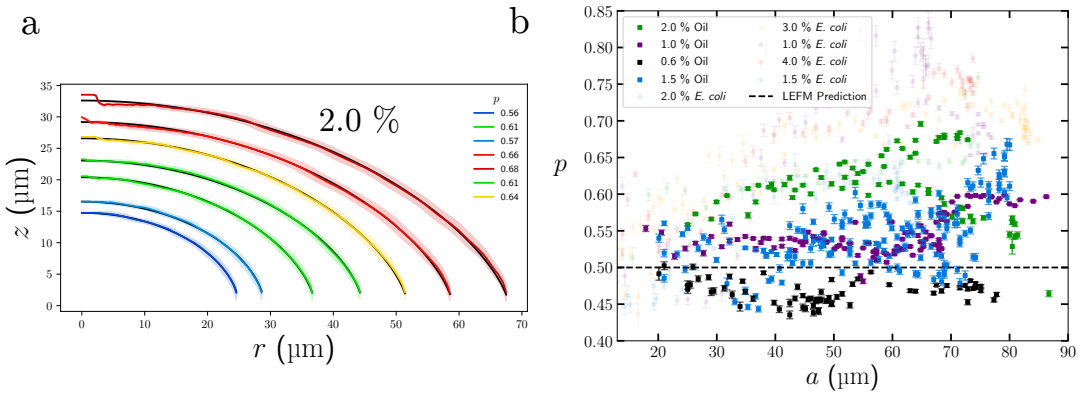

Figure 6.11 *Fitting super ellipse to oil bubble profiles. (a) Oil bubble profiles are fit with super ellipses of major and minor axis a and b respectively. Super ellipses with powers between 0.56 and 0.68 fit the bubble well. (b) The dependence of p on the size of the oil bubbles is plotted. The same plot for the bacterial colonies is shown faintly for comparison. The oil droplets tend to be more ellipsoidal than the colonies (p is closer to 0.5) and do not reveal any trend towards larger p for larger colonies.*

Displacement fields near to a hydraulic fracture.

When looking at the growth of the bacterial colonies I was able to track displacements from when the colony was only a few microns in diameter. This enabled me to compare measured displacements to those predicted by the simple model and to observe the formation of a damaged region. Unfortunately the oil bubbles grew rapidly after initiation due to capillary pressure, preventing accurate tracking between the initial (pre-bubble-initiation) position of the fiducial markers and the first set of positions after initiation. This prevented both the observation of any possible damaged zone and quantitative comparison of the displacement field.

However a few qualitative observations can be made from displacements tracked after initiation. Figure 6.13 shows displacements measured around two representative oil bubbles grown in 0.6 % and 2.0 % agarose. The displacements are shown in the Lagrangian frame of reference and are coloured according to their magnitude. The bubble is represented by an alpha volume (the grey polygonal mesh). Just like the colonies the displacements around the bubbles are indicative of fracture, with large displacements parallel to the bubbles minor axis and very little displacement in the plane perpendicular to the minor axis.

Interestingly in Figure 6.13b the gel near the apex of the bubble is being displaced

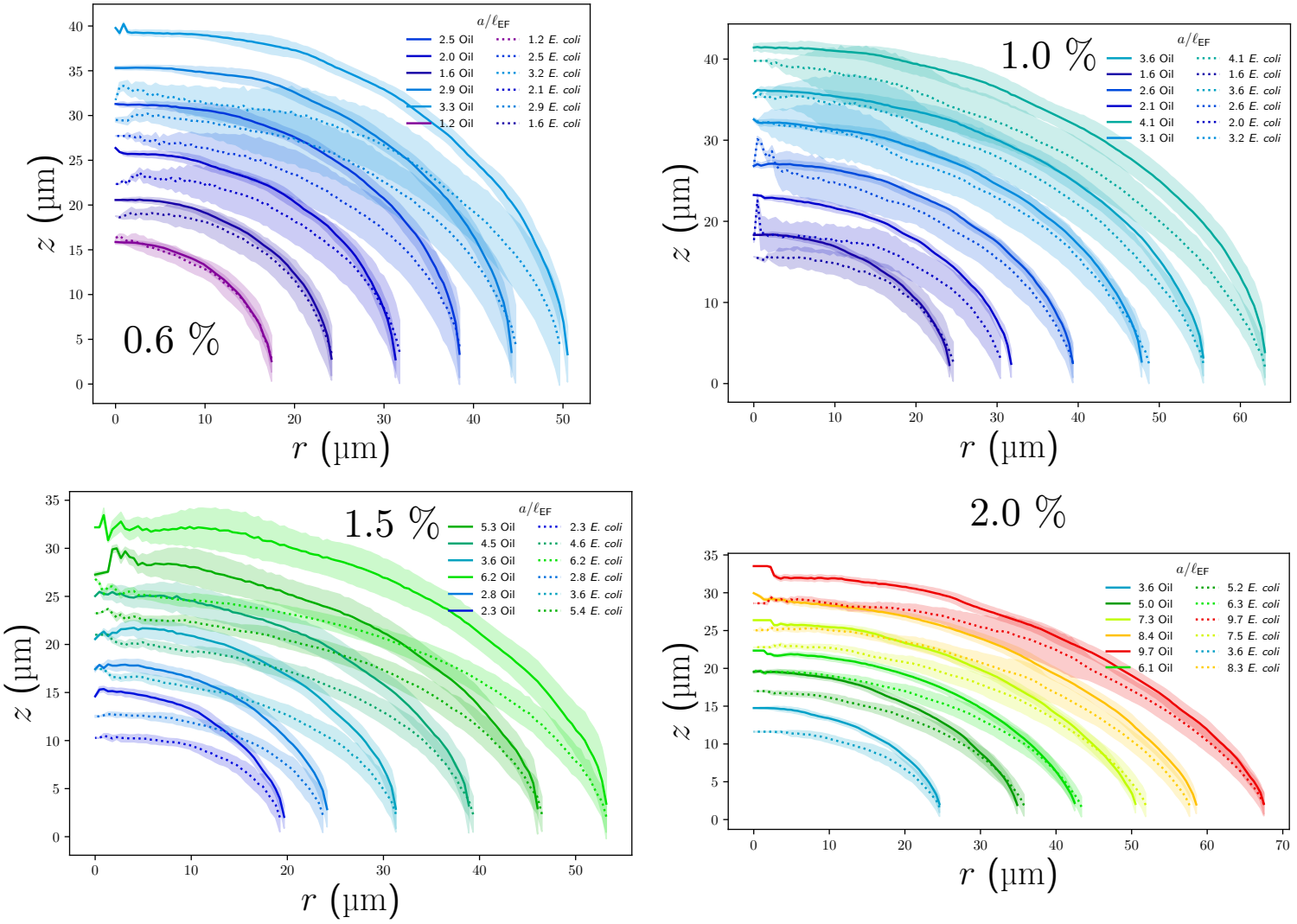

Figure 6.12 *Comparison of oil bubble and colony profiles. Colonies (Dotted lines) and oil droplets (solid lines) with the same major axis length a are plotted concurrently for multiple colony sizes and agarose concentrations. Plots are coloured by the size of the major axis with respect of ℓ_{EF}. In general the oil droplets are wider than bacterial colonies of the same major axis length.*

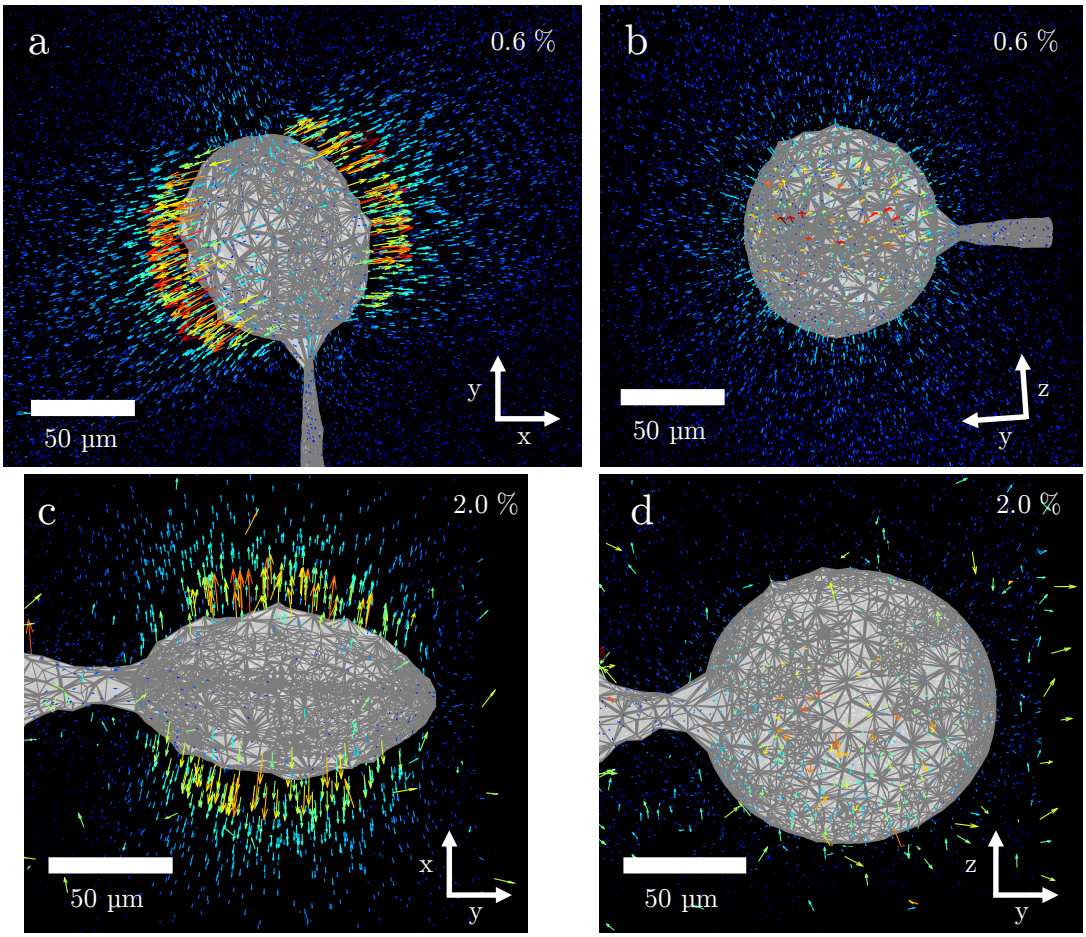

Figure 6.13 *Gel displacement around two nanolitre oil bubbles, grown in 0.6 % and 2.0 % agarose, were measured by tracking fiducial markers embedded in the gel. Displacements are shown in the Lagrangian frame of reference and are coloured according to their magnitude. (a) Similar to bacterial colonies the gel around the oil bubble is displaced in the direction of the bubble's minor axis and (b) their is little displacement in the plane perpendicular to the minor axis. Interestingly the gel near the apex of the bubble is displaced towards the bubble. These inwards displacements are indicative of a highly compressive (low ν) material, see Section 5.3.4. (c-d) The same pattern of displacements were observed around a bubble grown in 2.0 % agarose. Though in this case the measured displacement field was noisier due to artifacts at the edge of the field of view.*

towards the bubble slightly. This is the multipole effect that was predicted for highly compressible gels in Section 5.3.4 and Figure 5.15d,e. This multipole effect was observed in the displacements around bacterial colonies, however it was small enough to be largely smoothed out by noise in the azimuthally averaged displacement fields. For the bubbles in low agarose concentrations the effect was more pronounced, likely due to the larger displacement caused by the softer material. When the gel is compressible, the compressed volume of gel has to be replaced, hence the inward displacement of gel at the bubble apex.

6.4.4 Explaining the difference between oil bubbles and colony morphologies

In the previous sections I showed that the morphology of oil bubbles differ slightly from that of bacterial colonies. Oil bubbles are in general more prolate than colonies grown in the same concentration of agarose and are less "cuspy", conforming more to the ellipsoidal morphology predicted by the simple model outlined in Section 5.3. Both of these observations can potentially be explained by the difference in interfacial energy at the oil-agarose and *E. coli*-agarose boundary.

Given that the strain of *E. coli* used in Chapter5 (MG1655) are first grown in liquid media, where they form planktonic cultures without aggregation, they ought to have hydrophillic surfaces. Taking the view that bacterial adhesion is simply a reversible thermodynamic process (where the free energy in the system is minimised by the grouping of hydrophillic and hydrophobic surfaces), [170], a study showing that MG1655 *E. coli* prefer hydrophillic over hydrophobic surfaces, can be used as further evidence for their hydrophillic nature[12]. A study on the wetting angle of water droplets on the surface of *E. coli* biofilms have also shown *E. coli* to have a hydrophillic surface [172]. This is in contrast to the silicone oil which is hydrophobic. The oil bubbles will therefore have a higher interfacial energy when brought into contact with agarose (which is composed of > 96 % M9 media, which is predominantly water) than *E. coli*.

The differing interfacial energy between the oil-M9 media and *E. coli*-M9 media

[12]That *E. coli* prefer hydrophillic over hydrophobic surfaces is not irrefutable proof that they have a hydrophillic surface. It ignores the effect of pilli and flagellum on surface adhesion as well as the effect of irreversible adhesion by the van der Waals attractive force that can occur when the ionic strength of the fluid is large enough to disrupt energy barrier caused by the electrical double layer around the bacterium and the surface [171].

boundary should effect the fracture morphology for the following reason. In the previous chapter I showed that the crack tip radius of curvature is directly proportional to the elasto-fracture length scale, ℓ_{EF}, which is roughly the size of the distributed damage zone around the propagating crack tip. The elasto-fracture length scale depends on the interfacial energy between the fracturing substance and the fractured material and is given by

$$\ell_{\mathrm{EF}} = \frac{\Gamma}{E} = \frac{\Gamma_p + 2\gamma}{E}, \tag{6.13}$$

where Γ_p is the energy dissipated by plastic deformations (bond breakage, viscous dissipation, etc.). Therefore the crack tip radius of curvature, ρ, should be larger for the hydrophobic oil bubbles than for the *E. coli* colonies, which is exactly what we observe. Likewise the ratio between the minor and major axis of the fracture depends on $(\ell_{\mathrm{EF}})^{\sim 0.8}$, which explains why oil bubbles are wider than colonies grown in the same concentration of agarose, as seen in Figure 6.12.

The differing interfacial energy can also explain the increasing difference in crack tip radius of curvature between oil and *E. coli* at lower agarose concentrations. Γ increases with agarose concentration (see Chapter 7), whilst γ should be largely independent of agarose concentration (at low concentrations where the gel is > 90 % M9 media), therefore the relative contribution of γ to Γ becomes small compared to Γ_p at higher agarose concentrations. Consequently ρ becomes more similar between oil bubbles and *E. coli* colonies at higher agarose concentrations, as seen in Figure 6.4.3.

Estimating the interfacial energy between E. coli and agarose

The reasoning in the previous section can be taken a step further. If the interfacial energy between silicone oil and M9-media, γ_{oil}, is known then I should be able to use that information to estimate the interfacial energy between *E. coli* and Agarose, γ_{bac}.

Given that $\rho = \alpha \ell_{\mathrm{EF}}$, where α is a proportionality constant between 1.0 and 1.5 (reading from Figure 6.4.3), and assuming that Γ_p is the same for agarose being fractured by either *E. coli* colonies or oil bubbles, then Equation 6.13 can be rearranged so that

$$\Gamma_p = \frac{\rho_{\mathrm{oil}} E}{\alpha} - 2\gamma_{\mathrm{oil}} = \frac{\rho_{\mathrm{bac}} E}{\alpha} - 2\gamma_{\mathrm{bac}}, \tag{6.14}$$

where ρ_{oil} and ρ_{bac} refer to the crack tip radius of curvature measured for oil bubbles and *E. coli* respectively. Therefore γ_{bac} can be stated in terms of measurable quantities like so

$$\gamma_{\text{bac}} = \gamma_{\text{oil}} + \frac{E}{2\alpha}(\rho_{\text{bac}} - \rho_{\text{oil}}). \tag{6.15}$$

By measuring γ_{oil}, γ_{bac} can be determined.

Similarly γ_{bac} can be estimated using measurements of Γ taken from a mechanical test described in the next chapter. In that test a crack is propagated in air, so that

$$\Gamma_p = \Gamma - 2\gamma_{\text{air}}, \tag{6.16}$$

where Γ is calculated directly from the test and γair is the interfacial energy between agarose and air. A second Equation for γ_{bac} in terms of measurable quantities can therefore be set up as follows:

$$\gamma_{\text{bac}} = \gamma_{\text{air}} + \frac{1}{2}\left(\frac{E\rho_{\text{bac}}}{\alpha} + \Gamma\right) \tag{6.17}$$

In the next two sections I first measure γ_{oil} and γ_{air} and then, combined with measurements from Section 6.4.3 and Chapter 5, estimate γ_{bac} using Equations 6.15 and 6.17.

Measuring the interfacial energy between Oil and M9

Interfacial energies between the oil - M9 media and air - M9 media interfaces were measured using a Krüss pendant drop tensiometer. The effect of adding Nile red to the silicone oil was also measured. A pendant drop tensiometer measures the interfacial energy between two fluids by measuring the shape of a suspended droplet of one of the fluids in the other, Figure 6.14a. The shape of the droplet is described by the Young-Laplace equation,

$$\Delta P = \gamma\left(\frac{1}{R_1} - \frac{1}{R_2}\right), \tag{6.18}$$

where R_1 and R_2 are the principle radii of curvature at a particular point on the interface and ΔP is the pressure difference between the two fluids. ΔP results from gravitation plus some gauge pressure ΔP_0. The gravitational contribution

to ΔP is given by the droplet's buoyancy in the other fluid,

$$\Delta P \equiv \Delta P_0 + (\rho_c - \rho_d)gz \tag{6.19}$$

where ρ_d and ρ_c are the densities of the droplet fluid and surrounding fluid respectively, g is gravitational acceleration and z is the distance from an arbitrary plane. By fitting R_1 and R_2 over a range of z, γ can be measured.

It is important to note when measuring γ with a pendant drop tensiometer that the accuracy of the measurement is a function of the droplet volume. The accuracy of the measurement has been explored by Berry et al. [173]. They suggest using a dimensionless parameter termed the "Worthington number", W_0, that characterises the accuracy of the measurement ,

$$W_0 = \frac{(\rho_c - \rho_d)gV_d}{\pi\gamma D_n}. \tag{6.20}$$

This number scales the droplet volume by the theoretical maximum droplet volume prior to detachment of the bubble from the needle. Close to the maximum droplet volume measurements are more accurate because the interface shape will be more measurably perturbed by a change in γ.

Due to the small density difference between the silicone oil and water (26 kg/m^3), aiming for $W_0 \approx 1$ necessitates large droplets to be used compared to the maximum field of view of the Krüss tensiometer. The maximum W_0 attained with silicone oil in water was ~ 0.6.

Figure 6.14b-d shows the shape of a droplet of silicone oil permeated with Nile red for $W_0 \approx 0.02, 0.2$ and 0.6. The droplet changes from a more rounded shape at $W_0 \approx 0.02$ to one that is visibly deformed by gravity at $W_0 \approx 0.6$. This change is reflected in the measured interfacial energy in Figure 6.14e. The interfacial energy measurements increase with W_0 until they plateau at $W_0 \gtrsim 0.4$, the measurements marked in red were used to find the average and standard deviation of γ. The measurements with higher W_0 also correspond to those measurements with lower fit errors (inset Figure 6.14e), though taking only the fit errors one would assume a larger group of measurements to be valid than when looking at them combined with the W_0 number.

Interfacial energies were measured for the oil - M9 media and M9 Media - air boundaries along with calibration measurements of air in water. The interfacial energy between silicone oil and water was measured both with and without

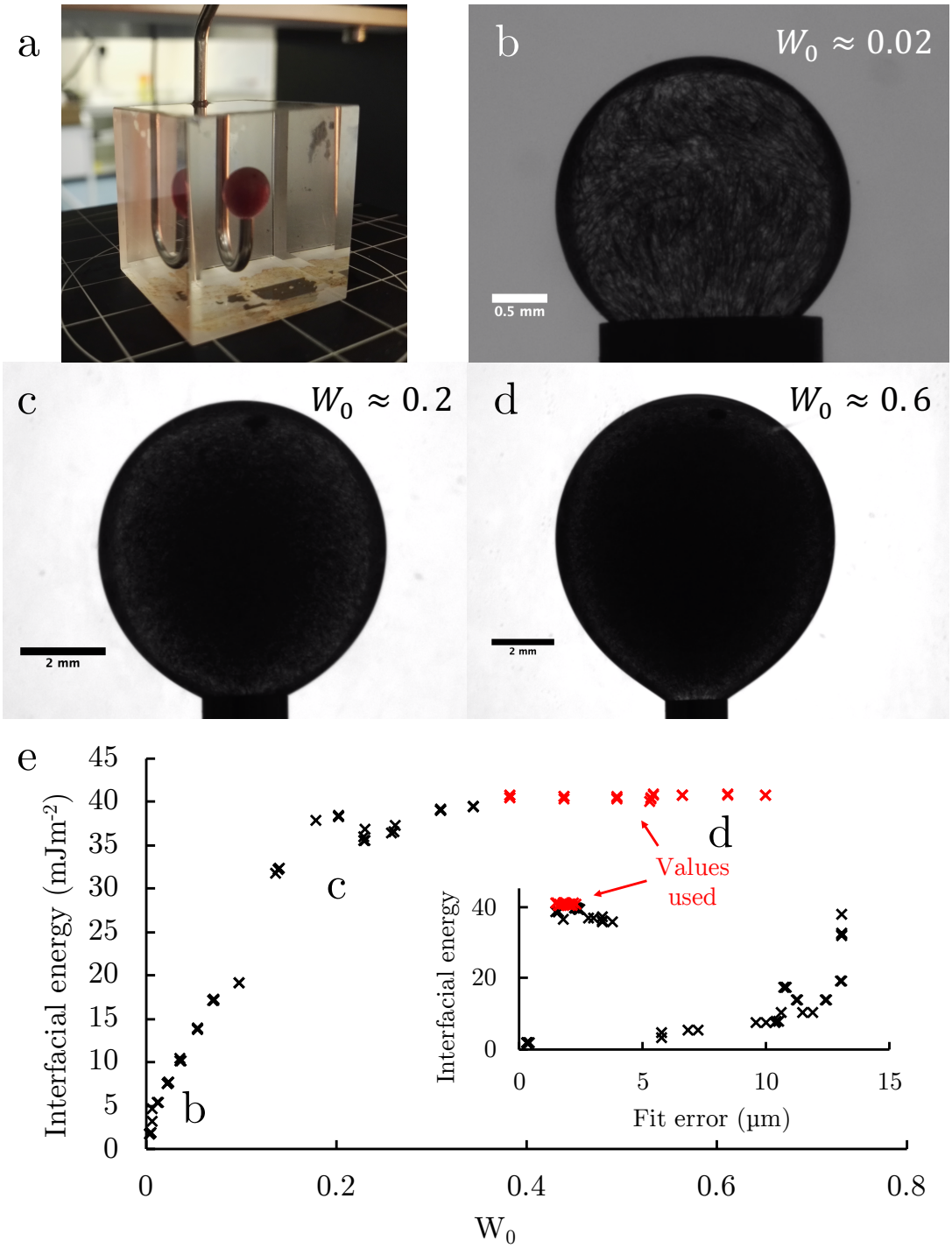

Figure 6.14 *Interfacial energies were measured using a pendant drop tensiometer. (a) Silicone oil is less dense than water so the capillary of the pendant drop tensiometer is inverted. (b-d) The density difference between water and silicone oil is small so care had to be taken to use large enough droplets so that the effects of surface tension became pronounced. (e) The Worthington number, W_0, characterises the droplet volume against the maximum achievable droplet volume. Energy measurements become reliable as $W_0 \to 1$.*

Interface	Interfacial Energy γ (mJ m^{-2})	Uncertainty $\delta\gamma$ (mJ m^{-2})
Air - Water	71.6	0.4
Air - M9 Media	70.9	0.2
Silicone Oil - Water	38.0	1.6
Silicone Oil + Nile Red - Water	39.4	1.7
Silicone Oil - M9 Media	28.1	1.1
Silicone Oil + Nile Red - M9 Media	28.2	1.3

Table 6.1 *The interfacial energy of various substance combinations.*

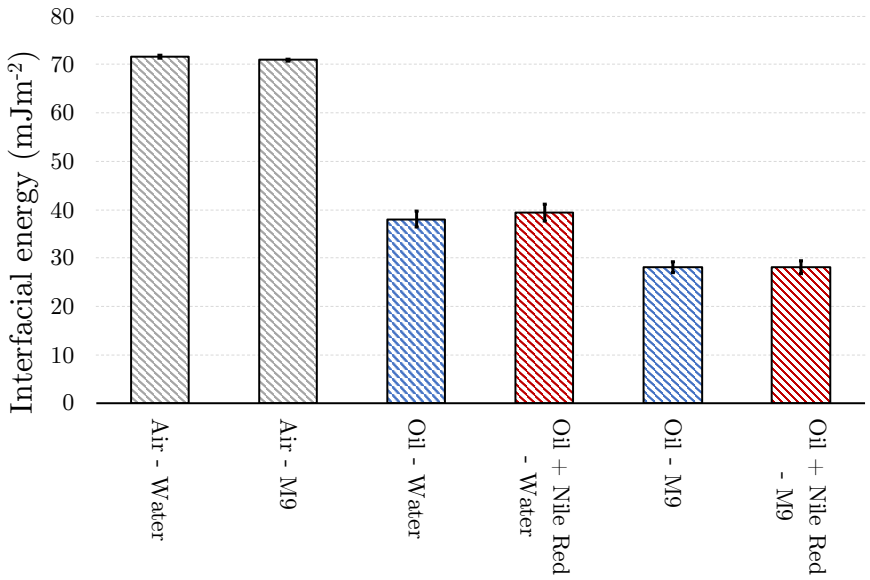

Figure 6.15 *The interfacial energy between various substances. The addition of Nile red to the silicone oil has no significant effect on interfacial energy. Whilst the addition of either the M9 salts or glucose to water decreases the interfacial energy.*

Nile red dispersed in the oil. This was done because in the oil bubble blowing experiments Nile red was added to the gel to make it fluorescent. The effect of M9 media on the interfacial energy was also investigated by comparison to measurements of the interfacial energy for the oil - water boundary. The room temperature was recorded to be 23.5 °C for all measurements.

Table 6.1 and Figure 6.15 show the results of the interfacial energy measurements. The interfacial energy of the air - water interface, $\gamma_{\text{air-water}}$, was measured to be 71.6(4) mJ m^{-2} which agrees with the literature value of 72 mJ m^{-2} at 25 °C. A value for $\gamma_{\text{air-water}}$ was measured before each other experiment to ensure that the tensiometer was clean.

When M9 salts (33.9 g/L Na_2HPO_4, 15 g/L KH_2PO_4, 5 g/L NH_4 Cl and 2.5 g/L NaCl) were added to the water only a small change in the interfacial energy at the air interface was observed ($\gamma_{\text{air-M9}} = 70.9(2)\,\text{mJ}\,\text{m}^{-2}$). In contrast when M9 salts were added to the water surrounding silicone oil the interfacial energy decreased by $10\,\text{mJ}\,\text{m}^{-2}$. This is likely due an increased concentration of co-ions in the surrounding fluid [174]. The addition of Nile red to the silicone oil had no significant effect on the interfacial energy.

Estimating the interfacial energy between E. coli and agarose gel

Using measurements of the interfacial energy between Nile red imbued silicone oil and M9 media, and by measuring the differences in the crack tip radius of curvature between oil bubbles and *E. coli* colonies (Figure 6.16a), the interfacial energy between *E. coli* and M9 media (γ_{bac}) can be estimated using Equation 6.15, Figure 6.16b.

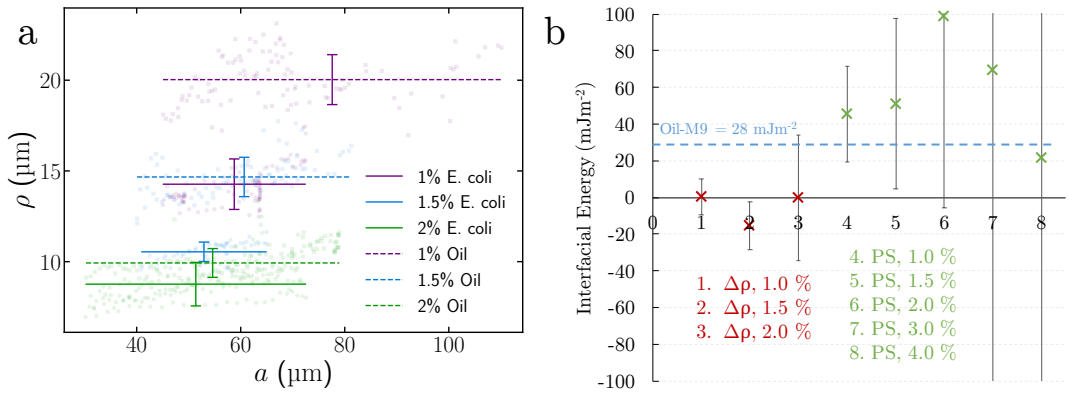

Figure 6.16 *Estimating the interfacial energy between E. coli and M9 media. (a) The plateau region from figure 6.8 is used to calculate the average and standard deviation of the crack tip radius of curvature, ρ, in each agarose concentration. The ρ measured for Oil bubbles is larger than that measured for E. coli colonies. (b) The interfacial energy calculated using Equations 6.15 (red) and 6.17 (green). Δρ refers to measurements made using the difference in crack tip radius of curvature whilst PS refers to calculations using values from the mechanical tests in the next chapter. The uncertainty in energy estimates made using values from the mechanical tests are very large and have been cropped in the figure.*

The uncertainty in the interfacial energy estimate using Equation 6.15 is given

by

$$\delta\gamma_{\text{bac}} = \sqrt{\left(\frac{E}{2\alpha}\delta\rho_{\text{bac}}\right)^2 + \left(\frac{E}{2\alpha}\delta\rho_{\text{oil}}\right)^2 + \left(\frac{E}{2\alpha^2}(\rho_{\text{bac}} - \rho_{\text{oil}})\delta\alpha\right)^2} \tag{6.21}$$

where δ implies the uncertainty in a given measurement. The uncertainty in measurements of ρ is equal to the standard deviation in ρ measurements from Figure 6.16a whilst α was set to 1.25 ± 0.1 using Figure 5.7b.

Interfacial energy estimates made by comparing crack tip radius of curvatures (Equation 6.15) are marked in red in Figure 6.16b. In general $\delta\gamma_{\text{bac}} \approx 0\,\text{mJ}\,\text{m}^{-2}$. The $\delta\gamma_{\text{bac}}$ estimates from oil-colony comparisons in different concentrations of agarose are self consistent within uncertainty. I would expect, given that this strain of *E. coli* are miscible in water[13], for γ to be less than zero so these estimates are at least plausible. Of course using the miscibility of planktonic cultures to estimate $\delta\gamma_{\text{bac}}$ ignores the possibility that the surface chemistry of the *E. coli* changes when they come into contact with a solid or are placed in close proximity to other cells. Such surface changes have been observed in biofilm forming bacteria, where biofilm initiation mechanisms are set into motion upon encountering a surface [175].

The interfacial energy at the colony boundary can also be estimated using Equation 6.17, these estimates are plotted in green in Figure 6.16b. However in this case the uncertainty is dominated by the uncertainty in Γ, $\delta\Gamma$, so that

$$\delta\gamma_{\text{bac}} \approx \frac{\delta\Gamma}{2}. \tag{6.22}$$

The resulting uncertainties are much larger than uncertainties for estimates made using Equation 6.15 and they have been cropped from the Figure 6.16. This method of estimating interfacial energy could prove more useful than the ρ comparison method if the fracture properties of agarose could be better characterised.

Overall, the method discussed in this section may present a novel way of measuring the interfacial energy of typically miscible substances such as bacteria

[13]Consider an infinite volume of a substance. If a region of that substance is removed and replaced with one that has a positive interfacial energy, then the free energy of the system will be minimised by minimising the interfacial area between the two substances. On the other hand, if the replacing substance has a negative interfacial energy the the free energy of the system will be minimised by the mixing of the two substances. Hence my reasoning for miscible substances having negative interfacial energies.

and growth media. However, there are many issues that need to be addressed if these measurements are to be made reliable. Foremost amongst these issues is the effect of agarose on the interfacial energy. The agarose biopolymer is hydrophillic so it stands to reason that the interfacial energy between silicone oil and agarose[14] may be larger than that measured between silicone oil and the gel solvant (M9 media in this case). For the measurements in this section I have simply assumed that it will have either no effect on the interfacial energy or will have the same effect in the presence of *E. coli* or silicone oil.

6.5 Conclusions

The primary conclusion from this chapter is that bacterial colonies submerged in agarose grow into morphologies almost identical to the morphology of oil bubble blown into the same agarose over the same length and time scales. The same pattern of displacement is observed around the bubbles as the colonies and the same "cuspy", super-ellipsoidal morphology is achieved. Whilst the oil bubbles were found to be more prolate in lower concentrations of agarose, conforming closer to the ellipsoidal morphology predicted by LEFM, this difference can plausibly be explained by the difference in interfacial energy at the oil-agarose and *E. coli*-agarose boundary.

The secondary aim of this chapter, to identify the mode of fracture using the rate at which oil flowed from the reservoir into the bubble and the initiation pressure of the bubble was less successful. The bubble initiation pressures and flow rates did not match those expected by the simple model and were extremely inconsistent. In the next section on future work I will outline some schemes for improving these measurements.

[14]The interfacial energy needs to be carefully defined here, as when considering a solid-liquid interface the interfacial energy is not the same as the interfacial tension. The interfacial energy is the work done in bringing a molecule from the bulk of the material to the interface, whereas the interfacial tension considers the work done in displacing the solid phase in addition to the interfacial energy. Hence interfacial tension measurements for agarose like those presented in [176] are misleading for the purpose of determining the effect of agarose on interfacial energy.

6.6 Future work

The central problem in this experiment was a combination of capillary pressure and the inability to rapidly change the pressure in the oil reservoir. This issue meant that the oil bubble grew rapidly at the start of the experiment, preventing morphological and displacement measurements in the period where they were most crucial. A few solutions immediately present themselves. First the oil could be degassed. This would allow the syringe plunger that controlled the pressure inside the oil reservoir to be moved much faster without creating gas bubbles. Secondly the simple bang-bang control system could be upgraded to a proportional–integral–derivative (PID) controller which would apply a correction proportional to difference in pressure between the set point and the measured pressure in the oil reservoir. Implementation of a PID controller would prevent the build up of pressure oscillations that were a result of gas ingress. If these oscillations could be prevented then the system would have a higher tolerance for gas ingress at the start of the experiment. Third, an even more viscous Silicone Oil (> 100 Stoke) could have been used, however this would make filling the system without introducing air bubbles even more difficult. Finally the oil reservoir could simply be made smaller, perhaps using a diaphragm that could fit onto the 4D stage of the SPIM setup. A smaller reservoir would result in more a rapid pressure response as there would be less backlash due to the stretching of elastic components (the FEP tubing).

Alternatively, to observe the change in fracture mode using flow rate, it may be simpler to scale up the oil injection system so that capillary pressure becomes negligible compared to the either the planar fracture pressure or cavitation pressure. This could be achieved by using a capillary with opening diameter $\sim 1\,\mathrm{mm}$ and a gel with $\ell_{\mathrm{EF}} \sim 1\,\mathrm{cm}$. Double network gels are a likely candidate for experiments of this kind, they combine two polymers with different cross-link densities to create a gel that has the high fracture energy of a poorly cross-linked gel and the Young's modulus of an abundantly cross-linked gel [177–179]. However, the production of these gels is complex and creating them in $\sim$100 ml volumes results in the separation of the polymer networks without careful preparation. Soft rubbers may also provide a suitable elasto-fracture length scales, with products such as EcoFlex$^{\mathrm{TM}}$ becoming extensively used in investigations into soft fracture [180–182].

The use of fracture morphology to measure the interfacial energy of miscible

substances such as bacteria bears further exploration. If the fracture properties of the gel could be more accurately measured, then by using bacteria with more hydrophillic/ hydrophobic surfaces, the explanation for the difference between colony and oil bubble morphology described in Section 6.4.4 could be confirmed. The species *P. putida* might be a useful candidate for testing as it has been shown to degrade various hydrophobic substrates such as toluene and so should have a more hydrophobic surface [183]. The explanation could also be tested by neutralising the surface charge of the bacteria with chitosan. Reportedly this neutralisation increase the hydrophbicity of bacterial cell surfaces significantly [184] and could be used to tune the colony shape.

Chapter 7

The Elastic and Fracture Properties of Agarose

7.1 Introduction

In previous chapters values for the elastic modulus, E, and fracture energy, Γ, of agarose have been used extensively. In this chapter, details of the measurement of these properties are given. These measurements involved the creation of a custom apparatus with which Rivlin and Thomas's pure shear method of measuring fracture energy could be applied to agarose, an extremely soft and brittle hydrogel.

There exists no standardized method for measuring the fracture properties of a hydrogel. This lack of standardization stems from hydrogels typically being both soft and brittle, which presents many problems when trying to apply the standard fracture tests that were designed for rubbers or metals [185]. For example, one of the more common methods of measuring the fracture properties of rubbers and tough hydrogels is the tearing or "trouser" test [186–188]. In the tearing test a rectangular cuboid sample is cut half way along it's length and the two arms or "trousers" created are clamped. The fracture energy can then be determined from the force required to extend the cut, Figure 7.1a,b. For tough materials this method works well as the weight of the uncut part of the sample is small compared to the force needed to extend the cut. For soft and brittle gels like agarose this is not the case, the cut would extend under the weight of the uncut

section of the sample. Indeed even the stresses exerted whilst handling the cut sample would be sufficient to extend the cut. In addition, for many of these simple mechanical tests (such as the tearing test and single-edge-notched test [150, 186, 189]) the relationship between force measurements and the fracture energy is found through empirically derived relationships which are dependent on the geometry and stress-strain relationship of the sample [73, 186]. Therefore methods more suitable for measuring the fracture properties of extremely soft and brittle hydrogels must be sought.

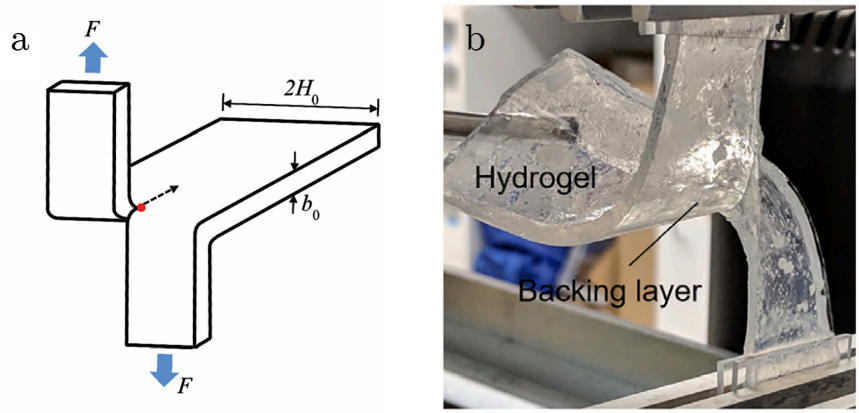

Figure 7.1 *An example of a tear test. (a) The rectangular cuboid sample is cut to form two arms or trousers which can be clamped. The strain energy release rate is given by* $G \approx 2F/b_0$*, where* F *is the force applied to the arms and* b_0 *is the thickness of the sample [186]. (b) Whilst this test is very simple, in practice it can only be performed when the weight of the uncut section of the sample is small compared to* F*. Making it useful only for tough hydrogels (pictured). Images reproduced from [186] and [190] respectively.*

The pure shear test provides one such method for measuring the fracture properties of a soft and brittle material. The pure shear test measures the critical strain energy release rate, G_c, which for quasi-static fractures (where no energy is lost to viscous dissipation) is equal to the fracture energy, Γ. The test was one of several designed by Rivlin and Thomas to measure G_c independent of sample geometry [55]. For soft materials, the pure shear test is the most practical of the methods suggested as large sections of the test piece are clamped, providing support for materials which might otherwise fracture under their own weight.

This chapter is structured as follows. First the theory behind the pure shear test is explained. Next, the practical implementation of the test is detailed, problems stemming from the extreme softness and brittleness of the gel are addressed. Experimental results are then presented and discussed in the context of the studies

in the previous chapters. Finally, possibilities for improvement to the method and opportunities for further study are discussed.

7.2 The pure shear test

In the pure shear test a long thin strip of material with length, l, height, h and thickness, t, with $l \gg h$ and t, is clamped along its long edges to a loading device, Figure 7.2. A notch of length $c \gtrsim h/2$ and $\ll l$ is made in one side of the sample, positioned centrally between clamped edges. An extension Δ is then imposed upon the clamped edges of the strip. At some critical extension Δ_c the tip of the notch will fracture and a crack will propagate along the sample.

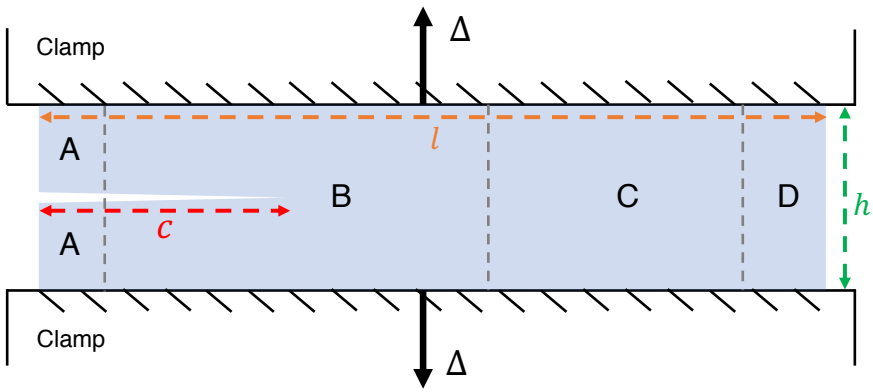

Figure 7.2 *The pure shear test configuration. A thin strip of material of width w, height h and thickness t (into the page) is held between rigid clamps and subjected to extension, Δ. At the instance of crack propagation the deformation in the material can be split into four regions, as described in the text. The thickness, t, of the sample is not shown.*

When Δ_c is reached, the deformation of the strip of material can be split into four regions as shown in Figure 7.2. In region A, the sample is largely undeformed; in region B, the condition that $l \gg h$ and $c \gtrsim h/2$ enables the translational invariance of the stress and strain fields around the crack tip, meaning that a *fixed* region around the crack tip is in some complex stress state; in region C, the condition that $l \gg c$ means that far ahead of the crack tip there is a region that is unaffected by the crack tip and therefore under a spatially uniform deformation, this region is in a state of pure shear[1]; finally, in region D, some slight departure

[1] i.e. if the stretch $\lambda = (h + \Delta)/h$, the principle stretches in region C are $\lambda_h = \lambda$, $\lambda_t = 1/\lambda$ and $\lambda_l = 1$. This is the definition of a pure shear stretch.

from the pure shear state occurs due to the presence of the force-free edge of the sample [186]. The condition that $l \gg t$ ensures that fracture does not propagate unevenly along the axis of propagation so that the cross sectional area of the crack remains constant.

When the crack propagates by a length dc, provided that the distance between the clamps does not change (so that the stress state in region B remains constant), region B is simply translated along the direction of crack propagation[2]. *This causes region A to grow at the expense of region C.* Therefore a volume $ht \cdot dc$ in a state of pure shear is being transformed to an undeformed state. The infinitesimal change of the elastic energy stored in the sample, dU_e, is therefore $-W(\Delta)ht \cdot dc$, where $W(\Delta)$ is the elastic energy density in the pure shear region, and is some function of the extension. The energy release per unit crack area evaluated at Δ_c (the definition of G_c) is therefore

$$G_c = \frac{1}{t}\left(\frac{dU_e}{dc}\right)_h = -W(\Delta_c)h. \tag{7.1}$$

$W(\Delta)$ can be found by measuring the force-load response of an unnotched sample (where the entire sample is approximately in the pure shear configuration). In an unnotched sample

$$W(\Delta) = \frac{F\Delta}{h_u t_u l_u}, \tag{7.2}$$

where h_u, l_u and t_u are the dimensions of the unnotched sample. Given that $h = h_u$, $l = l_u$ and that the test is performed at constant extension rate rather than constant force ($F(\Delta)$ may be non-linear), the critical strain energy release rate can be rewritten as

$$G_c = \frac{1}{t_u l}\int_0^{\Delta_c} F(\Delta)d\Delta. \tag{7.3}$$

If the force load response is linear then the G_c calculation can be simplified using the Young's modulus, E, so that

$$G_c \approx \frac{E\Delta_c^2}{2h_u}. \tag{7.4}$$

[2]The consequence of the condition that the distance between the clamps does not change, is that G_c must be measured at the instance of crack initiation.

7.3 Putting the pure shear test into practice

Performing the pure shear test on agarose presented numerous problems due to the gels extreme softness and brittleness . Foremost amongst these was the problem of clamping the gel. In order to apply a displacement, the gel must be held in some way, this introduces a boundary stress. If the boundary stress exceeds the stress at the tip of the notch, then the sample will fracture at the boundary instead of the notch, invalidating the measurement. Even if the boundary stress is lower than the notch tip stress it will limit the maximum Δ that can be reached during measurement of $W(\Delta)$. Mounting the sample into clamps is also a problem. The pure shear test requires long thin sheets of agarose. These sheets will bend under their own weight, and the stresses applied when manipulating the sheets into clamps are enough to cause premature fracture.

7.3.1 The pure shear test apparatus

To solve both these problems, a custom mould was made that could be disassembled into a pair of clamps, Figure 7.3. This disassembly could be carried out whilst the mould was attached to a tensile testing machine. In this way the sample was never exposed to external forces before a test began.

The mould/clamps consisted of two Perspex L frames, one of which could be attached via a threaded hole to the base of a LS5 AMETEK universal testing machine, Figure 7.3. The other attached to a Lloyd YLC series 20 N load cell via an annular ring with grub screws. The load cell is a strain gauge that measures the force applied to it via the change in electrical resistance of a long conductor that is stretched by the applied force. The load cell was calibrated using 100 g, 200 g and 500 g weights. The L frames were separated by a Perspex block, 2 cm in height and 14 cm in length. They were held together by Perspex blocks with holes and slots machined to allow the entire mould to be bolted together. The inner section of the L frames held two U-shaped spacers, 3 mm thick and with 10 cm between the forks of the U. The Perspex blocks were coated with Vaseline to prevent leaks when the agarose was poured into the mould. The Vaseline also prevented adhesion of the agarose to the Perspex.

To solve the clamping problem, a 10 cm strip of the hooked side of a Velcro pad was adhered to the L frames. Molten agarose was poured over the Velcro so

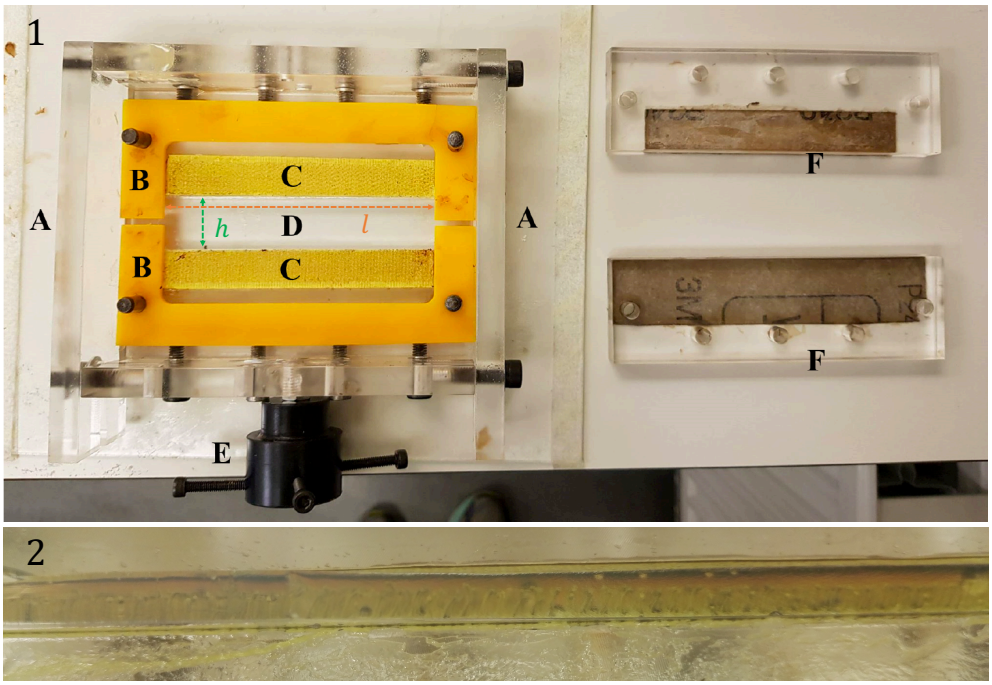

Figure 7.3 *1): The mould used to create pure shear test samples. Molten agarose was poured into the space between the yellow spacers before the secondary blocks were fixed in place above the spacers. A) A glass pane was used to keep the components of mould aligned. B) 3 mm thick, U shaped, spacers set the thickness of the agarose samples. Gaps were left between the spacers to prevent overfilling of the mould. C) Velcro strips were used to hold the agarose sample in place once it had set. D) A Perspex block setting the spacing between the Velcro pads. h and l from Figure 7.2 are shown. E) Annular ring with grub screws for attachment to tensile testing machine. F) Secondary Perspex blocks used as the opposite half of the "clamps". Strips of sand paper are adhered to the blocks. These blocks are a hold over from a previous design and were kept only to avoid changing experimental conditions. 2: Velcro hooks embedded in gel.*

that the Velcro was embedded in the gel. In this way the boundary stress at the connections between the frame and the gel was distributed across the Velcro hooks, lowering the stress concentration in the gel.

Slippage of the Velcro pads was a concern. If the stiffness of the adhesive layer on the Velcro pads was insufficient then a combined response of the adhesive layer and the agarose sheet to any applied displacement would be measured instead of the agarose sheet alone. The stiffness of the adhesive layer of the Velcro pads was checked by sticking the two L frames together using the Velcro pads. When this was done the 20 N load limit of the load cell was reached immediately at an extension rate of $0.01\,\mathrm{mm\,s^{-1}}$, this meant that the stiffness of the adhesive layer far exceeded that of the agarose and that the vast majority of deformation occurred in the agarose sheets during experiments. The lack of movement of the Velcro pads was confirmed in experiment video recordings.

Two moulds were made, one for performing the pure shear test and the other for measuring $W(\Delta)$. Samples for both tests were poured from the same batch of agarose to ensure consistency between Δ_c and $W(\Delta)$ measurements. $W(\Delta)$ was measured for each experiment instead of only once so that tensile modulus of the agarose could be ascertained. Repeated measurement of $W(\Delta)$ also gave some measure of the consistency of the gel between experiments.

7.3.2 Pure shear test protocol

Agarose was prepared in a similar manner to the method detailed in Section 4.3.1. 40 ml of agarose was prepared for each sample by first melting the required concentration of agarose in M9 media at 85 °C for 1 hour. The molten agarose was then transferred to a 50 °C water bath where a stirring rod was added, the agarose was stirred at 300 rpm for 1 hour until it had equilibrated with the temperature of the water bath. The molten agarose at 50 °C was then poured into the moulds and allowed to set for 30 minutes. Cling film was placed over the clamps to reduce evaporation. After 20 minutes the gel was cool to the touch. After 30 minutes the moulds were transferred to the universal testing machine for disassembly and testing, they were transported on a glass pane to ensure that they remained flat.

The mould was first screwed into the base of the universal testing machine before the cross head, with attached load cell and plastic cylinder, were lowered into the annular ring attached to the top of the mould. The annular ring was attached

to the plastic cylinder using four grub screws, care was taken that the force measurement before and after the attachment was the same, this meant that there were no off axis force acting on the mould, Figure 7.4b. The Perspex blocks on the sides of the mould were then removed and the Perspex block between the L-frames was carefully slid out from between them to prevent damage to the agarose sheet, Figure 7.4a. The tabs of agarose between the forks of the U-shaped spacers were removed using a scalpel. Then for one sample a notch was cut from the middle of the edge of the agarose sheet approximately 3 cm horizontally into the sample using a scalpel, the other sample was left unnotched.

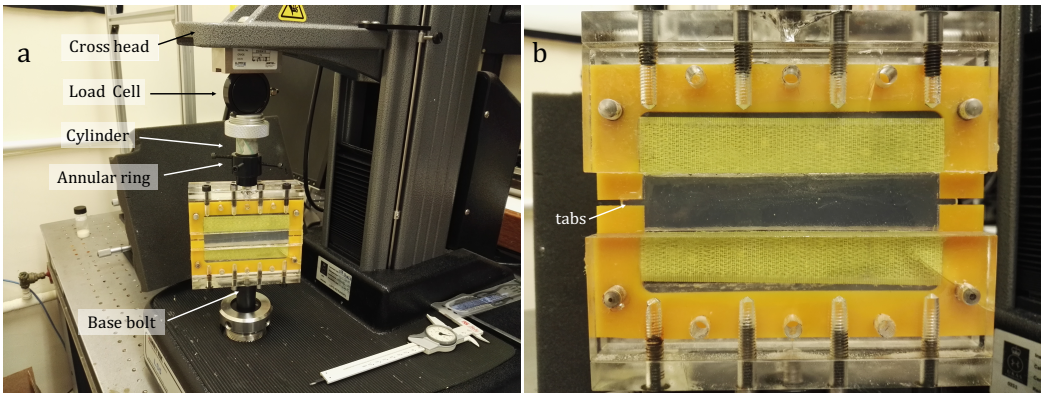

Figure 7.4 *The pure shear test rig is mounted to the universal testing machine. (a) The mould was first screwed into the base, then the cross head was lowered so that the load cell, with attached cylinder, fit into the annular ring. The grub screws on the annular ring were tightened whilst being careful not to introduce additional stress (which could be measured by the load cell). (b) The agarose tabs between the yellow U-shaped spacers were removed with a scalpel.*

When the notch was initially cut into the sample, the surfaces of the notch were held together by the surface tension of a layer of water expelled from the gel. If this layer were allowed to remain, then an additional energy ($\approx 2 \times 3\,\text{cm} \times 3\,\text{mm} \times 72\,\text{mJ}\,\text{m}^{-2} = 1.2 \times 10^{-5}$ J) would be needed to separate the surfaces. This additional energy meant that the crack only began to propagate after the two surfaces had separated, obscuring the point where fracture propagation began. Another issue with the initial setup of the notched sample was that the tip of scalpel-cut notch may have been in a different state between experiments, e.g. the notch tip may have a different initial radius of curvature dependant on how the sample was cut. To remove the layer of water and ensure that the crack tip was uniform between experiments, the extension and load readings of the testing machine were first "zeroed", and then the notch was opened by applying an extension with the cross head. The layer of water was removed with a paper towel.

Further extension was applied with the cross head until the notch fractured, at which point the cross head was returned to the zero extension point. By fracturing the notch by a couple of mm prior to each experiment it was assumed that the crack tip would be in a more reproducible state.

Samples were stretched by applying a constant extension rate of $0.01\,\mathrm{mm\,s^{-1}}$ to the cross head of the universal testing machine, the force applied to the sample was measured by the load cell, Figure 7.5. The extension rate used was slower than the rate at which the Γ of another type of agarose has been observed to be dependent on the extension rate[3] [150], this independence is verified for the type of agarose used in this work in Section 7.4.4. A webcam was used to record the time at which the notch fractured and began to propagate. The time of fracture was used to determine the corresponding critical extension (Δ_c). The fracture was allowed to propagate until the sample had separated into two halves along the fracture line. After separation the thickness of the samples was measured with calipers.

There was an error in the frame rate of the camera. Recordings appeared slightly shorter in duration than the true duration of the experiment. To account for this duration mismatch, the time recorded by the testing machine's data log was multiplied by the video duration divided by the true experiment duration. The time of fracture in the data log then matched the time of fracture observed in the video data. The true critical extension could then be found.

It was observed that there was a residual negative load after the samples had been split in two by the fracture, Figure 7.5. This residual load was taken to be some kind of self-stressing that occurred whilst the agarose set or possible due to stresses induced by drying of the surface of the gel [191]. The residual negative load indicated that the gel was already in a stressed state at the start of the experiment. Indeed when the two halves of the fractured sample were put back together, a gap remained between the two halves, suggesting that the sample was deformed at the start of the experiment. Figure 7.6 shows the degree of residual stress[4] in the agarose sheets. The magnitude of the stress increased with agarose concentration. No bias in the amount of residual stress present in notched and unnotched samples was observed, as shown in the inset.

[3] In a study by Kwon et al. a stiffer and tougher type of agarose was observed to have a rate independent fracture energy when cross head speeds of $\lesssim 0.03\,\mathrm{mm\,s^{-1}}$ were used.

[4] The residual stress is the load recorded at the end of the experiment divided by the horizontal cross section of the sheet ($l \times t$)

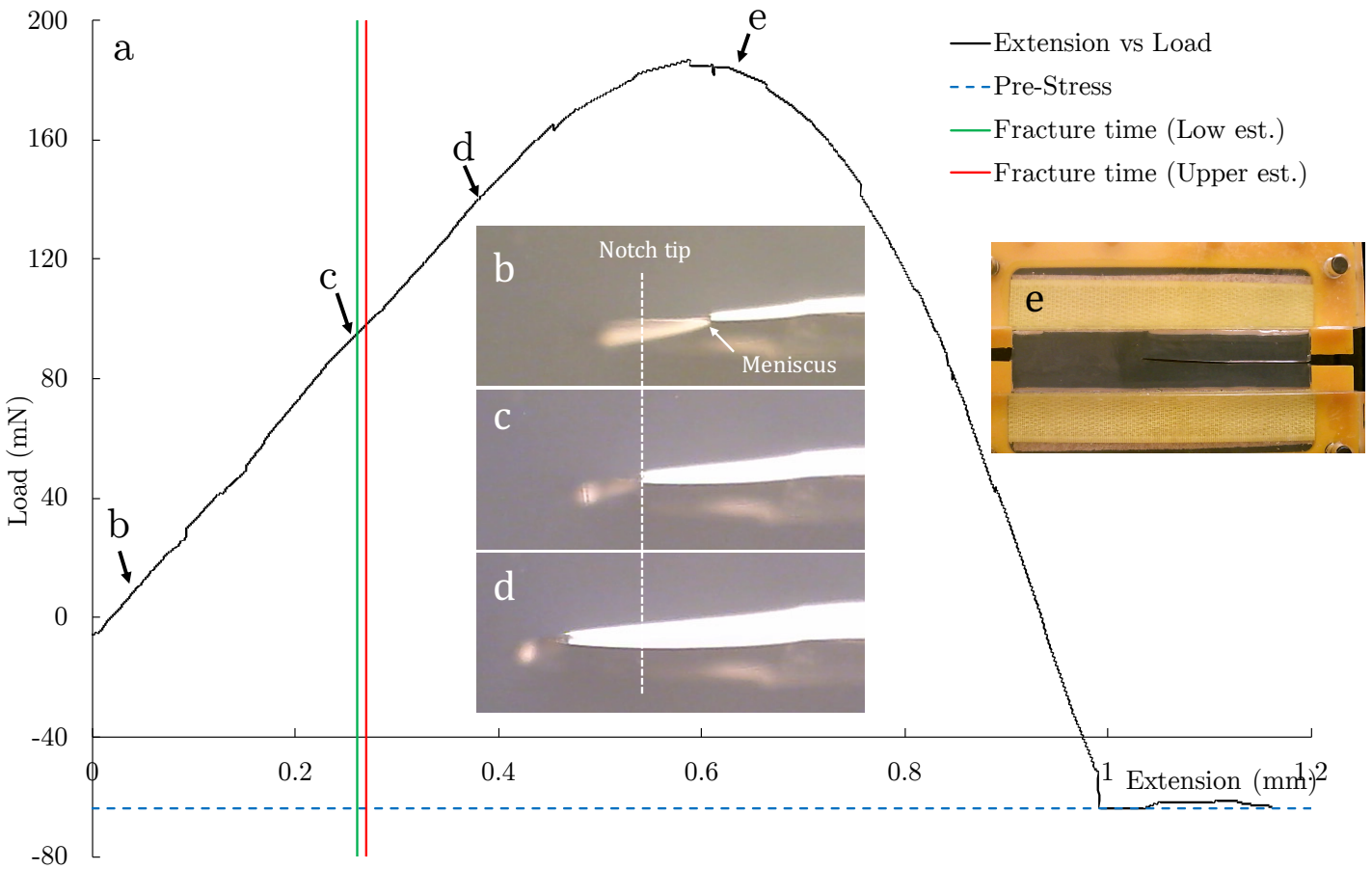

Figure 7.5 *An example of a load vs extension curve for the pure shear test. (a) The load vs extension for a* 2.1 mm *thick notched sample of 2% agarose, extended at* $0.01\,\mathrm{mm\,s^{-1}}$. *The load starts slightly negative due to the removal of the water holding the crack faces together. The stress at the end of the test, when the agarose sample has been split in two, is also negative due to a residual stress created either during setting or due to the drying of the gel surface. The inset images b, c, d and e show the notch tip at various stages of the experiment. Early on (b) the surfaces near the tip of the notch are held together by water expelled from the gel. At point (c) the tip of the notch fractures. The notch then propagates across the entirety of the sample (d, e).*

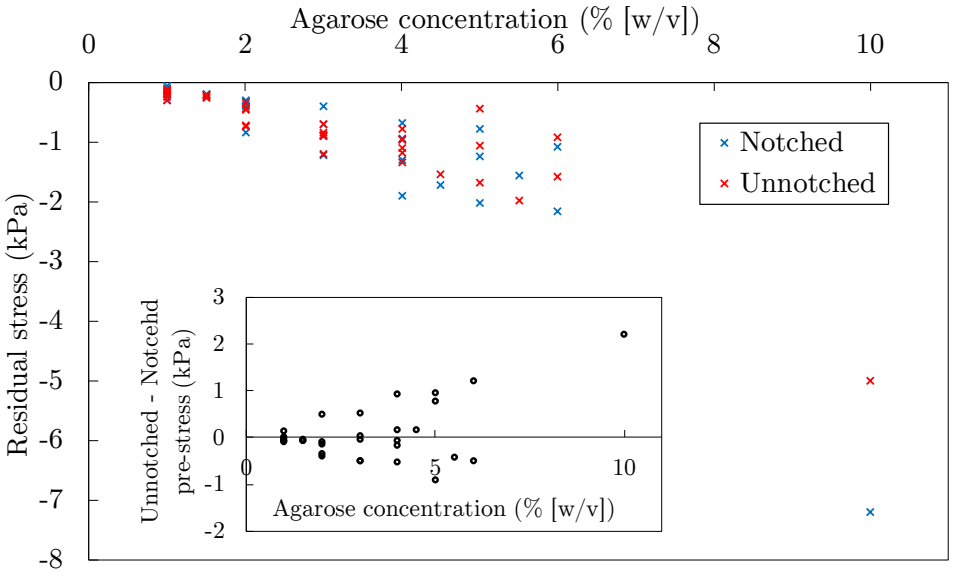

Figure 7.6 *The residual stress present in the agarose samples. The residual stress present at the end of each experiment is plotted as a function of agarose concentration. The stress is always negative (contractile) and increases in magnitude with increasing concentration. Inset: the difference in residual stresses measured between unnotched and notched samples, differences appear to become more variable with concentration but no significant bias is evident.*

To account for the residual stress, the load-extension (i.e. F-Δ) curve (e.g. Figure 7.5) was first shifted in load so that the final load measurement was equal to zero. Linear regression was used to fit the line $F = m\Delta + c$ to the curve between the start of the test and the fracture point. The virtual extension, Δ_v, imposed by the residual stress was therefore c/m. Δ_v was added to the initially measured Δ_c to get Δ_c', the true critical displacement. The same shift was applied to the unnotched sample (based on its residual stress), the unnotched load-extension relationship was fitted using only the first 50% of the data before the unnotched sample fractured to avoid potential non-linear regions, Figure 7.7. Γ was then measured by integrating under the shifted F-Δ curve of the unnotched sample (plus extrapolated linear region) from $\Delta = 0$ to Δ_c' as per Equation 7.3. The area integrated is shown by the shaded area in Figure 7.7.

Upper and lower estimates of the fracture energy (Γ_{high} and Γ_{low}) were calculated using upper and lower estimates of the fracture time. The previous analysis was repeated for upper and lower estimates of Δ_c. At the agarose concentrations used in the colony growth experiments (0.6, 1, 1.5, 2.0, 3.0 4.0%) at least five sets of samples were tested. A couple of samples at 5.0% and 6.0% and one sample at

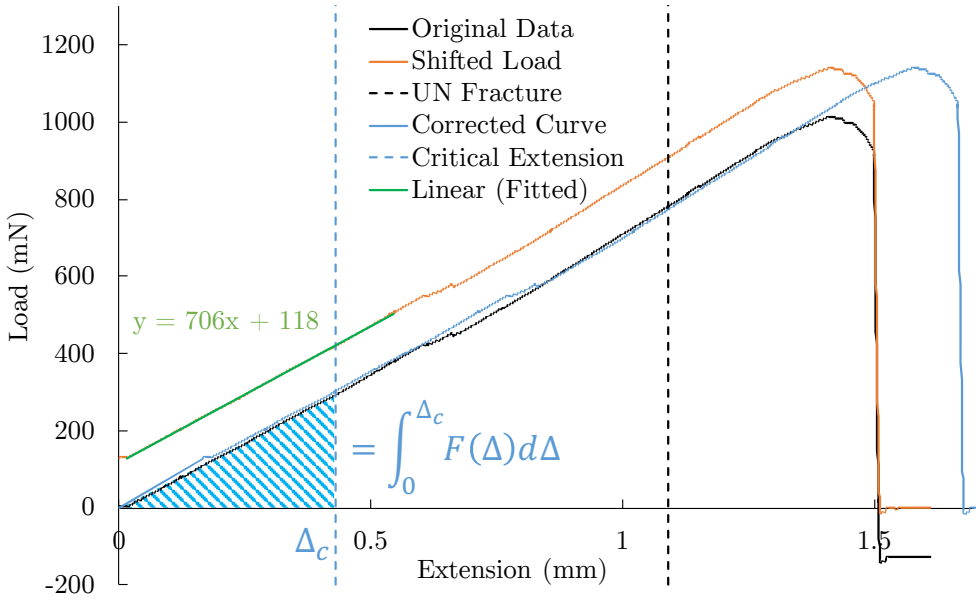

Figure 7.7 *The transformations applied to the force extension curve of a* 3.0 mm *thick unnotched sample corresponding to the notched sample in Figure 7.5. The original force extension data for the unnotched sample is shown by the black line, along with a dashed line indicating the time of its fracture. First the curve is shifted in load (orange), then a region between the lag time and 50% of the fracture extension is fit (green). The blue line shows the force extension curve after all corrections have been applied. Note that the sample was cut with a scalpel after the failure point, this is the cause of the sharp decrease in load at the end of the test. The sample was cut to reduce unnecessary data collection.*

10% were tested to better extrapolate beyond the range used in the colony growth experiments.

7.4 Experimental results and discussion

7.4.1 The fracture energy of agarose

Figure 7.8 and table 7.1 show the fracture energy, Γ, measured for each concentration of agarose tested. The values given are averages of at least 5 measurements made at each concentration. The uncertainty in Γ, $\delta\Gamma$, is estimated to be the maximum between the propagated uncertainty, $\delta\Gamma_{\text{prop}}$, and the standard deviation, σ_Γ, of measurements, i.e. $\delta\Gamma = \max(\delta\Gamma_{\text{prop}}, \sigma_\Gamma)$. The propagated uncertainty, given N measurements of Γ_{high} and Γ_{low}, is calculated using the variance formula, i.e.

$$\delta\Gamma_{\text{prop}} = \frac{1}{N}\sqrt{\sum_i^N \left(\frac{\Gamma_{\text{high},i} - \Gamma_{\text{low},i}}{2}\right)^2}. \tag{7.5}$$

The fracture energy increases with agarose concentration, C, and obeys the power law:

$$\Gamma = (0.16 \pm 0.02)C^{1.2\pm0.1}. \tag{7.6}$$

Though at low concentrations this trend is obscured by uncertainty in the measurements. The uncertainty in the measurements increases with concentration.

Agarose concentration (% [w/v])	**Fracture Energy** Γ (mJ m^{-2})	**Uncertainty** $\delta\Gamma$ (mJ m^{-2})
Water-Air boundary (20 °C)	72 [192]	0
1.0	190	20
1.5	230	50
2.0	420	150
3.0	480	190
4.0	720	160
5.0	1490	360
6.0	1500	160
10.0	2570	360

Table 7.1 *The fracture energy of agarose at various concentrations. The surface energy of the water air boundary at* 20 °C *is included for comparison.*

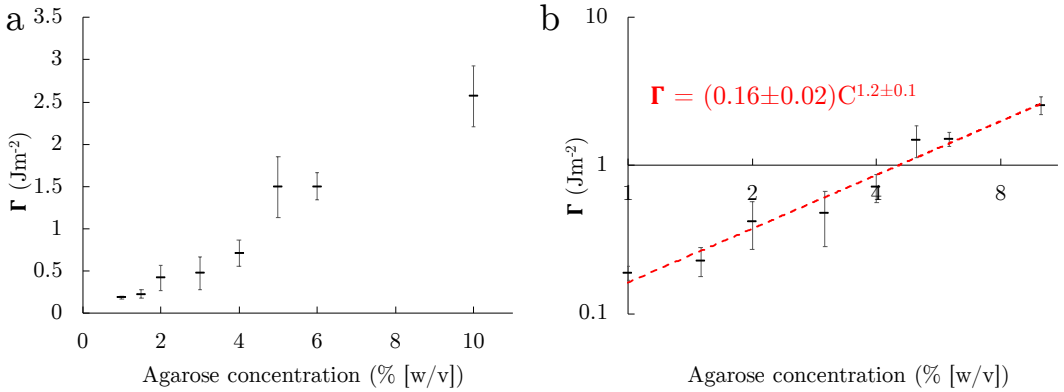

Figure 7.8 *The fracture energy, Γ, of agarose as a function of agarose concentration. (a) Γ increases with agarose concentration, however the uncertainty in the measurements obscures this trend unless concentrations of 4% and higher are included. Points are weighted averages of between 5 and 8 repeats below 4%, error bars are given by the maximum of the standard deviation between experiments and Equation 7.5. (b) A power law fit to the data.*

The scaling of Γ with agarose concentration can be estimated using the theory of Lake and Thomas. According to this theory, fracture will occur when the polymer chains, of areal density Σ, crossing the fracture plane are stretched to the point where they have stored an energy per bond equal to the bond dissociation energy, U_b. A single bond in a polymer chain will then break, dissipating all of the energy in that chain ($\sim nU_b$) so that the total energy dissipated per unit area is given by

$$\Gamma \sim nU_b\Sigma. \tag{7.7}$$

Thus the fracture energy should be directly proportional to the areal density of polymer chains crossing the fracture plane, i.e. $\Gamma \propto \Sigma$. Σ can be estimated from the mesh size of the polymer network, ξ, as

$$\Sigma \sim 1/\xi^2. \tag{7.8}$$

The mesh size of a polymer is, to first approximation, the pore size of the network [193]. The pore size of the agarose polymer network has been measured by atomic force microscopy in [104] and was found to be related to the concentration of agarose, C, by the power law:

$$\xi \propto C^{-0.64} \tag{7.9}$$

Therefore, combining Equations 7.7, 7.8 and 7.9 one might expect Γ to scale with

agarose concentration according to the power law

$$\Gamma \propto C^{1.28}, \tag{7.10}$$

which is very similar to the observed scaling relationship.

I can check whether Lake-Thomas's simple model gives a reasonable order of magnitude for the bond energy. Agarose chains consists many galactose monomers which have a diameter, d, of approximately 0.6 nm and contain ~ 10 bonds[5]. To estimate the number of bonds in an entire chain I need an estimate of the chain's contour length, l. An estimate for l can be found by considering the length of a polymer chain that has been pulled taut by a critical stress σ_c, as occurs before fracture. This chain length is exactly the displacement at the edge of the cohesive zone as discussed in Section 3.3.1 and is approximately equal to Γ/σ_c (Equation 3.35). For agarose $\sigma_c \sim E$ so, by cancelling Γ from Equation 7.7, I can write

$$\frac{nU_b\Sigma}{\Gamma} = \frac{1/E}{10d}U_b\frac{1}{\xi^2} \sim 1. \tag{7.11}$$

If $\xi \approx 300$ nm and $E \approx 100$ kPa (for 3 % agarose) then the bond energy U_b can be estimated to be of the order eVs which is around the bond energy of the carbon-carbon bonds in the galactose monomers [194].

I was unable to measure the fracture energy of 0.6% agarose samples. This was due to the softness of the gel. The surface tension of the layer of the water on the surface of the gel meant that removing the spacing block between the L-frames was impossible as the gel would stretch to failure when the block was moved. The addition of a layer of Vaseline between the agarose and the spacing block failed to alleviate this problem.

7.4.2 The Young's modulus of agarose

The stress-strain ($\sigma - \epsilon$) relationship and thus tensile modulus of the agarose was measured using the unnotched samples. The tensile modulus is given by,

$$E_T = \frac{\sigma}{\epsilon}. \tag{7.12}$$

[5]Monomer diameter was estimated from the molar mass and density of a galactose molecule.

The stress in the unnotched sample is given by

$$\sigma = \frac{F}{t_u l_u} \tag{7.13}$$

and, given that only small strains are considered when defining the tensile modulus, the Cauchy or engineering strain can be used as the strain measure, i.e.

$$\epsilon = \frac{\Delta}{h_u}. \tag{7.14}$$

The stress as a function of strain is plotted in Figure 7.9a for the concentrations of agarose used in the colony growth experiments. The curves are approximately linear until the failure of the sample. To quantify the linearity of the $\sigma - \epsilon$ relationship, the curve $\sigma = E\epsilon^P$ was fit to the data where $\epsilon < 0.03$. The fitted value of P is shown in the inset of 7.9b. $P \approx 1$ meaning that the relationship is linear. E_T could then be measured for $\epsilon < 0.03$.

Figure 7.9b and table 7.2 show the E_T measured for each agarose concentration, the relationship is approximately linear. However, the negative intercept of (-36 ± 6) kPa suggests that at small concentrations this linear relationship must break down. The breakdown of the linear relationship is likely because agarose only forms a gel (rather than a viscoelastic fluid) above ≈ 0.4 % w/v, this is not far from the 0.7 ± 0.1 intercept with the x axis. At larger strains of 3 to 4 % the higher concentrations of agarose appear to soften. This softening is contradictory to the observations in [86], where agarose prepared at concentrations above 1.6 % were shown to stiffen.

Agarose concentration (% [w/v])	**Tensile Modulus** E_T (kPa)	**Uncertainty** δE_T (kPa)
1.0	12	2
1.5	26	2
2.0	60	6
3.0	114	3
4.0	172	5
5.0	221	7
6.0	268	10
10.0	448	22

Table 7.2 *The tensile modulus of agarose at various concentrations.*

The uncertainty in E_T is estimated as the maximum between the standard deviation between measurements, σ_{E_T}, and the uncertainty propagated from the un-

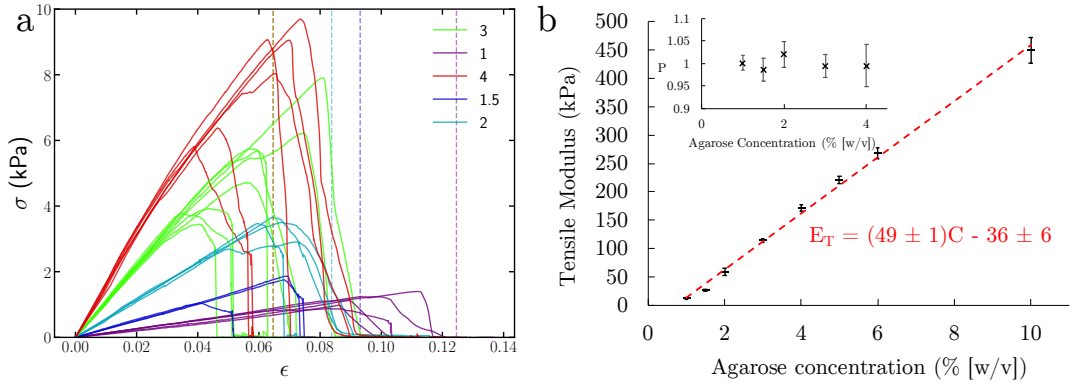

Figure 7.9 *The tensile stress-strain relationship of agarose. (a) Stress is plotted as a function of the engineering strain. The slope of the stress-strain curve increases with agarose concentration. Sudden drops in the stress are due sample failure. Dashed lines are the theoretical failure strains given* 1 mm *defects. (b) The tensile modulus vs agarose concentration, there error bars are too small to be rendered. A linear line of best fit is plotted in red along with the equation of the line. Inset: The curve* $\sigma = E\epsilon^P$ *was fit to the data where* $\epsilon < 0.03$*. P as a function of the agarose concentration is plotted along with the standard deviations between fitted P.* σ *has an approximately linear relationship (*$P \approx 1$*) to* ϵ *for all concentrations below* $\epsilon = 0.03$*.*

certainty in the thickness of the sample, $\delta E_{T,\text{prop}}$, i.e. $\delta E_T = \max(\delta E_{T,\text{prop}}, \sigma_{E_T})$. Given N samples with thickness $t \pm \delta t$, $\delta E_{T,\text{prop}}$ is given by,

$$\delta E_{T,\text{prop}} = \frac{1}{N}\sqrt{\sum_i^N \left(E_{T,i}\frac{\delta t_i}{t_i}\right)^2} \tag{7.15}$$

Of the various dimensions of the sample only the uncertainty in the thickness was considered, as it was far larger than the uncertainty in the other dimensions.

The dashed lines in Figure 7.9a are estimates of the expected failure strain, ϵ_c, given that the largest defect in the unnotched samples are the Velcro hooks with diameter 1 mm. The theoretical failure strain is estimated using Griffith's theory, i.e. that

$$\epsilon_c \approx \sqrt{\frac{\Gamma}{Ea}}, \tag{7.16}$$

where $a = 1\,\text{mm}$ (and any geometrical prefactors have been omitted). Whilst the samples did not reach the estimated strains before failure[6], the estimates are consistent with the observation that tests at higher agarose concentrations tend

[6]Either due to there being larger defects present in the samples, or the fact that the estimate make no attempt to determine the geometrical prefactor.

to fail before those at lower concentrations.

7.4.3 The elasto-fracture length scale of agarose

The elasto-fracture length scale, ℓ_{EF}, is used throughout this thesis. It can be determined from Γ and E_T as

$$\ell_{\mathrm{EF}} = \frac{\Gamma}{E_T}. \tag{7.17}$$

The uncertainty in ℓ_{EF} is estimated from the uncertainties in Γ and E_T using the formula

$$\delta\ell_{\mathrm{EF}} = \sqrt{\left(\frac{\delta\Gamma}{E_T}\right)^2 + \left(\frac{\Gamma}{E_T^2}\delta E_T\right)^2}. \tag{7.18}$$

The elasto-fracture length scale is shown in Figure 7.10 and table 7.3 for all concentrations measured.

Agarose concentration (% [w/v])	**Elasto-Fracture Scale** ℓ_{EF} (µm)	**Uncertainty** $\delta\ell_{\mathrm{EF}}$ (µm)
1.0	15.5	2.6
1.5	8.7	2.0
2.0	7.0	2.6
3.0	4.2	1.7
4.0	4.2	0.9
5.0	6.8	1.7
6.0	5.6	0.6
10.0	5.7	0.8

Table 7.3 *The elasto-fracture length scale of agarose measured at various concentrations.*

The red line plotted in Figure 7.10 is a combination of the linear and power law fits to the E_T vs concentration and Γ vs concentration data respectively. The uncertainty in the fit is given by the combination of the uncertainties in each fit:

$$\delta\ell_{\mathrm{EF}}^{\mathrm{Fit}} = \sqrt{\left(\frac{\delta\Gamma^{\mathrm{Fit}}}{E_T^{\mathrm{Fit}}}\right)^2 + \left(\frac{\Gamma^{\mathrm{Fit}}\delta E_T^{\mathrm{Fit}}}{(E_T^{\mathrm{Fit}})^2}\right)} \tag{7.19}$$

where

$$\delta\Gamma^{\mathrm{Fit}} = \sqrt{(C^B\delta A)^2 + (AC^B\log(C)\,\delta B)^2}. \tag{7.20}$$

A and B are the coefficient and power of the line of best fit to the Γ-concentration

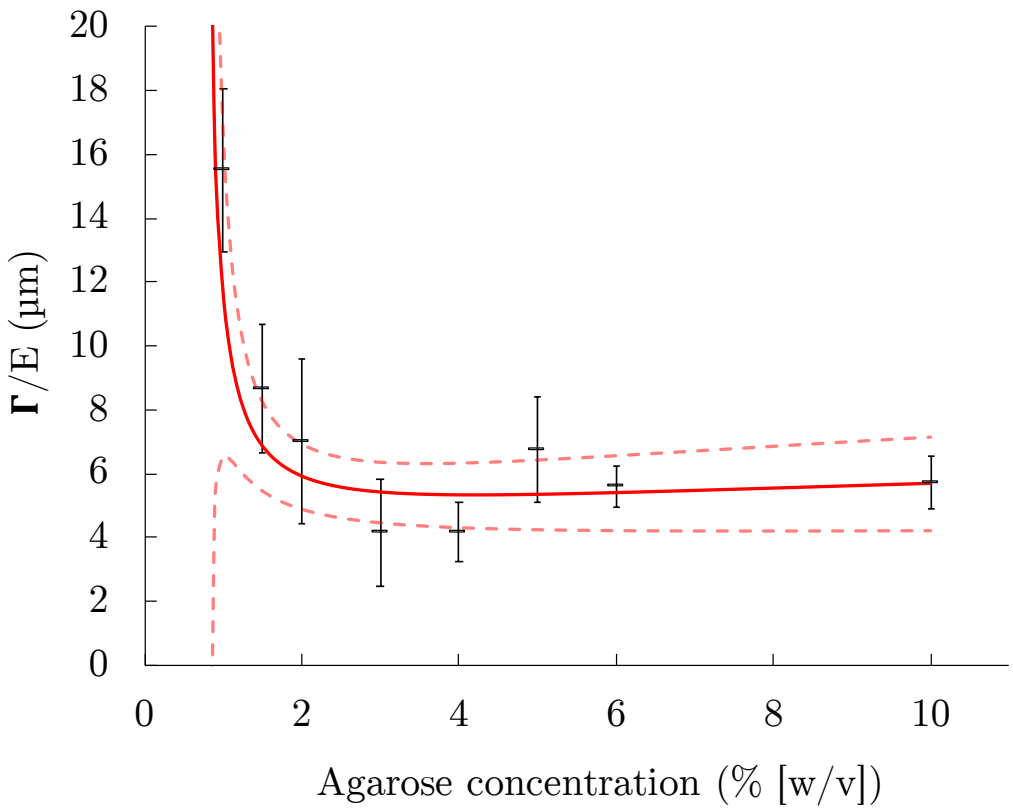

Figure 7.10 *The elasto-fracture length scale of agarose measured at various concentrations. The red fit line is a combination of separate fits to the* Γ *and* E_T *data set.*

relationship stated in Figure 7.8.

As was discussed in Chapter5 the rapid change in ℓ_{EF} at small agarose concentrations is likely the origin of the marked change in colony morphology that occurs at low agarose concentrations.

That ℓ_{EF} becomes roughly constant above 2 % agarose is interesting and could help explain observations in other studies. For example, the constant failure strain observed in tensile tests of agarose in [89] can be explained using Griffth's theory, i.e. that a defect of length a will fracture at a stress σ_f given by:

$$\sigma_f \approx \sqrt{\frac{\Gamma E}{a}}. \tag{7.21}$$

If the agarose samples behave in a linear elastic fashion ($\sigma = E\epsilon$) until some critical strain, ϵ_c, where the sample fractures, then one can state ϵ_c in terms of material properties as

$$\epsilon_c = \sqrt{\frac{\Gamma}{aE}}. \tag{7.22}$$

If Γ/E is constant as I have measured, then given that the defect size a is also likely constant (being some fixed size related to the how the samples were clamped), ϵ_c should be constant for agarose concentrations above 2 %. This is exactly what was observed in [89]. The independence of ℓ_{EF} from gel concentration has also been observed in tri-block co-polymers [195].

7.4.4 The validity of the quasi-static assumption

At the start of this chapter it was stated that the critical strain energy release rate G_c was equal to the fracture energy Γ for quasi static fractures. This statement stems from the observation that the critical strain energy release rate, G_c, is dependent on the loading rate[7] of a fracture, v. For physical gels (such as agarose) the relationship between G_c and v has been shown to have the form

$$G_c = \Gamma + f(v), \tag{7.23}$$

where Γ encompasses the energy cost of breaking bonds and making new surfaces and $f(v)$ stems from viscous dissipation in the region around the crack tip [196–

[7]Loading rate refers to the speed at which force is applied to the material around a fracture.

198]. The exact form of $f(v)$ is the subject of much research[8], but importantly is independent of Γ and monotonically increasing. Therefore when v is small, $G_c = \Gamma$ [73, 198]. For this reason materials tests made at loading rates far greater than the colonies growth rate[9] can still be applicable so long as $f(v) \ll \Gamma$ for both the materials test and the colony growth rate.

In this section I aim to verify that $f(v)$ is indeed much smaller than Γ for the measurements made with the pure shear apparatus and consequently for fractures propagated by bacterial colonies. The colonies in this work were shown to fracture the gel at a maximum velocity $\sim 10\,\mu\mathrm{m\,h^{-1}}$, whilst the loading rate used for the pure shear test was $0.01\,\mathrm{mm\,s^{-1}}$ or $3.6 \times 10^5\,\mu\mathrm{m\,h^{-1}}$. Therefore if $f(v) \ll \Gamma$ for pure shear test loading rates, then $f(v)$ should also be insignificant to the Γ of the gel around a growing colony.

The pure shear test was carried out using 4 % agarose at different loading rates by using cross head speeds between $0.01\,\mathrm{mm\,s^{-1}}$ and $0.0005\,\mathrm{mm\,s^{-1}}$. The measured G_c did not significantly change when the cross-head speed was lowered, Figure 7.11a. This loading speed independence suggests that $G_c = \Gamma$ for the experiments performed at $0.01\,\mathrm{mm\,s^{-1}}$ and that the measured values of Γ are representative of the energy required to fracture the gel at the propagation speeds experienced by bacterial colonies.

Only the rate dependence of 4 % agarose was tested as for physical gels (such as agarose) it has been shown that $f(v)$ monotonically increases with polymer concentration [151]. Therefore 4 % agarose should be the most sensitive to loading rate of the concentrations used in the experiments in Chapter 5 and 6. Results using 4 % agarose can therefore be used to rule out rate dependence for gels at lower agarose concentrations.

For reference the rate dependence of another type of agarose (2 % low electroendosmosis) are shown for higher cross-head speeds in Figure 7.11b. Figure 7.11b was taken from [150] where measurements of G_c were made using a single-edge-notched test. For this type of agarose a clear rate dependence was observed above cross head speeds of $0.03\,\mathrm{mm\,s^{-1}}$.

[8]For some physical gels (and specifically one type of agarose) $f(v)$ has empirically shown to fit the form βv^n. The value of the exponent n has been observed to vary between 0.1 and 1.0 depending on the material [73, 150, 151].

[9]The colony growth rate is assumed to be comparable to the rate at which the colony created crack tip is loaded.

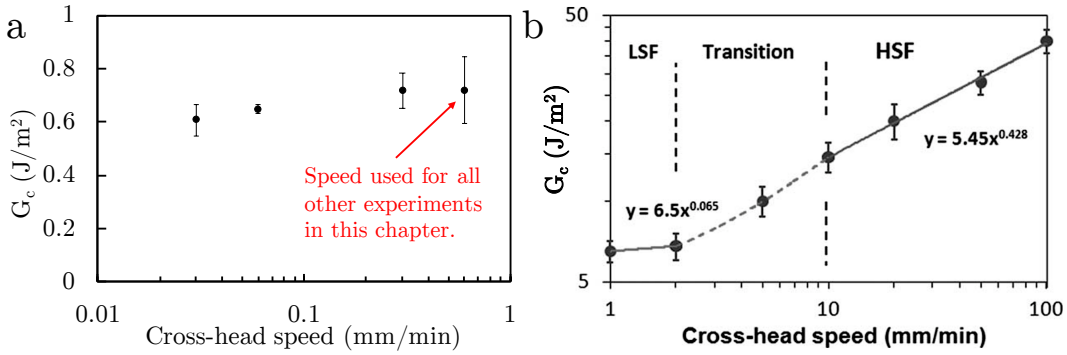

Figure 7.11 *The rate dependence of the fracture energy of agarose. (a) The variation of the fracture energy of 4% low melting point agarose with respect to the cross head speed. (b) The variation of the fracture energy of 2% low electroendosmosis agarose with respect to cross head speed. Taken from single-edge-notched tests performed in [150].*

7.5 Conclusions

The elastic and fracture properties of low melting point agarose were successfully measured using a custom apparatus to implement the pure shear test. The fracture energy of agarose was found to increase according to a power law with the concentration of agarose, in rough agreement with the theory of Lake and Thomas. The elastic modulus was measured in tension and was found to be linearly related to the concentration of agarose above 1 % concentration. This linear relationship meant that the elasto-fracture length scale is roughly constant above 2 % agarose and increases rapidly below 2 %. This qualitatively explains what was observed in Chapter5, where the morphology of colonies changes rapidly in agarose concentrations below 2% and undergoes only subtle changes at higher concentrations. Finally, the pure shear test was shown to have been carried out at a loading rate sufficiently slow that the fracture energy was unlikely to have a viscous component. Therefore the fracture energies measured should be the same as that observed by the slow growing bacterial colonies.

7.6 Future work

The uncertainty in values for the fracture energy of hydrogels given in previous works is larger than the entire range of my experimental values [150], therefore the measurements in this section represent an improvement on the state of the

art. However they are not without considerable uncertainty themselves and there are many improvements that could be made. The most important of these are as follows:

- Better control of evaporation from samples could be implemented. Although samples were covered with cling film during setting, they were exposed during testing. This was unlikely to have a significant effect for measurements at loading rates of $0.01\,\mathrm{mm\,s^{-1}}$ (where experiments took $\approx$ 5 minutes at most) but could present a problem when using slower loading rates. Implementation of a controlled humidity environment around the pure-shear rig during testing might reduce evaporation and improve the reliability of slow loading rate experiments.

- Better control of the state of the notch tip is needed. Whether the notch tip is wet or dry will effect the energy required to create new surfaces by approximately $72\,\mathrm{mJ\,m^{-2}}$ (the surface energy of a water-air boundary). The current method of drying the tip with a paper towel left a meniscus at the notch tip of varying size. In addition, notches made in higher concentrations of agarose tended to be dryer than those at lower concentrations, this may have led to a systematic error in my measurements. Perhaps immersing the sample and rig in oil so that the water on the surface of the notch was displaced could lead to more reliable measurements.

- The weight of the apparatus impeded measurements. If a lighter frame could have been made then a more precise load cells could have been used. The weight of the current frame is $\approx 5\,\mathrm{N}$ preventing the use of a smaller load cell which would have been more appropriate for the range of forces measured.

- A higher throughput method would be useful. The distribution of fracture energies between samples was difficult to ascertain with the low number of repeats used here. However, given that each test took 2.5-3.0 hours to prepare and carry out it was not feasible to measure more samples. Methods measuring the fracture energy by observing notch tip shapes, such as the one described in [143], can be carried out in parallel with small sample sizes and might present a high throughput method of fracture energy characterisation.

- The experiments detailed in this section took a single measurement of the fracture energy from each sample. If instead the extension was oscillated

around the critical extension, multiple measurements of the fracture time/ extension could have been recorded for each sample, perhaps improving the accuracy of measurements. However these oscillations may fatigue the hydrogel, which has been shown to alter the fracture properties of hydrogels [199].

Chapter 8

Conclusions

In this thesis I experimentally investigated the growth and morphology of colonies of *Escherichia coli* that were grown submerged in agarose gels using single plane illumination microscopy (SPIM).

In Chapter 4 I demonstrated how the sample chamber of a SPIM set up could be used as an incubator, allowing for bacteria submerged in agarose gels to be imaged in three dimensions. Colonies with sizes across multiple orders of magnitude were imaged, starting from clusters of only a few 10's of cells, up to to colonies consisting of many 100's of thousands of cells. I outlined an image processing pipeline that resulted in the averaging out of image artefacts caused by the highly scattering colonies and for measurement of colony morphology. I showed how fiducial markers could be embedded in the gel and how they can be used to track displacements caused by a growing colony. Furthermore, I detailed a method for interpolating the measured displacements into a continuous field by optimizing interpolation parameters using simulated data.

In Chapter 5 the methodology outlined in Chapter 4 was used to show that bacteria fracture the gel around them as they grow. Modelling the colony as a source of pressure inflating and propagating a penny-shaped fracture in a linear elastic material was found to be insufficient to predict colony morphology. Instead the fracture created by the colony was shown to go through a transition in growth modes, changing from one where the colony fractured the gel over the entire surface of the crack it inhabited, to one where the colony fractured the gel in a plane with a clear cohesive zone around the fracture propagation front. This switch in fracture modes was predicted by the theories of crack tip blunting and

cavitation that were discussed in Chapter 3, and suggests that at small scales the pressure required for a colony to grow is independent of the fracture energy of the gel. This independence may mean that bacteria can grow in far tougher gels than would previously have been expected.

In Chapter 5 I was successful in showing that colonies do not fracture the gel in accordance with linear elastic fracture mechanics, however I was unable to predict how the morphology of a colony should be altered by inelasticity. I could therefore not be certain of the true influence of biology on colony morphology. Consequently, I sought to create a physical simulation of the growing colonies by blowing silicone oil into the agarose gel at the same length and time scales as a bacterial colony grows. The results of this physical simulation were given in Chapter 6.

In Chapter 6 I first presented a method by which an oil bubble could be grown at a size smaller than the elasto-fracture length scale (ℓ_{EF}) of agarose, which was the length scale at which the transition in fracture growth mode was observed for bacterial colonies. Despite being unable to capture the oil droplet morphology below ℓ_{EF} due to the rapid expansion of the bubbles caused by the necessity to overcome capillary pressure, I showed that the morphology of growing oil bubbles is very similar to that of the bacterial colonies at sizes greater than ℓ_{EF}. In fact, what differences could be observed can be plausibly explained by the difference in interfacial energy between the agarose-*E. coli* and agarose-oil interface. In this way colonies larger than ℓ_{EF} were shown to simply act as a Newtonian fluid propagating a hydraulic fracture.

In addition to morphology measurements, Chapter 6 showed that by controlling the pressure of an oil reservoir attached to the bubble, the pressure at fracture initiation could be measured and the pressure inside the growing bubble inferred. These pressure measurements provided inconsistent results and could not be used to discriminate between fracture growth modes. Despite this, the nano-litre scale hydraulic fracture system that I describe could provide the basis for further experiments, if the pressure inside the reservoir could be more precisely controlled.

Finally in Chapter 7 a method for measuring the material properties of the agarose used in the previous chapters was detailed. I showed that by using a mould that could be disassembled once the gel had set, the fracture properties of a gel that is both extremely soft and extremely brittle could be measured. I found that

the fracture energy of agarose scales with the concentration of gel to the power 1.2 ± 1, which is in reasonable agreement with the theory of Lake and Thomas. The fracture energy was found to be independent of loading rate for rates below $0.01\,\mathrm{mm\,s^{-1}}$, allowing for measurements made with the pure shear apparatus to be applicable to the fracture of agarose by a colony of *E. coli*. The elastic modulus of agarose was observed to scale linearly with the concentration. The elasto-fracture length scale $\ell_{\mathrm{EF}} = \Gamma/E$ was therefore found to rapidly decrease below 2 % agarose before becoming effectively constant above 3 % agarose, this was consistent with the changes in colony and oil bubble morphology observed in Chapter 5 and Chapter 6.

Appendix A

The pressure-stretch relationship for a thick spherical shell

In section 3.5.1 I posed the problem of determining the relationship between the over-pressure, P, inside a thick walled spherical shell (figure A.1) and the stretch at the inner surface of that shell, λ_a, for a material with an arbitrary strain energy density function, W. The solution to this problem is given in this appendix.

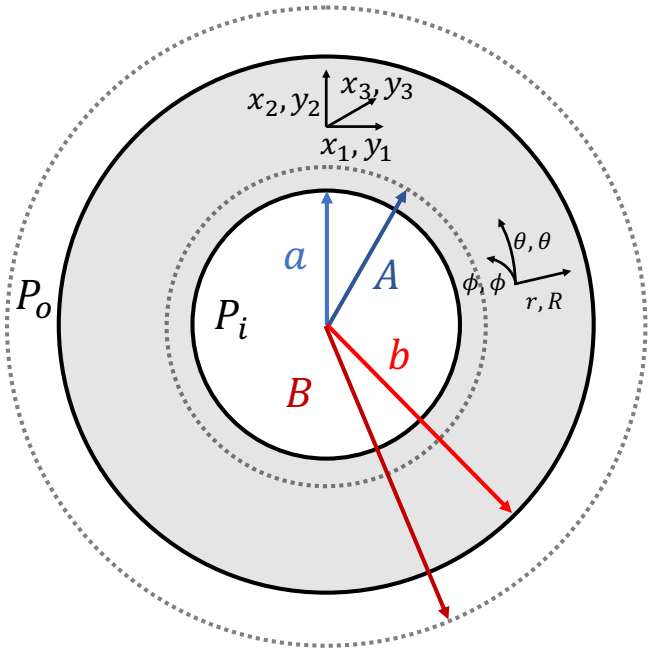

Figure A.1 *The cross section of a thick walled spherical shell. The cavity in the shell is pressurised to $P = P_i - P_o$. During pressurization the cavity wall deforms from a radius of a to A whilst the outer wall of the shell deforms from radius b to B.*

In order to solve the problem a curvilinear coordinate system is adopted and I take advantage of the solution for the stress-strain relationship for a homogeneous isotropic body in terms of the metric tensors of the strained and unstrained system given in [200].

The strained shell in figure A.1 can be described in terms of Cartesian (y_1, y_2, y_3) and spherical polar (R, θ, ϕ) coordinates with origin at the center of the shell so that,

$$\begin{gathered} \theta_1 = R, \quad \theta_2 = \theta, \quad \theta_3 = \phi, \\ y_1 = R\sin\theta\cos\phi, \quad y_2 = R\sin\theta\sin\phi, \quad y_3 = R\cos\theta \end{gathered} \tag{A.1}$$

the metric tensor for the strained body in euclidean space can therefore be written

$$G_{ij} = \frac{\partial y_1}{\partial \theta_i}\frac{\partial y_1}{\partial \theta_j} + \frac{\partial y_2}{\partial \theta_i}\frac{\partial y_2}{\partial \theta_j} + \frac{\partial y_3}{\partial \theta_i}\frac{\partial y_3}{\partial \theta_j} \tag{A.2}$$

hence

$$G_{ij} = \begin{bmatrix} 1 & 0 & 0 \\ 0 & R^2 & 0 \\ 0 & 0 & R^2\sin^2\theta \end{bmatrix}, \quad |G| = R^4\sin^2\theta. \tag{A.3}$$

To determine the metric tensor of the unstrained state, it is assumed that the displacement of the shell is spherically symmetric so that a point at (r, θ, ϕ) moves to the point (R, θ, ϕ). The stretch, λ, is therefore

$$\lambda = \frac{R}{r} = \frac{1}{Q} \tag{A.4}$$

where the inverse stretch Q will be used to simplify the algebra. Therefore if the unstrained Cartesian coordinate system (x_1, x_2, x_3) coincides with the strained Cartesian coordinate system

$$x_1 = QR\sin\theta\cos\phi, \quad x_2 = QR\sin\theta\sin\phi, \quad x_3 = QR\cos\theta. \tag{A.5}$$

To determine the metric tensor of the unstrained shell, g_{ij}, one must find $\partial x_1/\partial R$, this derivative can be computed using the incompressibility condition. Given that the shell has internal and external radii a and b in its unstrained state and internal and external radii A and B in its strained state, the incompressibility condition can be stated as

$$b^3 - a^3 = B^3 - A^3 \tag{A.6}$$

thus

$$A^3 - a^3 = B^3 - b^3 = R^3 - r^3. \tag{A.7}$$

Therefore, using equation A.4,

$$Q = \left(1 + \frac{a^3 - A^3}{R^3}\right)^{\frac{1}{3}} \tag{A.8}$$

and using equation A.7

$$\frac{dQ}{dR} = \frac{1}{R}\left(\frac{1}{Q^2} - Q\right) \tag{A.9}$$

so that g_{ij},

$$g_{ij} = \frac{\partial x_1}{\partial \theta_i}\frac{\partial x_1}{\partial \theta_j} + \frac{\partial x_2}{\partial \theta_i}\frac{\partial x_2}{\partial \theta_j} + \frac{\partial x_3}{\partial \theta_i}\frac{\partial x_3}{\partial \theta_j}, \tag{A.10}$$

can be computed as

$$g_{ij} = \begin{bmatrix} \frac{1}{Q^4} & 0 & 0 \\ 0 & Q^2R^2 & 0 \\ 0 & 0 & Q^2R^2\sin^2\theta \end{bmatrix}, \quad |g| = R^4\sin^2\theta. \tag{A.11}$$

When a body is elastic, an elastic potential exists [200], it has the property

$$\tau^{ij} = \frac{1}{2}\sqrt{\frac{|g|}{|G|}}\left(\frac{\partial W}{\partial \gamma_{ij}} + \frac{\partial W}{\partial \gamma_{ji}}\right) \tag{A.12}$$

where τ^{ij} is the contravariant stress tensor and the covarient strain tensor, γ_{ij}, is given by:

$$\gamma_{ij} = \frac{1}{2}\left(G_{ij} - g_{ij},\right). \tag{A.13}$$

For isotropic materials W can be written in terms of the invariants of the strain tensor,

$$W = W(I_1, I_2, I_3) \tag{A.14}$$

where

$$I_1 = g^{rs}G_{rs}, \quad I_2 = g_{rs}G^{rs}, \quad I_3 = \frac{|G|}{|g|}, \tag{A.15}$$

and $g^{ij} = 1/g_{ij}$, $G^{ij} = 1/G_{ij}$. Therefore after some manipulation

$$\tau^{ij} = \Phi g^{ij} + \Psi B^{ij} + pG^{ij} \tag{A.16}$$

where

$$\begin{gathered} \Phi = \frac{2}{\sqrt{I_3}}\frac{\partial W}{\partial I_1}, \quad \Psi = \frac{2}{\sqrt{I_3}}\frac{\partial W}{\partial I_2}, \quad p = 2\sqrt{I_3}\frac{\partial W}{\partial I_3}, \\ B^{ij} = I_1 g^{ij} - g^{ir}g^{js}G_{rs}. \end{gathered} \tag{A.17}$$

Given that the shell has been assumed to be incompressible $I_3 = 1$. Therefore

the stress strain relations for the shell can be written as

$$\begin{aligned} \tau^{11} &= Q^4\Phi + 2Q^2\Psi + p, \\ \tau^{22} = \tau^{33}\sin^2\theta &= \frac{\Phi}{R^2Q^2} + \left(Q^2 + \frac{1}{Q^4}\right)\frac{\Psi}{R^2} + \frac{p}{R^2}, \\ \tau^{12} &= \tau^{23} = \tau^{31} = 0. \end{aligned} \tag{A.18}$$

From here the aim is to determine the physical components of stress, σ_{ij}, given by:

$$\sigma_{ij} = \sqrt{\frac{G_{jj}}{G^{ii}}}\tau^{ij}, \tag{A.19}$$

Then, by using the boundary condition that at the cavity wall σ will be equal to the pressure, P, inside the cavity, I will have found the relationship between the P and λ.

First the equation of motion for the shell can be written,

$$\tau^{ij}||_i + \rho F^j = \rho f^i = 0 \tag{A.20}$$

where F^j are the contravariant components of the body forces, f^i are the contravariant components of the acceleration vector and ρ is the mass density of the strained shell. If there are no body forces the equilibrium equation is

$$\tau^{ij}||_i = 0, \tag{A.21}$$

performing the contravariant derivative ($||_i$) [200], equation A.21 becomes

$$\frac{dp}{dQ} + Q^4\frac{d\Phi}{dQ} + 2Q^2\frac{d\Psi}{dQ} + 2\left(Q^3 - 1\right)\Phi + 2\left(Q - \frac{1}{Q^2}\right)\Psi = 0. \tag{A.22}$$

Integrating, an expression for p is found

$$p = -\left(Q^4\Phi + 2Q^2\Psi\right) + 2\int_Q \left[\left(Q^3 + 1\right)\Phi + \left(Q + \frac{1}{Q^2}\right)\Psi\right] dQ. \tag{A.23}$$

bar some arbitrary constant. If P is the pressure normal to the inner surface of the shell,

$$P = \sigma^{11}|_{R=A} = \tau^{11}|_{R=A}, \tag{A.24}$$

combining this condition with the first equation of A.18 and A.23, P can be

expressed as

$$P = 2\int_{Q_a}^{Q}\left[\left(Q^3+1\right)\Phi + \left(Q+\frac{1}{Q^2}\right)\Psi\right]dQ, \tag{A.25}$$

where

$$Q_a = \frac{a}{A} = \frac{1}{\lambda_a}. \tag{A.26}$$

Equation A.25 can be expressed in a more convenient form using equations A.15, noting that

$$I_1 = Q^4 + \frac{2}{Q^2}, \quad I_2 = 2Q^2 + \frac{1}{Q^4}, \tag{A.27}$$

so that

$$\frac{dI_1}{dQ} = \frac{4\left(Q^3-1\right)\left(Q^3+1\right)}{Q^3}, \quad \frac{dI_2}{dQ} = \frac{4\left(Q^3-1\right)}{Q^3}\left(Q+\frac{1}{Q^2}\right) \tag{A.28}$$

and

$$\frac{dW}{dQ} = \frac{2(Q^3-1)}{Q^3}\left[\left(Q^3+1\right)\Phi + \left(Q+\frac{1}{Q^2}\right)\Psi\right] \tag{A.29}$$

Therefore combining equations A.25 and A.29, P can be expressed as

$$P = \int_{Q_a}^{Q}\frac{Q^3}{Q^3-1}\frac{dW}{dQ}dQ. \tag{A.30}$$

Finally, using equation A.4, the internal pressure of the cavity can be written in terms of the stretch at the cavity wall, λ_a, and W as,

$$P(\lambda_a) = \int_{1}^{\lambda_a}\frac{1}{\lambda^3-1}\frac{dW}{d\lambda}d\lambda \tag{A.31}$$

Appendix B

The pressurestat control system

The pressurestat control system uses an Arduino Uno microcontroller board to read the output voltage from the pressure sensor. That output voltage is converted into a pressure reading which is used to inform the commands sent to the syringe pump via the pumps transistor-transistor logic (TTL) input/output as described in section 6.2.1.

Figure B.1 shows how the various input and outputs of each component are connected. The employed TTL pin functions are as follows:

1. 5 V logic high reference
2. Start/Stop trigger
3. Pumping direction Input
8. Pumping direction output
9. 0 V logic low reference

The two main scripts used in conjunction with the pressurestat control system can be found here (`https://www.dropbox.com/sh/gegwihquhos28ac/AABfb-hFNcqDuR39f3EQo_H_a?dl=0`). The link contains two scripts: "Pump_Atmostat_Direction_Check.ino", which is the script uploaded to the Arduino micro-controller written in the Arduino programming language, and "Arduino_Monitor.py", which is a python script used to record output from the Arduino via a usb connection to the serial port of a connected computer.

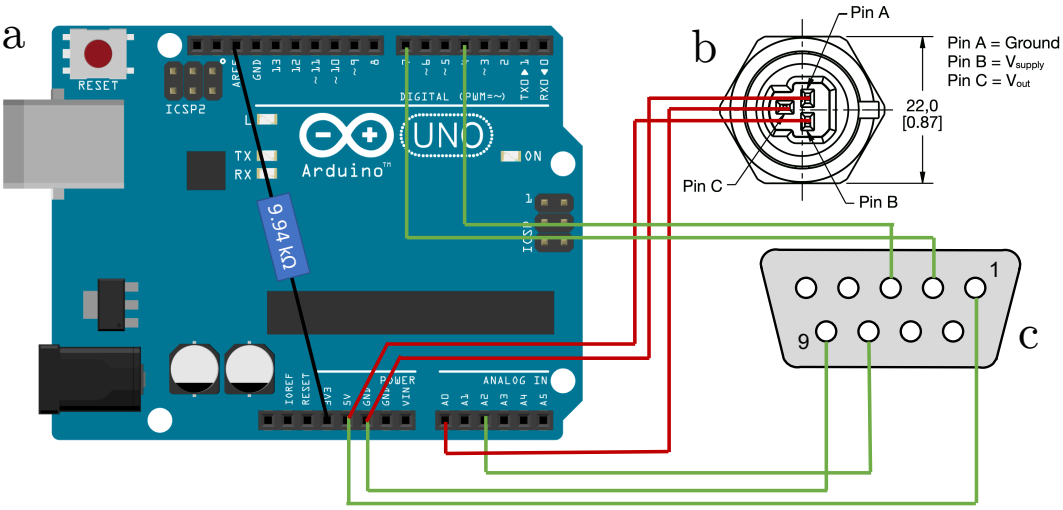

Figure B.1 *Schematic of the pressurestat control system. The pressure sensor (b) is connected to the reference voltage pins on the Arduino board. The output pin (Pin C) is connected to the main input pin (A0). The syringe pump is controlled via TTL input/output pins. Pins 1 and 9 check the high and low reference voltage respectively, whilst pins 2 and 3 start/stop the pump and control the pump direction respectively. Pin 8 is also used as input to the Arduino, outputting the current pumping direction, it is used to check for direction faults.*

Bibliography

[1] D'Arcy Wentworth Thompson. *On Growth and Form*. Canto Classics. Cambridge University Press, 2014.

[2] Nicolas Rashevsky. Topology and life: in search of general mathematical principles in biology and sociology. *The bulletin of mathematical biophysics*, 16(4):317–348, 1954.

[3] Julian Huxley. *Problems of relative growth*. Johns Hopkins University Press, 1993.

[4] Theodore Andrea Cook. *The curves of life: being an account of spiral formations and their application to growth in nature, to science, and to art: with special reference to the manuscripts of Leonardo da Vinci*. Courier Corporation, 1979.

[5] Otger Campas and L Mahadevan. Shape and dynamics of tip-growing cells. *Current Biology*, 19(24):2102–2107, 2009.

[6] Alexander Krichevsky, Stanislav V Kozlovsky, Guo-Wei Tian, Min-Huei Chen, Adi Zaltsman, and Vitaly Citovsky. How pollen tubes grow. *Developmental biology*, 303(2):405–420, 2007.

[7] APJ Trinci and PT Saunders. Tip growth of fungal hyphae. *Microbiology*, 103(2):243–248, 1977.

[8] I Brent Heath and Anja Geitmann. Cell biology of plant and fungal tip growth—getting to the point, 2000.

[9] Stephanie L Burg, Adam Washington, David M Coles, Antonino Bianco, Daragh McLoughlin, Oleksandr O Mykhaylyk, Julie Villanova, Andrew JC Dennison, Christopher J Hill, Pete Vukusic, et al. Liquid–liquid phase separation morphologies in ultra-white beetle scales and a synthetic equivalent. *Communications Chemistry*, 2(1):1–10, 2019.

[10] Andrew J Parnell, James E Bradford, Emma V Curran, Adam L Washington, Gracie Adams, Melanie N Brien, Stephanie L Burg, Carlos Morochz, J Patrick A Fairclough, Pete Vukusic, et al. Wing scale ultrastructure underlying convergent and divergent iridescent colours in

mimetic heliconius butterflies. *Journal of The Royal Society Interface*, 15(141):20170948, 2018.

[11] Michael D Bartlett, Andrew B Croll, Daniel R King, Beth M Paret, Duncan J Irschick, and Alfred J Crosby. Looking beyond fibrillar features to scale gecko-like adhesion. *Advanced Materials*, 24(8):1078–1083, 2012.

[12] Daniel R King, Michael D Bartlett, Casey A Gilman, Duncan J Irschick, and Alfred J Crosby. Creating gecko-like adhesives for "real world" surfaces. *Advanced Materials*, 26(25):4345–4351, 2014.

[13] LH Shu, K Ueda, I Chiu, and H Cheong. Biologically inspired design. *CIRP annals*, 60(2):673–693, 2011.

[14] Anton du Plessis, Chris Broeckhoven, Ina Yadroitsava, Igor Yadroitsev, Clive H Hands, Ravi Kunju, and Dhruv Bhate. Beautiful and functional: a review of biomimetic design in additive manufacturing. *Additive Manufacturing*, 2019.

[15] Edward F DeLong and Norman R Pace. Environmental diversity of bacteria and archaea. *Systematic biology*, 50(4):470–478, 2001.

[16] Aaron N Brooks, Serdar Turkarslan, Karlyn D Beer, Fang Yin Lo, and Nitin S Baliga. Adaptation of cells to new environments. *Wiley Interdisciplinary Reviews: Systems Biology and Medicine*, 3(5):544–561, 2011.

[17] Britt Koskella and Michiel Vos. Adaptation in natural microbial populations. *Annual Review of Ecology, Evolution, and Systematics*, 46, 2015.

[18] Ronnie N Glud, Frank Wenzhöfer, Mathias Middelboe, Kazumasa Oguri, Robert Turnewitsch, Donald E Canfield, and Hiroshi Kitazato. High rates of microbial carbon turnover in sediments in the deepest oceanic trench on earth. *Nature Geoscience*, 6(4):284–288, 2013.

[19] James K Fredrickson, John M Zachara, David L Balkwill, David Kennedy, W Li Shu-mei, Heather M Kostandarithes, Michael J Daly, Margaret F Romine, and Fred J Brockman. Geomicrobiology of high-level nuclear waste-contaminated vadose sediments at the hanford site, washington state. *Applied and environmental microbiology*, 70(7):4230–4241, 2004.

[20] Marcin Cyprowski, Agata Stobnicka-Kupiec, Anna Ławniczek-Wałczyk, Aleksandra Bakal-Kijek, Małgorzata Gołofit-Szymczak, and Rafał L Górny. Anaerobic bacteria in wastewater treatment plant. *International Archives of Occupational and Environmental Health*, 91(5):571–579, 2018.

[21] Altina Lacerda Nascimento, Adijailton Jose Souza, Pedro Avelino Maia Andrade, Fernando Dini Andreote, Aline Renée Coscione, Fernando Carvalho Oliveira, and Jussara Borges Regitano. Sewage sludge microbial structures

and relations to their sources, treatments, and chemical attributes. *Frontiers in microbiology*, 9:1462, 2018.

[22] E Abatenh, B Gizaw, Z Tsegaye, and M Wassie. The role of microorganisms in bioremediation-a review. *Open Journal of Environmental Biology*, 2(1):030–046, 2017.

[23] Nedaa Ali, Narjes Dashti, Majida Khanafer, Husain Al-Awadhi, and Samir Radwan. Bioremediation of soils saturated with spilled crude oil. *Scientific reports*, 10(1):1–9, 2020.

[24] James A Shapiro. The significances of bacterial colony patterns. *Bioessays*, 17(7):597–607, 1995.

[25] EG Velliou, E Noriega, Eva Van Derlinden, Laurence Mertens, Kathleen Boons, AH Geeraerd, Frank Devlieghere, and JF Van Impe. The effect of colony formation on the heat inactivation dynamics of escherichia coli k12 and salmonella typhimurium. *Food research international*, 54(2):1746–1752, 2013.

[26] Mary Ellen Davey and George A O'toole. Microbial biofilms: from ecology to molecular genetics. *Microbiology and molecular biology reviews*, 64(4):847–867, 2000.

[27] Hans-Curt Flemming, Jost Wingender, Ulrich Szewzyk, Peter Steinberg, Scott A Rice, and Staffan Kjelleberg. Biofilms: an emergent form of bacterial life. *Nature Reviews Microbiology*, 14(9):563, 2016.

[28] Carla CCR de Carvalho. Marine biofilms: a successful microbial strategy with economic implications. *Frontiers in Marine Science*, 5:126, 2018.

[29] Jordi Van Gestel, Hera Vlamakis, and Roberto Kolter. From cell differentiation to cell collectives: Bacillus subtilis uses division of labor to migrate. *PLoS Biol*, 13(4):e1002141, 2015.

[30] Bernhard Schink. Synergistic interactions in the microbial world. *Antonie Van Leeuwenhoek*, 81(1-4):257–261, 2002.

[31] Ana Margarida Sousa, Idalina Machado, Ana Nicolau, and Maria Olívia Pereira. Improvements on colony morphology identification towards bacterial profiling. *Journal of microbiological methods*, 95(3):327–335, 2013.

[32] Eshel Ben-Jacob, Inon Cohen, and Herbert Levine. Cooperative self-organization of microorganisms. *Advances in Physics*, 49(4):395–554, 2000.

[33] Matthew AA Grant, Bartłomiej Wacław, Rosalind J Allen, and Pietro Cicuta. The role of mechanical forces in the planar-to-bulk transition in growing escherichia coli microcolonies. *Journal of The Royal Society Interface*, 11(97):20140400, 2014.

[34] Zhihong You, Daniel JG Pearce, Anupam Sengupta, and Luca Giomi. Geometry and mechanics of microdomains in growing bacterial colonies. *Physical Review X*, 8(3):031065, 2018.

[35] D Dell'Arciprete, ML Blow, AT Brown, FDC Farrell, Juho S Lintuvuori, AF McVey, D Marenduzzo, and Wilson CK Poon. A growing bacterial colony in two dimensions as an active nematic. *Nature communications*, 9(1):1–9, 2018.

[36] PDG Wilson, TF Brocklehurst, S Arino, D Thuault, M Jakobsen, Martin Lange, J Farkas, JWT Wimpenny, and JF Van Impe. Modelling microbial growth in structured foods: towards a unified approach. *International journal of food microbiology*, 73(2-3):275–289, 2002.

[37] N Kabanova, I Stulova, and R Vilu. Microcalorimetric study of the growth of bacterial colonies of lactococcus lactis il1403 in agar gels. *Food microbiology*, 29(1):67–79, 2012.

[38] Michael Antwi, Annemie H Geeraerd, Karen M Vereecken, Rika Jenne, Kristel Bernaerts, and JF Van Impe. Influence of a gel microstructure as modified by gelatin concentration on listeria innocua growth. *Innovative Food Science & Emerging Technologies*, 7(1-2):124–131, 2006.

[39] Sophie Jeanson, Juliane Floury, Valérie Gagnaire, Sylvie Lortal, and Anne Thierry. Bacterial colonies in solid media and foods: a review on their growth and interactions with the micro-environment. *Frontiers in microbiology*, 6:1284, 2015.

[40] Estefanía Noriega, Eirini Velliou, Eva Van Derlinden, Laurence Mertens, and Jan FM Van Impe. Effect of cell immobilization on heat-induced sublethal injury of escherichia coli, salmonella typhimurium and listeria innocua. *Food microbiology*, 36(2):355–364, 2013.

[41] AJ Mitchell and JWT Wimpenny. The effects of agar concentration on the growth and morphology of submerged colonies of motile and non-motile bacteria. *Journal of applied microbiology*, 83(1):76–84, 1997.

[42] PK Malakar, TF Brocklehurst, AR Mackie, PDG Wilson, MH Zwietering, and K Van?t Riet. Microgradients in bacterial colonies: use of fluorescence ratio imaging, a non-invasive technique. *International journal of food microbiology*, 56(1):71–80, 2000.

[43] Kristen L Mills, Ralf Kemkemer, Shiva Rudraraju, and Krishna Garikipati. Elastic free energy drives the shape of prevascular solid tumors. *PLoS One*, 9(7):e103245, 2014.

[44] Gang Cheng, Janet Tse, Rakesh K Jain, and Lance L Munn. Micro-environmental mechanical stress controls tumor spheroid size and morphology by suppressing proliferation and inducing apoptosis in cancer cells. *PLoS one*, 4(2):e4632, 2009.

[45] David Robert Grimes and Frederick J Currell. Oxygen diffusion in ellipsoidal tumour spheroids. *Journal of The Royal Society Interface*, 15(145):20180256, 2018.

[46] Huanxin Zhang, Bo Li, Yue Shao, and Xi-Qiao Feng. Morphomechanics of tumors. *Current Opinion in Biomedical Engineering*, 15:51–58, 2020.

[47] Uwe Güth, Denise Brenckle, Dorothy Jane Huang, Andreas Schötzau, Carsten Thomas Viehl, Holger Dieterich, Wolfgang Holzgreve, Edward Wight, and Gad Singer. Three-dimensional pathological size assessment in primary breast carcinoma. *Breast cancer research and treatment*, 116(2):257–262, 2009.

[48] So M Wiederhorn. Fracture surface energy of glass. *Journal of the American Ceramic Society*, 52(2):99–105, 1969.

[49] Keith J Kasunic. *Optomechanical systems engineering*. John Wiley & Sons, 2015.

[50] E Reyssat, T Tallinen, M Le Merrer, and L Mahadevan. Slicing softly with shear. *Physical review letters*, 109(24):244301, 2012.

[51] Alan Arnold Griffith. Vi. the phenomena of rupture and flow in solids. *Philosophical transactions of the royal society of london. Series A, containing papers of a mathematical or physical character*, 221(582-593):163–198, 1921.

[52] Charles Edward Inglis. Stresses in a plate due to the presence of cracks and sharp corners. *Trans Inst Naval Archit*, 55:219–241, 1913.

[53] GR Irwin. Fracturing of metals. *ASM, Cleveland*, 147:19–9, 1948.

[54] E Orowan. Fracture and strength of solids. *Reports on Progress in Physics*, 12:183, 1948.

[55] RS Rivlin and A Gr Thomas. Rupture of rubber. i. characteristic energy for tearing. *Journal of polymer science*, 10(3):291–318, 1953.

[56] Ruobing Bai, Jiawei Yang, and Zhigang Suo. Fatigue of hydrogels. *European Journal of Mechanics-A/Solids*, 74:337–370, 2019.

[57] K Bertram Broberg. *Cracks and fracture*. Elsevier, 1999.

[58] Gilberto Brambilla and David N Payne. The ultimate strength of glass silica nanowires. *Nano Letters*, 9(2):831–835, 2009.

[59] RA Sack. Extension of griffith's theory of rupture to three dimensions. *Proceedings of the Physical Society*, 58(6):729, 1946.

[60] Ian Naismith Sneddon. The distribution of stress in the neighbourhood of a crack in an elastic solid. *Proceedings of the Royal Society of London. Series A. Mathematical and Physical Sciences*, 187(1009):229–260, 1946.

[61] IN Sneddon. Crack problems in the theory of elasticity. In *Developments in Theoretical and Applied Mechanics: Proceedings of the Third Southeastern Conference on Theoretical and Applied Mechanics*, page 73. Elsevier, 2013.

[62] Bruce D Johnson, Bernard P Boudreau, Bruce S Gardiner, and Regine Maass. Mechanical response of sediments to bubble growth. *Marine Geology*, 187(3-4):347–363, 2002.

[63] Donald S Dugdale. Yielding of steel sheets containing slits. *Journal of the Mechanics and Physics of Solids*, 8(2):100–104, 1960.

[64] Grigory Isaakovich Barenblatt et al. The mathematical theory of equilibrium cracks in brittle fracture. *Advances in applied mechanics*, 7(1):55–129, 1962.

[65] Kyoungsoo Park and Glaucio H Paulino. Cohesive zone models: a critical review of traction-separation relationships across fracture surfaces. *Applied Mechanics Reviews*, 64(6):060802, 2011.

[66] Kyoungsoo Park, Habeun Choi, and Glaucio H Paulino. Assessment of cohesive traction-separation relationships in abaqus: A comparative study. *Mechanics Research Communications*, 78:71–78, 2016.

[67] Chenglin Wu, Shravan Gowrishankar, Rui Huang, and Kenneth M Liechti. On determining mixed-mode traction–separation relations for interfaces. *International Journal of Fracture*, 202(1):1–19, 2016.

[68] Z-H Jin and CT Sun. *Fracture Mechanics*. Royal Society of Chemistry, 2012.

[69] Vyacheslav Mokryakov. Analytical solution for propagation of hydraulic fracture with barenblatt's cohesive tip zone. *International journal of fracture*, 169(2):159–168, 2011.

[70] AN Gent and S-M Lai. Interfacial bonding, energy dissipation, and adhesion. *Journal of Polymer Science Part B: Polymer Physics*, 32(8):1543–1555, 1994.

[71] C-Y Hui, SJ Bennison, and JD Londono. Crack blunting and the strength of soft elastic solids. *Proceedings of the Royal Society of London. Series A: Mathematical, Physical and Engineering Sciences*, 459(2034):1489–1516, 2003.

[72] S Timoshenko and J Goodier. Theory of elasticity. *The Journal of the Royal Aeronautical Society*, 56(496), 1952.

[73] Costantino Creton and Matteo Ciccotti. Fracture and adhesion of soft materials: a review. *Reports on Progress in Physics*, 79(4):046601, 2016.

[74] AN Gent and PB Lindley. Internal rupture of bonded rubber cylinders in tension. *Proceedings of the Royal Society of London. Series A. Mathematical and Physical Sciences*, 249(1257):195–205, 1959.

[75] K Cho and AN Gent. Cavitation in model elastomeric composites. *Journal of materials science*, 23(1):141–144, 1988.

[76] RSl Rivlin. Large elastic deformations of isotropic materials. i. fundamental concepts. *Philosophical Transactions of the Royal Society of London. Series A, Mathematical and Physical Sciences*, 240(822):459–490, 1948.

[77] Yu-Yun Lin and Chung-Yuen Hui. Cavity growth from crack-like defects in soft materials. *International journal of fracture*, 126(3):205–221, 2004.

[78] AN Gent and Chi Wang. Fracture mechanics and cavitation in rubber-like solids. *Journal of Materials Science*, 26(12):3392–3395, 1991.

[79] Santanu Kundu and Alfred J Crosby. Cavitation and fracture behavior of polyacrylamide hydrogels. *Soft Matter*, 5(20):3963–3968, 2009.

[80] ML Williams and RA Schapery. Spherical flaw instability in hydrostatic tension. *International Journal of Fracture Mechanics*, 1(1):64–72, 1965.

[81] Jessica A Zimberlin, Naomi Sanabria-DeLong, Gregory N Tew, and Alfred J Crosby. Cavitation rheology for soft materials. *Soft Matter*, 3(6):763–767, 2007.

[82] Xavier Poulain, Victor Lefevre, Oscar Lopez-Pamies, and K. S. Ravi-Chandran. Damage in elastomers: nucleation and growth of cavities, micro-cracks, and macro-cracks. *International Journal of Fracture*, 205(1):1–21, 2017.

[83] Jin Young Kim, Zezhou Liu, Byung Mook Weon, Tal Cohen, Chung-Yuen Hui, Eric R Dufresne, and Robert W Style. Extreme cavity expansion in soft solids: damage without fracture. *arXiv preprint arXiv:1811.00841*, 2018.

[84] Robert W Style, Tianqi Sai, Nicoló Fanelli, Mahdiye Ijavi, Katrina Smith-Mannschott, Qin Xu, Lawrence A Wilen, and Eric R Dufresne. Liquid-liquid phase separation in an elastic network. *Physical Review X*, 8(1):011028, 2018.

[85] Kathryn A Rosowski, Tianqi Sai, Robert W Style, and Eric R Dufresne. Elastic ripening and inhibition of liquid-liquid phase separation. *arXiv preprint arXiv:1907.08465*, 2019.

[86] Kia Bertula, Lahja Martikainen, Pauliina Munne, Sami Hietala, Juha Klefstrom, Olli Ikkala, and Nonappa. Strain-stiffening of agarose gels. *ACS Macro Letters*, 8:670–675, 2019.

[87] Martin M Chui, Ronald J Phillips, and Michael J McCarthy. Measurement of the porous microstructure of hydrogels by nuclear magnetic resonance. *Journal of colloid and interface science*, 174(2):336–344, 1995.

[88] Philip Serwer and Shirley J Hayes. Exclusion of spheres by agarose gels during agarose gel electrophoresis: dependence on the sphere's radius and the gel's concentration. *Analytical biochemistry*, 158(1):72–78, 1986.

[89] Valéry Normand, Didier L Lootens, Eleonora Amici, Kevin P Plucknett, and Pierre Aymard. New insight into agarose gel mechanical properties. *Biomacromolecules*, 1(4):730–738, 2000.

[90] D Taylor. Predicting the fracture strength of ceramic materials using the theory of critical distances. *Engineering Fracture Mechanics*, 71(16-17):2407–2416, 2004.

[91] David Taylor. The theory of critical distances. *Engineering Fracture Mechanics*, 75(7):1696–1705, 2008.

[92] Cambridge University Engineering Department. Materials data book. *Mater Courses*, pages 1–41, 2003.

[93] Xiao Yu, Changgeng Liu, David C Clark, and Myung K Kim. Measurement of young's modulus of polyacrylamide gel by digital holography. In *Digital Holography and Three-Dimensional Imaging*, page DTuC32. Optical Society of America, 2011.

[94] L Benguigui. Comparison between the elasticity of polyacrylamide and polyacrylic gels. *Journal de Physique II*, 5(3):437–443, 1995.

[95] H Cease, PF Derwent, HT Diehl, J Fast, and D Finley. Measurement of mechanical properties of three epoxy adhesives at cryogenic temperatures for ccd construction. *Fermi Lab Report Fermilab-TM-2366-A*, 2006.

[96] Keiichi Shirasu, Akihiro Nakamura, Go Yamamoto, Toshio Ogasawara, Yoshinobu Shimamura, Yoku Inoue, and Toshiyuki Hashida. Potential use of cnts for production of zero thermal expansion coefficient composite materials: An experimental evaluation of axial thermal expansion coefficient of cnts using a combination of thermal expansion and uniaxial tensile tests. *Composites Part A: Applied Science and Manufacturing*, 95:152–160, 2017.

[97] Mariola Pawlaczyk, Monika Lelonkiewicz, and Michał Wieczorowski. Age-dependent biomechanical properties of the skin. *Advances in Dermatology and Allergology/Postepy Dermatologii i Alergologii*, 30(5):302, 2013.

[98] Jae Young Rho, Richard B Ashman, and Charles H Turner. Young's modulus of trabecular and cortical bone material: ultrasonic and microtensile measurements. *Journal of biomechanics*, 26(2):111–119, 1993.

[99] Hai-Ping Cheng and Graham C Walker. Succinoglycan is required for initiation and elongation of infection threads during nodulation of alfalfa byrhizobium meliloti. *Journal of bacteriology*, 180(19):5183–5191, 1998.

[100] Philipp A Jaeger, Cameron McElfresh, Lily R Wong, and Trey Ideker. Beyond agar: gel substrates with improved optical clarity and drug efficiency and reduced autofluorescence for microbial growth experiments. *Appl. Environ. Microbiol.*, 81(16):5639–5649, 2015.

[101] Rashed Noor, Zahidul Islam, Saurab Kishore Munshi, and Farjana Rahman. Influence of temperature on escherichia coli growth in different culture media. *J Pure Appl Microbiol*, 7(2):899–904, 2013.

[102] Olivia J McQuestin, Craig T Shadbolt, and Tom Ross. Quantification of the relative effects of temperature, ph, and water activity on inactivation of escherichia coli in fermented meat by meta-analysis. *Appl. Environ. Microbiol.*, 75(22):6963–6972, 2009.

[103] JWT Wimpenny, L Leistner, Linda V Thomas, AJ Mitchell, K Katsaras, and Petra Peetz. Submerged bacterial colonies within food and model systems: their growth, distribution and interactions. *International journal of food microbiology*, 28(2):299–315, 1995.

[104] Nadine Pernodet, Mounir Maaloum, and Bernard Tinland. Pore size of agarose gels by atomic force microscopy. *Electrophoresis*, 18(1):55–58, 1997.

[105] Janaky Narayanan, Jun-Ying Xiong, and Xiang-Yang Liu. Determination of agarose gel pore size: Absorbance measurements vis a vis other techniques. In *Journal of Physics: Conference Series*, volume 28, page 83. IOP Publishing, 2006.

[106] Diarmuid Lloyd. Mg1655-pch60 strain characterisation. `wiki.ed.ac.uk/display/DLR/Strain+characterisation`. Accessed: 14/05/17.

[107] Pavel Tomancak, Jan Huisken, Peter Gabriela Pitrone, Kevin Eliceiri, Johannes Schindelin, Luke Stuyvenberg, Michael Weber, Vineeth Surendranath, and Stephan Preibisch. Open spim, step by step assembly. `http://openspim.org/Step_by_step_assembly`. Accessed: 2017-05-04.

[108] Orazio Svelto and David C Hanna. *Principles of lasers*, volume 1. Springer, 2010.

[109] Omar E Olarte, Jordi Andilla, Emilio J Gualda, and Pablo Loza-Alvarez. Light-sheet microscopy: a tutorial. *Advances in Optics and Photonics*, 10(1):111–179, 2018.

[110] Pavel Tomancak, Jan Huisken, Peter Gabriela Pitrone, Kevin Eliceiri, Johannes Schindelin, Luke Stuyvenberg, Michael Weber, Vineeth Surendranath, and Stephan Preibisch. Spim optics 101. `https://openspim.org/SPIM_Optics_101/Theoretical_basics`. Accessed: 25/05/20.

[111] Loling Song, EJ Hennink, I Ted Young, and Hans J Tanke. Photobleaching kinetics of fluorescein in quantitative fluorescence microscopy. *Biophysical journal*, 68(6):2588–2600, 1995.

[112] S Hell, G Reiner, C Cremer, and Ernst HK Stelzer. Aberrations in confocal fluorescence microscopy induced by mismatches in refractive index. *Journal of microscopy*, 169(3):391–405, 1993.

[113] Pe Matula, M Kozubek, F Staier, and M Hausmann. Precise 3d image alignment in micro-axial tomography. *Journal of microscopy*, 209(2):126–142, 2003.

[114] Stephan Preibisch, Stephan Saalfeld, Johannes Schindelin, and Pavel Tomancak. Software for bead-based registration of selective plane illumination microscopy data. *Nature methods*, 7(6):418–419, 2010.

[115] Stephan Preibisch, Fernando Amat, Evangelia Stamataki, Mihail Sarov, Robert H Singer, Eugene Myers, and Pavel Tomancak. Efficient bayesian-based multiview deconvolution. *Nature methods*, 11(6):645, 2014.

[116] Martin A Fischler and Robert C Bolles. Random sample consensus: a paradigm for model fitting with applications to image analysis and automated cartography. *Communications of the ACM*, 24(6):381–395, 1981.

[117] F Benvenuto and A Ferrari. Joint myopic deconvolution. *Inverse Problems*, 26(10):105011, 2010.

[118] RK Pina and RC Puetter. Bayesian image reconstruction: The pixon and optimal image modeling. *Publications of the Astronomical Society of the Pacific*, pages 630–637, 1993.

[119] Jan Kotera, Filip Šroubek, and Peyman Milanfar. Blind deconvolution using alternating maximum a posteriori estimation with heavy-tailed priors. In *International Conference on Computer Analysis of Images and Patterns*, pages 59–66. Springer, 2013.

[120] William Hadley Richardson. Bayesian-based iterative method of image restoration. *JoSA*, 62(1):55–59, 1972.

[121] Leon B Lucy. An iterative technique for the rectification of observed distributions. *The astronomical journal*, 79:745, 1974.

[122] Lawrence A Shepp and Yehuda Vardi. Maximum likelihood reconstruction for emission tomography. *IEEE transactions on medical imaging*, 1(2):113–122, 1982.

[123] Stephan Preibisch, Fernando Amat, Evangelia Stamataki, Mihail Sarov, Robert H Singer, Eugene Myers, and Pavel Tomancak. Efficient bayesian-based multiview deconvolution. *Nature methods*, 11(6):645, 2014.

[124] Brian F Hutton, H Malcolm Hudson, and Freek J Beekman. A clinical perspective of accelerated statistical reconstruction. *European journal of nuclear medicine*, 24(7):797–808, 1997.

[125] Nobuyuki Otsu. A threshold selection method from gray-level histograms. *IEEE transactions on systems, man, and cybernetics*, 9(1):62–66, 1979.

[126] Stefan Van der Walt, Johannes L Schönberger, Juan Nunez-Iglesias, François Boulogne, Joshua D Warner, Neil Yager, Emmanuelle Gouillart, and Tony Yu. scikit-image: image processing in python. *PeerJ*, 2:e453, 2014.

[127] Jeff Gostick, Zohaib Khan, Thomas Tranter, Matthew Kok, Mehrez Agnaou, Mohammadamin Sadeghi, and Rhodri Jervis. Porespy: A python toolkit for quantitative analysis of porous media images. *Journal of Open Source Software*, 4(37):1296, 2019.

[128] Pauli Virtanen, Ralf Gommers, Travis E. Oliphant, Matt Haberland, Tyler Reddy, David Cournapeau, Evgeni Burovski, Pearu Peterson, Warren Weckesser, Jonathan Bright, Stéfan J. van der Walt, Matthew Brett, Joshua Wilson, K. Jarrod Millman, Nikolay Mayorov, Andrew R. J. Nelson, Eric Jones, Robert Kern, Eric Larson, CJ Carey, İlhan Polat, Yu Feng, Eric W. Moore, Jake Vand erPlas, Denis Laxalde, Josef Perktold, Robert Cimrman, Ian Henriksen, E. A. Quintero, Charles R Harris, Anne M. Archibald, Antônio H. Ribeiro, Fabian Pedregosa, Paul van Mulbregt, and SciPy 1. 0 Contributors. SciPy 1.0: Fundamental Algorithms for Scientific Computing in Python. *Nature Methods*, 17:261–272, 2020.

[129] Ivo F Sbalzarini and Petros Koumoutsakos. Feature point tracking and trajectory analysis for video imaging in cell biology. *Journal of structural biology*, 151(2):182–195, 2005.

[130] Sergey Bochkanov. Fast rbf interpolation/fitting. `http://www.alglib.net/interpolation/fastrbf.php#rbfml`. Accessed: 14/05/17.

[131] K Katsaras and L Leistner. Distribution and development of bacterial colonies in fermented sausages. *Biofouling*, 5(1-2):115–124, 1991.

[132] Eran Bouchbinder, Ariel Livne, and Jay Fineberg. Weakly nonlinear fracture mechanics: experiments and theory. *International journal of fracture*, 162(1-2):3–20, 2010.

[133] Ariel Livne, Gil Cohen, Oded Ben-David, and Jay Fineberg. Universal aspects of dynamic fracture in brittle materials. In *AIP Conference Proceedings*, volume 742, pages 122–131. American Institute of Physics, 2004.

[134] Zong-Xian Zhang. *Rock fracture and blasting: theory and applications*. Butterworth-Heinemann, 2016.

[135] Carey D Nadell, Knut Drescher, and Kevin R Foster. Spatial structure, cooperation and competition in biofilms. *Nature Reviews Microbiology*, 14(9):589, 2016.

[136] Pierre Aymard, David R Martin, Kevin Plucknett, Tim J Foster, Allan H Clark, and Ian T Norton. Influence of thermal history on the structural and mechanical properties of agarose gels. *Biopolymers: Original Research on Biomolecules*, 59(3):131–144, 2001.

[137] Jesse V Jokerst, Jie Chou, James P Camp, Jorge Wong, Alexis Lennart, Amanda A Pollard, Pierre N Floriano, Nicolaos Christodoulides, Glennon W Simmons, Yanjie Zhou, et al. Location of biomarkers and reagents within agarose beads of a programmable bio-nano-chip. *Small*, 7(5):613–624, 2011.

[138] Galina Reshes, Sharon Vanounou, Itzhak Fishov, and Mario Feingold. Cell shape dynamics in escherichia coli. *Biophysical journal*, 94(1):251–264, 2008.

[139] BS Gardiner, BP Boudreau, and BD Johnson. Growth of disk-shaped bubbles in sediments. *Geochimica et Cosmochimica Acta*, 67(8):1485–1494, 2003.

[140] Bernard P Boudreau, Chris Algar, Bruce D Johnson, Ian Croudace, Allen Reed, Yoko Furukawa, Kelley M Dorgan, Peter A Jumars, Abraham S Grader, and Bruce S Gardiner. Bubble growth and rise in soft sediments. *Geology*, 33(6):517–520, 2005.

[141] CK Algar and BP Boudreau. Stability of bubbles in a linear elastic medium: Implications for bubble growth in marine sediments. *Journal of Geophysical Research: Earth Surface*, 115(F3), 2010.

[142] CK Algar and BP Boudreau. Transient growth of an isolated bubble in muddy, fine-grained sediments. *Geochimica et Cosmochimica Acta*, 73(9):2581–2591, 2009.

[143] Maxime Lefranc and Elisabeth Bouchaud. Mode i fracture of a biopolymer gel: Rate-dependent dissipation and large deformations disentangled. *Extreme Mechanics Letters*, 1:97–103, 2014.

[144] Rong Long, Maxime Lefranc, Elisabeth Bouchaud, and Chung-Yuen Hui. Large deformation effect in mode i crack opening displacement of an agar gel: A comparison of experiment and theory. *Extreme Mechanics Letters*, 9:66–73, 2016.

[145] Rong Long, Venkat R Krishnan, and Chung-Yuen Hui. Finite strain analysis of crack tip fields in incompressible hyperelastic solids loaded in plane stress. *Journal of the Mechanics and Physics of Solids*, 59(3):672–695, 2011.

[146] Hyock-Ju Kwon, Allan D Rogalsky, Christopher Kovalchick, and Guruswami Ravichandran. Application of digital image correlation method to biogel. *Polymer Engineering & Science*, 50(8):1585–1593, 2010.

[147] Fred D Farrell, Matti Gralka, Oskar Hallatschek, and Bartlomiej Waclaw. Mechanical interactions in bacterial colonies and the surfing probability of beneficial mutations. *Journal of The Royal Society Interface*, 14(131):20170073, 2017.

[148] Jin Young Kim, Zezhou Liu, Byung Mook Weon, Tal Cohen, Chung-Yuen Hui, Eric R Dufresne, and Robert W Style. Extreme cavity expansion in soft solids: Damage without fracture. *Science advances*, 6(13):eaaz0418, 2020.

[149] Bradley R Frieberg, Ray-Shimry Garatsa, Ronald L Jones, John O Bachert, Benjamin Crawshaw, X Michael Liu, and Edwin P Chan. Viscoplastic fracture transition of a biopolymer gel. *Soft Matter*, 14(23):4696–4701, 2018.

[150] HJ Kwon, Allan D Rogalsky, and Dong-Woo Kim. On the measurement of fracture toughness of soft biogel. *Polymer Engineering & Science*, 51(6):1078–1086, 2011.

[151] Tristan Baumberger and Olivier Ronsin. From thermally activated to viscosity controlled fracture of biopolymer hydrogels, 2009.

[152] Hannah H Tuson, George K Auer, Lars D Renner, Mariko Hasebe, Carolina Tropini, Max Salick, Wendy C Crone, Ajay Gopinathan, Kerwyn Casey Huang, and Douglas B Weibel. Measuring the stiffness of bacterial cells from growth rates in hydrogels of tunable elasticity. *Molecular microbiology*, 84(5):874–891, 2012.

[153] Z-H Jin and CT Sun. On j-integral and potential energy variation. *International journal of fracture*, 126(1):L19–L24, 2004.

[154] Huifang Song and Sheik S Rahman. An extended j-integral for evaluating fluid-driven cracks in hydraulic fracturing. *Journal of Rock Mechanics and Geotechnical Engineering*, 10(5):832–843, 2018.

[155] Shelby B Hutchens, Sami Fakhouri, and Alfred J Crosby. Elastic cavitation and fracture via injection. *Soft matter*, 12(9):2557–2566, 2016.

[156] Steven Yang, Davin Bahk, Jiho Kim, Amrita Kataruka, Alison C Dunn, and Shelby B Hutchens. Hydraulic fracture geometry in ultrasoft polymer networks. *International Journal of Fracture*, 219(1):89–99, 2019.

[157] Christopher W Barney, Carey E Dougan, Kelly R McLeod, Amir Kazemi-Moridani, Yue Zheng, Ziyu Ye, Sacchita Tiwari, Ipek Sacligil, Robert A Riggleman, Shengqiang Cai, et al. Cavitation in soft matter. *Proceedings of the National Academy of Sciences*, 117(17):9157–9165, 2020.

[158] Shabnam Raayai-Ardakani, Zhantao Chen, Darla Rachelle Earl, and Tal Cohen. Volume-controlled cavity expansion for probing of local elastic properties in soft materials. *Soft matter*, 15(3):381–392, 2019.

[159] Shabnam Raayai-Ardakani, Darla Rachelle Earl, and Tal Cohen. The intimate relationship between cavitation and fracture. *Soft matter*, 2019.

[160] Bert Sakmann and Erwin Neher. Patch clamp techniques for studying ionic channels in excitable membranes. *Annual review of physiology*, 46(1):455–472, 1984.

[161] Y Zhao, S Inayat, DA Dikin, JH Singer, RS Ruoff, and John B Troy. Patch clamp technique: review of the current state of the art and potential contributions from nanoengineering. *Proceedings of the Institution of Mechanical Engineers, Part N: Journal of Nanoengineering and Nanosystems*, 222(1):1–11, 2008.

[162] A Oesterle. Pipette cookbook 2015: P-97 & p-1000 micropipette pullers. *California: Sutter Instrument*, 2015.

[163] Richard Plenderleith, Thomas Swift, and Stephen Rimmer. Highly-branched poly (n-isopropyl acrylamide) s with core–shell morphology below the lower critical solution temperature. *RSC Advances*, 4(92):50932–50937, 2014.

[164] Phillip Greenspan, Eugene P Mayer, and Stanley D Fowler. Nile red: a selective fluorescent stain for intracellular lipid droplets. *The Journal of cell biology*, 100(3):965–973, 1985.

[165] Katsuyoshi Nishinari, Mineo Watase, and Kazuyoshi Ogino. On the temperature dependence of the elasticity of agarose gels. *Die Makromolekulare Chemie: Macromolecular Chemistry and Physics*, 185(12):2663–2668, 1984.

[166] Akira Takada. Experimental study on propagation of liquid-filled crack in gelatin: Shape and velocity in hydrostatic stress condition. *Journal of Geophysical Research: Solid Earth*, 95(B6):8471–8481, 1990.

[167] Jean de Bremond d'Ars, Nicholas T Arndt, and Erwan Hallot. Analog experimental insights into the formation of magmatic sulfide deposits. *Earth and Planetary Science Letters*, 186(3-4):371–381, 2001.

[168] Tohru Watanabe, Takayuki Masuyama, Kazuhiro Nagaoka, and Tsuyoshi Tahara. Analog experiments on magma-filled cracks. *Earth, planets and space*, 54(12):1247–1261, 2002.

[169] S Sutera and R Skalak. The history of poiseuille's law annual review of fluid mechanics. *25: 1*, 19, 1993.

[170] Li Hong Zhao and Pabitra N Sen. Hydrophobicity and biofilm growth of e-coli rp437, mg1655 and b/r. *MRS Online Proceedings Library Archive*, 1466, 2012.

[171] Katsutoshi Hori and Shinya Matsumoto. Bacterial adhesion: from mechanism to control. *Biochemical Engineering Journal*, 48(3):424–434, 2010.

[172] MC Van Loosdrecht, Johannes Lyklema, Willem Norde, Gosse Schraa, and AJ Zehnder. The role of bacterial cell wall hydrophobicity in adhesion. *Applied and environmental microbiology*, 53(8):1893–1897, 1987.

[173] Joseph D Berry, Michael J Neeson, Raymond R Dagastine, Derek YC Chan, and Rico F Tabor. Measurement of surface and interfacial tension using pendant drop tensiometry. *Journal of colloid and interface science*, 454:226–237, 2015.

[174] Krishnamurthy Sainath and Pallab Ghosh. Electrical properties of silicone oil-water interface in the presence of ionic surfactants and salt: Importance in the stability of oil-in-water emulsions. *Chemical Engineering Communications*, 201(12):1645–1663, 2014.

[175] Tom EP Kimkes and Matthias Heinemann. How bacteria recognise and respond to surface contact. *FEMS Microbiology Reviews*, 44(1):106–122, 2020.

[176] Nobuyuki Ichinose and Hodaka Ura. Concentration dependence of the sol-gel phase behavior of agarose-water system observed by the optical bubble pressure tensiometry. *Scientific reports*, 10(1):1–9, 2020.

[177] Jian Ping Gong. Why are double network hydrogels so tough? *Soft Matter*, 6(12):2583–2590, 2010.

[178] Qiang Chen, Hong Chen, Lin Zhu, and Jie Zheng. Fundamentals of double network hydrogels. *Journal of Materials Chemistry B*, 3(18):3654–3676, 2015.

[179] Qiang Chen, Lin Zhu, Chao Zhao, Qiuming Wang, and Jie Zheng. A robust, one-pot synthesis of highly mechanical and recoverable double network hydrogels using thermoreversible sol-gel polysaccharide. *Advanced materials*, 25(30):4171–4176, 2013.

[180] Gunjan Agarwal, Nicolas Besuchet, Basile Audergon, and Jamie Paik. Stretchable materials for robust soft actuators towards assistive wearable devices. *Scientific reports*, 6(1):1–8, 2016.

[181] Dilshad Ahmad, Sujit Kumar Sahu, and Karali Patra. Fracture toughness, hysteresis and stretchability of dielectric elastomers under equibiaxial and biaxial loading. *Polymer Testing*, 79:106038, 2019.

[182] Seunghyun Lee and Matt Pharr. Sideways and stable crack propagation in a silicone elastomer. *Proceedings of the National Academy of Sciences*, 116(19):9251–9256, 2019.

[183] Silvia Marqués and Juan L Ramos. Transcriptional control of the pseudomonas putida tol plasmid catabolic pathways. *Molecular microbiology*, 9(5):923–929, 1993.

[184] Orakan Hanpanich, Pravit Wongkongkatep, Thunyarat Pongtharangkul, and Jirarut Wongkongkatep. Turning hydrophilic bacteria into biorenewable hydrophobic material with potential antimicrobial activity via interaction with chitosan. *Bioresource technology*, 230:97–102, 2017.

[185] Xian-Kui Zhu and James A Joyce. Review of fracture toughness (g, k, j, ctod, ctoa) testing and standardization. *Engineering Fracture Mechanics*, 85:1–46, 2012.

[186] Rong Long and Chung-Yuen Hui. Fracture toughness of hydrogels: measurement and interpretation. *Soft Matter*, 12(39):8069–8086, 2016.

[187] HW Greensmith. Rupture of rubber. x. the change in stored energy on making a small cut in a test piece held in simple extension. *Journal of Applied Polymer Science*, 7(3):993–1002, 1963.

[188] Daniel R King, Tao Lin Sun, Yiwan Huang, Takayuki Kurokawa, Takayuki Nonoyama, Alfred J Crosby, and Jian Ping Gong. Extremely tough composites from fabric reinforced polyampholyte hydrogels. *Materials horizons*, 2(6):584–591, 2015.

[189] Antonella Cristiano, Alba Marcellan, Bert J Keestra, Paul Steeman, and Costantino Creton. Fracture of model polyurethane elastomeric networks. *Journal of Polymer Science Part B: Polymer Physics*, 49(5):355–367, 2011.

[190] Ruobing Bai, Baohong Chen, Jiawei Yang, and Zhigang Suo. Tearing a hydrogel of complex rheology. *Journal of the Mechanics and Physics of Solids*, 125:749–761, 2019.

[191] Jun Young Chung, Ido Regev, and L Mahadevan. Spontaneous exfoliation of a drying gel. *Soft matter*, 12(37):7855–7862, 2016.

[192] JA Caskey and WB Barlage Jr. An improved experimental technique for determining dynamic surface tension of water and surfactant solutions. *Journal of Colloid and Interface Science*, 35(1):46–52, 1971.

[193] Valerio Sorichetti, Virginie Hugouvieux, and Walter Kob. Determining the mesh size of polymer solutions via the pore size distribution. *Macromolecules*, 53(7):2568–2581, 2020.

[194] RB King, RH Crabtree, CM Lukehart, DA Atwood, and RA Scott. Bond energies. *Encyclopedia of Inorganic Chemistry*, pages 1–4, 2006.

[195] Shruti Rattan and Alfred J Crosby. Effect of polymer volume fraction on fracture initiation in soft gels at small length scales. *ACS Macro Letters*, 8(5):492–498, 2019.

[196] P-G de Gennes. Fracture d'un adhésif faiblement réticulé. *Comptes rendus de l'Académie des sciences. Série 2, Mécanique, Physique, Chimie, Sciences de l'univers, Sciences de la Terre*, 307(19):1949–1953, 1988.

[197] Chung-Yuen Hui, Da-Ben Xu, and Edward J Kramer. A fracture model for a weak interface in a viscoelastic material (small scale yielding analysis). *Journal of applied physics*, 72(8):3294–3304, 1992.

[198] Tristan Baumberger, Christiane Caroli, and David Martina. Fracture of a biopolymer gel as a viscoplastic disentanglement process. *The European Physical Journal E*, 21(1):81–89, 2006.

[199] Shaoting Lin, Xinyue Liu, Ji Liu, Hyunwoo Yuk, Hyun-Chae Loh, German A Parada, Charles Settens, Jake Song, Admir Masic, Gareth H McKinley, et al. Anti-fatigue-fracture hydrogels. *Science advances*, 5(1):eaau8528, 2019.

[200] Albert Edward Green and Wolfgang Zerna. *Theoretical elasticity*. Courier Corporation, 1992.